INHIBITION MECHANISM OF AMINO ACIDS AGAINST CARBONATION-INDUCED CORROSION IN REINFORCED CONCRETE

A Thesis

Submitted in fulfilment of the requirements for the award of the degree of

DOCTOR OF PHILOSOPHY

by

Purnima

(Roll No. 901802007)

Under the Guidance of

Dr. Shweta Goyal
Professor
Department of Civil Engineering

Dr. Vijay Luxami
Professor
School of Chemistry and Biochemistry

Department of Civil Engineering
Thapar Institute of Engineering and Technology, Patiala-147004
Punjab, India
November 2023

CERTIFICATE

Certified that the thesis "**INHIBITION MECHANISM OF AMINO ACIDS AGAINST CARBONATION-INDUCED CORROSION IN REINFORCED CONCRETE**" which is submitted by **Ms. Purnima**, in fulfilment of the requirement for the award of the degree of **Doctor of Philosophy** in the Department of Civil Engineering, Thapar Institute of Engineering & Technology, Patiala, India is a record of the candidate's own independent and original research work carried out by her under my supervision and guidance. The matter embodied in this thesis has not been submitted in part or full to any other University or Institute for the award of any degree.

3/11/2023

Dr. Shweta Goyal
Professor
Department of Civil Engineering
Thapar Institute of Engineering & Technology, Patiala

Vijay Luxami 3/11/23

Dr. Vijay Luxami
Professor
School of Chemistry and Biochemistry
Thapar Institute of Engineering & Technology, Patiala

DECLARATION

I hereby declare that the work presented in the thesis entitled "**INHIBITION MECHANISM OF AMINO ACIDS AGAINST CARBONATION-INDUCED CORROSION IN REINFORCED CONCRETE**" in the fulfilment of the requirement for the award of the Degree of **Doctor of Philosophy** in the Department of Civil Engineering, Thapar Institute of Engineering & Technology, Patiala, is an authentic record of my own work during the period July 2018 to September 2023, under the supervision of **Dr. Shweta Goyal**, Professor, Department of Civil Engineering and **Dr. Vijay Luxami**, Professor, School of Chemistry and Biochemistry at Thapar Institute of Engineering & Technology, Patiala. The material embodied in this thesis has not been submitted in parts or full in any other university or institute for the award of any degree in India or Abroad.

Place: Patiala
Date: 03-11-2023

Purnima
Department of Civil Engineering
Thapar Institute of Engineering & Technology

ACKNOWLEDGEMENT

A doctoral thesis is often described as a solitary endeavour; however, the long list that follows definitely proves the opposite. In pursuit of this academic endeavor, I have been exceptionally fortunate because inspiration, guidance, direction, cooperation, love, and care came my way in abundance. I feel nostalgic when I look back on my journey and find it difficult to put into words the never-ending support and encouragement of everyone throughout these years.

First and foremost, I would like to praise and thank God, the Almighty, who has granted countless blessing, knowledge, and opportunity, so that I have been finally able to accomplish the thesis. It was a long and challenging yet very fulfilling journey that I completed with His blessings.

With a deep gratitude, I want to state that I am grateful for the continuous support, insight and patience of my supervisors, Dr Shweta Goyal, Professor, Department of Civil Engineering and Dr. Vijay Luxami, Professor, School of Chemistry and Biochemistry, without their constant trust and, sometimes, gentle prodding, this thesis would not have been completed. Your advice on both research as well as on my career have been invaluable. I must also thank Dr Arpit Goyal, Assistant Professor, Department of Civil Engineering, for his interim supervision, especially during the final year of my research.

I am privileged to thank Dr. Prem Pal Bansal, Professor & Head (Department of Civil Engineering) for providing excellent academic and lab facilities. I am thankful to doctoral committee members Dr. Shruti Sharma, Professor , Dr. Trishna Chaudhary, Professor and Dr. Soumen Basu, Professor for their constant support and constructive criticism during my study.

I am deeply indebted to Dr. Ashish Kumar Tiwari for his unwavering support; without his efforts, my job would have been undoubtedly more difficult. I greatly benefited from his keen scientific insight, his knack of solving seemingly intractable practical problems and his ability to put complex ideas/problems into simple terms. Dr. Tiwari has served as both: a mentor and a friend, whenever needed. I thereby express my heartfelt gratitude for his role in keeping me inspired and providing stability during the challenging phases of my academic journey.

I thank my fellow lab-mates of Advanced Durability lab: Dr. Kamal Anand, Mr. Himanshu Guleria and Ms. Zinnia Nannar, for the stimulating discussions. I sincerely acknowledge, Dr. Kamal Anand who has been an extremely reliable source of practical scientific knowledge. His persistent encouragement to accomplish tasks ahead of schedule have been invaluable to my progress. Also, I thank my fellow researchers at TIET, Shubham Dangwal, Ritika Singla, Harvinder Singh, Ramneek Sidhu and Sanjoli Jain for stirring discussions and all the fun we had during the last five years. A special mention to Ms. Sonia Wadhwa who helped me with the development of inhibition mechanism and provided a helping hand during my lab work at Chemistry Department. I owe a word of thanks to Mr. Gurjeet and Mr. Ram Sumiran.

I find it difficult to express in words, my sincere sense of indebtedness towards my parents. My unquestionable gratitude is for the never-ending love and support of my father Mr. Ashok Kumar and mother Dr. Pernita Dogra; both emotionally and financially. My father is my backbone, and my mother is the pillar of my strength. I consider myself lucky to have such supportive and loving parents.

I would like to extend my gratitude to my younger brother, Mr. Nikhil Dogra, for supporting me throughout my life and taking care of our parents (singlehandedly) during my absence. I am grateful to one another person: my sister and my dearest friend, Ms. Neha Malia for helping me academically, emotionally, financially and in all the other ways possible. This journey would never have been completed without both of you by my side. I extend my respect to my other family members for their unconditional love.

Finally, I wish to acknowledge all those whose names have not been figured here but who helped me in any form during my research work.

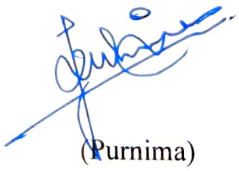

(Purnima)

Place: Patiala

Date: 03-11-2023

ABSTRACT

Deterioration of reinforced concrete (RC) structures, due to exposure of steel reinforcing bar (rebar) to aggressive environment, is a major cause of concern in terms of durability and overall structural integrity. The two main aggressive environments for rebar corrosion are the ingress of chloride ions and carbonation. While the former cause pitting corrosion and localized breakdown of passive film, the latter results in a uniform corrosion of the rebar surface.

Protection of RC against corrosion can be done by employing various techniques. Amongst all, application of corrosion inhibitors is found to be one of the most effective in terms of cost, application, environment and ease of handling. Corrosion inhibitors are chemicals that can effectively reduce the corrosion rate even when used in small quantities. The inhibition characteristics depend on their molecular structure, polarity and presence of heteroatoms. On the basis of their mode of application, they are generally categorized as admixed inhibitor or surface applied inhibitors. The major advantage of using surface applied inhibitor is that, it does not cause any negative affect on the concrete properties. Another advantage of surface applied inhibitors is that they can be used as repair strategy (i.e., application after the steel has reached active corrosion state). Present study explores the potential of these surface applied inhibitor inhibitors to act as repair measure.

Eight different amino acids, that are 100 % environmentally safe, economically viable, namely, Serine (*Ser*), Cysteine (*Cys*), Phenylalanine (*Phe*), Tryptophan (*Trp*), Aspartic Acid (*Asp*), Glutamic Acid (*Glu*), Asparagine (*Asn*) and Glutamine (*Gln*) were selected on the basis of the presence of heteroatoms in their molecular structure and their solubility in high pH simulated concrete pore solution. The effectiveness of the selected compounds to reduce the carbonation-induced corrosion rates was assessed by conducting tests on steel in simulated concrete pore solution as well as concrete. The study was divided into three levels; pore solution test, migration studies and eventual application on reinforced concrete (RC) surface. In Level 1, the corrosion inhibition efficiency and corrosion inhibition mechanism were determined by conducting electrochemical testing and surface analysis tests, respectively. In Level 2, the percolation ability of the amino acids and percolation of CO_2 through concrete (in presence and absence of amino acids) was determined by conducting ultra-violet visible spectroscopic analysis and carbonation depth test, respectively. Finally, in Level 3, the efficient amino acids from Level 1 (that performed well during concrete simulated pore solution test)

and Level 2 (that percolated well through concrete) were applied on RC specimens and their ability to re-passivate the corroding rebars was assessed. Accelerated carbonation tests on the specimens were carried out by placing them in carbonation chamber where CO_2 concentration was 5 %, temperature was 30 °C and relative humidity was 60 – 70 %. The corrosion rate was determined at regular intervals and once, active corrosion of rebars was confirmed, amino acids were applied on the specimens and left in laboratory environment to ensure sufficient percolation for 15 days. The specimens were again kept in the carbonation chamber and corrosion rates were again monitored.

The effectiveness of the repair system was also determined by applying the corrosion inhibitors on a carbonation-induced corroding site structure. An un-sheltered corroding RC slab situated at Civil Engineering Department, Thapar Institute of Engineering and Technology, Punjab, India was repaired.

Results of the study conducted reveal that most of the amino acids when used as surface applied corrosion inhibitors are capable of reducing the corrosion rates under carbonation conditions in laboratory specimens as well as on-site.

LIST OF PUBLICATIONS

The following publications in peer reviewed journals are the outcome of the present research work:

1. **Purnima**, Shweta Goyal and Vijay Luxami. "Exploring the corrosion inhibition mechanism of Serine (Ser) and Cysteine (Cys) in alkaline concrete pore solution simulating carbonated environment." *Construction and Building Materials* 384 (2023): 131433. https://doi.org/10.1016/j.conbuildmat.2023.131433 **Impact Factor: 7.4**

2. **Purnima**, Shweta Goyal and Vijay Luxami. "Corrosion inhibition mechanism of aromatic amino acids for steel in alkaline pore solution simulating carbonated concrete environment." *Materials and Corrosion* (2023). https://doi.org/10.1002/maco.202313949 **Impact Factor: 1.8**

3. **Purnima**, Ashish Kumar Tiwari, Shweta Goyal and Vijay Luxami. "Developing the inhibition mechanism for amide-based amino acids in carbonated concrete environment and assessing the migration ability in concrete." *Journal of Building Engineering* (2023): 107048. https://doi.org/10.1016/j.jobe.2023.107048 **Impact Factor: 6.4**

TABLE OF CONTENTS

LIST OF FIGURES

LIST OF TABLES

CHAPTER 1 : INTRODUCTION

1.1 GENERAL

Reinforced concrete is the most versatile, economical, and successful construction material; used worldwide from many decades. The widespread adoption and utilization of this material surged due to its manifold structural advantages. Concrete's strong compression capabilities are effectively enhanced by steel's capacity to withstand substantial tensile loads. The synergy of these two elements yields adequate strength, stability, and durability to reinforced concrete (RC) structures. However, it is challenged by various factors like inadequate material selection, poor workmanship, inadequate design, and more severe environmental conditions than anticipated and/or combination of the mentioned factors *(Heiyantuduwa et al., 2006).* As a consequence, the service life of the RC structure gets adversely affected.

The major cause of deterioration in RC structures is due to corrosion-induced damage of the reinforcement bars (rebars) (*Ahmad, 2003*). In the concrete pore solution with pH between 12.5 to 13.5, a stable passive film typically forms on the surface of the rebar, rendering it in a passive state with a very low corrosion rate (*Gao et al., 2023*). However, when aggressive ions from the external environment infiltrate the concrete matrix and reach the rebar surface, the passive film is disrupted, initiating corrosion and subsequently accelerating the corrosion rate of the embedded rebar. Two primary factors which instigate corrosion damage in RC are carbon dioxide (CO_2) and chloride ions (*Angst et al., 2009; Cao et al., 2019; Liu et al., 2016*). Carbonation induced by CO_2 reduces the alkalinity of the concrete pore solution, causing the breakdown of the passive film and resulting in uniform corrosion damage of the rebar. In contrast, chloride ions, due to their small ion radius and high chemical reactivity, readily diffuse through defects in the passive film, directly reaching the rebar surface. This occurrence induces and intensifies localized corrosion damage to the rebar. Furthermore, the stress associated with the volume expansion of the corrosion products can lead to the formation of cracks and subsequent spalling of the concrete cover (*Xu et al., 2023*). This, in turn, may further accelerate the corrosion damage to the rebars.

As per a report by NACE, the worldwide economic burden associated with corrosion-related distress in RC structures is estimated at approximately 2.5 trillion US dollars, equivalent to 3.4 % of the global Gross Domestic Product (GDP). The annual cost of corrosion in India is

projected to reach approximately 1670 billion US dollars *(Koch et al., 2016)*. This substantial financial burden emphasizes the critical need for corrosion protection in all nations.

1.2 SCOPE AND OBJECTIVE OF THE PRESENT RESEARCH WORK

The construction industry accounts for 38% of the global CO_2 emissions in particular, the cement industry contributes to ≈8% of global anthropogenic CO_2 emissions *(Nie et al., 2022)*. The use of supplementary cementitious materials (SCMs) such as fly ash, slag, limestone calcined clay in making cement is one way to reduce the carbon footprint. To curb the impact on carbon footprint, the cement industry worldwide is bound to use SCMs in a big way. Concretes with SCMs can exhibit significant delay in the ingress of chlorides towards the embedded steel and hence, delay the initiation of chloride-induced corrosion in RC structures *(Joseline & Pillai, 2020)*. However, their resistance against the ingress of carbonation is not that promising *(Dhanya et al., 2019)*.

Many parts of India experience hot & humid and composite climates which are favorable for carbonation in concrete and the subsequent carbonation-induced corrosion of rebars embedded in concrete. The reinforced concrete (RC) structures, made with SCM-based concrete in the past 20-50 years are undergoing carbonation-induced corrosion. But at the same time, it is vital to reduce the clinker content in cement so as to reduce the CO_2 emission *(Angulo Ramirez et al., 2023)*. Hence, the immediate challenge to the researchers and the practitioners is to restore such corroding structures and also, to produce durable concrete with low clinker ratio for future use.

Out of all the restoration techniques available, the implementation of surface applied corrosion inhibitors (SACoI) presents a technically viable approach for restoration of RC structures; providing ease of application, cost-effectiveness, and efficiency of protection *(Jiang et al., 2017; Priya & Rao, 2017; Zheng et al., 2012).* These compounds are chemicals which after being surface applied on concrete, are expected to penetrate through the cover, reach the rebar level and reduce the ionic movement on the metal surface. The presence of functional groups greatly influences the inhibition mechanism by the SACoI. Depending upon the type of functional groups, the compounds are generally classified as inorganic and organic inhibitors. While many inorganic compounds are reported to be toxic (humans as well as environment); organic compounds pose no such threat to the environment *(Chigondo & Chigondo, 2016; Zomorodian et al., 2021).* This category of environmentally benign corrosion inhibitors (CoI) is known as “Green

Corrosion Inhibitors". They are naturally occurring substances that are biodegradable and do not contain heavy metals or other toxic compounds. Green CoI's contain polar functional groups (e.g.–NH2, –OH, -SH, –COOH), heteroatoms (e.g., P, S, N and O) and benzene ring which facilitates exquisite surface coverage and protection to metal in corrosive media. The green CoI compounds get adsorbed on the metal surface by sharing of un-bonded electrons, hydrogen bonding or van der waals forces *(Zomorodian et al., 2021)*.

In this regard, amino acids stand as promising candidates because of the presence of similar components along with additional traits of being completely soluble in aqueous media, economically viable, easy to produce with high purity, non-toxic and considered as ecologically safe compounds. The structure of a typical amino acid comprises central carbon atom (called α-carbon) to which a carboxylic group (–COOH) and an amine group ($–NH_2$) are attached; the other two bonds of α-carbon are satisfied by a hydrogen atom and a side chain (called as 'R' group). The 'R' group may be alkyl (aliphatic) or aryl (aromatic) in nature with different functional groups. The nature/presence of additional functional group(s) in the side chain decides the chemical property of each amino acid and makes them unique from one another. Therefore, the capability of amino acids to restore the passivation of steel was assessed in this study. Also, as amino acids have not been used as CoIs in carbonated concrete environment until now, the mechanism involved in their inhibition is also important to be studied.

Based on the thorough understanding of the above related issues of carbonation-induced corrosion on SCM based concrete and potential ability of the employment of SACoIs to repair such corroding systems, the following objective were outlined:

1. To study the efficiency of amino acids as corrosion inhibitors in carbonated environment.
2. To study the durability performance of concrete using amino acids as migratory corrosion inhibitors.
3. To study the probable mechanisms involved in the inhibition action of amino acids.

1.3 ORIENTATION OF THESIS

The thesis presentation has been divided into seven chapters. In the first chapter, introduction about the topic along with the research objective has been outlined. In the second chapter, basic concepts of corrosion in different environments and extensive review on the application, type and efficiency of CoI's in different environments are presented.

To achieve the stated objectives, the study is divided into three levels: pore solution testing, migration studies through concrete, and application of SACoI on RC surface. Chapters 3 and 4 comprehensively detail the outcomes of Level 1. Chapter 3 discusses the corrosion inhibition capacity of various amino acids through gravimetric and electrochemical tests; while Chapter 4 provides insights about the corrosion inhibition mechanism of amino acids conjectured by performing various surface analysis tests. Chapter 5 shifts the focus to Levels 2 and 3, emphasizing the potential of amino acids to permeate the concrete microstructure and re-passivate corroding rebars. In this phase, amino acids were applied to the surfaces of RC prisms to function as SACoIs for repairing corroded systems.

Further, the effectiveness of the proposed repair system was also determined by applying it on a carbonation-induced corroding site structure. Chapter 6 presents the results from the on-site investigation.

Chapter 7 summarizes the key conclusions drawn from the study and outlines potential avenues for future research. Appendices and a comprehensive list of cited references used in the work are provided at the end.

CHAPTER 2 : LITERATURE REVIEW

2.1 INTRODUCTION

In general, corrosion is a natural phenomenon that converts processed/refined metal to its more stable oxide/carbonated/sulphide form under favorable reactive environment. It can be considered as the main cause of degradation of metal where metal loses its surface area in the form of wastage. Thus, it can be said that no metal is immune to ravages of corrosion process. RC under certain environmental conditions undergo corrosion that effect the structural integrity, strength, durability, and service life of structure. According to NACE report the global cost of corrosion is estimated to be about 2.5 trillion US dollar, which is about 3-4% of global GDP *(Kania, 2023; Sirojiddin, 2023)*. This amount can be minimized by adopting a suitable corrosion control measure. The present chapter deals with the basics of reinforced steel corrosion and the literature review on the effectiveness of corrosion inhibitors for its mitigation.

2.2 CORROSION OF STEEL IN CONCRETE

The corrosion of steel in reinforced concrete (RC) is considered as an electrochemical process with anodes and cathodes formed adjacently on the rebar and are surrounded by the concrete pore solution which acts as the electrolyte allowing the movement of ions between anodic and cathodic sites. Figure 2.1 schematically shows the corrosion of steel in concrete. This electrochemical process involves following reactions:

At anode, iron atoms losses its electron and move into a surrounding concrete as ferrous ions. This process is called half-cell oxidation reaction or anodic reaction (equation 2.1). The electrons remain in the bar and flow to sites called cathodes, where they combine with water and oxygen in the concrete. The reaction at the cathode is called a reduction reaction (eq. 2.2).

$$2Fe \rightarrow 2Fe^{2+} + 4e^{-} \quad \ldots(2.1)$$

$$2H_2O + O_2 + 4e^{-} \rightarrow 4OH^{-} \quad \ldots(2.2)$$

The hydroxyl ions ($4OH^{-}$) are generated in cathodic reaction which increases the local alkalinity and therefore, strengthens the passivity around the steel surface. The anodic and cathodic

reactions are only the first step in the process of creating rust. Several more stages must occur for rust to form. This must be expressed in several ways:

$$2Fe^{2+} + 4OH^{-} \rightarrow 2Fe(OH)_2 \quad \ldots(2.3)$$

$$4Fe(OH)_2 + 2H_2O + O_2 \rightarrow 4Fe(OH)_3 \quad \ldots(2.4)$$

$$2Fe(OH)_3 \rightarrow Fe_2O_3.H_2O + H_2O \quad \ldots(2.5)$$

Un-hydrated ferric oxide (Fe_2O_3) has a volume of about twice than that of steel. When it becomes hydrated, it swells even more and becomes porous. This results in increased volume at steel/concrete interface leading to cracking and spalling of concrete and becomes the cause of corrosion of steel in concrete *(Broomfield, 2006)*.

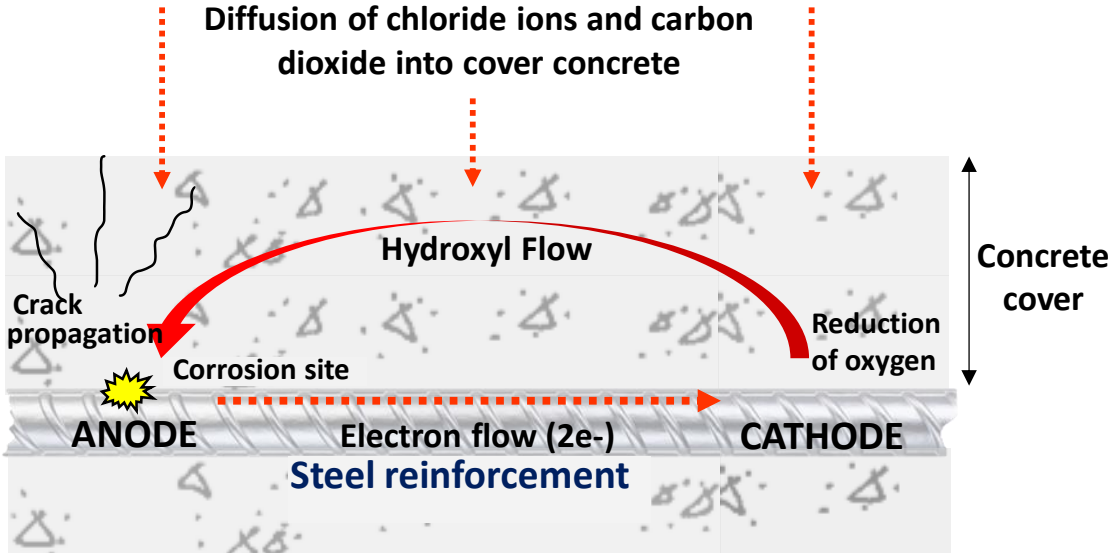

Figure 2.1 Schematic of corrosion of steel reinforcement (rebar) in concrete

2.3 EFFECT OF CORROSION ON SERVICEABILITY OF RC STRUCTURES

Serviceability is the ability of a building product, component, assembly, or construction to fulfill its intended functions as per its design and construction. Corrosion in reinforced concrete (RC) compromises the desired serviceability *(Gilbert, 2011; Stewart & Rosowsky, 1998; Zhu et al., 2016).* The loss of serviceability is typically represented as a two-stage process involving initiation and propagation (as shown in Figure 2.2); proposed by Tuuti in 1982. This model has a widespread acceptance till date *(Omoare et al., 2022).* The two phases can be explained as:

- Initiation: Reinforcement corrosion begins due to attack of aggressive ions, often accompanied by factors like reduced concrete cover, unsuitable concrete quality for environmental conditions, and inadequate compaction and curing. Corrosion starts when aggressive species like chloride and/or carbon dioxide reach the rebar level; more than the threshold values. Conditions like drying shrinkage, flexural stresses, and cracks wide enough to allow ingress of chlorides, oxygen, and moisture can also initiate corrosion. Essentially, this phase involves the availability of oxygen and water.
- Propagation: In this stage, corrosion results in metal loss and increased corrosion product volume (rust). These products induce tensile stresses in the concrete, leading to internal microcracking, surface longitudinal cracking, and spalling. This can accelerate corrosion and weaken the bond between concrete and reinforcement, potentially causing serviceability issues and structural integrity loss.

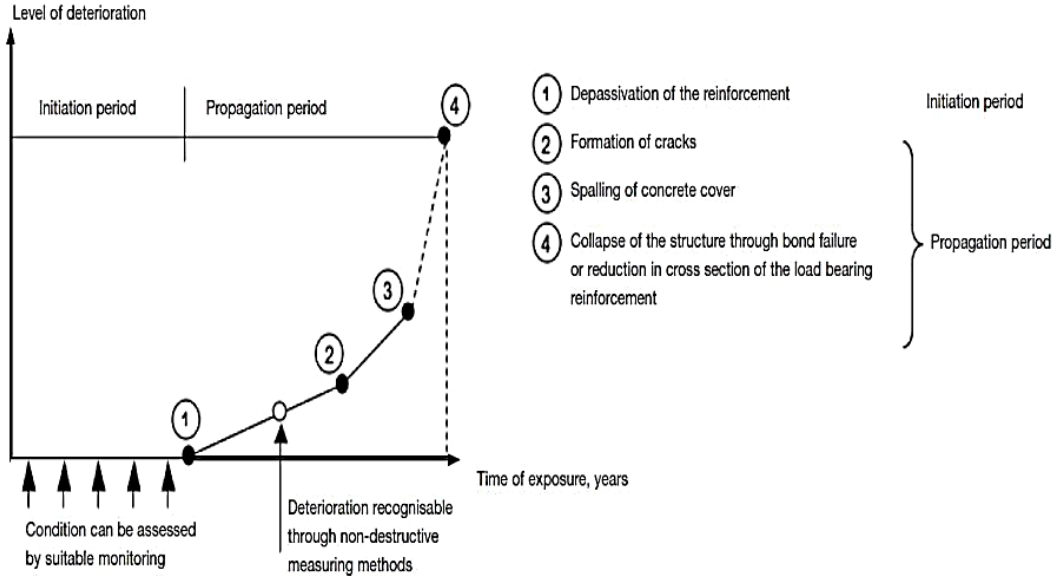

Figure 2.2 Two-stage Tuuti Model *(Omoare et al., 2022)*

Recent experimental investigations have led to the development of new models of corrosion deterioration in RC. *R.E. Melchers* had presented a modified Tuuti model where the author has stated that an additional phase: 'Activation Phase', exists between the initiation phase and the propagation phase. During this phase, the rates of corrosion in RC are seen to be comparable to that of a passive rebar. This happens due to the accumulation of corrosion products in the vicinity of the bars that causes the depletion of oxygen and moisture at the steel-concrete interface. This phenomenon reduced the corrosion reactions at the surface of rebar and hence,

reduced corrosion rates. Further, the rate of corrosion in initiation phase is dependent on the permeability characteristics of concrete. In high-quality, low-permeability concretes, a significant reduction in the corrosion rate becomes evident after the initiation time; while, for poor-quality, higher-permeability concretes, the subsequent corrosion rate tends to be higher. The modified Tuuti model proposed by *R. E. Melchers* is shown in Figure 2.3. The time to corrosion activation and the effect of concrete permeability is distinctly illustrated in the figure.

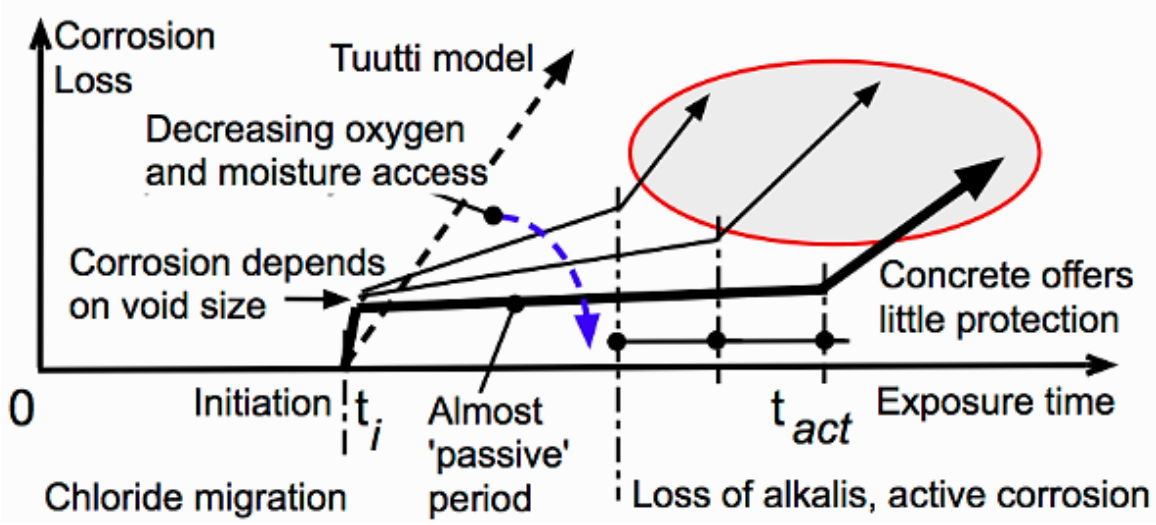

Figure 2.3 Modified Tuuti model proposed by R. E. Melchers (*Melchers, 2020; Melchers & Jeffrey, 2007)*

From the SACoI perspective, the application shall be done during the activation phase or propagation phase in order to control the rates of on-going corrosion.

2.4 CAUSES OF CORROSION

Concrete is an ideal material that protects the steel rebar from corrosion. Environment within concrete is completely alkaline (with pH more than 12) due to which a thin oxide layer ($\gamma Fe_2O_3.H_2O$) is formed over the steel surface that protect steel rebar from corrosion *(Heiyantuduwa et al., 2006; Montemor et al., 2003)*. Yet, the two main reasons that can cause break down this passive layer are: ingress of chloride ions and carbonation. While the former causes pitting corrosion and localized breakdown of passive film, the later results in a uniform corrosion of the rebar surface. The following sections describe the two types of corrosion and their effect on RC.

2.4.1 Chloride Induced Corrosion

The ingress of chloride is the most important factor that is responsible for steel corrosion in RCC structure. It is capable of destroying the passive layer surrounding steel and causing localized corrosion. Figure 2.4 shows the example of corroding rebars due to chloride ions' ingress. The mechanism by which chlorides promote corrosion is still not entirely understood, but the most popular theory is that chloride ions penetrate the protective oxide layer easier than other ions, leaving the steel vulnerable to corrosion. Neville 1995 stated that chloride ions activate the surface of steel to form an anode, the passivated surface being the cathode *(Neville, 1995)*. The reactions involved are as follows:

$$Fe^{2+} + 2Cl^{-} \rightarrow FeCl_2 \quad \ldots(2.6)$$

$$FeCl_2 + 2H_2O \rightarrow Fe(OH)_2 + 2HCl \quad \ldots(2.7)$$

Figure 2.4 Structures corroding due to chloride ions' ingress *(Bisschop, 2016)*

It is clear from equation 2.6 and 2.7 that chloride ions are regenerated so that rust contains no chloride and chloride ions remain available for further corrosion reaction to carry out. When chloride ions enter the concrete and reach steel/concrete interface, the normal passivity is disrupted. This disruption causes an active pitting corrosion initiation on steel surface. As corrosion occurs in a pit, the local pH becomes lower and a more active corrosion process occurs in which more of the surface starts corroding, resulting an increase in the corrosion rate *(Berke & Hicks, 2004)*.

The breakdown of the passive film occurs when the chloride concentration reaches or exceed to a critical value called critical chloride level or chloride threshold level (CTL) *(Bolzoni et al., 2006)*. Thus, the number of chlorides in the concrete and in turn, the number of free chlorides in the aqueous phase (which is partly a function of cement content and partly, cement type) will influence the risk of corrosion.

2.4.2 Carbonation Induced Corrosion

Carbonation is a major process that occurs in RC and limits the service life of RC structures. Since, the focus of this thesis is to determine the effectiveness of surface applied corrosion inhibitors (SACoI) on controlling carbonation-induced corrosion, the process of carbonation corrosion will be dealt with more detail.

Carbonation is a process in which CO_2 from atmosphere penetrates within the concrete through pores and react with hydrated compounds' hydroxide like calcium hydroxide ($Ca(OH)_2$ and calcium silicate hydrate (C-S-H) *(Singh et al., 2017)* gel to form calcium carbonates ($CaCO_3$). The basic chemical reactions involved during carbonation of concrete are:

$$CO_2 + H_2O \rightarrow H_2CO_3 \quad \ldots(2.8)$$

$$H_2CO_3 + Ca(OH)_2 \rightarrow CaCO_3 + 2H_2O \quad \ldots(2.9)$$

$$C\text{-}S\text{-}H + CO_2 + H_2O \rightarrow CaCO_3 + SiO_2 + H_2O \quad \ldots(2.10)$$

The formation of $CaCO_3$ (shown in equation 2.9 and 2.10) is normally responsible for clogging of the microstructure and reducing the porosity of concrete; but the process also reduces the pH from ~13 to pH<9 at the steel-concrete interface. Thus, causing de-passivation of surrounding gamma-ferric oxide layer, known as the 'passive layer' (*B. Q. Dong et al., 2014*). In the presence of adequate O_2 and moisture, the carbonation-induced corrosion starts which also stimulates the development of corrosion-induced cracks running parallel to the rebar. This process is followed by the spalling and delamination of concrete which leads to loss of structural load carrying capability. The cracks, spalling and delamination of concrete is inevitable as the corrosion products formed are nearly six times voluminous than steel before corrosion *(Wong et al., 2010)*. Also, decalcification of C-S-H gel (shown in equation 2.10) may increase the porosity by increasing the number of capillary pores within the concrete pore structure if the amount of un-reacted $Ca(OH)_2$ is less for CO_2 to react. The actions of CO_2 take place even at a small

concentration such as are present in rural air, where the CO_2 content is about 0.003 percent by volume. In an unventilated laboratory, the content may rise above 0.1 per cent. In large cities it varies from 0.3-1 per cent *(Naville, 2011)*. Carbonation occurs progressively from the outside of concrete exposed to CO_2 but does so at a decreasing rate because CO_2 has to diffuse through the pore system, including the already carbonated surface zone of concrete. Figure 2.5 shows the example of corroding rebars due to carbonation.

Carbonation also causes volume reduction in concrete, known as 'carbonation shrinkage'; an irreversible process that occurs over long duration. In some cases, this may result in drying shrinkage also *(Ye et al., 2017)*. Generally, the carbonated layer is more resistant to the ingress of aggressive species as carbonation reduces the permeability of concrete. The rate of carbonation is dependent upon the $Ca(OH)_2$ amount present in concrete. In SCM-based concrete, as the amount of $Ca(OH)_2$ is reduced, the rate of carbonation gets increased.

Figure 2.5 Structures corroding due to carbonation *(Uddin et al., 2013)*

2.4.2.1 Factors Influencing the Rate of Carbonation

Several efforts have been made by the researchers to quantify the carbonation rate within concrete structures. The prevailing approach, widely adopted, expresses the carbonation depth's progression through a power-law relationship, denoted as equation 2.11 *(Kaur et al., 2016)*.

$$D = k\sqrt{t} \qquad \ldots(2.11)$$

Where, D is the measured carbonation depth in 'mm', t is the time in 'years and k is the carbonation depth constant for concrete.

Various more intricate iterations of this correlation exist, which consider the initial alkalinity level and an array of environmental conditions. Nevertheless, for practical contexts, it is commonly asserted that the presented relationship suffices. Further, the carbonation constant 'k' serves as the pivotal determinant governing the rate at which carbonation infiltrates concrete. Numerous factors influence ‘k’, with the most notable among them are:

- ***CO_2 concentration:*** Throughout the 20th century, there was a significant surge in atmospheric CO_2 levels due to industrial emissions. This elevation in CO_2 concentration holds profound significance in the context of advancing the carbonation front. Essentially, a higher atmospheric CO_2 content accelerates the rate of carbonation. Drawing insights from experimental findings conducted under both natural and accelerated conditions, researchers propose that subjecting concrete to 100% CO_2 acceleration results in a carbonation rate approximately 40 times more rapid than what occurs under natural atmospheric conditions *(Sanjuán et al., 2003)*. Furthermore, when exposed to 5% CO_2 acceleration, the carbonation rate is approximately five times that of the natural atmospheric conditions *(Aperador et al., 2012; Montemor et al., 2002)*.

- ***Relative humidity and temperature***: The rate of diffusion of CO_2 through concrete decreases when the relative humidity of the concrete increases. In 100% water saturation conditions, CO_2 can't get inside the concrete at all. However, as water is needed for the carbonation reaction to happen, so it doesn't affect dry concrete (rate of carbonation is negligible). When equilibrium is maintained, the rate of carbonation can be associated with the RH conditions as shown in Figure 2.6 *(Bertolini et al., 2004).* The best conditions for the carbonation process to progress well are when the air's humidity is between 50% and 75%, and the temperature is in the range of 20-30ºC *(Aperador et al., 2012; Montemor et al., 2002).*

- ***Water-cement ratio and curing:*** The physical properties of concrete, including density, porosity, permeability, and diffusivity, are strongly influenced by the water-to-cement (w/c) ratio in the mix. Increasing the w/c ratio, as found by Dong et al. (2014), leads to greater internal porosity and subsequent carbonation *(B. Dong et al., 2014)*. However, the advantages of a lower w/c ratio are only realized with proper curing, as poor curing impedes cement paste hydration and results in a more porous matrix. *Kulakowski et al.* (2009)

discovered that pozzolanic reactions had minimal impact below a w/b ratio of 0.5 but became significant thereafter *(Kulakowski et al., 2009)*. Aguiar and Junior (2013) found higher carbonation diffusion coefficients in unprotected concrete with high w/c ratios *(Aguiar & Júnior, 2013)*, while Bogas et al. (2016) observed increased carbonation coefficients with higher w/c ratios and aggregate porosity *(Bogas et al., 2016)*.

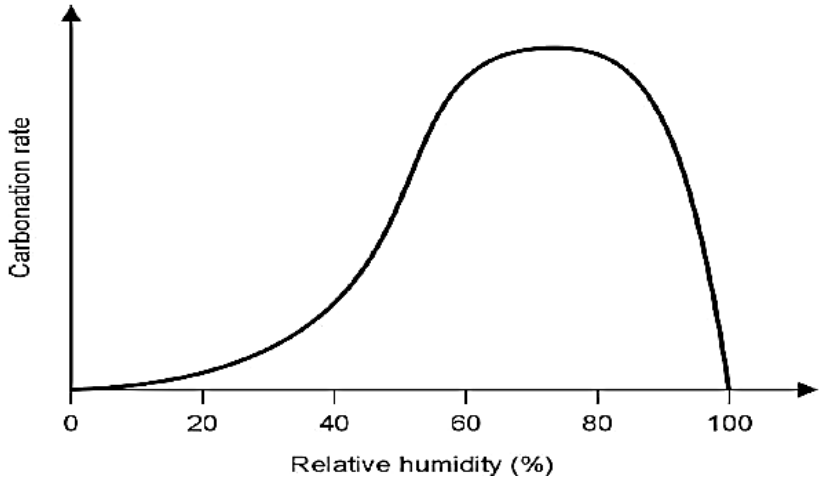

Figure 2.6 Variation in Carbonation rate with RH *(Bertolini et al., 2004)*

- ***Cement composition:*** The choice of cement type significantly impacts carbonation front progression. *Montemor et al*. (2002) found that concrete with Ordinary Portland Cement (OPC) displays better carbonation resistance than pozzolanic cement-based concrete due to availability of $Ca(OH)_2$. CO_2 from the environment reacts with available $Ca(OH)_2$ in OPC and forms an insoluble calcium carbonate ($CaCO_3$) precipitate that has an ability to densify pore structure. Whereas in SCM based concrete system, $Ca(OH)_2$ gets consumed during secondary pozzolanic reactions resulting free carbonation progression *(Montemor et al., 2002)*. *Rabehi et al.* (2013) linked initial absorption, carbonation depth, and compressive strength in concrete made with different cements (OPC and compound cement) *(Rabehi et al., 2013)*. The authors observed faster carbonation in compound cement concrete due to its lower $Ca(OH)_2$ content, providing valuable insights into cement selection for enhanced concrete durability.
- ***SCM addition:*** The use of supplementary cementitious materials, such as silica fume and fly ash, significantly impacts concrete's carbonation behavior. *Leemann et al*. (2015) found that adding minerals like GGBS and silica fume reduced carbonation resistance *(Leemann et al., 2015)*; while, Bogas et al. (2016) reported higher carbonation coefficients with

mineral admixture replacement *(Bogas et al., 2016)*. Further, fly-ash is the most commonly used SCM and fly-ash based concrete (PPC concrete) has shown 2-4 times higher corrosion rates in carbonation corrosive environment than OPC due to higher carbonation rate *(Justnes et al., 2020; Karthick et al., 2016; Królikowski & Kuziak, 2011; Lye et al., 2015; Priya & Rao, 2017).*

2.5 METHODS TO MITIGATE CORROSION

Corrosion inhibition in RC can be achieved by selecting efficient techniques. There are various techniques available that can be effectively used either as preventive or repair strategy. These techniques can be characterized as physical, chemical, and electrochemical techniques. Table 2.1 gives the details of preventive and repair techniques used for corrosion mitigation.

Table 2.1 Corrosion mitigation techniques

S. No.	Preventive Techniques	Repair Techniques
1	High quality and Impermeable concrete	Patch repair
2	Steel coatings	Electrochemical chloride extraction
3	Galvanization protection	Electrochemical re-alkalization
4	Cathodic prevention	Cathodic protection
5	Organic coating on concrete	Corrosion inhibitors
6	Corrosion inhibitors	-

The selection of an effective technique is a strenuous task as each technique has its own merits and demerits. For instance, the challenge with the electrochemical technique is that it requires constant power supply; while physical techniques like coatings on steel and concrete have limited-service life say 10 to 12 years only. Furthermore, methods such as using high quality concrete or galvanized steel need high investment initially. Amongst the available preventive and repair techniques, use of corrosion inhibitors as chemical technique is proved to better solution in terms of inhibition efficiency, cost effectiveness, ease in application and environmental concerns.

2.6 CORROSION INHIBITORS (CoI)

A chemical compound that can effectively decrease the corrosion rate of a corroded system when present at suitable concentration without significantly changing the concentration of any corrosive agent called as corrosion inhibitor (CoI) *(ISO 8044-2020, 2020).* Use of CoI for corrosion

inhibition started in the early 1940's. Initially, their application was limited to oil and gas industry, water treatment plants and chemical related industries only. It was also reported that in oil and gas industry their application could effectively reduce corrosion rate by 90% to 95% *(Elsener, 2000).*

The application of CoI in controlling corrosion of rebar embedded in concrete was first reported in 1960's. In terms of concrete, it can be state that "Corrosion inhibitors are the chemical compounds that reduce corrosion rate significantly without affecting any important property of concrete and without varying the concentration of any corrosive agent" *(Goyal et al., 2021)*. During its early use, CoIs were introduced in concrete in admixed form i.e. mixed during casting process and called as "admixed inhibitors". With time, their importance as a repair material also grew due to their ease in application, cost effectiveness and its inhibition efficiency. While using as repair material, CoI were applied on hardened concrete, allowed to percolate, and called as migratory inhibitors (MCoI) or surface applied inhibitors or penetrating inhibitors. Considering their inhibition mechanism, most of them protect the rebar by forming a stabilized protective film over the its surface; or by reducing the permeability of concrete *(Kaur et al., 2016)*. Basically, CoI reduce the ionic movement on the metal surface by blocking cathodic and/or anodic sites, or prevent corrosion by increasing electrical resistance of the steel surface *(Lee et al., 2018).*

2.7 CLASSIFICATION OF CoI's

On the basis of electrochemical mechanism of action, they can be classified as anodic, cathodic or mixed inhibitor. These inhibitors compound can be organic, or inorganic depending upon their attached functional group and can be used as an admixture or can be applied on hardened concrete surface as migratory inhibitor. All these classifications are discussed in detail in the upcoming sub-sections.

2.7.1 Based on physical mode of application

On the basis of physical mode of application, CoI can be classified as admixed CoI and migratory CoI.

- *Admixed CoI*: Admixed CoI are considered to be a chemical compound that were used as corrosion inhibitors and introduced in concrete during mixing process. From early 1960's commercial CoI were mostly inorganic based namely, salt of nitrite (sodium or calcium),

sodium salt of phosphate, benzoate and chromate and zinc oxide were used as an admixed CoI *(Ann et al., 2006; Gaidis, 2004)*. Whereas, organic compound such as amines, amino-acids, alkanol-amines, unsaturated fatty acid esters of carboxylic acid and fatty acid esters were introduced later as admixed CoI *(De Schutter & Luo, 2004; Jamil et al., 2004; Nmai, 2004).*

- *Migratory CoI*: They are considered to be a compound that is applied on hardened concrete surface and allowed to diffuse through concrete microstructure with time. After the application on the concrete surface, MCoI percolate through the cover concrete and protect steel either by forming a protective layer on rebar *(Ryu et al., 2016)* or/and by reducing the permeability of concrete *(Kaur et al., 2016).* Application of MCoI increases the electrical resistance of steel against corrosion which in turn postpones the initiation of corrosion/reduces the rate of on-going corrosion *(Goyal et al., 2021; Lee et al., 2018).*

Various negative effects on the fresh and hardened concrete properties have been observed when CoI are used in admixed form (Shi et al., 2022) but when employed on to the hardened concrete no such drawbacks have been observed (Kaur et al., 2016; Söylev et al., 2007; Zheng et al., 2012). Thus, it can be said that migratory inhibitors can be employed as a corrosion protection technique that will not cause any detrimental effect on concrete's important properties.

2.7.2 Based on protection mechanism

On the basis of protection mechanism, CoIs can be classified as anodic inhibitors, cathodic inhibitors and mixed inhibitors. Further details of their protection mechanism are discussed below:

- *Protection mechanism of anodic inhibitors:* These corrosion inhibitors also called passivation inhibitor, blocks the anodic sites and supports the natural passivation reaction of metal surface. They help in reducing the corrosion rate by increasing the corrosion potential of steel *(Söylev et al., 2007)*. There are two types of passivating inhibitors: oxidizing ions and non-oxidizing ions. Oxidizing ions are able to passivate in the absence of oxygen (such as chromates and nitrites), while non-oxidizing shows its efficiency in the presence of oxygen (e.g.- phosphates and molybdates) *(Lee et al., 2018)***.** Such inhibitors attack and react with Me^{n+} produced on the anode and form an insoluble hydroxide which is deposited on the steel surface as an impermeable and insoluble to the metallic ions Figure

2.7a shows the mechanism of anodic inhibitors. For the effective inhibition, such inhibitors must be in high concentration within the solution and it should be higher enough to for the perfect inhibition *(Saraswathy & Song, 2007)*. Concentration must be above the critical value because inappropriate concentration affects the formation of film, and leaves site of the metal exposed as it will not cover the complete metal surface, thus causing the localized corrosion *(Dariva & Galio, 2014)*. Some of the examples of anodic inhibitors are nitrates, molybdates, phosphate, chromates, hydroxide and silicates.

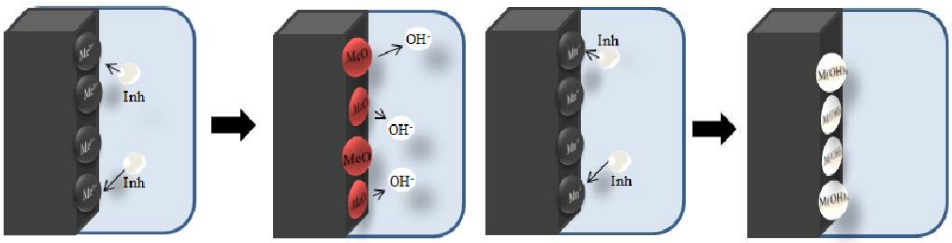

Figure 2.7 Mechanism of action of (a) anodic inhibitor (b) cathodic inhibitor *(Dariva & Galio, 2014)*

- *Protection mechanism of cathodic inhibitor:* Cathodic inhibitors block the cathodic sites thus, preventing the occurrence of cathodic reaction of the metal during the corrosion process. Presence of metal ions in these inhibitors form an insoluble compound that precipitates selectively on cathodic sites and blocks the reduction reaction. These inhibitors are also known as precipitation inhibitors *(Koch et al., 2016)*. Such CoIs deposit over the metal and form an adherent protective film, restricting the diffusion of reducible species in these areas. They reduce the corrosion rate by shifting the corrosion potential towards more negative value. Due to this inhibition mechanism, the concentration of inhibitor is not of much importance as in case of anodic inhibitors and is considered to be more secure than anodic inhibitors in terms of toxicity and negative effect on concrete properties *(Dariva & Galio, 2014)***.** Some effectively used cathodic inhibitors are the salts of magnesium, zinc and nickel. It was also observed that they undergo hard water kind of inhibition mechanism, react with hydroxyl ions of water and form insoluble hydroxide (i.e. $Mg(OH)_2$, $Zn(OH)_2$, $Ni(OH)_2$) which are deposited on the cathodic site on the metal surface which protects it

for being exposed for corrosion process *(Heiyantuduwa et al., 2006)*. Figure 2.7 shows the mechanism of cathodic inhibitors.

- *Protection mechanism of mixed CoI:* Mixed inhibitors are those which are able to block both ongoing cathodic and anodic reactions on the steel surface. Mixed CoIs reduce the corrosion rate by forming a thin adsorbed hydrophobic film on metal surface through adsorption mechanism *(Kondratova et al., 2003)*. Mixed inhibitors are also known as adsorption inhibitors or film-forming inhibitors, as these are the materials consist of hydrophobic group that contains effective polar groups like N, S, and OH. The effectiveness of the film depends upon molecular structure, chemical composition and their affinities for the metal surface *(Magdalena Osial, 2016)*. Organic inhibitors are considered to be a mixed kind of inhibitor and are capable of forming a protecting film over the steel surface. Amines and amino alcohol are the most commonly used mixed type inhibitor, which displace the chloride ions and forms a durable passivating film *(Jamil et al., 2004)*. Organic inhibitors can protect steel by either or both type of adsorption mechanism i.e., chemisorption or physisorption or physio-chemisorption. Chemisorption involves the charge transfer between iron surface and heteroatoms or sharing of charge to form the coordinate bond; whereas, physisorption on steel involves electrostatic interactions between the charges of rebar metal surface and charges of dipoles of organic molecules *(Lee et al., 2018; Magdalena Osial, 2016; Ormellese et al., 2011)*. In physio-chemisorption, both mechanisms occur simultaneously.

2.7.3 Based on functional group present

On the basis of functional group in molecular structure, CoI can be categorized as inorganic CoI and organic CoI. The various functional groups used in the protection of steel along with their type of mechanism are tabulated in Table 2.2.

- *Inorganic CoI*: Amongst various inorganic inhibitors, nitrites stand out as the most used. These inhibitors, mainly added to the blend of fresh concrete as a preventive action, began to be tested in the 1950s. Initially sodium nitrite was studied. However, due to side effects, such as poorer of concrete strength and increased occurrence of the probability of alkali-silica reaction (ASR), which have negative effects on the concrete, it was replaced by calcium nitrite, the first to be widely commercialized on a large

scale. In general, the inorganic inhibitors have cathodic actions or anodic action. Inorganic compounds such as nitrite, nitrate, chromate, and dichromate have been extensively investigated as inhibitors. Toxicity of these compounds limits their use in corrosion protection.

- *Organic CoI:* The use of organic compounds to inhibit corrosion of mild steel and iron has assumed great significance due to their application in preventing corrosion under various corrosive environments. A variety of organic compounds have been reported to be effective as corrosion inhibitors during acidization in industrial cleaning processes *(Al-Mehthel et al. 2009*). The development of corrosion inhibitors is based on organic compounds containing nitrogen, oxygen, sulfur atoms and multiple bonds in the molecules that facilitate adsorption on the metal surface. The corrosion inhibition efficiency of organic compounds is related to their adsorption properties *(Moreno et al., 2004; Ormellese et al., 2009)*. Adsorption depends on the nature and the state of the metal surface on the type of corrosive medium and on the chemical structure of the inhibitor. Studies report that the adsorption of the organic inhibitors mainly depends on some physicochemical properties of the molecule related to its functional groups, to the possible steric effects and electronic density of donor atoms; adsorption is suppose also to depend on the possible interaction of p-orbitals of the inhibitor with d-orbitals of the surface atoms, which induce greater adsorption of the inhibitor molecules onto the surface of carbon steel, leading to the formation of a corrosion protecting film.

Organic inhibitors cover the entire surface area of the corroding metal with a thick film consisting of several monolayers and change the structure of the double layer at the metal interface, decreasing depolarization rate. They may also act as a barrier film by blocking anodic and cathodic active sites or decreasing electro active species transport rate to or from the metal surface. Morris et al. 2004 states that organic inhibitors offer protection by adsorbing and forming a protective film on the passive steel surface *(Moreno et al., 2004)*. The organic molecule usually contains a polar group that adsorbs on the metal and a non-polar, hydrophobic chain oriented perpendicular to this surface. On one hand these chains act by repelling aggressive contaminants dissolved in the pore solution and on the other, forming a tight film (barrier) on the metallic surface.

Table 2.2 Various functional groups used as corrosion inhibitor.

	Functional group	Molecular structure	Inhibition type	Inhibition mechanism
Inorganic	Nitrites	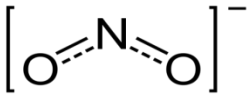	Anodic	Nitrite ions battle with chloride ions for ferrous ions to form protective ferric oxide film
	Molybdate	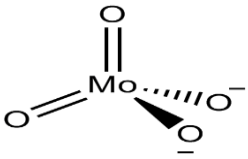	Anodic	Molybdate ions help promote the passivation of steel's active site through more effective film. They lessen the passivation current through the passive film, increase passive region area by displacing the corrosion potentials to more anodic values, promoting re-passivation of corroded regions
	Chromates	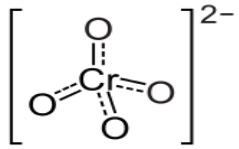	Anodic	Chromate helps maintain rebar in passive state preventing its disruption and impairment that can instigatepitting.
	Phosphates	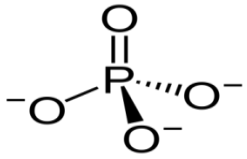	Anodic	By forming a passive layer of Fe_3O_4, γFe_2O_3, and $FePO_4.H_2O$.
	Phosphates		Mixed or cathodic	Behave as cathodic inhibitors for $[PO_4^{-3}]/[Cl^-]<$ 0.6; behave as mixed inhibitors for $[PO4^{-3}]/[Cl^-]$ >0.6.
Organic	Amines	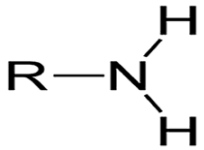	Mixed	Adsorption process is instigated as lone pairs of electron and polar nature become the reaction centre.

	Carboxylic Acid	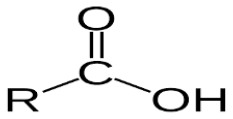	Mixed	A protective barrieris established on the steel surface through chelation process; carboxyl group (-COOH) being a good chelating agent.
	Aldehyde	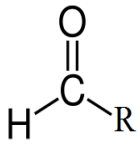	Mixed	Physically absorb on the steel surface via functional aldehydic oxygen atom of the inhibitor
Multifunctional	Alkanolamines	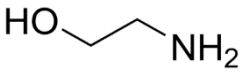	Mixed	Amino-alcohols absorb on the steel surface forming a film against erodic species like chloride or sulphate ions
	Amine-ester	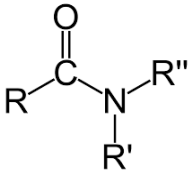	Mixed	The amine compound acts as an inhibitor while the carboxylate ester compound blocks the concrete pores, which further blocks the ingress of the aggressive ions; exhibiting a twin action of inhibition.

2.8 PERFORMANCE OF CoI IN DIFFERENT ENVIRONMENTS

In the past, there are enormous list of chemicals which has been used either in chloride contaminated environment or in carbonated environment. They introduced in concrete either in admixed form or by applying on surface as migratory inhibitor. The performance of these inhibitors in different corrosive environment has been discussed in detail in succeeding sections.

2.8.1 Performance of CoI in chloride contaminated environment

In early studies, the main focus of researchers was to investigate the effectiveness of these chemicals in chloride rich environment, as it was considered that most prominent cause of corrosion in RC. For preventing chloride induced corrosion they admixed during mixing process and for the repairing of chloride effected structure, chemicals were applied on the concrete surface after the corrosion encountered. Rosenberg and Gaidis, 1979 studied the effectiveness of calcium nitrite on chloride contaminated concrete structure by using polarization technique. From the study it was concluded that calcium nitrite reduces the corrosion rate by 15 times when admixed at 2%

and 4% *concentration (Rosenberg & Gaidis, 1979)*. Ormellese et. al, 2009 investigated the influence of calcium nitrite-based inhibitor to study their effectiveness against rebar corrosion along with three different organic inhibitors *(Ormellese et al., 2009)*. They observed that, all the inhibitors were effective in reducing the corrosion rate, but calcium nitrate-based inhibitor showed the best inhibition effect among these in terms of reducing corrosion rate as well as weight loss of steel but at higher dosage. Similar observations were also made by *(Ann et al., 2006).* They also concluded that the inhibitive effectiveness of calcium nitrate-based inhibitor depends on [NO^-/Cl^-] molar ratio, which should be higher than 0.5-0.6 to prevent corrosion that confirms the study of *Elsener 2000; Berke and Hicks 2004; Sideris and Savva 2005* studied the influence of calcium nitrate based inhibitor on the corrosion of reinforcing steel embedded in 14 mortars and found that the addition of calcium nitrate increases the chloride induced corrosion resistance of all mixtures, but protection offered strongly depends on the quality of cement used. Similar conclusions were also made by *(Montes et al., 2004)*

Apart from nitrite, other inorganic inhibitors such as phosphate, molybdate, chromate has also been investigated extensively in the past. *Zhou et al,* 2015 studied the inhibitive mechanism of NO^{2-} and MoO_4^{2-} on the initiation and propagation of pitting corrosion for mild steel in chloride solution by using electrochemical methods and X-ray photoelectron spectroscopy (XPS) *(Zhou & Zuo, 2015).* Based on the result author concludes that, molybdate able to protect pitting corrosion by effectively promoted passivation of mild steel. *Omotosho et al. 2010* examined the effectiveness of potassium dichromate and potassium chromate inhibitors on the corrosion of steel rebar embedded in concrete (admixed in different concentrations) partially immersed in sulfuric acid and NaCl medium *(Omotosho et al. 2010).* The results acquired showed that there was much less fluctuations observed in the potential readings when the concrete was admixed with CoI. The inhibition mechanism of phosphate is not clearly understood yet. Some researcher reported while using monofluorophosphate, it behaves as an anodic inhibitor and cause formation of passive layer of Fe_3O_4, γFe_2O_3, and $FePO_4.H_2O$ *(Alonso et al., 1996; Chaussadent et al., 2006)*. While another study concludes that this functional group has a dual action i.e. at low value of inhibitor to chloride ratio, phosphate acts as a cathodic inhibitor, whereas at higher ratio its acts as mixed inhibitor. Various researchers studied the inhibition efficiency of phosphate ion in chloride contaminated pore simulating solution, keeping equal concentration of phosphate and chloride ion (i.e.,$[PO_4^{3-}]/[Cl^-] = 1$) *(Dhouibi et al., 2003; Nahali et al., 2014; Yohai et al., 2013).*

In addition to this, some organic inhibitors have also been used effectively to inhibit chloride induced corrosion. DMEA (Dimethyl ethanolamine) and AMA (amino alcohol) were reported to be absorbed on rebar surface forming a protective layer of thickness 2-10 nm. In this study, it was concluded that there is limit in concentration required to for AMA to form protective layer. Higher concentration and higher chloride level did not have any effect on the protective film. Rakanta et al. 2013 concluded that DMEA forms an interfacial layer and able to reduce corrosion rate and mass loss of steel rebar (*Rakanta et al., 2013)*. Gaidis 2004 suggests that amino-alcohol (i.e. ethanolamine and diethanolamine) decreases corrosion by blocking cathodic sites only where O_2 picks up electrons and is reduced to OH^- ions *(Gaidis, 2004).* On the other hand, Jamil et al. 2004 concluded that an inhibitor film was formed on the surface hindering the anodic sites and act as an anodic inhibitor *(Jamil et al., 2004).* Ormellese et al. 2009 studied the inhibition efficiency of several compounds like amines, amino-acids, alkanolamines and carboxylates *(Ormellese et al., 2009).* Carboxylates (mono- and polycarboxylates) was concluded to be the best among all in terms of inhibition capacity. It was found that in spite of the electrostatic character and steric effect of carboxyl group, the carboxylates compounds are also able to form complexes due to chelation process. *Ormellese et al. 2011* studied the inhibition properties of 2 amines, 4 amino acids and 3 carboxylate compounds in pore solutions and concrete with chloride induced corrosion. Test results revealed that amino-acids perform better than amines (Ormellese et al., 2011). Sodium aspartate and sodium glutamate enhanced critical chlorides content upto 0.4 mol/L. after analyzing all the tests performed, sodium glutamate and sodium tartrate were amongst the best inhibiting compounds. Cabrini et al. 2015 investigated the inhibitive property of aspartic acid in comparison with nitrite in alkaline pore solution (chloride containing*) (Cabrini et al., 2015)*. The tests were performed on carbon steel specimens in simulated pore solutions with initial pH range of 12.6 to 13.8 and admixed with critical chloride threshold concentration. The investigation discloses that the aspartate ions probably adsorb on Fe (II) oxide surface due to its chelating property and inhibits corrosion through negative charge repulsion by its non-adsorbed carboxylate group. This may also effectively increase the critical chloride content

2.8.2 Performance of CoI in carbonated environment

Literature on the use of CoI suggest that most of the compounds used to inhibit carbonation induced corrosion was organic based compounds. *Trabanelli et al. 2005* examined the efficacy of benzoic acid (BEN) and its derivatives (2-aminobenzoic acid (2AMB), dicarboxylic acid and

tricyclohexylammonium) in synthetic solution and in carbonated concrete. Electrochemical results concludes that BEN and its derivatives forms a long-lasting layer on the steel surface in synthetic pore solution, but in concrete only benzoic acid and 2-aminobenzoic acid was able to perform efficiently. On comparing two, benzoic acid lost its inhibitive action after 400 days of carbonation exposure, while 2AB maintained its inhibition efficiency (60%) even at the end of testing age. *Criado et al. 2012)* tested combination of disodium glycerophosphate (GPH) with sodium 3 aminobenzoate (3AMB) and sodium N-phenyl anthranilate (PhAMB). Results based on polarization curves and EIS analysis suggests that combination of GPH and PhAMB performs best in low pH environment. Heiyantuduwa et al. (2006) investigates the inhibition performance of commercially available CoI (blend of organic amino-alcohol and inorganic component) in carbonated environment *(Heiyantuduwa et al., 2006)*. The inhibitor was used as MCoI in different concrete mixtures (M20, M30, M40 and M50). From the results it was found that the percolation of compound was most effective in M30 grade of concrete, and its application was helpful in delaying the carbonation induced corrosion. Kaur et al. 2016 assessed the inhibition performance of two generic compounds (ethanolamine and anthranilic acid) along with two commercially available compounds (amine-ether based (COM1) and amino-alcohol based (COM2)) in synthetic pore solution and in concrete as migratory inhibitor. Among the tested inhibitors, both commercial inhibitors and anthranilic acid were able to perform in synthetic pore solution, while in concrete only COM2 and anthranilic acid were able to inhibit carbonation induced corrosion *(Kaur et al., 2016).*

2.9 AMINO ACIDS AS CORROSION INHIBITORS IN CONCRETE

Amino acids are non-toxic, relatively cheap, and easy to produce with purities greater than 99%. They are considered to be more promising green inhibitors *(Eddy, 2010)*. As most of the successful inhibitors known are toxic and non-biodegradable *(Olivares-Xometl et al., 2006),* trends have shifted towards choosing organic, non-toxic and environment friendly corrosion inhibitors (Fu et al., 2011). These compounds were reported to show corrosion resistant behavior on copper, mild steel and aluminum alloy *(Ashassi-Sorkhabi et al., 2004; Blajiev & Hubin, 2004; Eddy, 2011; Zhang et al., 2008).*

In previous literature, attention has been paid towards the inhibition efficiency of amino acids in acidic environments. From the available literature we have developed an understanding

about the factors on which the performance of these compounds would be dependent upon. Some of them are the physicochemical properties of inhibitors, such as functional groups, steric effects, and electronic density at the donor atom, π orbital character and corrosive environment.

Eddy et al, 2011 studied the efficiency of 9 amino acids as corrosion inhibitor in 0.1M H_2SO_4 grouped under 3 skeletons. The first skeleton consisted of serine, cysteine and amino butyric acid; the second had threonine, alanine and valine while the third had all aromatic compounds, namely, phenylalanine, tryptophan and tyrosine. The author used quantum chemical parameters to study the variation of corrosion inhibitors in the 3 different skeletons. The highest inhibition efficiencies were found in skeleton 3 and are attributed to the presence of aromatic rings in the molecules. Performance of skeletons 1 and 2 are powered by the presence of –SH and –OH functional groups. Further literature focused more on the application of amino acids on protection of steel in concrete. Ormellese 2009 studied the inhibition efficiency of 6 different amino acids in 3 different chloride concentrations which were 0.1, 0.3 and 1 mol/L and found that the amino acids showed some inhibition effect, but not sufficient for industrial applications *(Ormellese et al., 2009)*. Heiyantuduwa et al., 2006 studied the effect of a commercial inhibitor which was a blend of an amino acid (organic) and an inorganic constituent. The objective was to not only check the inhibition efficiency but also to evaluate its penetrating capacity. For this purpose, the inhibitor was applied on different grades of concrete in the carbonated and un-carbonated environment. The results indicated that grade and especially the porosity of the concrete was the major factor controlling the percolation capacity of the inhibitor as more compact and high-grade concretes did not allow the blend to percolate any further than a few millimeters. Penetration was most effective in Grade 30 concrete where sufficient amounts of inhibitors were present at all depths up to 60 mm. The penetrating corrosion inhibitor was effective in delaying the onset of corrosion as shown by specimens treated with inhibitor before carbonation.

Laboratory findings indicate that the application of the penetrating corrosion inhibitor prior to carbonation delayed the onset of carbonation-induced corrosion, and after 50 wetting and drying cycles, corrosion rates were at passive levels. Treatment of corroding reinforced concrete with penetrating corrosion inhibitor was able to decrease the corrosion rate under conditions of carbonation-induced corrosion, both for laboratory conditions and site structures. Results indicate that penetrating corrosion inhibitors can be effective, when applied to the surface of existing or

new structures, in extending the useful life of reinforced concrete exposed to carbonation *(Heiyantuduwa et al., 2006). Ormellese et al., 2011* studied the inhibition properties of 2 amines, 4 amino acids and 3 carboxylate compounds in pore solutions and concrete with chloride induced corrosion. Test results revealed that amino acids perform better than amines. Sodium aspartate and sodium glutamate enhanced critical chlorides content upto 0.4 mol/L. after analyzing all the tests performed, sodium glutamate and sodium tartrate were amongst the best inhibiting compounds *(Ormellese et al., 2011). Cabrini et al., 2015* evaluated the inhibition properties of aspartic and lactic acid salts with regard to their effect on critical chloride concentrations, further; he compared the findings with nitrite ions. During tests, chloride ions were progressively added to the synthetic pore solution until all specimens showed localized attack after which the corrosion inhibitors were added. Aspartate ions appear to adsorb on Fe(II) oxide surface due to their chelating properties and exert their inhibiting properties through a negative charge repulsion by their non adsorbed carboxylate group effectively increasing the critical chloride content. This inhibitor was found to be effective in concentration 0.1 M, but its beneficial action decreased when the concentration was increased to 0.5M *(Cabrini et al., 2015)*.

Hamadi et al., 2018 reviewed a number of investigations using glutamic acid as corrosion inhibitor in different environments on different metals. The results indicated that glutamic acid could act as an effective corrosion inhibitor for metals due to its large molecular size and its adsorption on the metal surface by the oxygen atoms that exist in its structure. In some cases, glutamic acid can also show an opposite effect which accelerates the corrosion process; all depend on the operating conditions as the efficiency of those compounds has been found to be greatly influenced by many factors, such as the metal (surface state, chemical nature), the medium (concentration, pH, and temperature), inhibitor (concentration, structure molecular, solubility, the inhibitor-metal surface bonding), immersion time etc. Mechanism of inhibition by glutamic acid is found to be principally due to adsorption of its polar groups onto the metal surface *(Hamadi et al., 2018).*

2.9.1 Inhibition Mechanism of Amino Acids

Principally, the inhibition mechanism proposed by various authors who worked on the application of amino acids on concrete, is adsorption of the inhibitor molecules on the steel's surface either by complex formation or by chelation. However, the in-depth probe regarding the same is an area of

interest. Generally, when used as corrosion inhibitors for metals such as copper, mild steel, aluminum amino acids get adsorbed on the metal surface by the presence of polar atoms i.e., N, O and protective films are formed, and various adsorption isotherms are obeyed. They inhibit corrosion by selectively absorbing it on the metal surface and creating a barrier that prevents access of corrosive agents to the metal surface.

With larger electronegativity and smaller atomic radius, N is more easily absorbed to the steel surface than Cl, thereby preventing the steel surface adsorption of Cl to work on corrosion inhibition. Corrosion inhibition of glycine, leucine, aspartate, arginine, and methionine for Fe was studied by *(Zerfaoui et al., 2004)* which indicated that arginine and methionine containing more N and S did best on corrosion inhibition. When substances containing N absorbed to the steel surface by physical or chemical means, unshared electron pairs of N can be supplied to the outer rail space of iron atoms, and form a dense layer of adsorption film via a coordinate bond with iron atoms. The adsorption film could effectively reduce the chance of corrosion of metal surfaces in contact with the medium, thereby preventing metal corrosion and protecting reinforcement from rust.

2.10 CLOSING REMARKS

This chapter deals with the understanding of basic corrosion mechanisms, causes of rebar corrosion and efficacy of corrosion inhibitors in mitigating the corrosion under various aggressive environments. From the literature, it is clear that previous researchers focused on the use of numerous commercial and generic inhibitors, for protection of RC structures against chloride induced corrosion; nevertheless, also some results about **carbonation induced corrosion** have been got for **commercial inhibitors**. Use of organic type of corrosion inhibitors that are non- toxic and biodegradable is a recent area of interest for researchers. Study of the decades:n mechanism has been the major objective of the study in the past few decades; study of the **inhibition mechanism** is the area of the research that needs to be explored thoroughly. Prediction of the direction of the inhibition reaction and the sites for electrophilic/nucleophilic attacks are yet to be dug deeply. The inhibitors can either be used in admixed form or can be applied to the concrete surface as a migratory inhibitor. The latter is used mostly for the repair purpose and the application of amino acids on concrete to protect the steel rebars from corrosion is a modernistic field but yet to be explored. The **percolation capacity** of the amino acids is still unknown to us. Sometimes the efficiency can

be achieved in simulated pore solution but not in the concrete. The reason of low inhibiting properties in concrete has been attributed to the fact that one of the inhibitor constituents does not reach the embedded steel, reacting with cement paste. Based on the extensive literature review, proposed objectives for the present research work were finalized.

CHAPTER 3 : CORROSION INHIBITION EFFICIENCY OF AMINO ACIDS IN SIMULATED PORE SOLUTION

3.1 GENERAL

The major aim of the present work is to understand the corrosion inhibition efficiency of amino acids as surface applied corrosion inhibitors (SACoI) for the protection of rebar embedded in portland pozzolana cement (PPC) concrete. In particular, the efficiency of the compounds is evaluated when the rebars have de-passivated due to the lowering of pH as carbonation ingresses in PPC concrete. Amino acids are finalized to be used as SACoIs due to their non-toxic nature and presence of multiple functional groups that raise the chances of inhibition efficiency.

For this purpose, the study was divided into majorly three levels of testing: pore solution testing, migration studies and application on concrete.

The current chapter is focused on evaluating the corrosion inhibition efficiency of amino acids in synthetic pore solution simulating carbonated concrete environment (B0) i.e., Level 1 of the study. To achieve the above-mentioned objectives, the work plan for this chapter was divided into two parts: gravimetric testing and electrochemical testing. The gravimetric testing is conducted to acquire the information about the efficient compounds (broadly) while the electrochemical testing is conducted to have an insight about the mechanism of corrosion/inhibition as well as to find the corrosion inhibition efficiency of different compounds. The test regime is presented in Figure 3.1. In reinforced concrete (RC), the actual corrosion phenomena take a little longer for its occurrence. Therefore, alternative ways to introduce corrosion in a relatively smaller duration are thoughtfully formulated to preliminary check the efficiencies of the tested inhibitors in a short period of time. It consists of accessing the effectiveness of selected inhibitors in the simulated concrete pore solution (SCP) which is considered to imitate the pore water chemistry of concrete that normally surrounds the rebar. Although, this system does not represent the actual condition of rebar in concrete, it can be used for comparing the inhibition efficiencies of various tested generic chemicals in relatively shorter time span. The material used in pore solution tests, experimental setup, corrosion monitoring and the test results of pore solution tests are discussed in the succeeding sections.

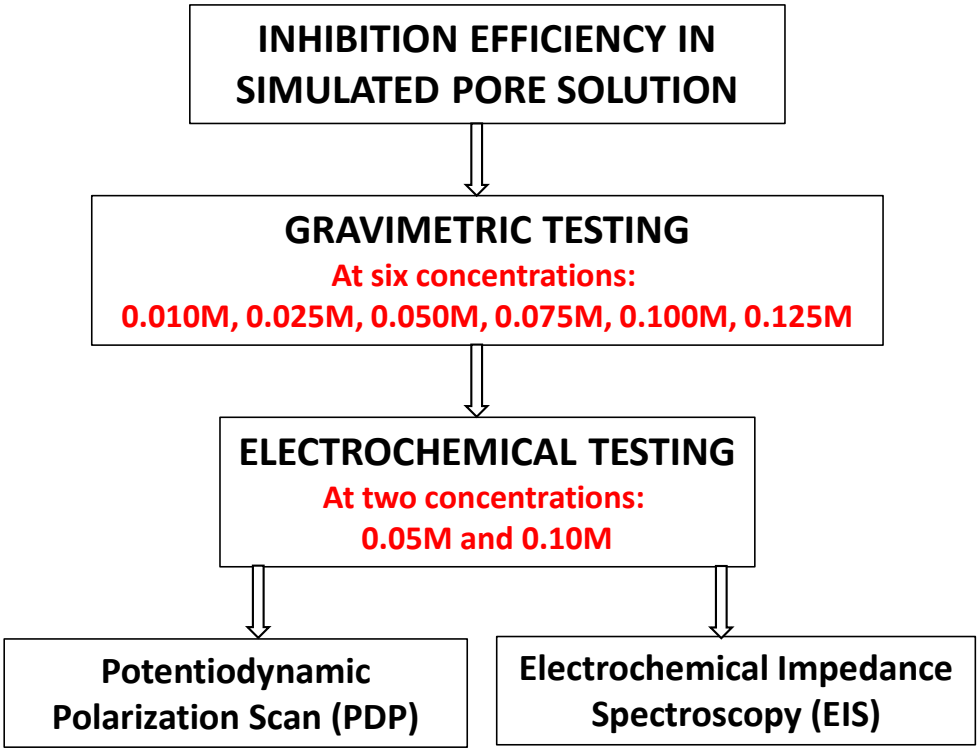

Figure 3.1 Test regime for pore solution testing

3.2 MATERIAL SYSTEM

The major materials used for inhibitor efficiency analysis in Level 1 on pore solution are SCP, bare steel specimens and generic compounds. The details of all these materials are presented in the following sections:

3.2.1 Steel

12 mm and 8 mm diameter ribbed thermos-mechanically treated (TMT) steel bars confirming to IS: 1786:2008 (IS:1786-2008, 2008), widely used in RC structures were tested for their performance in corrosive environment. The chemical composition and properties of steel bars was provided by the manufacturer and is presented in Table 3.1and Table 3.2, respectively.

Table 3.1 Chemical composition of TMT steel bars

Compound (%)	Carbon (C)	Sulphur (S)	Phosphorus (P)	S+P
TMT	0.250	0.040	0.040	0.075

.

Table 3.2 Physical properties of TMT bars

Property	Results obtained	As per IS 1786 Fe 500D (Minimum)
Manufacturer	Tata Tiscon	-
Diameter	12 mm	-
Yield Strength (YS)	520	500
Ultimate Tensile Strength (UTS) (N/mm^2)	580	565
Ratio of UTS/YS	1.15	1.08

3.2.2 Corrosion Inhibitors

Corrosion inhibitor (CoIs), broadly, are the chemicals that have potential to reduce a rate of corrosion by interfering with anodic and/or cathodic reactions of the corrosion process; intended not to detriment any important engineering property of concrete or steel (*Gaidis, 2004*). CoIs are characterized as inorganic and organic on the basis of functional groups present in the compound. Inorganic compounds either inhibit the anodic reaction or cathodic reaction of the corrosion process; while organic compounds inhibit both anodic and cathodic half-cell reactions *(Dariva & Galio, 2014*). Recently, global concerns have developed regarding the toxicity and non-biodegradability induced due to the usage of different categories of CoI *(Chigondo & Chigondo, 2016; Zomorodian et al., 2021*) demanding the replacement of such substances with environmentally benign CoI; such inhibitors are said to be "Green Corrosion Inhibitors". They are naturally occurring substances that are biodegradable and do not contain heavy metals or other toxic compounds. Green CoI's contain polar functional groups (e.g.–NH2, –OH, -SH, –COOH), heteroatoms (e.g., P, S, N and O) and benzene ring which facilitates exquisite surface coverage and protection to metal in corrosive media. The green CoI compounds get adsorbed on the metal surface by sharing of un-bonded electrons, hydrogen bonding or van der waals forces *(Y. Zhang et al., 2021*).

In this regard, amino acids stand as promising candidates because of the presence of similar components along with additional traits of being completely soluble in aqueous media, economically viable, easy to produce with high purity, non-toxic and considered as ecologically safe compounds. The structure of a typical amino acid comprises central carbon atom (called α-carbon) to which a carboxylic group (–COOH) and an amine group (–NH2) are attached; the other two bonds of α-carbon are satisfied by a hydrogen atom and a side chain (called as 'R' group). The 'R' group may be alkyl (aliphatic) or aryl (aromatic) in nature with different functional groups.

The chemical structure of an amino acid is presented in Figure 3.2. The nature/presence of additional functional group(s) in the side chain decides the chemical property of each amino acid and makes them unique from one another.

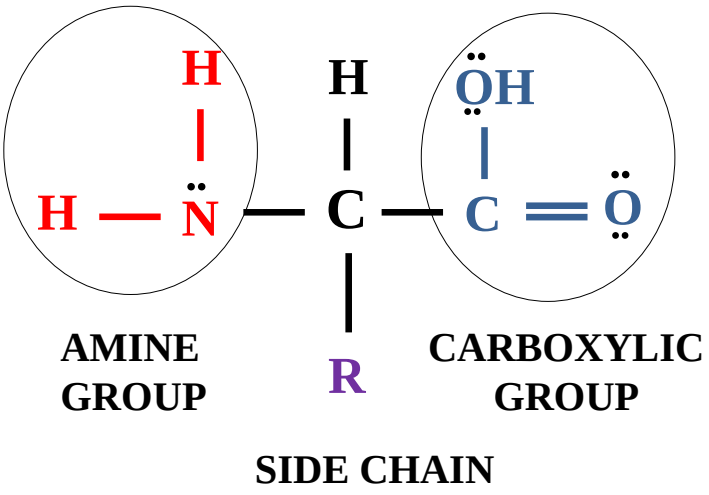

Figure 3.2 Chemical structure of an amino acid

For the current research work, out of twenty amino acids, eight were selected based on their solubility and variation in chemical structure i.e., presence and variability in the positioning of functional groups. These eight amino acids were further divided into four sets based on the above-mentioned characteristics. An important information about the compounds is that the amino caids selected are also categorized based on their polarity and net charge on them. Set 1 and 4 compounds are 'polar with no charge', Set 2 compounds are non-polar and Set compounds are 'polar with negative charge'. These four different sets of amino acids have been organized to bring in more diversity as they have even more functional groups like thiol, alcohol, amide, imidazole, sulfide etc. attached in the chain length. The finalized sets are shown in Table 3.3. The structures, molecular weight and solubility of the compounds are also presented in the same table.

3.2.3 Epoxy

To ensure that the corrosion is imitated over a specific area, only a small portion of the bare steel specimen was exposed to corrosion process and the remaining area was sealed with epoxy. Epoxy used in the present study was available in the market with the trade name "Fevitite Rapid". It was a two-component adhesive, consisting of resin and hardener. Both the components were required to be mixed in equal proportions before use.

Table 3.3 Distribution of amino acids into different sets, their chemical structures, molecular weights and solubility information

Sets	Compound (and its abbreviation)	Chemical structure	Molecular weight (g/mol)	Solubility
SET 1 (Polar with no charge)	Serine (*Ser*)	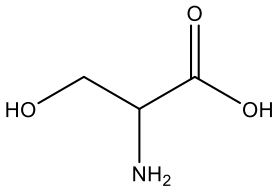	105.09	Freely Soluble
	Cysteine (*Cys*)	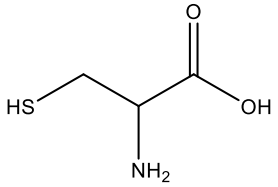	121.16	Freely Soluble
SET 2 (non-polar)	Phenylalanine (*Phe*)	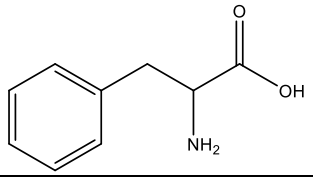	165.19	Freely Soluble
	Tryptophan (*Trp*)	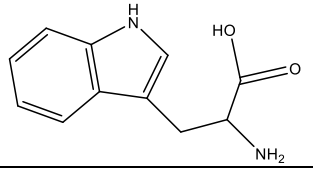	204.23	Hot alcohol & alkali hydroxides
SET 3 (polar with negative charge)	Aspartic Acid (*Asp*)	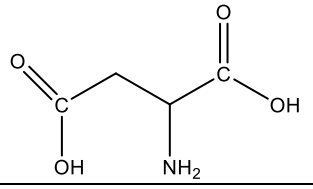	133.10	4.5g/L
	Glutamic Acid (*Glu*)	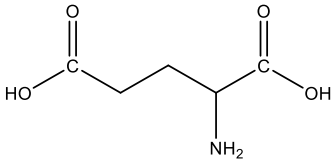	147.13	7.5g/L (20°C)
SET 4 (polar with no charge)	Asparagine (*Asn*)	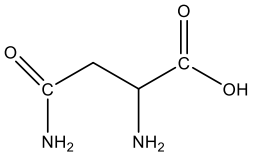	132.10	29.4g/L
	Glutamine (*Gln*)	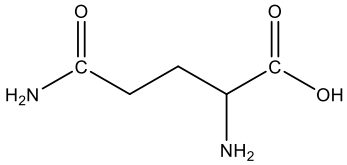	146.14	Freely Soluble

3.2.4 Other chemical

Besides the generic compounds that were investigated for their use as CoIs, some other chemicals were also used for preparation of SCP that mimics the interstitial concrete pore solution. In order to prepare a synthetic pore solution, reagent grade calcium hydroxide ($Ca(OH)_2$), potassium hydroxide (KOH), and sodium hydroxide (NaOH) were used. Grade with this, analytical reagent grade hexane and methanol was used for cleaning of steel specimens and laboratory glassware.

3.3 PREPRATION PROCEDURE

The test set up required preparation of synthetic mixture which could simulate real concrete pore solution that surrounds the steel rebar. Also, the steel bars were to be prepared in order to expose a definite surface area for corrosion. The details of preparation of both bare steel specimens and of synthetic pore solution are presented in the following sections.

3.3.1 Preparation of steel specimens

8 mm diameter bar was cut into coupons of 5 mm height (8ϕ-5 mm), shown in Figure 3.3a, and were utilized for the gravimetric test; while, 12 mm diameter bar was cut into cylindrical samples of 60 mm length (12ϕ-60 mm) and were utilized for the electrochemical testing. In order to ensure an initial rust-free surface, both type of test pieces was rubbed with silicon carbide papers (#400 to #2000) and rinsed with distilled water. The rebars were then degreased with hexane and allowed to dry at room temperature (25 ± 2 °C). Two layers of epoxy was then applied on 12ϕ- 60 mm specimens leaving an exposed length of 4 mm at bottom for active corrosion process. In order to ensure electrical connectivity, a threaded hole was driven on top of the bar. A stainless-steel screw and nut were then inserted into the hole and a copper wire was wound around the nut (shown in Figure 3.3b).

3.3.2 Preparation of Synthetic Pore Solution

Synthetic pore solution simulating carbonated concrete was prepared in two steps; (i) a solution of sodium hydroxide (0.1 M NaOH), potassium hydroxide (0.3 M KOH) and calcium hydroxide (0.01 M $Ca(OH)_2$) was prepared in distilled water mimicking the non-carbonated condition inside the concrete pores, (ii) The prepared solution was bubbled with 99 % pure CO_2 to reach the pH value of near 9 in order to simulate the carbonated state of the pore solution after the diffusion of CO_2 in

real conditions. The prepared pore solution was then filtered using Whatman Filter No. 1 to remove $CaCO_3$ (calcium carbonate) precipitates. The finally obtained solution is referred to as base solution (B0).

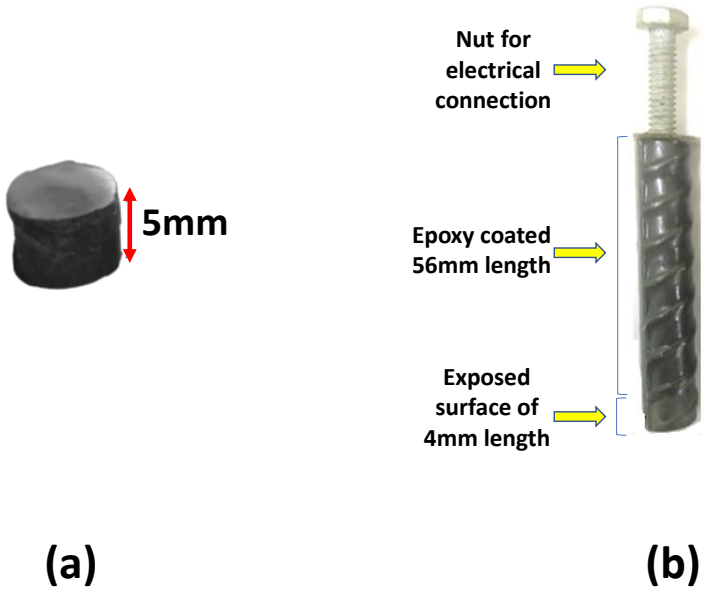

Figure 3.3 Steel specimens prepared for (a) gravimetric test and (b) electrochemical test

Once the corrosive solution was prepared, the CoI was added in B0 in specific concentrations. To find the optimum concentration of the compounds, gravimetric testing was first conducted at six concentrations. The basis of the nomenclature definition of different solutions used in the present study to define the solution composition including the base solution, CoI name and its concentration is illustrated through Figure 3.4. For instance, B0+Ser0.05 signifies that the base solution has *Ser* as CoI at 0.05M concentration admixed in it. After mixing the CoIs in the base solution, a slight change in the pH value of the resultant solution was observed. To maintain pH value of the solution at around 9, the solution was either bubbled with CO_2 (if the inhibitor addition increased the pH value) or sodium hydroxide was added (if the inhibitor addition lowered the pH value).

After mixing the CoIs in the base solution, a slight change in the pH value of the resultant solution was observed. To maintain pH value of the solution at around 9, the solution was either bubbled with CO_2 (if the inhibitor addition increased the pH value) or sodium hydroxide was added (if the inhibitor addition lowered the pH value).

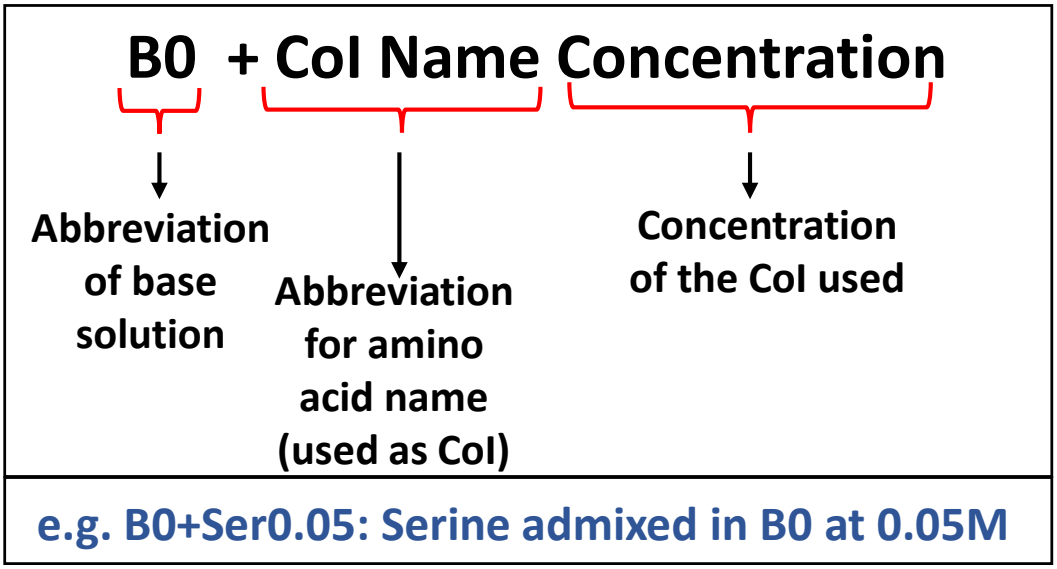

Figure 3.4 Basis of nomenclature adopted to define different tested solutions

3.4 TECHNIQUE EMPLOYED

3.4.1 Gravimetric Testing

The 8ϕ-5mm steel coupons were used for gravimetric analysis. The purpose of the test was (i) to find the ***optimum concentration*** of CoIs for best inhibitory effect by calculating the corrosion rate and (ii) to find the ***type of adsorption*** followed by inhibitors over the steel surface based on the thermodynamic parameters and to find the ***type of isotherm*** obeyed by the selected organic compound. A range of six varying inhibitor concentrations i.e., 0.01 M, 0.025 M, 0.05 M, 0.075 M, 0.1 M and 0.125 M were considered. The test was performed by immersing the pre-weighed steel coupons in their respective test solutions kept in double walled glass vials at room temperature of 25 ± 2 °C for 240 hours (hrs). After that, the coupons were removed from the vials, cleaned as per ASTMG1-03 (*G1-03, 1999*) and re-weighed.

The corrosion rate (CR_{Grav}) was calculated in millimeters per year (mm/yr) by using equation 3.1 (*Tharial Xavier et al., 2015)*:

$$CR_{Grav,} = \frac{87.6 \times (w_1 - w_2)}{D \times A \times T} \quad \ldots 3.1$$

where, w_1 and w_2 are the masses in 'mg' (average of three replicates) of steel coupons before and after immersion in the test pore solutions, D is density of steel in 'gm/cm^3', 87.6 is the

constant for determining the CR in 'mm/yr', A is the area of coupon exposed to the pore solution in 'cm^2' and T is the immersion time in 'hours'.

The degree of surface coverage (θ_{Grav}) by the amino acids were calculated by using the equation 3.2 (Ismail, 2007) :

$$\theta_{Grav} = \left[1 - \left(\frac{CR_i}{CR_0}\right)\right] \quad ...3.2$$

where CR_0 and CR_i is the corrosion rate for steel in B0 and B0 admixed with CoI, respectively.

The values of θ_{Grav} were further used to identify the type of adsorption isotherm obeyed by the inhibitors by calculating the equilibrium constant of adsorption (k_{ads}) and Gibb's free energy ($\triangle G°_{Ads}$) which are discussed in the results section.

Briefly, adsorption isotherm represents the variation in the number of organic molecules adsorbed on the metal surface with change in concentration at a constant temperature. It is a tool that helps to understand (i) if the adsorption is feasible or not (by calculating equilibrium constant of adsorption); (ii) the type of adsorption, physisorption/chemisorption/ physio-chemisorption (by calculating the Gibb's free energy). In corrosion studies, various adsorption isotherms have been employed to identify the adsorption mechanisms by utilizing the values of CR_{Grav} and θ_{Grav} calculated using equations 3.1 and 3.2. Some of the most common isotherms that have been seen to be followed in literature with metals immersed in different corrosive solutions are tabulated in Table 3.4. The table also includes the equation, postulates and important feature of the particular adsorption isotherm.

3.4.2 Electrochemical Testing

The 12ϕ-60mm steel specimens were immersed in B0 in the absence and presence of CoI at various concentrations finalized from the gravimetric test results. The corrosion activity of the specimens was tested at 24 hrs, 72 hrs, 120 hrs and 240 hrs of immersion by conducting electrochemical tests, namely, electrochemical impedance spectroscopy (EIS) and potentiodynamic polarization test (PDP). The sequence of conducting the test was EIS and PDP scan. A three-electrode cell was used for all measurements, which consisted of the steel specimens as working electrode (WE), platinum counter electrode and saturated calomel reference electrode. The test setup is shown in Figure 3.5.

Table 3.4 Most commonly followed adsorption isotherms by corrosion inhibitors on metals immersed in corrosive solutions.

Type of Adsorption Isotherm	Equation	Postulates
Langmuir	$\frac{C}{\theta_{Grav}} = \frac{1}{k_{ads}} + C$	Monolayer adsorption of CoI molecules at specific sites with no lateral interaction between adsorbed molecules.
Frumkin	$log\left[\frac{\theta_{Grav}}{(1-\theta_{Grav})C}\right] = 2.303.logk_{ads} + 2.\alpha.\theta_{Grav}$	The Frumkin adsorption isotherm assumes metallic surfaces to be heterogeneous and the lateral interaction effect among the adsorbed molecules is apparent
Freundlich	$\log\theta_{Grav} = n.logC + logk_{ads}$	Multilayer adsorption of CoI molecules on heterogeneous surfaces of adsorbate. Intensity of adsorption decreases with coverage.
Temkin	$\exp(-2.a.\theta_{Grav}) = k_{ads}.C$	Consider adsorbate-adsorbate interactions. Linear decrease in heat of adsorption with degree of surface coverage will be observed.

where, α is the interaction parameter, n is a constant depending upon the characteristics of the adsorbed molecule and C is the concentration of inhibitor.

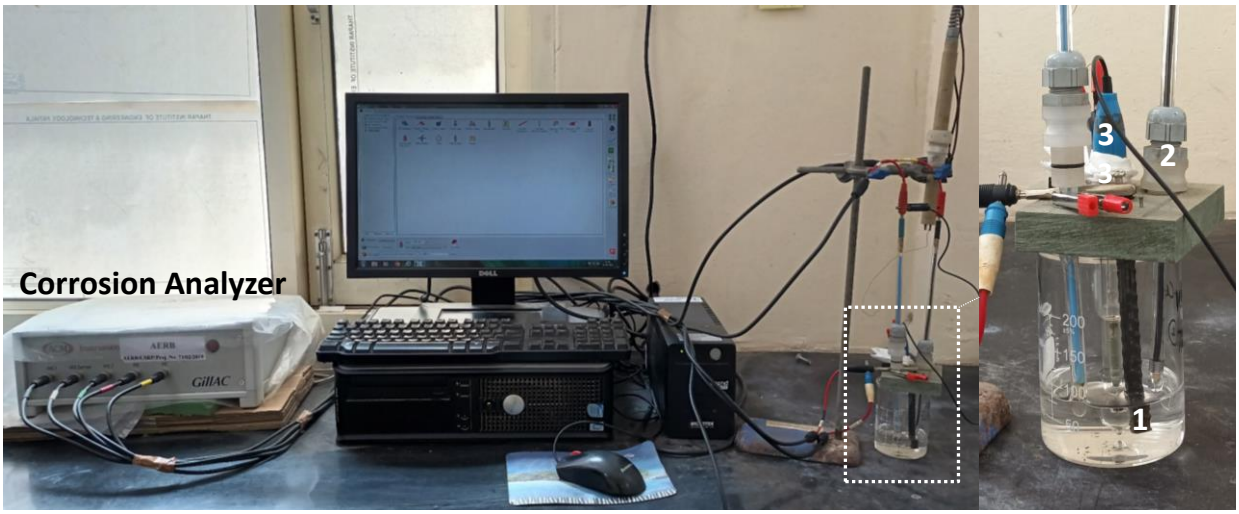

Figure 3.5 Setup for electrochemical test (1-Working electrode; 2-Counter electrode; 3-Reference electrode)

The testing duration of 240 hrs was chosen after carefully reviewing the previous literature related to pore solution testing of inhibitor admixed systems *(Tiwari, Goyal, Luxami, Chakraborty, & Gundlapalli, 2021; Tiwari, Goyal, Luxami, Chakraborty, & Prabhakar, 2021*). A few other researchers also chose similar testing ages to study the performance of different corrosion inhibitors in pore solutions *(Kaur et al., 2017; R. Liu et al., 2014; Poursaee & Hansson, 2007*).

EIS and polarization tests were carried out in open-air conditions at room temperature 25 ± 2 °C by the means of Gill AC, ACM Instrument (Serial no. 1924).

Before the commencement of tests, WE were held at open circuit potential (OCP) for 30 minutes to minimize solution effects. The sequence of the electrochemical tests adopted was EIS first, followed by potentiodynamic polarization (PDP) scan. EIS was conducted between frequency range 100 kHz to 10 mHz at sinusoidal potential perturbation of 10 mV at the attained OCP. PDP scan was then carried out after EIS for each specimen at a scan rate of 0.5mV/sec over a potential range of -250 to 1500 mV v/s OCP. The specimen was discarded after conducting the PDP scan since the high scan range makes the test highly perturbing to the electrodes. The readings for each test duration were taken on different sets of undisturbed samples each time. Testing was carried out on triplicate specimens in order to ensure reliability.

The EIS results were analyzed by elaborating on models of the corresponding equivalent circuit to extract factors such as charge transfer resistance (R_{ct}) relating to the corrosion mechanisms.

Figure 3.6a shows the typical Nyquist plot obtained from EIS test, while Figure 3.6b shows the typical polarization curve obtained from PDP test. The EIS data is generally represented in two formats: Nyquist plots and Bode plots. Further, the Bode plots are represented into two formats: Bode frequency plots and Bode phase angle plots. Figure 3.6a shows the Nyquist plot drawn with real and imaginary impedance as abscissa and ordinate, respectively, at different frequencies. As can be seen from the figure, generally two semicircles exist in a Nyquist plot; (i) large semicircle (low-frequency limit), which is associated with the electrochemical processes occurring at the steel-concrete interface. It is typically attributed to the charge transfer resistance (R_{ct}) associated with the corrosion reactions taking place on the steel surface. The diameter of this semicircle provides information about the corrosion rate and the protective properties of any passive film formed on the steel's surface. The other is the small semicircle (high-frequency limit) which corresponds to the impedance of the concrete itself, including its resistive properties and any other processes occurring within the concrete matrix. The diameter of this semicircle is related to the concrete's resistivity and any capacitive effects due to its microstructure. For testing in pore solution, as the WE (steel) is directly immersed in pore solution, only one semicircle appears.

Changes in the spectra over time or under different conditions can indicate the development of corrosion and the effectiveness of CoI (*Kim et al., 2022*). Further, during the pore solution testing, Nyquist plots has a depressed semi-circle, which signifies that the corrosion of the test steel in CPS is controlled by the charge transfer process and formation of a protective layer over steel surface in the presence of inhibitors. The deviations from the perfect semi-circle are mainly due to the frequency dispersion and also, due to the mass transfer process, inhomogeneity and roughness on the surface of steel under test.

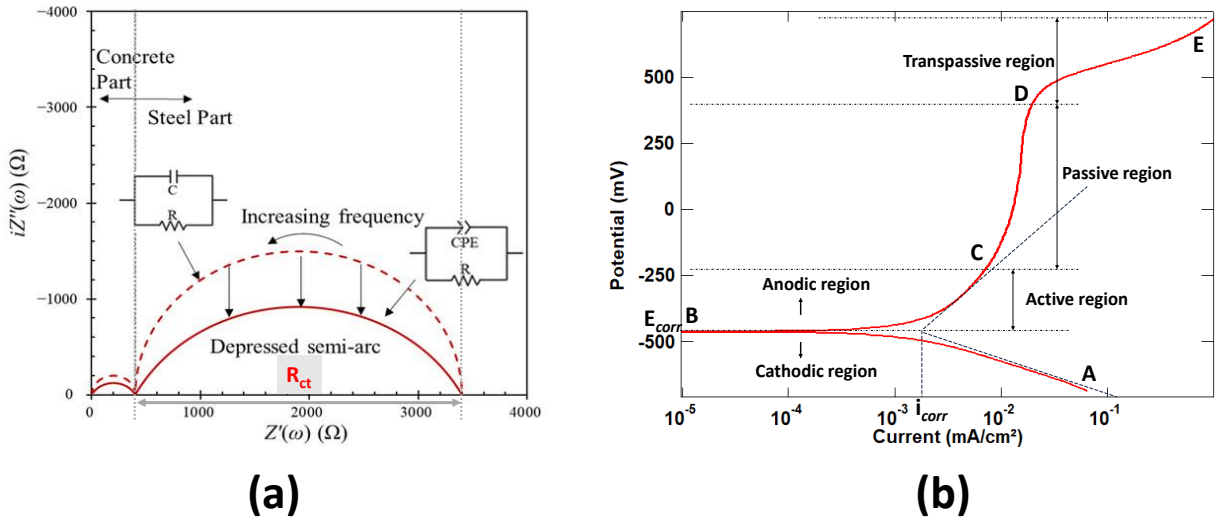

Figure 3.6 Typical (a) Nyquist plot and (b) Polarization curve obtained from EIS and PDP scans in pore solution with metal as a working electrode

The typical polarization curve obtained from PDP scans (Figure 3.6b) consists of two distinct regions namely, cathodic and anodic region. The open circuit or rest potential is located at point B. At this potential the sum of anodic and cathodic reaction rates on the electrode surface is zero. As a result, the measured current will be close to zero. The region below horizontal line from B is called cathodic region and represents cathodic behavior of steel, while the region above B is anodic region. The anodic branch is further divided into three distinct regions namely, active, passive and transpassive region. As the potential increases from B, region BC is recorded in which dissolution of metal cause significant increase in current density with little change in potential. The region BC is referred to as the active region. Region CD is referred to as passive region, in which change in current density is relatively small with large increase in potential. This region represents the stability of passive layer over the metal surface. Once the potential reaches a sufficiently positive value (Point D, sometimes termed the breakaway potential) the applied current

rapidly increases (region DE) with small variation in potential. For some systems (e.g., iron in salt water) this sudden increase in current may be pitting (localized breakdown of passivity), while for others it may be transpassive dissolution. The i_{corr} was of the embedded rebar by extrapolating Tafel slopes of anodic and cathodic branches of the recorded polarization curves. Further this value was used to calculate the corrosion inhibition efficiency through equation 3.3 *(Berdimurodov et al., 2022*).

$$\eta_{PDP}, \% = \left[\frac{i_{corr,0} - i_{corr,1}}{i_{corr,0}}\right] \times 100 \quad \text{....3.3}$$

where, $i_{corr,0}$ and $i_{corr,1}$ are the corrosion current density at 240 hrs in B0 and B0 admixed with CoI, respectively.

3.5 RESULTS AND DISCUSSIONS

The results obtained by performing the above-mentioned tests in pore solution are presented in the upcoming sections. Gravimetric and electrochemical test results are discussed in detail corresponding to each Set as per Table 3.3.

3.5.1 Analysis of results obtained from B0

3.5.1.1 Gravimetric test results for B0

Corrosion rate: The corrosion rate (CR) of steel coupon after immersion in B0 was calculated using equation 3.1 after 240 hrs of immersion. The CR calculated was 1.84 mm/yr. This value is quite high and can be attributed to the corrosion processes occurring at the steel-electrolyte interface. The low pH conditions simulated in B0 caused by bubbling of CO_2 caused the oxidative dissolution of the steel surface.

3.5.1.2 Electrochemical test results for B0

EIS study and equivalent circuit modelling: The typical comparative Nyquist plot obtained for steel specimen immersed in B0 is Figure 3.7. The corresponding Bode plots are presented in *Annexure A* (Figure. A1). The capacitive arc at all testing durations had a single semi-circle (depressed), which signifies that corrosion of the steel specimen in B0 is controlled by the charge transfer process. Further, deviations from the perfect semi-circle are mainly due to the frequency

dispersion and also, due to the mass transfer process, inhomogeneity and roughness on the surface of steel under test.

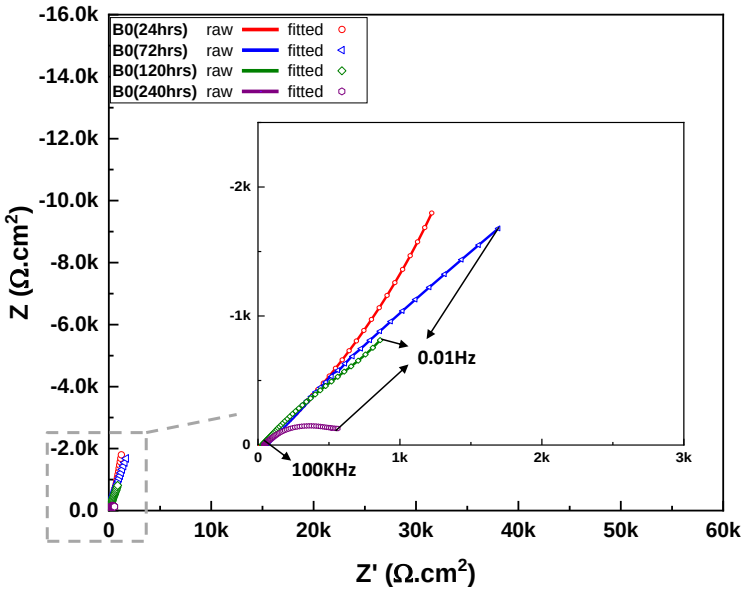

Figure 3.7 Nyquist plot of steel samples immersed in inhibitor-free pore solution (B0)

From the figure (Figure 3.7), it can be seen that the size of the frequency arcs is very small which keeps on decreasing with exposure time which finally diminished at 240 hrs. This is due to the low pH of the carbonated solution which caused de-passivation of the rebar. Passive films formed during the early age of immersion become less protective and less stable due to carbonation (*Shi et al., 2020*). From the Bode plot also, decrease in impedance value at 0.01Hz shows the reduction in steel passivity with immersion time. The impedance value decreases from 2.6 kΩcm^2 to 0.8 kΩcm^2 (24 hrs to 240 hrs) clearly stating the decreased resistivity of the rebar surface after 240 hrs of immersion in carbonated corrosive media.

Furthermore, the impedance plots were fitted using Zman view software. The equivalent circuit model (ECM) representative of the obtained plots is given in Figure 3.8. The adopted ECM has also been frequently used by various other researchers where two interfaces have developed (*Teymouri et al., 2021; Yohai et al., 2016; Y. Zhao et al., 2019*). The first interface is between the steel substrate and the corrosive layer formed while; the second interface is between the corrosive layer and the electrolyte (i.e., carbonated concrete pore solution). The various elements of ECM have the following physical meaning: R_s is the pore solution resistance; CPE_f and R_f represents the capacitance and resistance related to the corrosive film at the first time constant; at the second time

constant, CPE_{dl} and R_{ct} represent the double layer capacitance and charge transfer resistance of the electrochemical reaction process occurring at the steel surface. The CPE_{dl} is the double layer CPE which is representing the corrosion product accumulation on the coupon substrate (Dong et al., 2011). The circuit modelling of EIS parameters enables the calculation of numerical values to correlate with the physical and/or chemical properties of the electrochemical system that is under exploration (Bai et al., 2015). The fitting results for B0 based on the ECM are presented in Table 3.5.

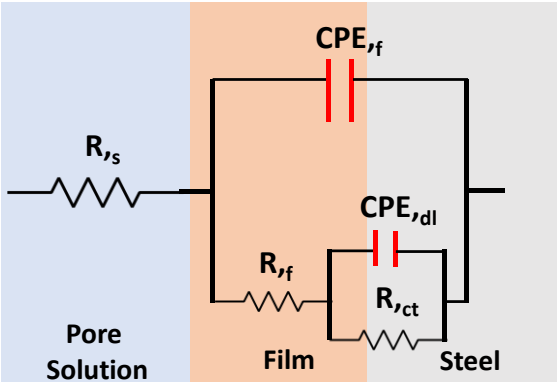

Figure 3.8 ECM obtained for steel coupons immersed in B0

As can be seen from the table, the R_{ct} and R_f values of B0 are observed to decrease with time showing easy exchange of ions from the rebar surface to the electrolyte. This is associated with the development of a highly porous corrosive layer on the steel rebar in carbonated pore solution. Along with this, increasing values of CPE_{dl} and CPE_f shows that the area exposed to corrosion was increasing. The values of n_{dl} is the measure of roughness of the rebar surface (*Berdimurodov et al., 2022*). For the samples dipped in carbonated solution, n_{dl} values decreased from 0.94 to 0.42. This represents the increase in heterogeneity of the metal surface upon the formation of corrosion products.

Table 3.5 EIS fitting parameters for B0

Solution	Immersion Time (hrs)	Pore solution parameters	Passive film parameters			Steel surface parameters		
			CPE$_f$			CPE$_{dl}$		
		R_s (Ω)	Y_0 ($\mu\Omega^{-1}s^n$)	n_f	R_f (kΩ)	Y_0 ($\mu\Omega^{-1}s^n$)	n_{dl}	R_{ct} (kΩ)
B0	24	28.11	1361	0.85	1.85	75.9	0.94	8.79
	72	22.89	1532	0.78	7.67	2355	0.82	7.67
	120	30.01	7088	0.57	4.52	2454	0.6	5.48
	240	44.25	36274	0.58	0.554	1946	0.42	0.6

PDP scan: The PDP curve of B0 (carbonated corrosive solution without CoI) at different intervals is shown in Figure 3.9

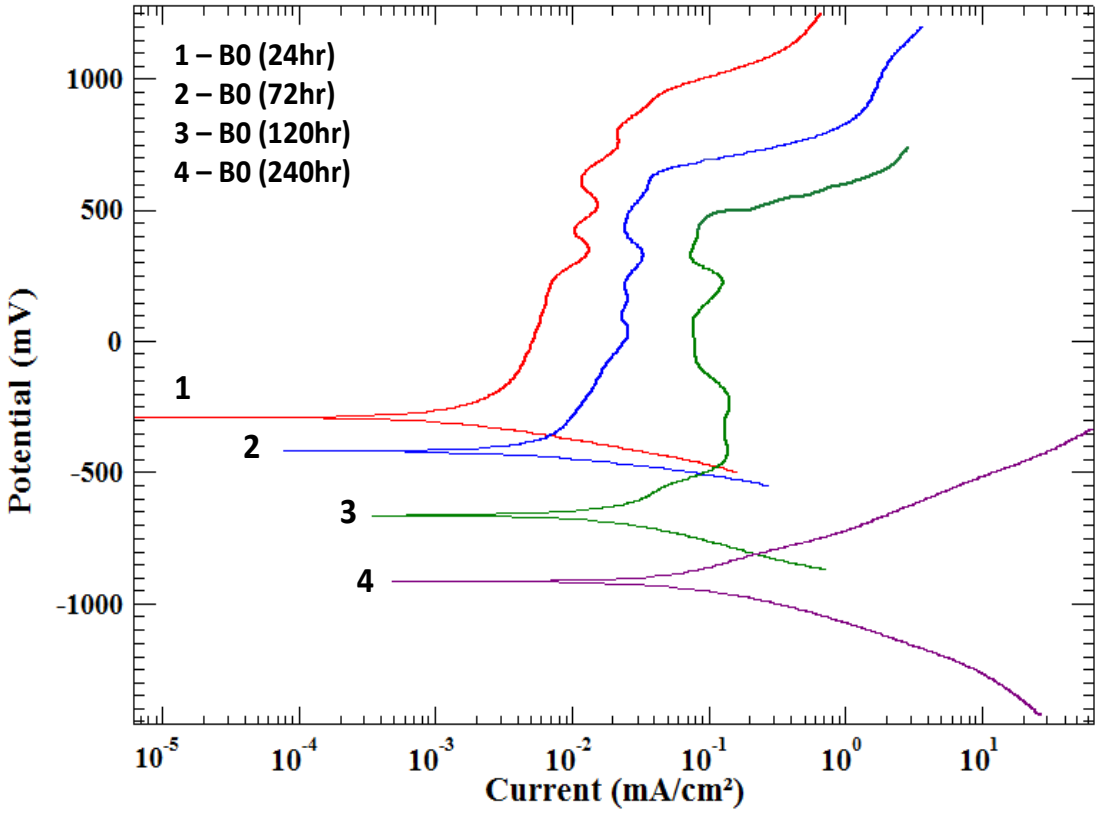

Figure 3.9 PDP curve of steel sample immersed in B0

The obtained electrochemical parameters are shown in **Error! Not a valid bookmark self-reference.**. From the obtained curves and the table, it can be interpreted that the E_{corr} value shifted towards active region (-283 mV_{sce} to -826.8 mV_{sce}) and the i_{corr} value increased from 0.0025 mA/cm^2 to 0.148 mA/cm^2 as the exposure duration is increased from 24 to 240 hrs. This shift of potential towards active side and increase in current density is indicative of active state of corrosion of steel specimen exposed to carbonated environment (*Monticelli et al., 2011*). The curve also indicates that during the initial immersion duration (i.e., 24 and 72 hrs), the steel surface was surrounded by passive layer due to presence of alkali ions; but with immersion time, the layer becomes unstable, and curve displays transpassive behavior. At 240 hrs, a uniform increase in anodic current density with increase in potential (towards negative side) was recorded, indicating active corrosion due to negative impact of the carbonation. Hence, it can be deduced that carbonated environment is highly detrimental for the reinforcement. Active corrosion gets initiated

on steel surface after 240 hrs of immersion in such media. Addition of corrosion inhibitors (CoI) is therefore necessary to reduce the corrosion of rebars in B0.

In the upcoming sections, the effect of addition of amino acids as CoI in B0 was evaluated and the results are discussed.

Table 3.6 Electrochemical parameters from PDP curves for Set 1 compounds.

Solution	Immersion duration (hours)	E_{corr} (mV_{sce})	i_{corr} ($\mu A/cm^2$)
B0	**24**	-283.70	2.5
	72	-496.40	9.10
	120	-624.06	67
	240	-826.82	148

3.5.2 Analysis of results obtained for Set 1 compounds: *Ser* and *Cys*

3.5.2.1 Gravimetric test results for Set 1

Corrosion rate: Firstly, the corrosion rate (CR) of steel coupons was calculated by the gravimetric method and the results obtained are presented in Table 3.7. It is observed from the table that the CR of samples without the inhibitors (B0) was very high (1.84 mm/yr); however, the CR values declined significantly with the introduction of CoIs at all concentration levels. It clearly indicates that *Ser* and *Cys* are efficient in protecting the steel surface in B0 which can be attributed to the adsorption of inhibitor ions on steel surface that acted as barrier for corrosive ion attack. Further, it was observed that with the increase in concentration of CoI, the CR values reached a saturation point, after which the values either decreased or remained unchanged *(Mohammad Mobin, Irfan Ahmad, Megha Basik, Manilal Murmu, 2020*). In the current research also, a similar trend was seen. This point was taken as the optimum concentration of the compound. In *Ser,* the CR decreased to reach 0.248 mm/yr at 0.05M and started to rise with further increase in concentration. In the case of *Cys*, the CR was seen to continuously fall with increase in inhibitor concentration, with the saturation point observed at 0.1 M. The minimum CR of 0.184mm/yr was obtained at 0.05M.

Based on the saturation points, the concentrations 0.05M and 0.1M were considered for *Ser* and *Cys* in order to perform the electrochemical tests.

Adsorption isotherm: Fitting of the data into different isotherms (Langmuir, Frumkin, Temkin, Freundlich) reveal that both the inhibitors obeyed Langmuir adsorption isotherm with strong correlation co-efficient (R^2), 0.988 for *Ser* and 0.995 for *Cys*. Langmuir model indicates a monolayer adsorption of organic species without any steric hindrance between the adsorbed inhibitor molecules (Vijayaraghavan et al., 2006). The model relates the concentration (C) of the adsorbate (here, inhibitor ions) in the solution to the degree of surface coverage (θ_{Grav}) by equation 3.2. It was calculated from the intercept of the fitted line Figure 3.10 and the values are presented in Table 3.8. Positive and high values of k_{ads} indicated that adsorption of *Ser* and *Cys* is feasible over the metal surface. Higher k_{ads} values for *Cys,* nearly twice as that for *Ser*, suggests that *Cys* molecules are more strongly adsorbed to the steel discs than *Ser* (*Yadav et al., 2015*). It has been observed from the previous literature that the adsorption process of amino-acids on the surface of steel generally follows the Langmuir adsorption isotherm with positive values of k_{ads} values *(Eddy, 2010; Fouda et al., 2011; Fu, Li, Cao, et al., 2010; Fu, Li, Wang, et al., 2010; D. Q. Zhang et al., 2008*). Alongside, according to equation 3.4, equilibrium constant of adsorption, k_{ads} can be related to Gibb's free energy of adsorption $\Delta G^{o}_{ads.}$

Table 3.7 Corrosion rate and surface coverage for Set 1 compounds.

Inhibitor	Concentration	Nomenclature	Corrosion Rate (CR_{Grav}, mm/yr)	Surface coverage (θ_{Grav})	Concentration chosen for electrochemical tests
-	-	B0 (inhibitor-free solution)	1.840	-	
Ser	0.010M	B0+Ser0.010	0.368	0.800	-
	0.025M	B0+ Ser 0.025	0.294	0.840	-
	0.050M	B0+ Ser 0.050	0.248	0.865	✓
	0.075M	B0+ Ser 0.075	0.525	0.863	-
	0.100M	B0+ Ser 0.100	0.287	0.844	✓
	0.125M	B0+ Ser 0.125	0.313	0.830	-
Cys	0.010M	B0+ Cys0.010	0.405	0.780	-
	0.025M	B0+Cys 0.025	0.221	0.880	-
	0.050M	B0+Cys 0.050	0.184	0.900	✓
	0.075M	B0+Cys 0.075	0.184	0.901	-
	0.100M	B0+Cys 0.100	0.221	0.880	✓
	0.125M	B0+Cys 0.125	0.239	0.870	-

$$\Delta G^{o}_{ads} = 2.303\ RT\ \log[55.5 k_{ads}] \quad \ldots.(3.4)$$

where, R is the universal gas constant, T is absolute temperature in Kelvin and the value 55.5 is concentration of water in pore solution in $molL^{-1}$. The calculated values of ΔG^{o}_{ads} are listed in Table 3.8.

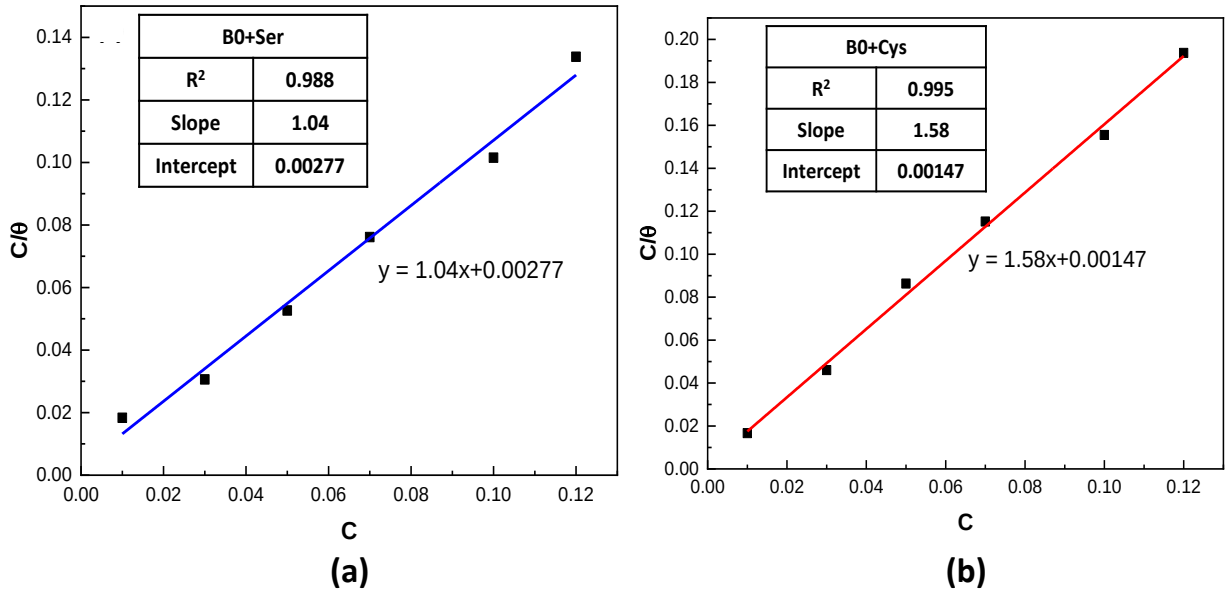

Figure 3.10 Langmuir isotherm accurately describing the adsorption of (a) *Ser* and (b) *Cys* over steel surface.

Table 3.8 Thermodynamic and fitting parameters for Set 1 amino acids.

Solutions	Thermodynamic parameters		Fitting parameters	
	k_{ads} (M^{-1})	ΔG^{o}	R^2	Slope
B0+Ser	361.01	-24.55	0.988	1.58
B0+Cys	680.27	-25.94	0.995	1.04

3.5.2.2 Electrochemical test results for Set 1

EIS study and equivalent circuit modelling: The typical Nyquist plots for *Ser* and *Cys* at different testing durations are shown in Figure 3.11 and Figure 3.12.

Additionally, a comparative Nyquist plot for *Ser* and *Cys* in comparison with B0, at 240 hrs is shown in Figure 3.13. Alongside, the Bode plots are presented in *Annexure A* (Figures. A2 and

A3). The scale of abscissa and ordinate for all the graphs is kept the same for more clarity during comparison. A notable trait that can be noticed in all the Nyquist plots, whether in the absence of inhibitors or in the presence of inhibitors, is the occurrence of single semi-circle (depressed) for carbonated pore solution and those with inhibitors. This signifies that the corrosion of the test steel in B0 is controlled by the charge transfer process and formation of a protective layer over steel surface in the presence of inhibitors. Further, deviations from the perfect semi-circle are mainly due to the frequency dispersion and also, due to the mass transfer process, inhomogeneities and roughness on the surface of steel under test. Long-term tests (240 hours) were set up to evaluate the corrosion resistance and stability provided by *Ser* and *Cys* in aggressive carbonated pore solution.

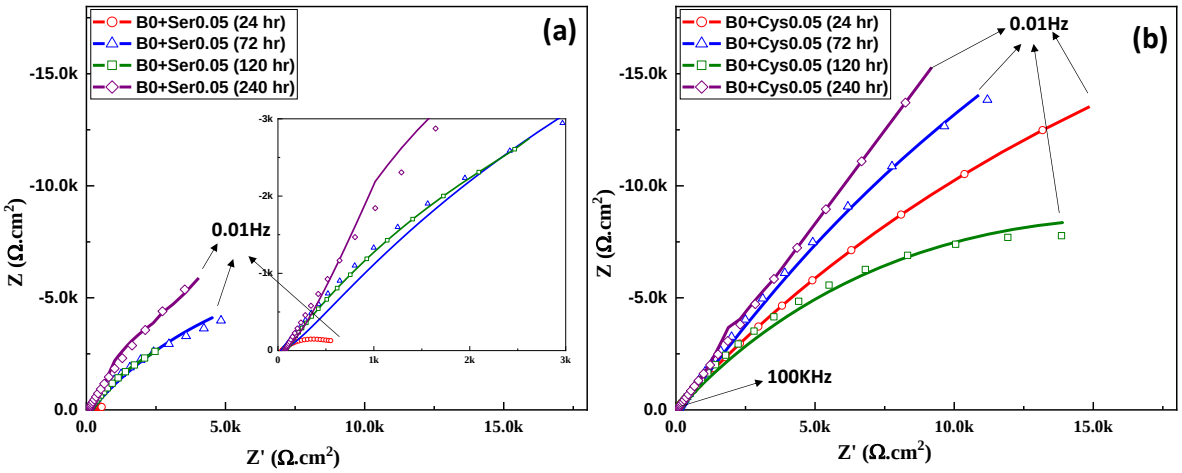

Figure 3.11 Nyquist plots for (a) *Ser* and (b) *Cys* at <u>0.05 M</u>

From the Nyquist plots displayed in Figure 3.11a and b, it can be seen that the radius of capacitive loop in case of B0 remained un-changed till 72hrs which could be due to the formation of a passive layer over rebar in pore solution. A thin oxide layer could form on the steel surface during initial period of immersion (from 24 to 72hrs). However, with increasing duration, the size of the arc decreased and finally diminished at 240hrs. This is due to the low pH of the carbonated solution making it highly oxidizing. Passive films formed during the early age of immersion become less protective and less stable due to the ruinous effect of carbonation (*Shi et al., 2020*). When seeing the behavior of inhibitors (*Ser* and *Cys*), w.r.t. the B0, B0+Ser0.05 showed an increase in the size of the arc with immersion time. Although, the radius of this arc was smaller than B0 at 24hrs but increased from 72 to 240 hrs suggesting that *Ser* molecules took some time for their settlement in the solution and after 72hrs, an adsorbed layer is observed to develop which

grew with time shielding the rebar from corrosion. Further, the radius of arc of B0+Cys0.05 was larger than B0 from 24 hours, indicating its protective effect from the very start; the radius kept constant during the entire testing duration. This exhibits that *Cys* formed a protective layer over the exposed surface of rebar from the time of immersion and maintained its inhibitive nature even till the end of exposure duration of 240hrs. The layer development effectively reduced the number of contact sites between the corrosive media and the metal surface, hence, avoiding its dissolution (*Berdimurodov et al., 2022*). It can be therefore said that both, *Ser* and *Cys* safeguarded the rebar from corrosion at 0.05M concentration in B0 by forming a protective passive film. *Ser* developed the inhibitive layer slowly whose thickness increased with time, while *Cys* adsorbed over the rebar forming a barrier layer within 24hrs; the layer remained intact till the end of the testing duration.

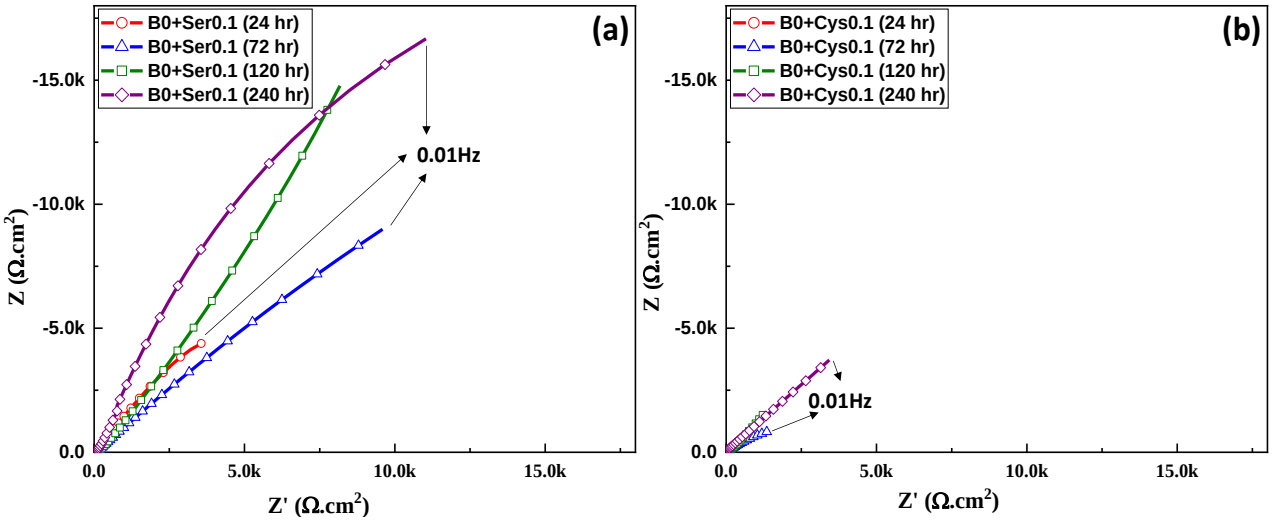

Figure 3.12 Nyquist plots for (a) *Ser* and (b) *Cys* at <u>0.1 M</u>

Moreover, when comparing the performance of two amino acids, the radius of B0+Cys0.05 was very large as compared to B0+Ser0.05 irrespective of the testing duration.

Further, the effect of concentration on the inhibition capacity of CoIs was monitored. Figure 3.12a and b show Nyquist plots at different testing durations for B0 and pore solution with CoI's at 0.1M concentration. The behavior of B0+Ser0.1 is identical to that of B0+Ser0.05 except that an increase in *Ser* concentration led the inhibitor to start performing from the initial testing duration i.e., 24hrs as seen from the fact the radius of its capacitive loop which was higher than that of B0 (Figure 3.12a). Further, this radius was seen to increase till 240hrs. The rise in concentration of *Ser* increased its inhibiting power which can be allied to the increased surface

coverage. On the other hand, the behavior of B0+Cys0.1 was different from that of B0+Cys0.05. The diameter of the semi-circle is seen to be comparable to that of the base solution, B0. Till 120 hrs, the size of the capacitive curve is seen to increase slightly which is not that significant, indicating very weak adsorption of the inhibitor molecules. Though the radius increases to reach a value of 4 kΩcm^2 at 240hrs, this value is very less as compared to that obtained at the same time for B0+Cys0.05. This suggests that increase in the concentration of *Cys* decreased its inhibition capacity which can be due to some kind of increased coulombic repulsion between *Cys* ions in the aqueous solution (*Morad, 2008*).

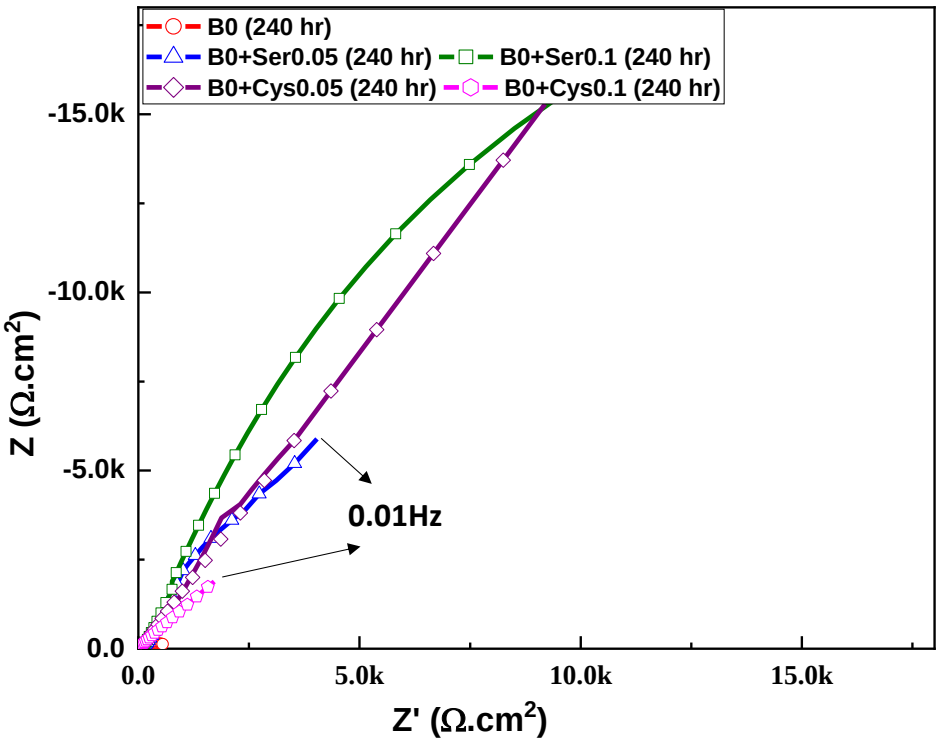

Figure 3.13 Comparative Nyquist plots of steel in B0 and B0 admixed with CoI (*Ser* and *Cys*) at 0.05M and 0.1M after 240hrs of immersion.

Hence, it can be inferred that *Ser* and *Cys* have the tendency to make an adsorbed film on the metal surface whose protecting power improves with the immersion duration. The layer formed in the case of *Cys* as CoI is more impermeable and thicker as compared to that formed by *Ser* on steel substrate as conveyed from the Nyquist plots irrespective of the concentrations admixed. Further, the impedance plots after fitting the EIS results using ZMAN view software and the equivalent circuit model (ECM) obtained is given in Figure 3.14 was found to be representative for all Nyquist plots.

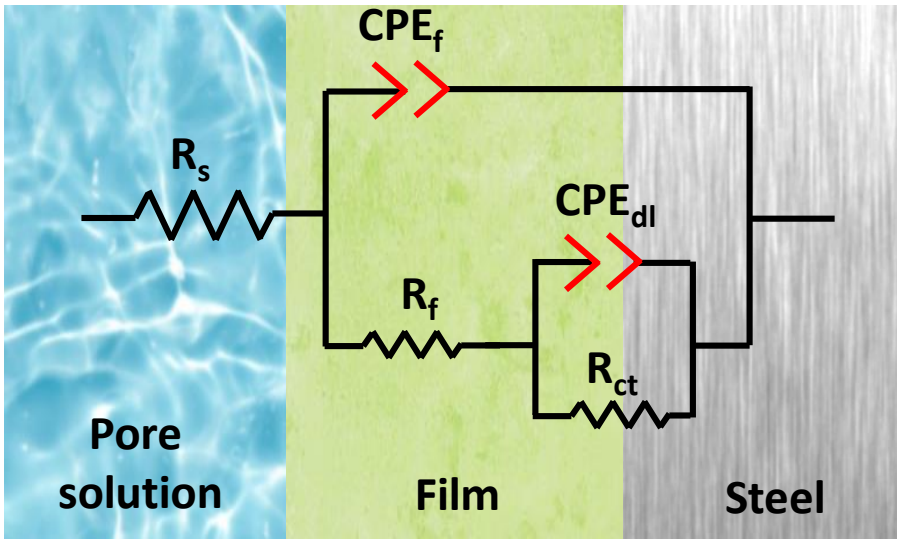

R$_s$=Pore solution resistance | **R$_f$=Film resistance** | **R$_{ct}$=Charge transfer resistance**

CPE$_f$=Film capacitance | **CPE$_{dl}$=Double layer capacitance**

Figure 3.14 Equivalent circuit model (ECM) after fitting the EIS data for Set 1

The various elements of ECM have the following physical meaning: R_s is the pore solution resistance; CPE_{dl} and R_{ct} represent the double layer capacitance and charge transfer resistance of the electrochemical reaction process occurring at the steel surface; CPE_f and R_f represents the capacitance and resistance related to the steel passive film and adsorption film. The circuit modelling of EIS parameters enables the calculation of numerical values to correlate with the physical and/or chemical properties of the electrochemical system that is under exploration (*Bai et al., 2015*). The fitting results calculated from EIS plots based on the ECM are presented in Table 3.9. Constant phase elements (CPE) were used in the place of ideal capacitance in order to vindicate the changes caused due to the surface heterogeneity, presence of corrosion products/adsorbed inhibitor molecules *(Varvara et al., 2021*). Further, in reference to the correlation of obtained electrochemical parameters, it has been developed lower R_{ct} values along with increased CPE_{dl} values indicate active corrosion process occurring at the steel-solution interface. On the contrary, if the values of R_{ct} are seen to rise along with predominant falling of C_{dl} values in the presence of inhibitor ions, these suggest the inhibitor molecules are functioning by adsorption on the metal surface (*Lagrenée et al., 2002*). Lower capacitance values recorded for *Ser* and *Cys* admixed solutions in comparison with the base solution (B0) which is allied with the

protection provided by the amino acid molecules against corrosion. On the addition of inhibitors irrespective of its concentration, increase in R_{ct} values was observed alongside the diminishing values of C_{dl} as compared to that obtained in B0. This signifies the formation of highly protective passive film on rebar increasing its resistance against charge transfer phenomenon. Increase in R_f and consequent decrease in C_f values in the case of *Ser* as well as *Cys* also demonstrates the strengthening and thickening of the passive film leading to the hindrance in the electrochemical corrosion processes. It also suggests that there has occurred a decrease in the dissolution rate of metal upon addition of CoI (for *Ser* and *Cys*).

Additionally, the values of n_{dl} were seen to remain close to unity during the entire testing duration. This reveals that upon the inhibitor addition, a smooth adsorptive layer was formed over the rebar surface. These findings confirm that the rebar got covered with a non-porous, non-conducting inhibitor layer that protected steel against corrosion action. Additionally, the resistance values at 240 hours for solutions with *Cys* as CoI are more than that for *Ser* irrespective of their concentrations signifying that in the presence of *Cys*, the layer developed on the steel surface is more stable, thicker and non-conducting to that formed in the presence of *Ser*. Similar observations were made by *J. Fu et al. (2011)* where the R_{ct} values of *Cys* were obtained to be higher than *Ser* when used as CoI for mild steel (*Fu, Li, Wang, et al., 2010*).

PDP Scan: The PDP curves in their respective solutions are shown in Figure 3.15 and Figure 3.16. The recorded electrochemical parameters are tabulated in Table 3.10. The tests were performed in triplicate, however, because of good repeatability, only one measurement (representative of the three trials) is shown here.

Figure 3.15a and b represent the PDP curves of B0 admixed with *Ser* and *Cys* at 0.05M concentration at different testing durations. In Figure 3.15, PDP curves of *Ser* are shown where a passive region is visible at 24 hrs but after 72 hrs, spikes were observed in the passive region which is exhibitive of some instability in the development of the layer. The instability disappeared as the exposure duration increased, rather a stable passive region is seen. The i_{corr} value of B0+Ser0.05 lowered itself by one order of magnitude from 24 to 240 hrs of exposure to carbonated environment (from 81to 5.4 $\mu A/cm^2$) depicting the protective nature of *Ser* which enhanced with time. As can be seen, after adding *Cys*, the PDP curves showed (Figure 3.15b) the presence of passive layer is

evinced from the initial hours which sustained itself at all testing durations. During the initial hours, the passive region demonstrated slight instability which got stabilized by the end of the testing program (240 hrs). The i_{corr} values decreased by one order of magnitude from that obtained initially, i.e., 1.5 μA/cm^2 at 24 hrs and 0.52 μA/cm^2 at 240 hrs. It can be stated that *Cys* readily forms a protective layer on the steel surface that prevents the metal against corrosion even after being exposed to corrosive solution for 240 hrs as observed in the Nyquist plots. Hence, both the amino acids have the capability of reducing steel corrosion even at a low concentration of 0.05M. Amongst the two chosen compounds, *Cys* displays ten times lower value of i_{corr} than *Ser*.

Table 3.9 EIS fitting parameters for Set 1 amino acids

Solution	Immersion Time (hrs)	Pore solution parameters	Passive film parameters			Steel surface parameters		
			CPE_f			CPE_{dl}		
		R_s (Ω)	Y_0 (μΩ^{-1}s^n)	n_f	R_f (10^3 Ω)	Y_0 (μΩ^{-1}s^n)	n_{dl}	R_{ct} (10^3 Ω)
B0	24	28.11	1361	0.85	1.85	75.9	0.94	8.79
	72	22.89	1532	0.78	7.67	2355	0.82	7.67
	120	30.01	7088	0.57	4.52	2454	0.6	5.48
	240	44.25	36274	0.58	0.554	1946	0.42	0.6
B0+Ser0.05	24	44.25	1946	0.58	0.554	36270	0.42	607.49
	72	70.67	2226	0.51	7.25	2014	0.72	39.77
	120	67.23	644.5	0.65	15.36	962.0	0.98	39.6
	240	49.23	294.1	0.67	22.97	2.879	0.8	115
B0+Cys0.05	24	32.74	570	0.79	2.2	215.5	0.89	32.77
	72	60.84	208	0.67	12.1	878.3	0.84	56.49
	120	47.61	202.9	0.66	16.86	21.94	0.87	81.64
	240	40.92	242.6	0.66	26.41	2.2	0.82	182.22
B0+Ser0.1	24	65.59	308.9	0.63	2.7	2085	0.99	0.12
	72	51.66	202.9	0.65	15.23	3303	0.89	35.9
	120	47.04	222	0.56	39.26	244.8	0.73	57.48
	240	39.80	30.93	0.53	60.8	1.09	0.39	60.8
B0+Cys0.1	24	22.54	7707	0.92	0.05	5274	0.52	0.107
	72	25.14	1042	0.89	0.66	1678	0.46	6.03
	120	36.59	1093	0.56	14.28	1096	0.56	14.28
	240	48.48	70.85	0.52	64.7	46.63	0.98	81.8

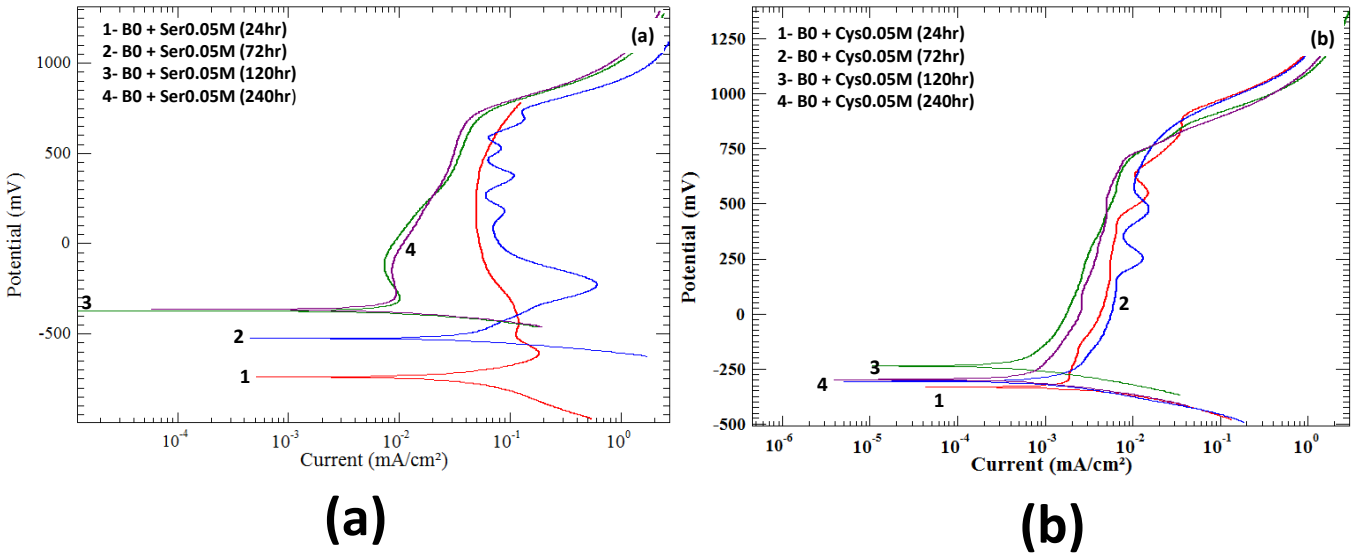

Figure 3.15 PDP curves of steel samples immersed in B0 admixed with (a) *Ser*; (b) *Cys* at <u>0.05M</u> concentration at various testing durations

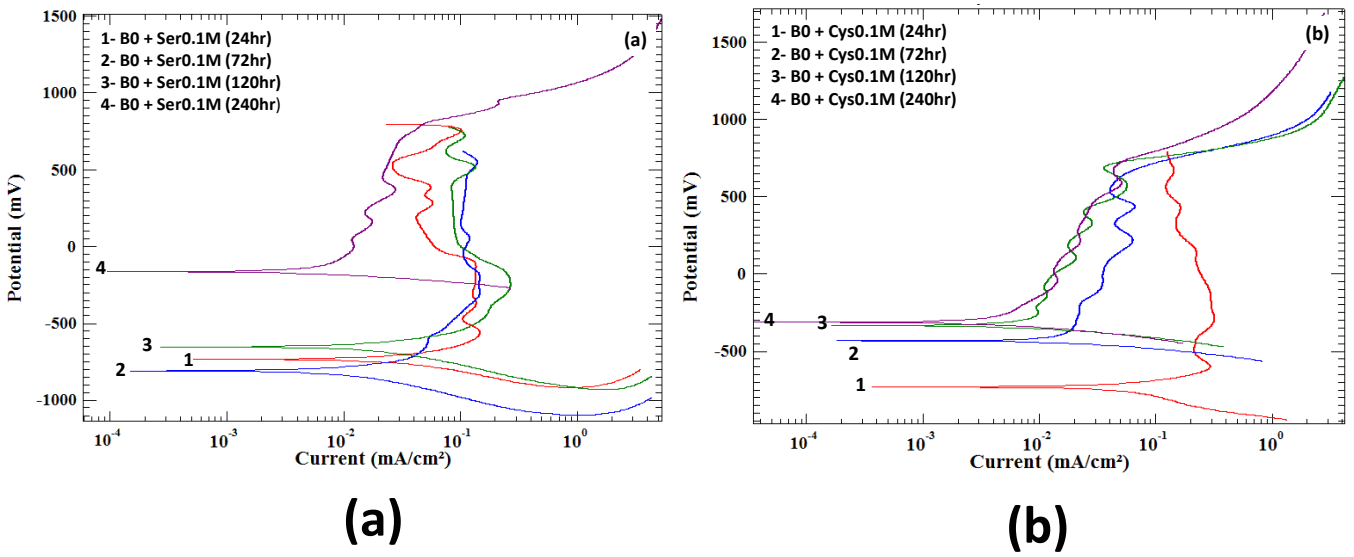

Figure 3.16 PDP curves of steel samples immersed in B0 admixed with (a) *Ser*; (b) *Cys* at <u>0.1M</u> concentration at various testing durations.

The PDP curve (Figure 3.16a) obtained at 24, 72 and 120 hrs revealed unstable passive regions due to the competition between formation and depletion of passive layer. However, the curve obtained at 240 hrs showed decrease in the corrosion current density values by one order of magnitude (from 69 µA/cm^2 at 24hrs to 9.4 µA/cm^2 at 240 hrs). Another important thing worth

stating is that B0+Ser0.05 took 72 hrs to stabilize, while B0+Ser0.1 took 120 hrs. This signifies that with the increase in number of ions of *Ser*, intermolecular interactions increase which takes more time to stabilize. However, the final i_{corr} values obtained at 0.05M and 0.1M are of the same order..

Table 3.10 Electrochemical parameters from PDP curves for Set 1 compounds.

Solution	Immersion duration (hours)	E_{corr} (mV_{sce})	i_{corr} ($\mu A/cm^2$)	IE_{PDP},%
B0	24	-283.70	2.5	-
	72	-496.40	9.10	-
	120	-624.06	67	-
	240	-826.82	148	-
B0+Ser0.05	24	-737.60	81	45.27
	72	-502.40	85	42.56
	120	-402.50	7.3	95.06
	240	-385.90	5.4	96.35
B0+Ser0.1	24	-711.00	69	53.33
	72	-803.70	50	66.21
	120	-650.70	53	64.18
	240	-158.30	9.4	93.64
B0+Cys0.05	24	-318.40	1.5	98.98
	72	-302.40	2.3	98.44
	120	-301.50	0.58	99.60
	240	-391.10	0.52	99.64
B0+Cys0.1	24	-735.20	142	4.050
	72	-443.30	13	91.21
	120	-313.40	6	95.88
	240	-315.30	5.9	96.00

Figure 3.16a and b represent the PDP curves of B0 admixed with *Ser* and *Cys* at 0.1M concentration at different testing durations. With increase in concentration from 0.05M to 0.1M, the behaviour of PDP curve for specimen immersed in solution B0+Ser0.1 remained un-changed.

The PDP behavior (Figure 3.16b) of *Cys* at 0.1M concentration displayed variation in its behavior compared to that observed at lower concentration. More instability in the curves was observed with the rise in number of *Cys* molecules. Higher i_{corr} value along with higher E_{corr} was also recorded initially (i.e., 142 μA/cm^2 and -735.2mV at 24 hrs) which decreased with the exposure duration (i.e., 5.91 μA/cm^2 and -315.3mV at 240 hrs). This suggests that the *Cys* can suppress metal corrosion at 0.1M as well. After comparing the electrochemical parameters of B0+Cys0.05 and B0+Cys0.1, it can be inferred that i_{corr} declined by 10 times when the concentration is doubled. *Cys* molecules are bulkier than *Ser* due to the larger size of sulphur atom (in -SH) than oxygen atom (in -OH). Also, the chance of hydrogen bonding amongst *Ser* molecules is much higher than Cys molecules due to low electronegativity of sulphur than oxygen. The intermolecular hydrogen bonding amongst *Ser* molecules makes them stable even at an increased concentration.

Further, as the major change is observed in anodic branch of PDP curves and the shift of E_{corr} was more than 85 mV (seen from Table 3.10), *Ser* and *Cys* act as anodic-type inhibitors at 0.05 M and 0.1 M concentrations (*R. Zhao et al., 2022*).

3.5.3 Analysis of results obtained for Set 2 compounds: *Phe* and *Trp*

3.5.3.1 Gravimetric test results for Set 2 compounds

Corrosion rate: The variation in corrosion rate and surface coverage of *Phe* and *Trp* at different concentration levels are presented in Table 3.11**.**

The corrosion rate of the steel coupons in B0 was very high (1.84 mm/yr) as described previously (Section 3.5.1.1, Table 3.5); however, the values of CR declined significantly with the introduction of *Phe* and *Trp* at all concentration levels. It clearly indicates that both the inhibitors prevented the formation of corrosion products which can be attributed to the adsorption of the inhibitor ions on the steel surface that acts as barrier from corrosive media. In *Phe,* the CR decreased to reach 0.38 mm/yr at 0.05M and started to rise with further increase in concentration; while, for *Trp*, the CR was seen to continuously reduce with increase in CoI concentration. The saturation point was observed at 0.1 M for *Trp* as the minimum CR of 0.38 mm/yr was obtained at this concertation level. Based on the saturation points of both the inhibitors, the concentrations 0.05M and 0.1M were considered for *Phe* and *Trp* in order to perform the electrochemical test.

Table 3.11 Corrosion rate and surface coverage for Set 2 compounds.

Inhibitor	Concentration	Nomenclature	Corrosion Rate (CR_{Grav}, mm/yr)	Surface coverage (θ_{Grav})	Concentration chosen for electrochemical tests
-	-	B0 (inhibitor-free solution)	1.840	-	
Phe	0.010M	C0+Phe0.010	0.43	0.76	-
	0.025M	C0+ Phe0.025	0.41	0.77	-
	0.050M	C0+ Phe0.050	0.38	0.79	✓
	0.075M	C0+ Phe0.075	0.39	0.78	-
	0.100M	C0+ Phe0.100	0.56	0.69	✓
	0.125M	C0+ Phe0.125	0.57	0.69	-
Trp	0.010M	C0+Trp0.010	0.58	0.68	-
	0.025M	C0+Trp0.025	0.48	0.73	-
	0.050M	C0+Trp0.050	0.45	0.75	✓
	0.075M	C0+Trp0.075	0.39	0.78	-
	0.100M	C0+Trp0.100	0.38	0.79	✓
	0.125M	C0+ Trp0.125	0.38	0.79	-

Adsorption isotherm: Similar to Set 1 compounds, Set 2 compounds were also seen to follow the Langmuir isotherm for adsorption (data of CR was fitted to multiple isotherms, Langmuir was seen to be followed). The graphs obtained after fitting the isotherm (refer Figure 3.17) shows high correlation coefficients (R^2) of 0.990 and 0.997 for *Phe* and *Trp*, respectively. The fitting as well as thermodynamic parameters are provided in Table 3.12. Higher k_{ads} values were obtained for *Trp* than *Phe* (two times higher) suggesting stronger adsorption of *Trp* molecules on the steel surface than *Phe.* The ΔG^{o}_{ads} for set 2 compounds indicate physio-chemisorption processes occurring at the rebar surface. *Phe* and *Trp* molecules chemically interconnect with the ferrous ions on the metal surface and form chemical bonds; also, they are electrostatically attracted towards the metal surface.

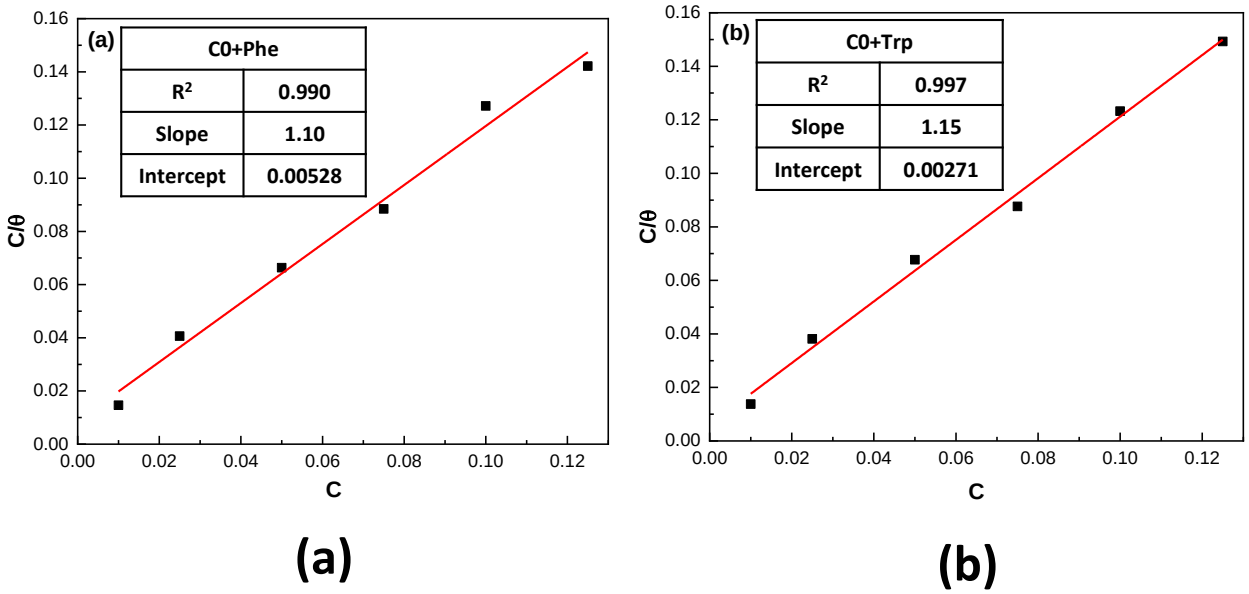

Figure 3.17 Langmuir adsorption isotherms for (a)*Phe;* (b)*Trp* in B0

Table 3.12 Fitting and thermodynamic parameters

Solution	Fitting parameters		Thermodynamic parameters	
	R^2	Slope	$k_{ads}(M^{-1})$	$\Delta G°_{ads}$ (kJ/mol)
C0 + *Phe*	0.990	1.178 ± 0.037	189.34	-22.954
C0 + *Trp*	0.997	1.219 ± 0.024	369.03	-24.607

3.5.3.2 Electrochemical test for Set 2 compounds

EIS study and equivalent circuit modelling: The Nyquist plots showing behavior of *Phe* and *Trp* at 0.05M and 0.1M concentration are shown in Figure 3.18 and 3.19. Additionally, the Bode plots are shown in *Annexure A* (Figure A4 and A5). Addition of *Phe* at 0.05M concentration in the B0 shows increase in the diameter of capacitive arc with immersion age as shown by Figure 3.18a. When the concentration of *Phe* was increased from 0.05M to 0.1M, change in inhibition behavior was observed through Nyquist plots. Figure 3.18b shows a high diameter capacitive loop after 24 hrs of immersion which suggests that the inhibitive ions readily deposited at the anodic sites by adsorption. A large diameter loop was recorded even after 240 hrs of exposure in carbonated solution with a small deviation at 120 hrs. The presence of films and their protective action has also been reported by various other authors with inhibitors in concrete simulating pore solutions (*Zavala Olivares et al., 2007*). The size of the frequency arcs is comparable in case of B0+Phe0.05 and B0+Phe0.1 at 240 hrs.

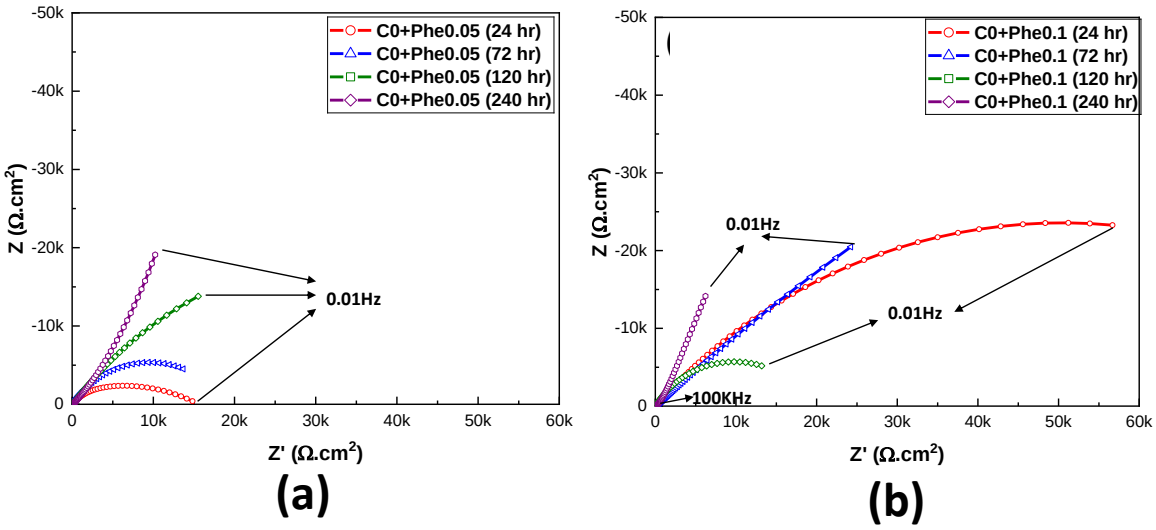

Figure 3.18 Nyquist plots for *Phe* as CoI at (a)0.05M; (b)0.1M at different time durations

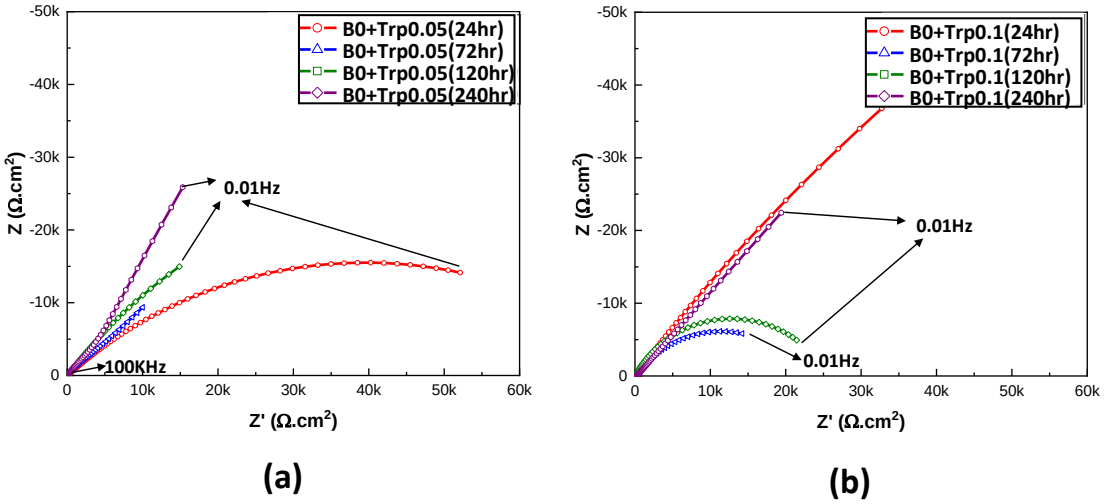

Figure 3.19 Nyquist plots for *Trp* as CoI at (a)0.05M; (b)0.1M at different time durations

The Nyquist plot obtained after the addition of *Trp* at 0.05M and 0.1M concentrations in the B0 are shown in Figure 3.19a and b. Initially, at 24 hrs, a large diameter capacitive loop is seen. *Trp* molecules covered the available anodic sites over the rebar and formed a passive layer after its addition to B0. With time, the radius is seen to decrease which might be due to the action of corrosive ions in the solution; but after 240 hours, a final intact layer is developed over the rebar as seen from a large capacitive curve. With the increase in concentration, similar behavior is seen

where the diameter of the capacitive loop decreased from 24 to 72 hrs, followed by significant increase from 120 to 240 hrs. The diameter of the capacitive arc obtained at 240 hrs for B0+Trp0.05 and B0+Trp0.1 are comparable suggesting no significant change in the inhibition efficacy upon doubling the number of *Trp* molecules. Furthermore, after observing the Nyquist plots of *Phe* and *Trp* collectively, the working mechanism is seen to be different. *Phe* molecules get deposited on the metal surface from the initial hours and show their inhibitive effect, whereas *Trp* molecules take some time to synchronize amongst themselves and once they get stabilized, their chelation effect can be seen from large diameter capacitive loops. The difference in inhibition mechanism can be attributed to the difference in molecular structure of both the compounds; *Trp* molecules have an additional pyrrole ring in its structure as compared to *Phe*. The presence of pyrrole ring makes the *Trp* molecules bulkier than *Phe*, hence, causing them to take more time to stabilize. The positive effect of the presence of pyrrole ring although can be seen as the layer formed in the case of *Trp* is more adherent due to increased number of reaction centres in its molecule and seems to be thicker than *Phe* as observed from the EIS results.

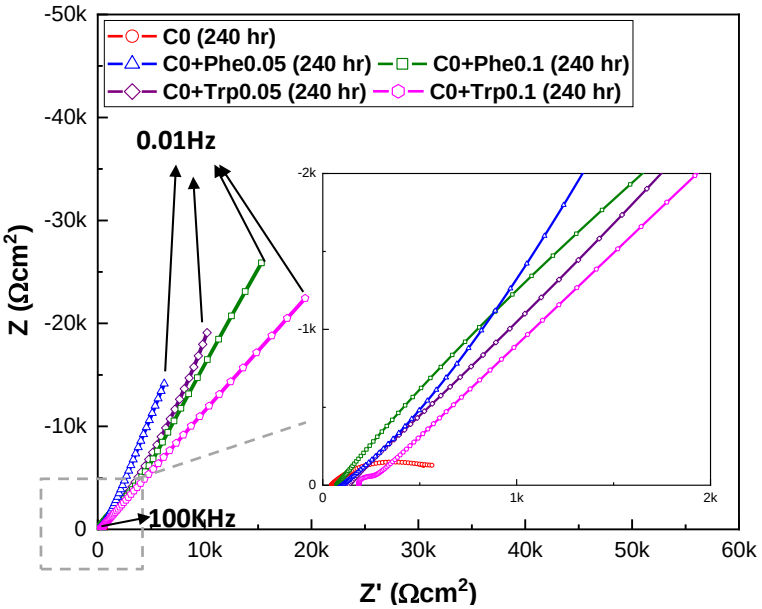

Figure 3.20 Comparative Nyquist plots of steel in B0 and B0 admixed with CoI (*Phe* and *Trp*) at 0.05M and 0.1M after 240hrs of immersion

After fitting the EIS parameters into ECM, it was noticed that similar ECM as that obtained Figure 3.20 displays a comparative Nyquist plot of steel specimens immersed in B0 and that

admixed with *Phe* and *Trp* as CoI at 240 hours. The figure clearly shows that addition of amino acids improves the resistance of rebar against corrosion. The diameter of the curves with inhibitors are very large as compared to the shrunken capacitive loop in the case of B0, suggesting they worked effectively to inhibit corrosion at admixed concentration in prolonged period. Similar amount of protection was achieved by both the CoI (*Phe* as well as *Trp*) and all the tested concentrations Or Set 1 compounds (shown in Figure 3.14) fitted the data obtained in Set 2 (*Phe* and *Trp*). The obtained electrochemical parameters after fitting are illustrated in Table 3.13.

Table 3.13 EIS fitting parameters for Set 2 compounds (*Phe* and *Trp*)

Solution	Immersion Time (hrs)	Pore solution parameters	Passive film parameters			Steel surface parameters		
			C_f			C_{dl}		
		R_s ($\Omega.cm^2$)	Y_0 ($\mu\Omega^{-1}s^n$)	n_f	R_f ($K\Omega.cm^2$)	Y_{dl} ($\mu\Omega^{-1}s^n$)	n_{dl}	R_{ct} ($K\Omega.cm^2$)
B0+Phe0.05	24	59.04	27.09	0.69	10.94	22.80	0.63	14.50
	72	34.12	21.01	0.65	18.92	9.07	0.65	42.65
	120	67.66	15.60	0.60	77.79	3.34	0.58	76.82
	240	67.66	15.05	0.63	81.15	3.00	0.66	82.18
B0+Phe0.10	24	96.43	3.788	0.60	96.61	4.023	0.54	89.00
	72	122.39	11.30	0.55	80.56	13.31	0.65	76.32
	120	32.52	19.12	0.61	55.00	16.10	0.60	60.95
	240	71.13	16.59	0.59	75.97	12.21	0.85	78.23
B0+Trp0.05	24	39.19	26.62	0.74	49.07	45.39	0.76	52.23
	72	65.57	76.61	0.68	22.87	89.00	0.76	27.87
	120	59.54	29.53	0.69	45.74	22.36	0.68	55.73
	240	71.85	16.22	0.71	85.91	19.90	0.80	88.25
B0+Trp0.10	24	31.73	18.54	0.81	152.93	12.63	0.91	152.99
	72	185.51	56.22	0.80	40.93	56.06	0.88	60.57
	120	66.68	50.06	0.78	65.72	36.60	0.72	58.74
	240	24.84	19.91	0.88	92.49	8.54	0.89	87.24

The trend in the arc diameter of the Nyquist plots is in line with the R_{ct} values obtained after fitting the curves. Conclusively, it can be said that both the compounds had the capacity to inhibit the Fe dissolution in carbonated concrete environment via adsorption mechanism; with *Trp* being more adherent to the Fe surface than *Phe*. Similar to Set 1, Set 2 compounds also inhibit corrosion by reducing charge transfer mechanism. Increase in R_f values and decrease in C_f values clearly suggest that the increase in resistance of passive film, whereas increase in R_{ct} values for

both *Phe* and *Trp* signifies that addition of these compounds reduces the charge transfer phenomena from the steel surface to the electrolyte solution. Comparing the resistive parameters of both compounds, the R_{ct} and R_f values for *Trp* is more than *Phe* after 240 hr of testing. This might be correlated with the better adsorption phenomena of *Trp* as indicated by high k_{ads} value during thermodynamic studies presented in Section 3.5.2.1

PDP scan: Figure 3.21a and b represent the PDP curves of B0 admixed with *Phe* at 0.05M and 0.1M concentration, respectively, after different testing durations. The obtained electrochemical parameters from the PDP tests are tabulated in Table 3.14. As can be seen from Figure 3.21a, after the addition of *Phe*, the PDP curves showed similar behavior at all testing durations; a stable passive zone along with small zone of trans-passivity was noticed. A large passive region is obtained in the range of -250 mV to 800 mV that can be linked with the formation of protective film by *Phe* ions on metal surface with immersion time. The i_{corr} values also support this statement as it can be seen that the i_{corr} value remained in the same order of magnitude as obtained initially (i.e., 1.28 μA/cm^2 at 24 hrs and 1.44 μA/cm^2 at 120 hrs); but after 240 hrs, the i_{corr} values decreased by one order magnitude lower than initial value indicating the transformation from a stable to stabler film with time. The increase in concentration displayed a variation in the behavior of the PDP curves (shown in Figure 3.21b). The i_{corr} values were seen to rise till 120 hrs, however, after 240hrs, the values decreased to reach its lowest, 0.85 μA/cm^2. The slight initial rise in the i_{corr} values is due to the increase in number of *Phe* ions which took some time to stabilize and form a synchronization amongst themselves (as seen in Set 1 compounds as well). Low current density values recorded at 240 hrs suggests that an inhibitive layer is formed by *Phe* at the metal solution interface which safeguarded the steel specimen from getting corroded.

Figure 3.22a and b represent PDP curves of B0 admixed with *Trp* at 0.05M and 0.1M concentration at different testing times. PDP curve of B0+Trp0.05 shows large passive region (with slight instability) at all testing durations. It is observed that the E_{corr} value shifted towards more negative side and i_{corr} value also increased from 0.57 to 2.98 μA/cm^2 from 24 to 120 hrs, however, after 240 hrs, the PDP scan clearly displays a shift in potential towards noble side with tenfold decrease in i_{corr} values (from 2.98 to 0.84 μA/cm^2). This suggests that the surface coverage of *Trp* molecules increased from 24 to 240hours which resulted in decreased i_{corr} values at 240 hours. Another prominent observation that can be made from the PDP curve of B0+Trp0.05 at 120hrs

was the emergence of a potential window where the current is seen to decrease sharply to smaller values (passive side); implying the inhibitive nature of *Trp* molecules *(Viramontes-Gamboa et al., 2007*).

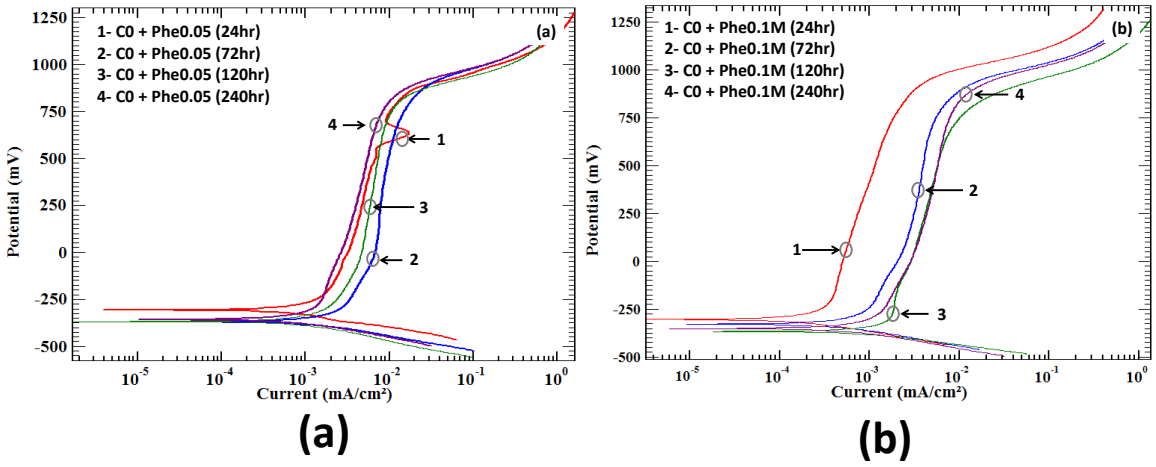

Figure 3.21 PDP curves of steel samples in B0 admixed with *Phe* at (a)0.05M; (b)0.1M

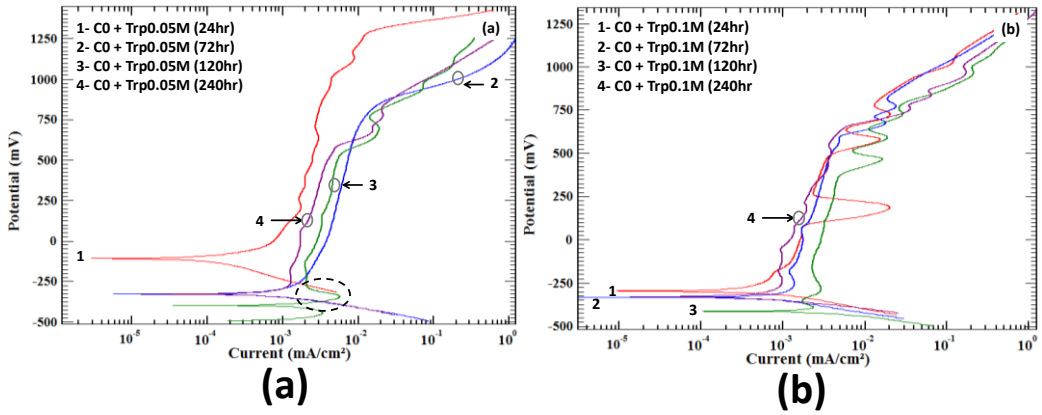

Figure 3.22 PDP curves of steel samples in B0 admixed with *Trp* at (a)0.05M; (b)0.1M

With increase in concentration (PDP curve shown in Figure 3.22b), spikes are more visible in PDP curves that might be due to instability of passive layer. The active-passive transitions in PDP curve of B0+Trp0.1 suggest that a protective film formed on rebar specimens during initial hours and tried to stabilize itself in the aggressive solution with immersion duration. The obtained electrochemical parameters display increment in i_{corr} value from 24 hrs (0.68 µA/cm^2) to 72 hrs (2.98 µA/cm^2) which then started to decrease to reach a value of 0.69 µA/cm^2 at 240 hrs of testing

duration. As the i_{corr} values are seen to be similar at 24 and that at 240 hrs, this clearly indicates that *Trp* has the capability to stop the corrosion of steel in prolonged exposure to carbonated media. An important observation is that B0+Trp0.05 took 120 hrs to stabilize however, B0+Trp0.1 got stabilized within 72 hrs. The most probable reason is the presence of indole ring in its structure which resulted in the formation of chelation with the ferrous ions. As the number of ions increased, so does the surface coverage by *Trp* and its subsequent chelation with the steel surface. Further, as the major change is observed in anodic branch of PDP curves and the shift of E_{corr} was more than 85 mV, *Phe* and *Trp* act as anodic-type inhibitors at 0.05 M and 0.1 M concentrations *(R. Zhao et al., 2022*).

Table 3.14 Electrochemical parameters from PDP curves for Set 2 compounds.

Solution	Immersion duration (hours)	E_{corr} (mV_{sce})	i_{corr} ($\mu A/cm^2$)	IE_{PDP},%
B0	24	-283.70	2.5	-
	72	-496.40	9.1	-
	120	-624.06	67	-
	240	-826.82	148	-
B0+Phe0.05	24	-295.14	1.28	48.80
	72	-366.02	1.88	79.34
	120	-363.30	1.44	97.85
	240	-341.97	0.84	99.43
B0+Phe0.1	24	-303.20	0.23	90.80
	72	-327.80	0.62	93.18
	120	-368.60	1.16	98.26
	240	-344.20	0.85	99.42
B0+Trp0.05	24	-107.82	0.57	77.20
	72	-335.18	1.20	86.81
	120	-395.78	2.98	95.55
	240	-324.00	0.84	99.43
B0+Trp0.1	24	-265.02	0.68	72.80
	72	-324.00	2.98	67.25
	120	-387.70	1.85	97.23
	240	-317.06	0.69	99.53

3.5.4 Analysis of results obtained for Set 3 compounds: *Asp* and *Glu*

3.5.4.1 Gravimetric test results for Set 3 compounds

Corrosion rate: The corrosion rate (CR_{Grav}) and surface coverage by the Set 3 compounds (i.e., *Asp* and *Glu*) are shown in Table 3.15.

Table 3.15 Corrosion rate and surface coverage for Set 3 compounds.

Inhibitor	Concentration	Nomenclature	Corrosion Rate (CR_{Grav}, mm/yr)	Surface coverage (θ_{Grav})	pH
-	-	B0 (inhibitor-free solution)	1.840	-	
Asp	0.010M	B0+Asp0.010	1.839	0.0005	8.40
	0.025M	B0+Asp0.025	1.839	0.0005	8.36
	0.050M	B0+Asp0.050	1.842	-0.0010	8.30
	0.075M	B0+Asp0.075	1.900	-0.0326	8.29
	0.100M	B0+Asp0.100	1.903	-0.0342	8.29
	0.125M	B0+Asp0.125	1.920	-0.0434	8.27
Glu	0.010M	B0+Glu0.010	1.940	-0.0543	7.90
	0.025M	B0+Glu0.025	1.943	-0.0559	7.89
	0.050M	B0+Glu0.050	2.070	-0.1250	7.88
	0.075M	B0+Glu 0.075	2.072	-0.1260	7.86
	0.100M	B0+Glu0.100	2.071	-0.1255	7.87
	0.125M	B0+ Glu0.125	2.072	-0.1260	7.80

From the table the CR_{Grav} for the steel coupons immersed in CoI admixed pore solutions (either *Asp* or *Glu*) is greater than that obtained for B0 (i.e., inhibitor-free solution). This observation suggested that these compounds were unable to inhibit the corrosion processes; rather aggravated it to higher corrosion rates. The probable reason could be the presence of two carboxylic acid functional groups in the structures of *Asp* and *Glu*; being an acidic functional group, the compounds, probably slight acidic conditions in B0. The calculated surface coverage for these compounds was also found to be negative; signifying that rather than adsorbing on the metal surface and protecting it from corrosion, Set 3 compounds aggravated the dissolution of Fe

ions from the steel coupon surface. The compounds were, hence, not taken forward for any electrochemical investigations and discarded at the preliminary test age.

To confirm the same, the pH of the solutions was monitored, and the values so obtained are displayed in Table 3.15.

3.5.5 Analysis of results obtained for Set 4 compounds: *Asn* and *Gln*

3.5.5.1 Gravimetric test results for Set 4 compounds

Corrosion rate: The corrosion rate (CR_{Grav}) and surface coverage by the Set 4 compounds (i.e., *Asn* and *Gln*) are shown in Table 3.16.

Table 3.16 Corrosion rate and surface coverage for Set 4 compounds.

Inhibitor	Concentration	Nomenclature	Corrosion Rate (CR_{Grav}, mm/yr)	Surface coverage (θ_{Grav})	Concentration chosen for electrochemical tests
	-	B0 (inhibitor-free solution)	1.840	-	
Asn	0.010M	B0+Asn0.010	0.561	0.69	-
	0.025M	B0+Asn0.025	0.434	0.76	-
	0.050M	B0+Asn0.050	0.430	0.76	✓
	0.075M	B0+Asn0.075	0.488	0.73	-
	0.100M	B0+Asn0.100	0.547	0.70	✓
	0.125M	B0+Asn0.125	0.596	0.67	-
Gln	0.010M	B0+Gln0.010	0.499	0.73	-
	0.025M	B0+Gln0.025	0.436	0.76	-
	0.050M	B0+Gln0.050	0.421	0.77	✓
	0.075M	B0+Gln0.075	0.416	0.77	-
	0.100M	B0+Gln0.100	0.390	0.78	✓
	0.125M	B0+Gln0.125	0.391	0.78	-

As can be seen from the table, the corrosion rate of steel was seen to decline with the introduction of Set 4 compounds at various concentration levels. An important point to notice was that unlike Set 1 and 2 compounds (where optimum concentration was achieved as 0.05 M for the constituent compounds), an optimum concentration of 0.05 M was recorded for *Asn;* while, for *Gln*, the optimum concentration was 0.1M. Further, the saturation level for Asn was 0.05 M, while that for

Gln was 0.1M. Hence, 0.05 M and 0.1 M were the two concentrations at which set 4 compounds were tested electrochemically.

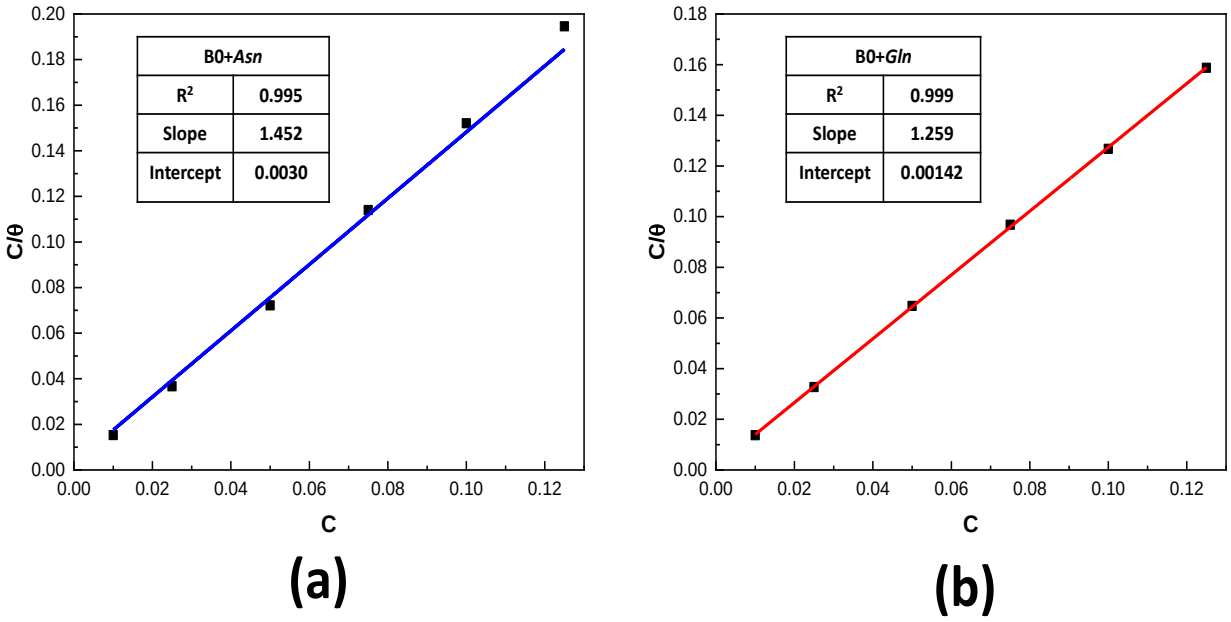

Figure 3.23 Langmuir adsorption isotherms for (a) *Asn;* (b)*Gln* as inhibitors in B0

Adsorption isotherm: Similar to Set 1 and 2 compounds, Set 4 compounds were also seen to follow the Langmuir isotherm for adsorption. The graphs obtained after fitting the isotherm (refer Figure 3.23) show high correlation coefficients (R^2) of 0.995 for *Asn* and 0.999 for *Gln*. The fitting as well as thermodynamic parameters are provided in Table 3.17. Higher k_{ads} values were obtained for *Gln* than *Asp* (2.11 times higher) suggesting stronger adsorption of *Gln* molecules on the steel surface than *Asp.* The ΔG^{o}_{ads} for Set 4 compounds indicate physio-chemisorption processes occurring at the rebar surface. The molecules of Set 4 chemically interconnect with the ferrous ions on the metal surface and form chemical bonds; also, they are electrostatically attracted towards the metal surface.

Table 3.17 Fitting and thermodynamic parameters for Set 4 compounds.

Solution	Fitting parameters		Thermodynamic parameters	
	R^2	Slope	k_{ads} (M^{-1})	$\Delta G°_{ads}$ (kJ/mol)
B0 + Asn	0.995	1.452 ± 0.0005	333.33	-24.355
B0 + Gln	0.999	1.259 ± 0.0060	704.22	-26.209

3.5.5.2 Electrochemical test results for Set 4 compounds

EIS study and equivalent circuit modelling: The typical comparative Nyquist plots for Set 4 compounds are shown in Figure 3.24. Alongside, the Bode plots are presented in *Annexure A* (Figures A6 and A7). Firstly, the behavior of the compounds is studied on the basis of its concentration (at 0.05 M and 0.1 M), thereafter, the performance is compared with Nyquist plots obtained for B0 (i.e., inhibitor-free solution); shown in Figure 3.25.

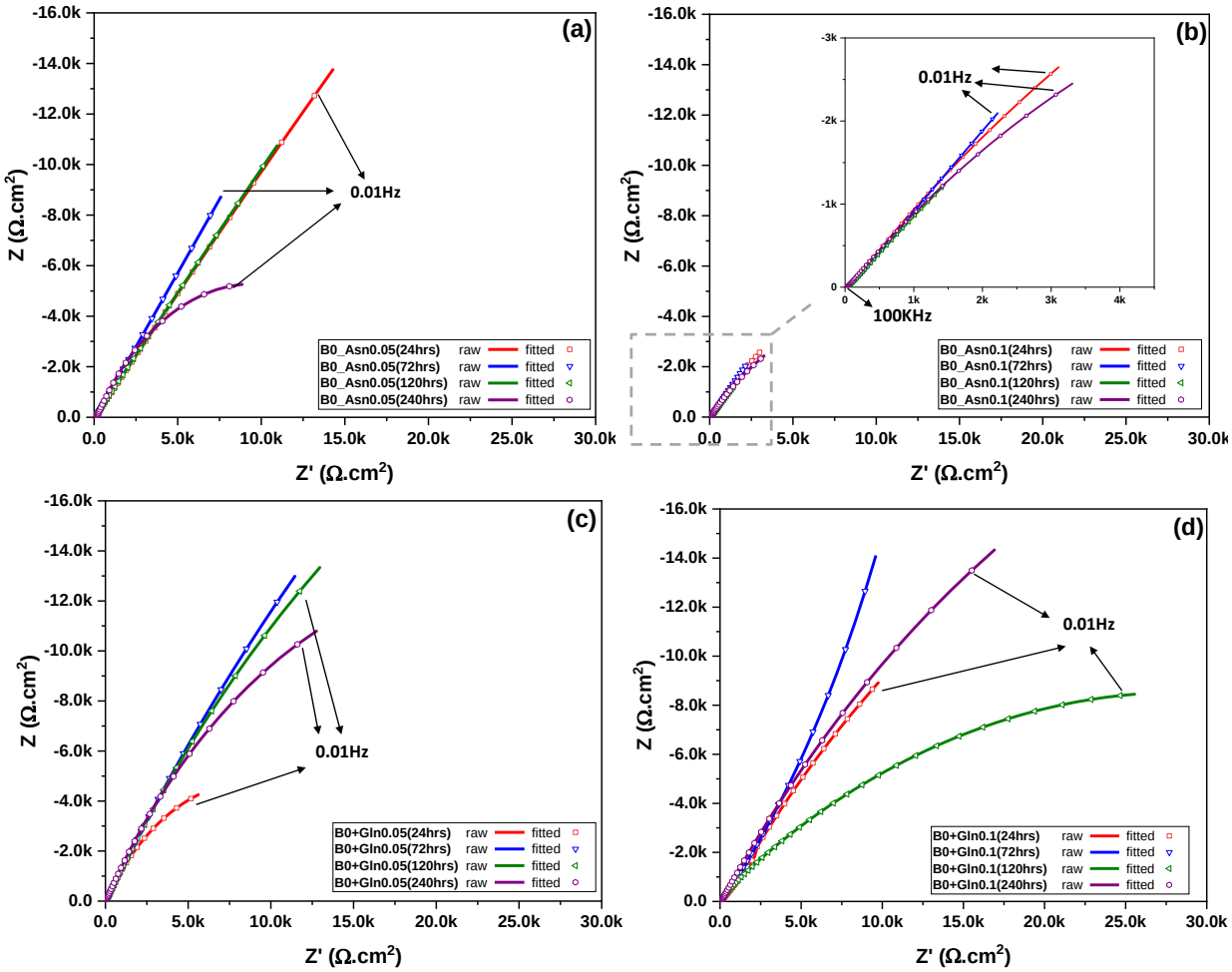

Figure 3.24 Nyquist plots of steel samples immersed in (a)B0+Asn0.05; (b)B0+Asn0.1; (c)B0+Gln0.05 and (d)B0+Gln0.1

With the addition of *Asn* at 0.05M concentration, the recorded low frequency arc for 24 hrs had a quite large diameter, suggesting that *Asn* ions readily deposited on the rebar surface after admixing in carbonated concrete pore solution as shown in Figure 3.24a. Even after 240 hrs of immersion, the semicircle sustained its diameter unlike in B0 which completely subsided at the end of testing program. This shows that *Asn* molecules have the capability to protect rebar against

corrosion. The layer development effectively reduced the number of contact sites between the corrosive media and the metal surface, hence, avoiding its dissolution (*Berdimurodov et al., 2022*). When the concentration of *Asn* was increased from 0.05M to 0.1M, change in inhibition behavior was observed through Nyquist plots. Figure 3.24b shows that the size of the capacitive loops at all the testing durations have shrunk with the increase in the number of inhibitor ions. The possible reason could be that at higher concentrations, inhibitor-inhibitor interactions dominated than the inhibitor-metal interaction because of which the adsorption could not take place. Another possible reason could be the desorption of the inhibitor molecules from the coupon surface when the number of *Asn* molecules were doubled; desorption being the probable reason (*Q. Liu et al., 2023*). Figure 3.25 displays the comparative Nyquist plot for inhibitor-free and inhibitor-admixed solutions at 240 hours of testing. The diameter of the curves with amino acids is highly accentuated as compared to the shrunken capacitive loop of samples immersed in inhibitor-free solution (B0). The result can be attributed to the adsorption of the inhibitor molecules on the rebar surface which created a barrier film over rebars. Hence, it can be inferred that *Asn* and *Gln* have the tendency to make an extremely resistant adsorbed film on the metal surface whose protecting power improves with the immersion duration. The layer formed in the case of *Gln* as CoI is definitely more impermeable and thicker as compared to that formed by *Asn* on steel substrate as conveyed from the Nyquist plots. Notably, the largest diameter loop was obtained for rebar in B0+Gln0.1.

Figure 3.24c and d present the Nyquist graphs for B0 admixed with *Gln* at 0.05M and 0.1M concentration, respectively. The diameter of the arc is seen to rise from 24 to 240hrs with slight deviations during the intermediate recordings. This clearly suggests that the inhibitor ions developed the inhibitive layer slowly whose thickness increased with time. The finally formed layer (at 240 hours) has a very high adherence to the steel surface as expected from the calculated values of k_{ads} for *Gln.* This suggests the highly protective nature of *Gln* against carbonation-induced corrosion. Similar behaviour of the Nyquist plots was recorded with the rise in the inhibitor concentration (Figure 3.24d). Unlike *Asn,* the diameter of the low frequency arcs is seen to increase with the doubling of the inhibitor ions. These observations suggest that *Gln* ions raise the surface coverage and hence, the protection capability with the increase in number of inhibitor molecules.

.

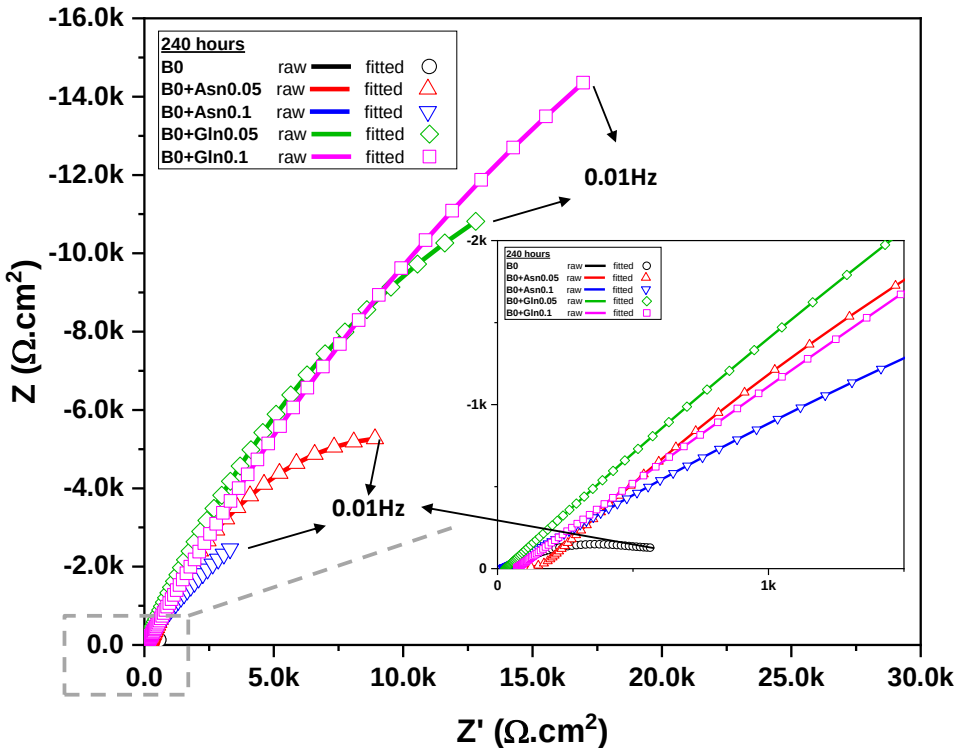

Figure 3.25 Comparative Nyquist plots of steel in pore solution without CoI (B0) and with CoI (*Asn* and *Gln*) at 0.05M and 0.1M after 240hrs of immersion

Figure 3.25 displays the comparative Nyquist plot for inhibitor-free and inhibitor-admixed solutions at 240 hours of testing. The diameter of the curves with amino acids is highly accentuated as compared to the shrunken capacitive loop of samples immersed in inhibitor-free solution (B0). The result can be attributed to the adsorption of the inhibitor molecules on the rebar surface which created a barrier film over rebars. Hence, it can be inferred that *Asn* and *Gln* have the tendency to make an extremely resistant adsorbed film on the metal surface whose protecting power improves with the immersion duration. The layer formed in the case of *Gln* as CoI is definitely more impermeable and thicker as compared to that formed by *Asn* on steel substrate as conveyed from the Nyquist plots. Notably, the largest diameter loop was obtained for rebar in B0+Gln0.1.

After fitting the EIS parameters into ECM, it was noticed that similar ECM as that obtained for Set 1 compounds (shown in Figure 3.14). The obtained electrochemical parameters after fitting are illustrated in Table 3.18. The trend in the arc diameter of the Nyquist plots is in line with the R_{ct} values trend seen from the table of electrochemical parameters. Conclusively, it can be said that both the compounds had the capacity to inhibit the Fe dissolution in carbonated concrete environment via adsorption mechanism; with *Gln* being more adherent to the Fe surface than *Asn*.

Table 3.18 EIS fitting parameters for Set 4 amino acids.

Solution	Immersion Time (hrs)	Pore solution parameters	Passive film parameters			Steel surface parameters		
			CPE_f			CPE_{dl}		
		R_s (Ω)	Y_0 ($\mu\Omega^{-1}s^n$)	n_f	R_f ($10^3\ \Omega$)	Y_0 ($\mu\Omega^{-1}s^n$)	n_{dl}	R_{ct} ($10^3\ \Omega$)
B0	24	28.11	1361	0.85	1.85	75.9	0.94	8.791
	72	22.89	1532	0.78	7.67	2355	0.82	7.672
	120	30.01	7088	0.57	4.52	2454	0.6	5.487
	240	44.25	36274	0.58	0.55	1946	0.42	0.6
B0+Asn 0.05	24	22.25	9.68	0.80	82.77	0.88	0.65	55.95
	72	31.41	4.12	0.6	117.23	1.34	0.65	42.56
	120	42.15	5.23	0.67	141.67	2.65	0.67	38.93
	240	43.62	2.02	0.7	92.65	3.5	0.64	28.9
B0+Asn 0.1	24	26.25	5.3	0.52	30.73	35.26	0.58	30.78
	72	35.46	17.77	0.5	28.23	56.38	0.6	18.24
	120	39.75	36.44	0.43	22.24	88.4	0.55	11.09
	240	42.11	58.38	0.5	19.7	127.1	0.52	8.01
B0+Gln 0.05	24	43.62	4.84	0.78	57.25	8.88	0.64	42.03
	72	41.69	2.77	0.74	67.94	6.24	0.64	37.94
	120	43.45	3.15	0.65	74	5.52	0.66	59.2
	240	39.63	2.8	0.6	85.4	1.94	0.72	95.46
B0+Gln 0.1	24	30.16	5.8	0.62	48.67	0.08	0.71	37.96
	72	43.76	2.81	0.69	67.93	0.92	0.72	78.13
	120	42.21	2.55	0.6	99.36	1.54	0.64	91.66
	240	40.66	2.66	0.63	115.36	3.45	0.67	154.93

PDP Scan: The polarization curves obtained for Asn and Gln at 0.05 M and 0.1 M are shown in Figure 3.26 and corresponding electrochemical parameters (for Set 4 compounds in comparison with B0 parameters) are displayed in Table 3.19.

Figure 3.26a and b represent the PDP curves of B0 admixed with *Asn* at 0.05M and 0.1M concentration at different testing durations. PDP curve of B0+Asn0.05 shows large passive region (with slight instability) at all testing durations. Also, the inhibition efficiency from Table 3.19 is also seen to rise from 20% to 98.2% with increase in immersion duration from 24 hours to 240 hours. This suggests that *Asn* molecules increased their surface coverage over rebar with time which resulted in enhanced protection efficiency in longer duration. Further, the increase in concentration from 0.05M to 0.1M of *Asn* in B0 led to the change in behavior of PDP curves as

shown in Figure 3.26b. Stabler passive regions are visible in the figure but the i_{corr} values recorded are comparable with those obtained for the un-inhibited samples till 120 hours. It was only after 240 hours, an inhibition efficiency of 60.13% was recorded. This suggests that with the increase in number of *Asn* ions, the inhibition capacity decreases. The possible reason could be that at higher concentrations, inhibitor-inhibitor interactions dominated than the inhibitor-metal interaction till 120 hours which prevented the molecules of *Asn* from getting adsorbed on rebar surface. However, after prolonged duration, the molecules got stabilized and started creating a film over rebar preventing it from corrosion which can be confirmed from lowered i_{corr} values at 240 hours. It is also worth noting that although, the ions took 120hrs to stabilize and the efficiency reduced with rise in concentration, still the i_{corr} values recorded for specimens immersed in B0+Asn0.1 is 2.5 times lower than that obtained in B0; signifying its protection ability.

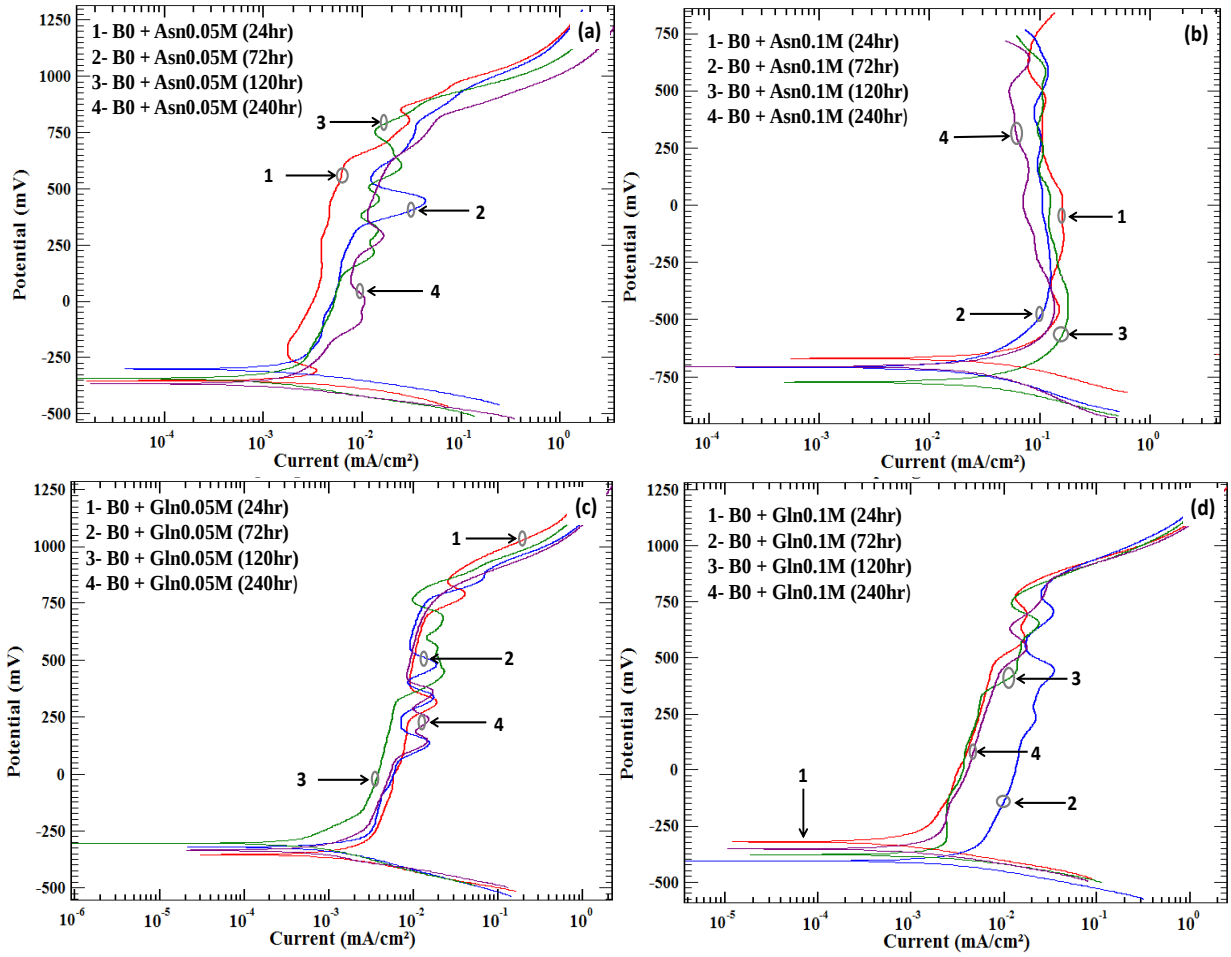

Figure 3.26 PDP curves of steel samples immersed in (a)B0+Asn0.05; (b)B0+Asn0.1; (c)B0+Gln0.05 and (d)B0+Gln0.1

Table 3.19 Electrochemical parameters from PDP curves of Set 4 amino acids

Solution	Immersion duration (hours)	E_{corr} (mV_{sce})	i_{corr} ($\mu A/cm^2$)	IE_{PDP},%
B0	24	-283.70	2.50	-
	72	-496.40	9.10	-
	120	-624.06	67.00	-
	240	-826.82	148.00	-
B0+Asn0.05	24	-336.32	2.00	20.00
	72	-285.04	2.50	72.50
	120	-323.64	1.50	97.70
	240	-344.48	2.60	98.20
B0+Asn0.1	24	-657.94	89.00	-
	72	-709.13	4.60	49.45
	120	-774.82	89.00	-
	240	-704.65	59.00	60.13
B0+Gln0.05	24	-346.91	1.87	25.20
	72	-313.21	2.00	78.02
	120	-295.24	1.43	97.86
	240	-327.76	1.50	98.98
B0+Gln0.1	24	-331.52	1.00	60.00
	72	-410.37	3.70	59.34
	120	-389.87	1.60	97.61
	240	-357.86	1.20	99.18

Figure 3.26c shows the PDP curves recorded for rebar specimens immersed in B0+Gln0.05. A metastability in the curves is visible at all testing durations which is indicative of the formation and breaking of the passive film over rebar. Also, a transpassive zone is seen near -750mV at all testing hours. This evinces that a layer of adsorbed *Gln* molecules is developed on the rebar surface which is getting stabilized with time. The values of inhibition efficiencies also indicate the same, as a rise in efficiency is seen from 25.20% to 98.98% with testing duration. With the rise in concentration, not much change in the nature of the PDP curves is seen (Figure 3.26d). However, it is worth mentioning that with the increase in the number of *Gln* molecules, higher inhibition efficiency was noted at each testing duration for B0+Gln0.1 as compared to B0+Gln0.05. This indicates that *Gln* molecules had strong interaction with the Fe ions present on the rebar. More number of inhibitor ions got adsorbed on the rebar surface with doubling the concentration which resulted in better protection than at lower concentration. An inhibition efficiency of 99.18% was recorded at 240 hours.

Further, as the major change is observed in anodic branch of PDP curves and the shift of E_{corr} was more than 85 mV, *Asn* and *Gln* act as anodic-type inhibitors at 0.05 M and 0.1 M concentrations (*R. Zhao et al., 2022*). This means that the inhibition of the metal dissolution process is greater; additionally, there was no change in trend of the cathodic domain indicating that the oxidation reaction was not much affected in the presence of *Asn* and *Gln*. In aqueous solutions, the ionic state of amino acids is dependent on pH. In the alkaline environment, above pH 8.16, the molecules exist in their anionic form (Ismail, 2007); such negatively charged structure is expected to get highly attracted by the positively charged anodic sites on the metal surface.

The results, hence, indicate that both *Asn* and *Gln* efficiently protected the rebar from carbonation-induced corrosion at 0.05M as well as 0.1M concentration. The highest protection ability is displayed by *Gln* at 0.1M concentration (performance similar to that seen through EIS studies). The observations are in line with the work of other researchers where *Gln* was seen to perform better than *Asn* in different corrosive pore solutions. Better performance of *Gln* as compared to *Asn* was attributed to the longer chain length of *Gln* than *Asn*. *Chauhan et al. (2021*) stated that organic compounds with long hydrocarbon chains orient themselves parallelly on the metal surfaces and increase their surface coverage thus, providing high corrosion inhibition capacity (*Chauhan et al., 2021*). *Verma et al. (2022)* also reported that the inhibition efficiency of organic compounds increases with the increase in the chain length upto a particular level *(Verma et al., 2022*).

3.6 COMPARITIVE PERFORMANCE EVALUATION OF COI

Eight amino acids chosen for the inhibition efficiency evaluation in synthetic pore solution simulating carbonated concrete (B0) were tested electrochemically via EIS and PDP tests. The result analysis conveys that the presence of heteroatoms and ring in the chemical structure of an organic compound plays a vital role in the inhibition performance. Furthermore, the physical bonding between the amino acids and Fe ions also plays an important role in curbing the corrosion processes. Amino acids exist in their anionic form (due to lone pair of electrons and convergence of -COOH to $-COO^-$) while Fe ions possess positive charge due to oxidation reaction (loss of electrons). The compiled results from the analysis are displayed in Table 3.20.

Table 3.20 Effective amino acids with their inhibition efficiencies (%) and remarks on their probable reaction centers

Set	Amino acid	Solution	Efficient/Not	Inhibition Efficiency (%)	Remarks	
SET 1	*Ser*	B0+Ser0.05	✓	96.35	Oxygen (O) of alcohol (-OH) functional group at one end and O of -COO^- and N of -NH_2 from the other end of the compound are the probable reaction centres.	
		B0+Ser0.10	✓	93.63		
	Cys	B0+Cys0.05	✓	99.64	Sulphur (S) of thiol (-SH) functional group at one end and O of -COO^- and N of -NH_2 from the other end of the compound are the probable reaction centres.	
		B0+Cys0.10	✓	96.01		
SET 2	*Phe*	B0+Phe0.05	✓	99.43	Delocalized π electrons of benzene ring from one end and O of -COO^- and N of -NH_2 from the other end of the compound are the probable reaction centres.	
		B0+Phe0.10	✓	99.41		
	Trp	B0+Trp0.05	✓	99.43	N atom of the heterocycle (pyrrole ring) from one end and O of -COO^- and N of -NH_2 from the other end of the compound are the probable reaction centres.	
		B0+Trp0.10	✓	99.52		
SET 3	*Asp*	B0+Asp0.05	✗	-	pH lowering of the base solution (B0) with the addition of these compounds aggravated the corrosion processes.	
		B0+Asp0.10	✗	-		
	Glu	B0+Glu0.05	✗	-		
		B0+Glu0.10	✗	-		
SET 4	*Asp*	B0+Asn0.05	✓	98.24	O and N of amide functional group (-$CONH_2$) from one end and O of -COO^- and N of -NH_2 from the other end of the compound are the probable reaction centres.	Shorter chain length can lead to steric hinderance during chelate formation.
		B0+Asn0.10	✓	60.13		
	Gln	B0+Gln0.05	✓	98.98		Longer chain length of the compound results in lesser steric hinderance during chelate formation.
		B0+Gln0.10	✓	99.19		

3.7 CLOSING REMARKS

The pore solution test was conducted to check the inhibition efficiency of amino acids as Green CoIs in synthetic pore solution simulating carbonated concrete in a short period of time and to study the effect of slight change in functional group on the inhibition efficiency of the amino acids.

The gravimetric testing and electrochemical tests indicate that most of the amino acids are efficient in inhibiting the corrosion of steel in. All the efficient amino acids inhibit the anodic-half cell reaction of the corrosion process, hence, can be classified as anodic-type inhibitors in carbonated concrete environment (pH ~ 9). Also, the presence of functional group, heteroatom, heterocyclic ring and chain length of an amino acid; along with, the pH of the solution so obtained greatly influences the inhibition capacity of the amino acid. Based on pore solution testing, six out of eight amino acids i.e., *Ser, Cys, Phe , Trp, Asn and Gln* have the inhibitor efficacy of > 95%. An important point to mention is that Set 4 compounds belonging to the category 'polar with negative charge' were found to be in-efficient.

The next important aspect to study is the inhibition mechanism of the efficient amino acids in carbonated concrete environment in a more detailed manner (as amino acids have not been used as CoI for carbonated concrete environment until now). The upcoming chapter (Chapter 4) deals with this aspect.

CHAPTER 4 : DEVELOPMENT OF CORROSION INHIBITION MECHANISM OF AMINO ACIDS

4.1 GENERAL

The major aim of the present work is to understand the corrosion inhibition efficiency of amino acids as surface applied corrosion inhibitors (SACoI) for the protection of rebar embedded in portland pozzolana cement (PPC) concrete. The efficiency of the compounds was evaluated through pore solution testing in the previous chapter, and it was found that most of the amino acids successfully reduced the corrosion of steel reinforcement in carbonated concrete environment. Hence, efficient compounds can be taken forward for further investigations.

The current chapter is focused on the development of inhibition mechanism of the amino acids in carbonated concrete environment (B0). Eight amino acids were chosen initially, out of which six amino acids exhibited inhibition efficiency of more than 95% in carbonated synthetic pore solution B0 (presented in the previous chapter). The probable reaction centers of the compounds are known (i.e., hetero-atoms and de-localized π electrons); however, the exact binding sites from the amino acid with the Fe ion still needs to be explored. Furthermore, it was observed in the previous chapter that in a particular Set of two amino acids, one performs slightly better than the other, in terms of thermodynamic stability of passive layer formed. To study the reason behind this difference in the performance of two similar amino acids, the study of the inhibition mechanism is vital. The inhibition mechanism was developed based on the analysis of data obtained from analytical imaging tools and characterization tools. Figure 4.1 briefly describes the test methodology adopted for the current chapter.

4.2 MATERIAL SYSTEM

The major materials used for the study of inhibition mechanisms in pore solution are synthetic pore solution simulating carbonated concrete environment (B0), bare steel specimens and amino acids (as corrosion inhibitors). The details of all these materials are presented in the following sections:

4.2.1 Steel

8 mm diameter ribbed thermo mechanically treated (TMT) steel bars confirming to IS: 1786:2008 (IS:1786-2008, 2008), widely used in RC structures were tested for their performance in corrosive environment. The chemical composition and properties of steel bars was provided by the manufacturer and presented in Table 3.1 and Table 3.2, respectively, in the previous chapter (CHAPTER 3).

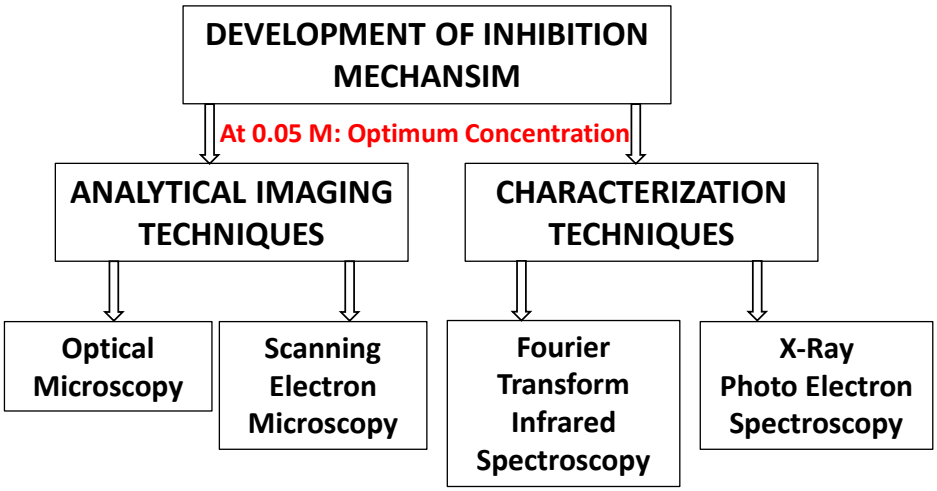

Figure 4.1 Techniques employed for the study of inhibition mechanism of amino acids

4.2.2 Corrosion Inhibitors

Amino acids are green organic compounds that were used as corrosion inhibitors (CoIs) in the current study. Eight amino acids were chosen on the basis of their solubility, presence/positioning of functional groups and their chain lengths. Further, the compounds were divided into four sets, each containing two amino acids. The sets were finalized on the basis of the similarity of either chain length or functional group or presence of benzene rings. The compounds in each set had a slight variation in their structure to understand the difference in the inhibition mechanism. The finalized sets and their molecular structures in presented in Table 4.1 and the variability in the molecular structures of the constituent compounds considered in each set (other information about the compounds is presented in Table 3.3 in CHAPTER 3).

4.2.3 Other Chemicals

Besides the amino acids that were investigated for their use as CoIs, some other chemicals were also used for preparation of B0 that mimics the interstitial concrete pore solution of carbonated

concrete. In order to prepare B0, reagent grade calcium hydroxide ($Ca(OH)_2$), potassium hydroxide (KOH), and sodium hydroxide (NaOH) were used. Along with this, analytical reagent grade hexane and methanol was used for cleaning of steel specimens and laboratory glassware.

Table 4.1 Distribution of amino acids into different sets, their chemical structures, molecular weights and solubility information.

Sets	Compound (and its abbreviation)	Chemical structure	Variability in the sets and other important information regarding the molecular structures.
SET 1	Serine (*Ser*)	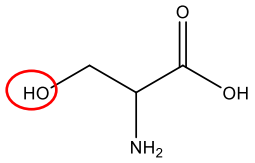	• -OH (alcohol) in *Ser* and -SH (thiol) in *Cys.* • Chain length is similar.
	Cysteine (*Cys*)	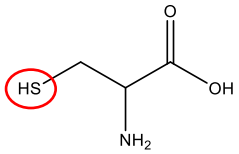	
SET 2	Phenylalanine (*Phe*)	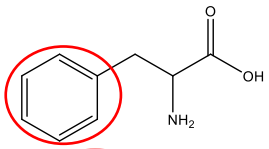	• Benzene ring in *Phe* and benzene ring fused with indole (pyrrole) in *Trp.* • *Trp* is heterocyclic (N atom in its benzene ring); while, *Phe* is not. • Chain length is similar.
	Tryptophan (*Trp*)	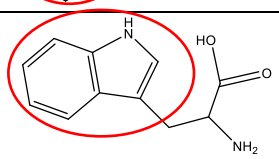	
SET 3	Aspartic Acid (*Asp*)	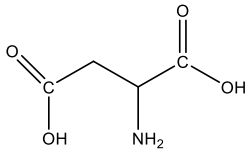	• Both the compounds have –COOH (carboxylic acid) as an additional functional group. • Variable chain length. • 4 carbon (C) atoms in *Asp* and 5 C atoms in *Glu*.
	Glutamic Acid (*Glu*)	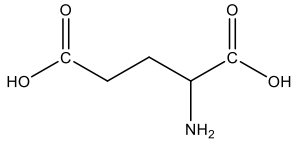	
SET 4	Asparagine (*Asn*)	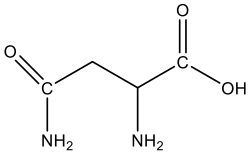	• Both the compounds have $–CONH_2$ (amide) as an additional functional group. • Variable chain length. • 4 carbon (C) atoms in *Asn* and 5 C atoms in *Gln*.

4.3 PREPARATION PROCEDURE

The test set up required preparation of synthetic mixture which could simulate real concrete pore solution that surrounds the steel rebar. Also, the steel bars were to be prepared in order to expose a definite surface area for corrosion. The details of preparation of both bare steel specimens and of synthetic pore solution are presented in the following sections.

4.3.1 Preparation of Steel Specimens

8 mm diameter bar was cut into coupons of 2 mm height (8ϕ-2mm) and were utilized for the analytical imaging as well as characterization tests. In order to ensure a rust-free surface, both type of test pieces was rubbed with silicon carbide papers (#400 to #2000) and rinsed with distilled water. The rebars were than degreased with hexane and allowed to dry at room temperature (25 ± 2 °C). Figure 4.2 shows the 8ϕ-2mm steel coupon used for the mechanism studies.

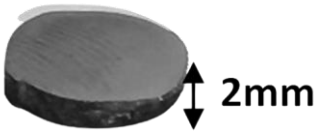

Figure 4.2 Steel specimens prepared for analytical imaging and characterization tests

4.3.2 Preparation of Synthetic Pore Solution

Synthetic pore solution simulating carbonated concrete was prepared in two steps; (i) a solution of sodium hydroxide (0.1 M NaOH), potassium hydroxide (0.3 M KOH) and calcium hydroxide (0.01 M Ca $(OH)_2$) was prepared in distilled water mimicking the non-carbonated condition inside the concrete pores, (ii) The prepared solution was bubbled with 99 % pure CO_2 to reach the pH value of near 9 in order to simulate the carbonated state of the pore solution after the diffusion of CO_2 in real conditions. The prepared pore solution was then filtered using Whatman Filter No. 1 to remove $CaCO_3$ (calcium carbonate) precipitates. The finally obtained solution is referred to as base solution (B0).

Once the corrosive solution was prepared, CoIs were added in B0 at their optimum concentration of 0.05M finalized from the electrochemical tests. Different solutions in which the steel coupons were immersed in order to study the mechanism of corrosion and inhibition is given in Table 4.2. Set 1, Set 2 and Set 4 compounds displayed >95% inhibition efficiency during the electrochemical tests and hence, were analyzed for mechanism development; while Set 3

compounds were in-efficient in inhibiting the corrosion of steel and hence, were not investigated further. The nomenclature used is same as defined in the previous chapter i.e., CHAPTER 3, Section 3.3.2, Figure 3.4. After mixing the CoIs in the base solution, a slight change in the pH value of the resultant solution was observed. To maintain pH value of the solution at around 9, the solution was either bubbled with CO_2 (if the inhibitor addition increased the pH value) or sodium hydroxide was added (if the inhibitor addition lowered the pH value).

Table 4.2 Solution description and purpose for immersion of steel coupon (8ϕ-2mm)

S.No.	Solution	Description	Purpose
1.	B0	Synthetic pore solution simulating carbonated concrete environment	To study the corrosion mechanism and products formed in carbonated corrosive environment
2.	B0+Ser0.05	Amino acid admixed as CoI at a concentration of 0.05 M in B0	To study the inhibition mechanism of amino acids as CoI in concrete simulating environment
3.	B0+Cys0.05		
4.	B0+Phe0.05		
5.	B0+Trp0.05		
6.	B0+Asn0.05		
7.	B0+Gln0.05		

4.4 TECHNIQUE EMPLOYED

To understand the possible inhibition mechanism and the impact of amino acids on the surface characteristics, a thorough surface analysis of steel specimen was conducted. The tests were performed on one optimum concentration of inhibitor which was decided based on electrochemical test results. All the surface related tests were carried out after immersing the steel coupons in their respective solutions for 240 hours (hrs). The samples were carefully taken out from the vials without disturbing the layer formed and dried before subjecting to the respective test.

4.4.1 Analytical imaging techniques: Optical Microscopy (OM) and Scanning electron microscopy (SEM)

The basic principle of optical microscopy (OM) involves using visible light to illuminate a sample, which interacts with the sample and produces an image that can be magnified and observed. Light from a source pass through or reflects off the sample, and this interaction alters the direction, phase, or intensity of the light. The altered light is then collected by lenses, which focus it onto the eyepiece or camera, allowing us to see the details of the sample. In the context of corrosion and inhibition studies, the principle of optical microscopy involves using visible light to examine the surfaces of materials to understand their corrosion behavior and the effectiveness of inhibition

measures. When studying corrosion, the sample's surface is observed under magnification, allowing researchers to identify corrosion products, pits, and other forms of material degradation. In the case of inhibition studies, the impact of protective coatings or inhibitors can be visually assessed. By illuminating the sample with visible light, researchers can observe and document changes in surface features, corrosion patterns, and the extent of protection provided by inhibitors. Hence, OM serves as a valuable tool for directly observing and documenting the visible effects of corrosion and the success of inhibition strategies on the material's surface. The surface of steel coupons kept in the pore solution admixed with and without the inhibitors was observed by using Dino Lite Edge Digital Microscope (AM7915 series) in the current research study. OM images were captured at 1mm and were analyzed to study the effect of corrosive and inhibitive media on steel coupons.

Scanning Electron Microscopy (SEM), on the other hand, is a powerful technique used in corrosion and inhibition studies to investigate material surfaces at a detailed level. It operates on the principle of electron-matter interactions. A focused beam of electrons is scanned across the sample's surface; as the electrons interact with the sample, they generate various signals, such as secondary electrons and backscattered electrons, which provide information about the sample's topography, composition, and morphology. In corrosion studies, SEM allows researchers to closely examine the microstructural changes caused by corrosion processes. When studying inhibition processes, SEM helps visualize the effectiveness of protective measures by providing high-resolution images of the surface. Its ability to capture fine details at a nanoscale level makes it valuable for understanding the intricate interactions between materials and inhibitors, as well as the progression of corrosion mechanisms. During the current research, JEOL JSM – 6100 SEM was employed to characterize the morphology of the corrosion products and metal-inhibitor complex formed on coupon surface in B0. 10 kV of accelerating voltage was used for SEM imaging with varying low and high magnifications.

Both OM and SEM were hence, employed as analytical imaging techniques to study the corrosion/inhibition processes. OM helped in studying the surface conditions and larger-scale phenomena in corrosion and inhibition studies; while, SEM offered high-resolution images that revealed intricate surface features, microstructural changes, and corrosion patterns. Both techniques contributed significantly to understanding the processes involved in rebar degradation

and protection by inhibitors in B0 (synthetic pore solution simulating carbonated concrete, pH ~ 9).

4.4.2 Characterization Techniques: Fourier Transform Infrared Spectroscopy (FTIR) and X-Ray Photoelectron Spectroscopy (XPS)

FTIR spectroscopy employs mid-infrared energy to scrutinize the makeup and arrangement of molecules in substances. This is done by measuring how certain frequencies of infrared light are absorbed, generating a unique pattern similar to a fingerprint. This technique is highly useful for both the identification and analysis of substances. Since every functional group in an organic compound is composed of different atoms and bond strengths, vibrations are unique to functional groups, and classes of functional groups (e.g., O-H and C-H stretches appear around 3200 cm-1 and 2900 cm-1, respectively). Hence, the collection of vibrational energy bands for all of the functional groups a molecule is unique to every molecule, these peaks can be used for identification using library searches of comprehensive sample databases. For the corrosion/ inhibition studies, FTIR is generally employed to identify the functional groups present in the layer that gets developed on the steel surface after its immersion in corrosive media. In the current research, FTIR was employed, firstly, to study the composition of the corrosion products formed on steel coupon when immersed in B0 (inhibitor-free solution) and secondly, to study the composition of the reaction products formed on the steel coupon when immersed in B0 admixed with different amino acids as CoI. FTIR was recorded on Perkin Elmer-Spectrum RX-IFTIR spectrometer under the frequency range of 400–4000 cm^{-1} and resolution ratio of 1 cm^{-1}. The automatic baseline and the original spectral data were corrected by FTIR software.

On the other side, a more sophisticated technique for compositional analysis of the surface film is X-ray Photoelectron Spectroscopy (XPS), also known as Electron Spectroscopy for Chemical Analysis (ESCA). It is a technique used to analyze the elemental composition and chemical states of the surface of a material. It involves exposing a sample to X-rays, which cause electrons to be emitted from the surface. By measuring the energy and number of emitted electrons, valuable information about the elements present, their chemical environments, and their oxidation states can be obtained. It provides insights into surface phenomena, interfaces, and thin films, aiding researchers in understanding how materials behave on a molecular level. In the context of corrosion and inhibition studies, XPS allows researchers to examine the chemical changes occurring at a material's surface during corrosion processes. It can identify the oxidation states of

elements involved in corrosion reactions and characterize corrosion products formed on the surface. This helps in understanding the mechanisms of corrosion and aids in developing effective corrosion prevention strategies. Furthermore, in inhibition studies, XPS helps analyze the interaction between corrosion inhibitors and metal surfaces. By studying the chemical composition of inhibitor-treated surfaces, researchers can assess the effectiveness of various inhibitors and understand how they form protective layers on the surface, preventing or reducing corrosion. In the current study, XPS was performed on Thermo Scientific Nexca Base with X-ray (400µm, 72w, 12000V) monochromatic Al-Kα source (hυ=1486.6eV), a hemispherical analyzer and a 128-channel plate detector. A flood gun was used to reduce the charge shift. The XPS results were corrected by C 1s peak (binding energy of 284.6eV). Gaussian-Lorentzian product function was used for peak fitting through XPS Peak software (Version 4.1). FTIR and XPS peaks can confirm the presence of organic moieties from the amino acids present on the steel coupon surface.

Holistically, the aim of employing the two techniques is the same yet the information provided by them varies at micro level. FTIR provides molecular-level information about functional groups, while XPS reveals elemental composition and oxidation states on surfaces. Therefore, these techniques can provide comprehensive information about functional groups that are involved in interaction with the Fe ions on metal surface; helpful in developing the corrosion as well as inhibition mechanism

4.5 RESULTS AND DISCUSSION

The results obtained by performing the above-mentioned tests in pore solution are presented in the upcoming sections. Analytical imaging and characterization test results are discussed in detail corresponding to each Set as per Table 4.1

4.5.1 Analysis of Test Results Obtained for B0 (CoI Free Solution)

4.5.1.1 Analytical Imaging Test Results for B0

The Figure 4.3 (left) shows the corroded surface of specimen immersed in B0, after 240 hrs. It can be observed that due to low pH environment, the exposed surface was uniformly corroded and formed corrosion products which are clearly visible over the surface. The surface morphologies of dipped sample in B0 were further studied by SEM images which were taken at different magnification range. The metallic surface lustre of the sample immersed in B0 was lost due to

formation of visible corrosion products (shown in Figure 4.3 (right)). The higher magnified image shows formation of blocky and globular oxide with porous microstructure in the form of FeOOH and Fe_2O_3 (i).

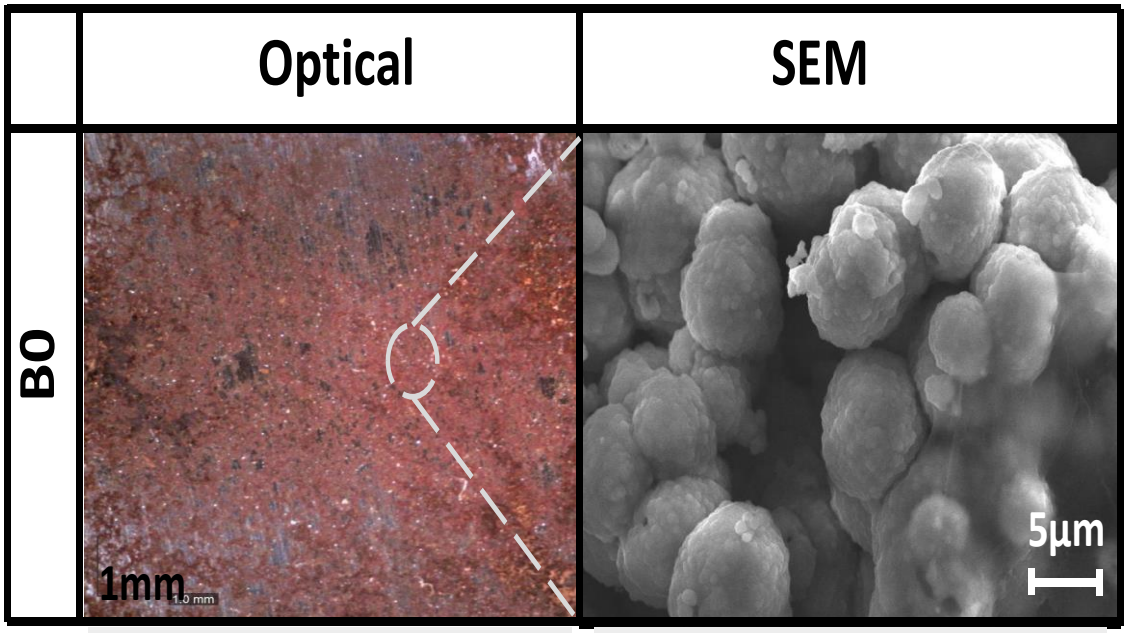

Figure 4.3 Optical and SEM image of steel coupon immersed in B0 for 240 hours

4.5.1.2 Characterization Test Results for B0

Fig. 4.4 depicts the FTIR spectrum of steel coupon immersed in B0 for 240 hrs. A broad peak at 3338 cm^{-1} confirms the presence of hydroxyl functional group in the corroded layer representing the polymorphic form of FeOOH (*Cabrini et al., 2015*). The spectra obtained in between 1650 and 1540 cm^{-1} along with the peaks observed at 958 and 840 cm^{-1} are respectively assigned to the amorphous or crystalline Fe (II) and Fe(III) hydroxides and carbonates *(Cabrini et al., 2015; Inam et al., 2018*). The bending vibration of Fe-O-H (i.e. γFeOOH and αFeOOH) can be confirmed by the peaks appearing at 750 cm^{-1} to 1100 cm^{-1} (*Corrêa et al., 2016; Vernekar & Jagadeesan, 2015*). A peak that appeared at 1360 cm^{-1} can be subjected to the bending vibration of the hydroxyl group associated with Fe (Inam et al., 2018). The observed peak at 695 cm^{-1} is assigned to Fe_3O_4 formation on steel surface in carbonated pore solution *(Vergnat et al., 2021*). Therefore, the FTIR spectrum of the steel sample immersed in B0 clearly indicates that the corroded film comprises of FeOOH, Fe_2O_3 and Fe_3O_4.

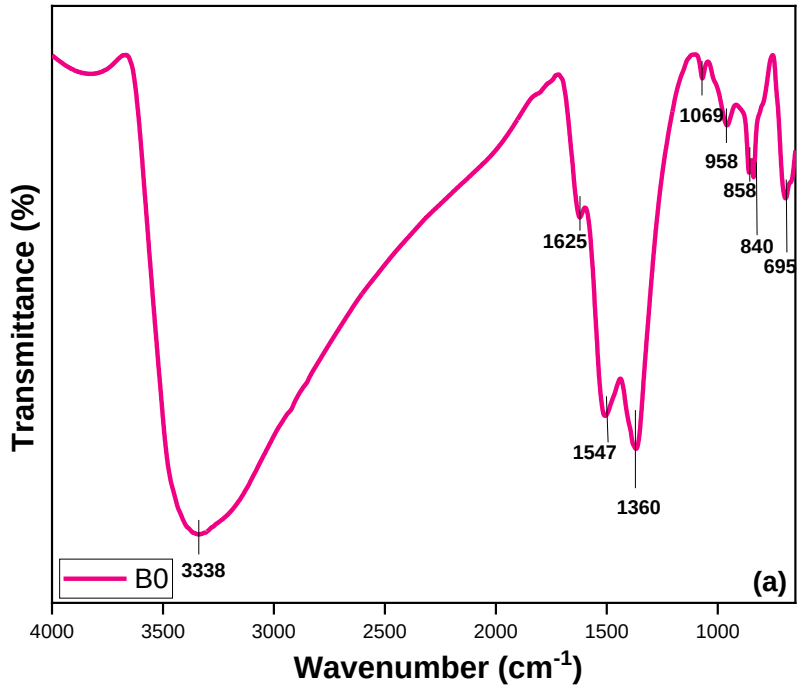

Figure 4.4 FTIR spectra of steel discs immersed in B0 for 240 hours

4.5.1.3 Corrosion Mechanism in Carbonation Environment

When CO_2 was bubbled into the alkaline pore solution simulating un-contaminated concrete pore solution, it reacted with water and formed carbonic acid (H_2CO_3); resulting in pH drop from 13 to ~9. When steel specimens were immersed in this carbonated pore solution, dissolution of the passive layer of steel started occurring at a very early age leading to corrosion of rebars. The metal surface gets destroyed by the conversion of iron to ferrous ions as shown by the anodic half-reaction in equation 4.1. The cathodic half-reactions involve the following reduction reactions shown by equations 4.2 to 4.4.

$$Fe(s) \rightarrow Fe^{2+}(aq.) + 2e^{-} \quad \text{...(4.1)}$$

$$H_2CO_3(aq.) + 2e^{-} \rightarrow H_2(g) + 2HCO_3^{-}(aq.) \quad \text{...(4.2)}$$

$$2H^{+}(aq.) + 2e^{-} \rightarrow H_2(g) \quad \text{...(4.3)}$$

$$2H_2O(l) + 2e^{-} \rightarrow H_2(g) + 2OH^{-}(aq.) \quad \text{...(4.)4}$$

The dominant reaction is considered to be the carbonic acid reduction (equation 4.2) and the other cathodic reactions involve proton reduction (equation 4.3) and water reduction (equation 4.4). The whole process of carbonation-induced corrosion led to the formation of various corrosion products such as FeOOH, Fe_2O_3 and Fe_3O_4 on the steel surface that are validated by characterization techniques.

4.5.2 Analysis of test results obtained for Set 1 compounds: Ser and Cys

4.5.2.1 Analytical imaging test results for Set 1

Optical and SEM results: The surface of specimen immersed in B0+Ser0.05 was non-corroded along with some white products on the surface, visible from Figure 4.5a1. This shows that the addition of *Ser* retarded the dissolution process of Fe efficiently. The optical image of specimen immersed in B0+Cys0.05 solution is found to be covered with thick white layer with no signs of corrosion, as shown in Figure 4.5b1. Some defects are also visible in the optical image that might be due instability of the protective layer suggested by PDP curves.

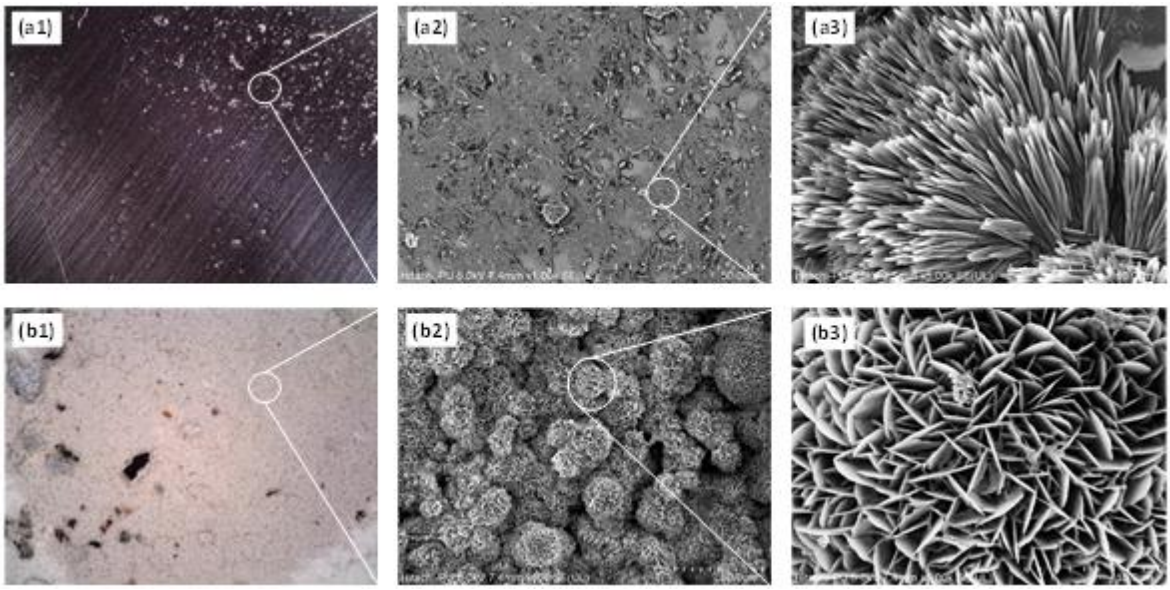

Figure 4.5 Optical images of steel immersed in (a1) B0+Ser0.05, (b1) B0+Cys0.05 and SEM morphology of steel immersed in (a2), (a3) B0+Ser0.05, (b2), (b3) B0+Cys0.05

Further, the high-resolution SEM images were also analyzed, and it was found that the surface morphology improved significantly after the introduction of *Ser* into B0; the flat exterior with no corrosion product confirmed the effective protection effect of the CoI (visible from Figure 4.5a2 and a3). From the SEM images of B0 in *Ser*, the thin covered layer is clearly visible with lamellar adsorbent. However, the steel surface in B0+Cys0.05 was covered with off-white coloured layer. The SEM image showed a formation of thick layer from which it appeared that the discrete particles of *Cys* had nucleated and grown like the ‘‘petals’’ of the flowers (Ghelichkhah et al., 2015) as can be seen from Figure 4.5b2 and b3. This reveals that the inhibition mechanism of *Cys* involves formation of protective layer that enables to form thick adsorbed layer on the exposed surface. When comparing the layer formation by two chemicals, it can be seen that unevenly

distributed products are visible in the case of *Ser* whereas an evenly distributed layer is formed on steel specimens inhibited with *Cys*.

4.5.2.2 Characterization Test Results for Set 1

FTIR results: Figure 4.6a displays the IR spectrum obtained for sample immersed in pore solution with *Ser* as CoI. Generally, the appearance of broad absorption band centered at 3400 cm^{-1} is attributed to the stretching bands of O-H and N-H for amino acids; as these peaks have shifted to 3341 cm^{-1} for *Ser*, respectively, there are high chances for both/either of these groups are involved in the complexation reaction with the ferrous ions (*Khan et al., 2016; Maréchal & Chanzy, 2000*). At 1590.71 cm^{-1}, a prominent peak was observed that is assigned to –C=O bonds *(Jayaprakash et al., 2015*). The symmetric stretching of the carbonyl group was evident from the peak at 1369 cm-1 (*Łojewski et al., 2010*). The peaks spotted at 1078 cm^{-1}, 879 cm^{-1} and 681 cm^{-1} were allocated to Fe-O bonding bending vibration (*T. Zhang et al., 2017*), C-H out of plane deformation and $-COO^-$ rocking, respectively (*Jayaprakash et al., 2015*). The bonds obtained are consistent with the complex or chelate bonds between *Ser* and Fe. A protective layer is expected to adsorb on the rebar surface spontaneously formed by the process of physio-chemisorption. As -OH and C-N ($-NH_2$) bonds are confirmed in the protective film formed on the disc, $-COO^-$ becomes the potential reaction centre for *Ser* at 0.05M concentration.

In the IR spectra of layer formed on steel surface after immersing in B0+Cys0.05 (Figure 4.6b), the N-H stretching of aliphatic primary amine can be observed at 3402 cm^{-1}. The presence of a sharp and bundle of peaks, well-separated free O–H stretch near 3800 cm^{-1} is attributed to water molecules on the iron surface (*Lengyel et al., 2017*). The peak at 2906 cm^{-1} is assigned to sp^3 hybridized C-H bond (*Zhuang et al., 2020*). The band near 1768.58 cm^{-1} represents the carbonyl -C=O stretching (*Arias et al., 2015; Kogelheide et al., 2016*). The aliphatic C-N stretching vibration gives rise to absorption band at 1122 cm^{-1} *(Lalitha et al., 2005; Nikolic et. al., 2010*). Two peaks that appeared at 991.42 cm^{-1} and 846 cm^{-1} are characteristic of C-S bond (*Susanti et al., 2018*). The IR band around 2500-3000 cm^{-1} and 2550-2670 cm^{-1} usually show the presence of carboxylic (-COOH) and thiol group (-SH) respectively *(Mokubung et al. 2018*) but in the spectrum of B0+CY0.05M, no strong peaks in either of these ranges were recorded. The absence of thiol group is due to the formation of covalent bonds between Fe surface and $–S^-$, as observed by (*Mokubung et al., 2018*) where *Cys* showed similar interactions with the Cu surface.

Chandrabhan Verma et al. (*Verma et al., 2021*) reviewed the importance of thiol substituent for effective corrosion protection of metals in which the author states that when metal-inhibitor interactions take place between thiol containing compounds and metals, -SH functional group has a high probability to act as adsorption centre. The sulphur atom donates its lone pair of electrons to the empty d-orbital of surface metallic ions (Finšgar, 2013). Alongside, carboxylic group probably got converted into $–COO^-$ that further contributed its electrons to the Fe^{2+} ions present on the corroded iron surface thus, forming a strong bond and a subsequent protective film on the rebar surface.

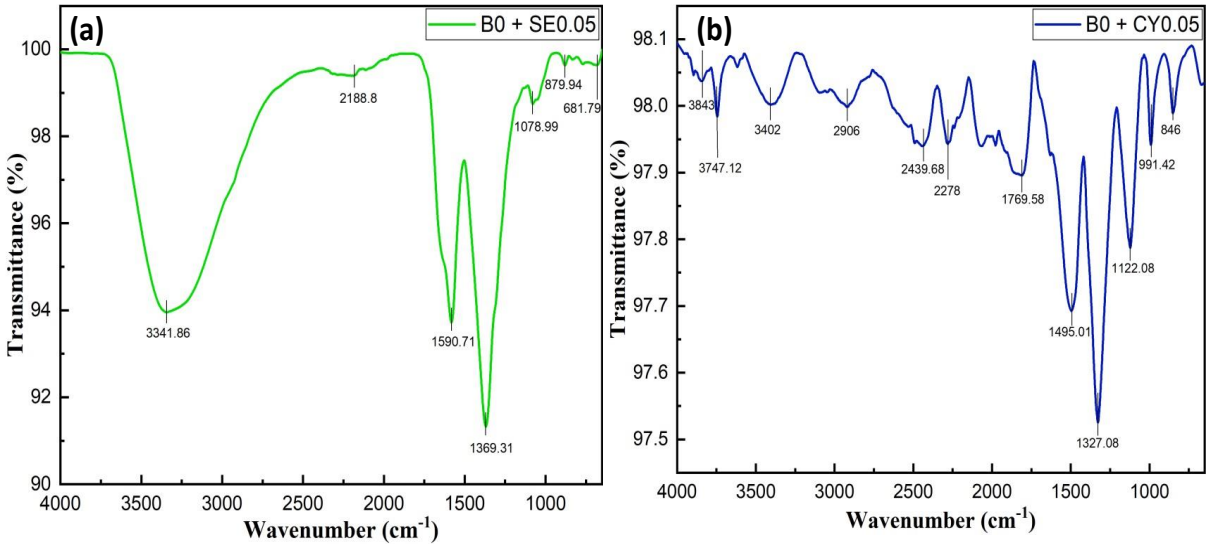

Figure 4.6 FTIR micrographs for steel coupons immersed in (a) B0+Ser0.05 and (b) B0+Cys0.05 for 240 hours.

XPS results: XPS was used to obtain composition information and validate the formation of the adsorbed layer of the film developed on rebar surface. Figure 4.7 shows the survey spectra of layer formed on cylindrical disc specimens when immersed in pore solution without inhibitors and with inhibitors i.e., B0, B0+Ser0.05 and B0+Cys0.05. The corroded film formed on specimen dipped in B0 is mainly composed of three elements, C, Fe and O. For samples in B0+Ser0.05, similar major peaks were observed along with N, while for the samples immersed in B0+Cys0.05, major peaks include S, N, C, Fe and O. The additional peaks of heteroatoms, N and S signifies that these elements were involved in formation of an adsorbed layer over the steel specimen. Fe and O elements in the corroded as well as passive films come from the steel matrix and hydroxides present in the carbonated pore solution, respectively. Table 4.3 presents the atomic percentage of various atoms calculated from the XPS results.

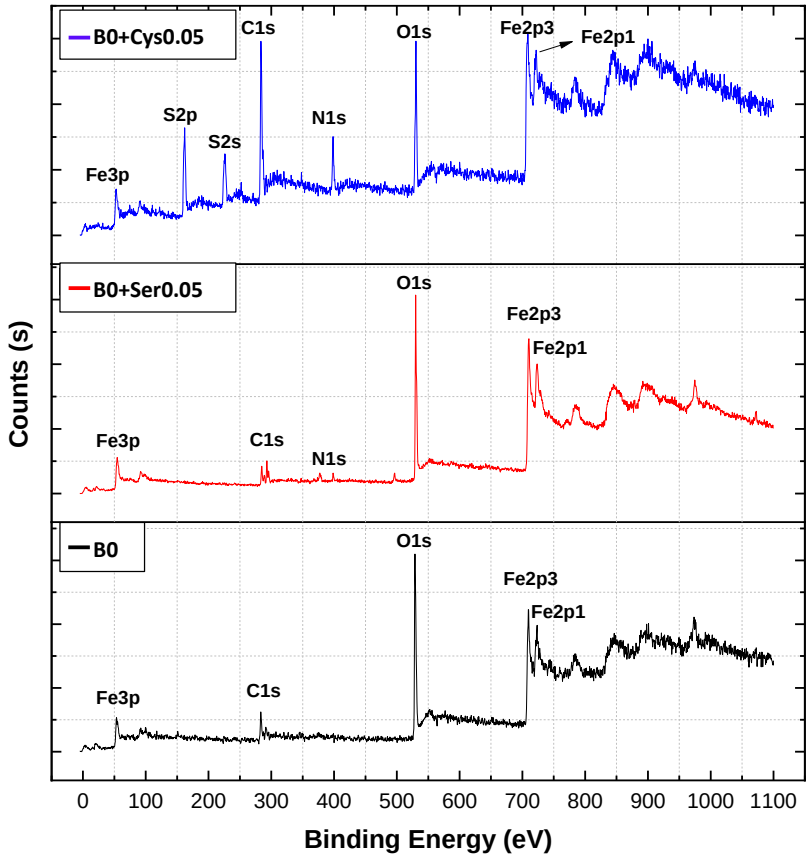

Figure 4.7 XPS surface survey scan of cylindrical steel disc immersed in solutions with and without the corrosion inhibitors

Table 4.3 Atomic percentage of various elements obtained from XPS analysis

Solutions	Fe (at.%)	C (at.%)	N (at.%)	O (at.%)	S (at.%)
B0	21.65	21.34	-	57	-
B0+Ser0.05	30.53	25.91	3.09	40.47	-
B0+Cys0.05	16.03	40.88	6.57	10.72	25.79

Figure 4.8a, b, c and d show high resolution spectra of Fe2p, O1s, C1s and N1s respectively, for inhibitor, *Ser*. From the Fe2p spectrum (Figure 4.8a), the peaks at 728.82 eV is associated to Fe^{2+} (satellite) and those at 724.39 and 721.91eV are ascribed to $Fe2p_{1/2}$(O_2, Fe, FeOOH, Fe_2O_3). Satellite peak for Fe (II) i.e., $Fe2p_{3/2}$ was also recorded at BE of 715.01 eV. The peaks at 713.55 and 710.89 eV are associated with the presence of Fe^{3+} ions and Fe-O functionality (*Li et al., 2021*) originated from the interaction between *Ser* molecules and ferrous ions on the surface layer. Further, the peaks at 706.57 eV and 708.31 eV are ascribed to Fe^0 state of iron (metallic iron) *(Li et al., 2021; Lin & Zuo, 2019*). In the O1s spectrum (Figure 4.8b), two sharp peaks at 530.0 eV

and 531.74 eV can be assigned to the lattice oxygen of Fe_3O_4 (Fe-O) *(Li et al., 2021; Wang e al., 2016*) and O-H from FeOOH hydroxide (*Saraswat et al., 2022*), respectively. The peaks displayed at 529.9 eV and 532.6 eV correspond to O from iron oxides (*Idczak et al., 2016*) and surface adsorbed water molecules (Li et al., 2021; Saraswat et al., 2022), respectively. For the observed C1s spectra (Figure 4.8c), binding energies at 284.91 eV, 288.71 eV and 289.89 eV are generated from C-C or C-H, C=O and COO^- moieties in the surface film *(Cañón & Teplyakov, 2021*), respectively. Two peaks occurring together at 285.49 eV and 286.31 eV are ascribed to C-N functionality (*Kozlica et al., 2021*) arising from the molecular structure of *Ser* CoI. Figure 4.8d presents the fine spectrum of N1s where the peaks at 397.02 eV, 399 eV and 400.56 eV correspond to N-H, C-N and N-Fe (*Saraswat et al., 2022*), respectively.

Figure 4.8a, b, c and d show high resolution spectra of Fe2p, O1s, C1s and N1s respectively, for inhibitor, *Ser*. From the Fe2p spectrum (Figure 4.8a), the peaks at 728.82 eV is associated to Fe^{2+} (satellite) and those at 724.39 and 721.91eV are ascribed to $Fe2p_{1/2}$(O_2, Fe, FeOOH, Fe_2O_3). Satellite peak for Fe (II) i.e., $Fe2p_{3/2}$ was also recorded at BE of 715.01 eV. The peaks at 713.55 and 710.89 eV are associated with the presence of Fe^{3+} ions and Fe-O functionality (*Li et al., 2021*) originated from the interaction between *Ser* molecules and ferrous ions on the surface layer. Further, the peaks at 706.57 eV and 708.31 eV are ascribed to Fe^0 state of iron (metallic iron) *(Li et al., 2021; Lin & Zuo, 2019*). In the O1s spectrum (Figure 4.8b), two sharp peaks at 530.0 eV and 531.74 eV can be assigned to the lattice oxygen of Fe_3O_4 (Fe-O) *(Li et al., 2021; Wang et al., 2016*) and O-H from FeOOH hydroxide (*Saraswat et al., 2022*), respectively. The peaks displayed at 529.9 eV and 532.6 eV correspond to O from iron oxides (*Idczak et al., 2016*) and surface adsorbed water molecules (*Li et al., 2021; Saraswat et al., 2022*), respectively. For the observed C1s spectra (Figure 4.8c), binding energies at 284.91 eV, 288.71 eV and 289.89 eV are generated from C-C or C-H, C=O and COO^- moieties in the surface film *(Cañón & Teplyakov, 2021*), respectively. Two peaks occurring together at 285.49 eV and 286.31 eV are ascribed to C-N functionality (*Kozlica et al., 2021*) arising from the molecular structure of *Ser* CoI. Figure 4.8d presents the fine spectrum of N1s where the peaks at 397.02 eV, 399 eV and 400.56 eV correspond to N-H, C-N and N-Fe (Saraswat et al., 2022) respectively.

As shown in Figure 4.9a, there are five characteristic peaks of Fe2p for the steel sample, situated at BE of 709.41 eV, 710 eV, 712 eV, 713.6 and 716.55 eV, representing the different

valence states of iron element, respectively. The peaks at 709.41 eV, 710 eV and 712 eV originated from Fe_2O_3, FeO and $FeOOH/Fe(OH)_3$ (*Jin et al., 2022*) respectively. The peak at 713.6 eV is arising from FeS compound whereas, 716.55 eV peak is due to Fe^{3+}(satellite). From these results, it can be stated that on the surface of the passive film, there's more iron in high valent state. Further, Figure 4.9b, shows the high resolution XPS spectra of O1s which is composed of three peaks corresponding to signals from to oxygen in carbonyl (–C=O) at BE of 530.83 eV, Fe_2O_3 at BE 529.53 eV and organic carbon oxygen bond (–C-O) at 531.69 eV

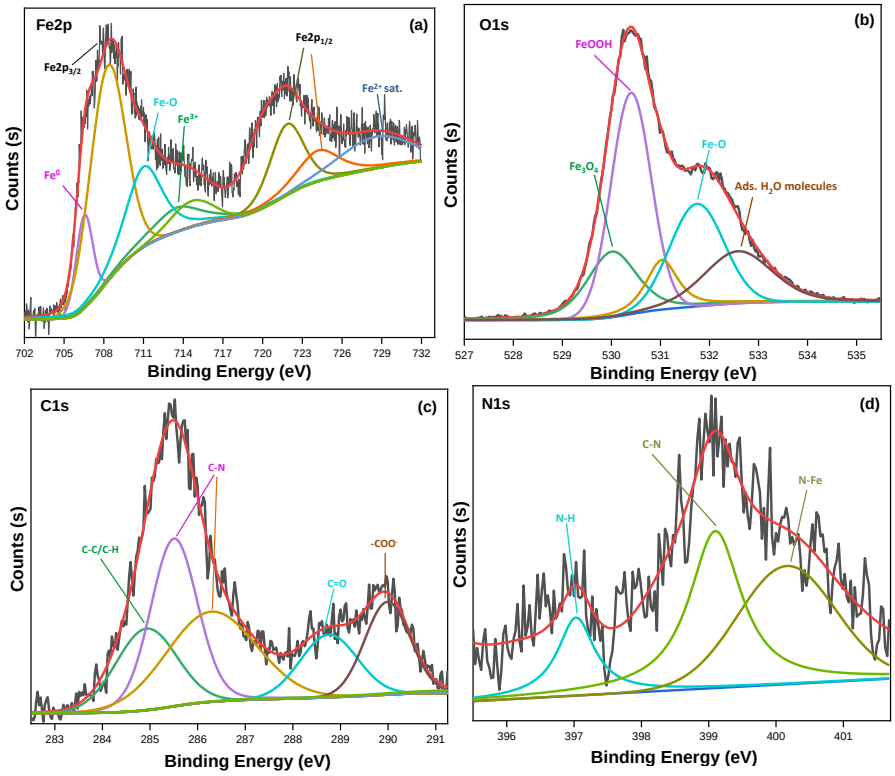

Figure 4.8 High resolution XPS spectra of (a) Fe2p; (b) O1s; (c) C1s and (d) N1s for steel samples immersed in B0+Ser0.05

Figure 4.9c shows the spectra for C1s which the signals from carbon containing groups are ascribed to C-C at BE 283.63 eV and 284.41 eV, C-N at BE of 285.43eV (*Jin et al., 2022*) and $–COO^-$ to BE 287.71 eV (Idczak et al., 2016). Two peaks are deconvoluted for N1s spectra (Figure 4.9d) which imply to the presence of $C-NH_2$ at BE of 399.91 eV and N-Fe at 398.81 eV (*Q. H. Zhang et al., 2022*). The XPS spectrum of S2p is shown in Figure 4.9e which was interpreted in terms of two chemically different forms of sulphur viz. sulphide and elemental sulphur. Additionally, the figure reveals a peak at 161.2 eV which is less than that reported for elemental S (164 eV), indicating the presence of S in a thiolate form (*El-Deab, 2011*).

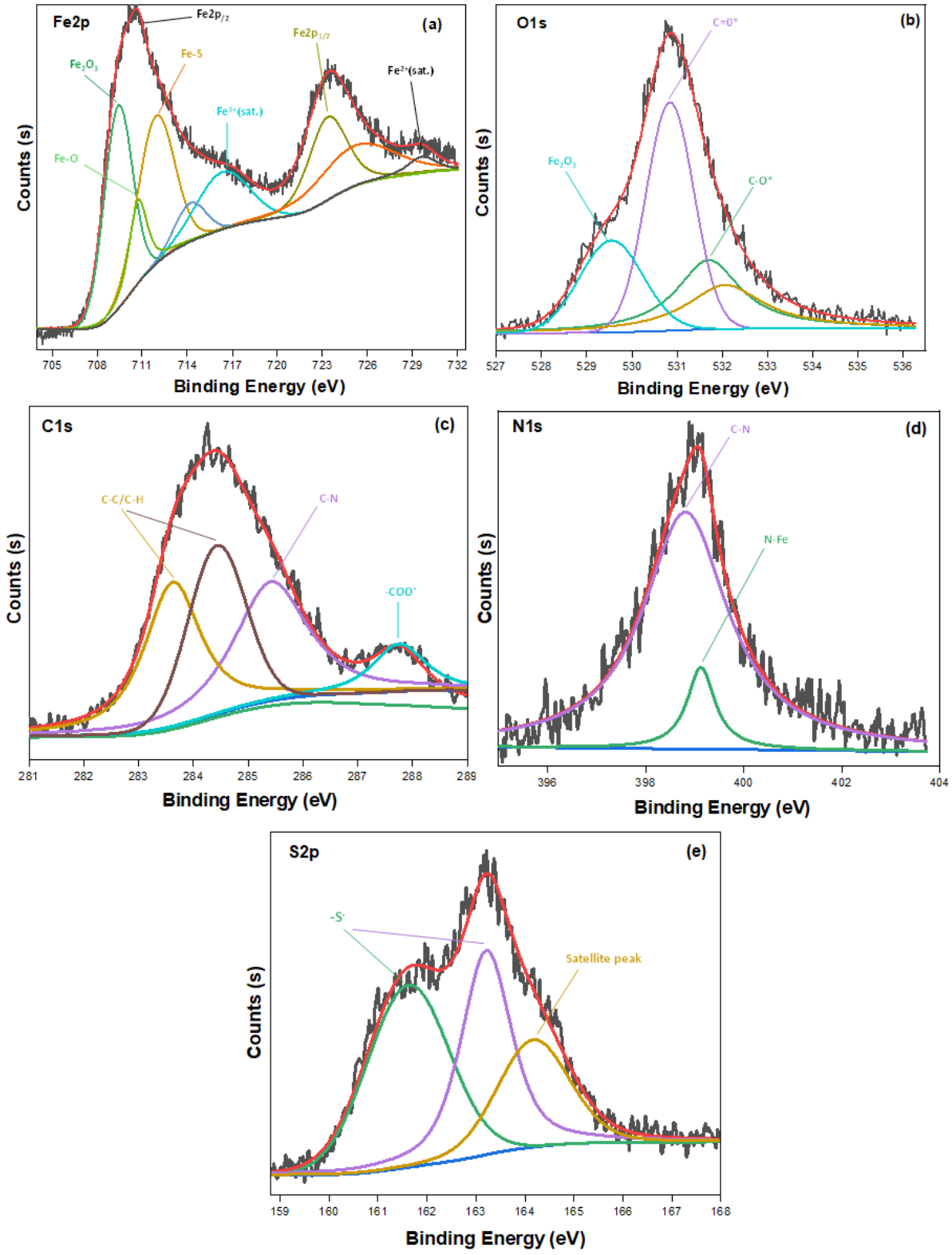

Figure 4.9 High resolution XPS spectra of (a) Fe2p; (b) O1s; (c) C1s and (d) N1s for steel samples immersed in B0+Cys0.05

4.5.2.3 Inhibition mechanism for Set 1 compounds

Ser and *Cys* are efficient as corrosion inhibitors with >90% efficiency at 0.05M and 0.1M concentration in aggressive carbonated concrete environment (as presented in CHAPTER 3 set 1 results). The optimum concentration of inhibition is 0.05M. The efficiency of *Ser* and *Cys* is attributed to the passive layer formation through physio-chemisorption process. The interactions of the Set 1 compounds (*Ser* and *Cys*) with the Fe ions are further illustrated through Figure 4.10. Slight changes in the nature of the protective layer so formed are observed which are associated with the variation in their molecular structure; -OH (alcohol) in *Ser* and -SH (thiol) in *Cys*.

When comparing the layer so formed in the presence of *Ser* and *Cys* through optical microscopy and SEM imaging, it can be seen that unevenly distributed products are visible in the case of *Ser* whereas an evenly distributed layer is formed on steel specimens inhibited with *Cys*. From FTIR and XPS, it was deduced that *Ser* interacted with the Fe ions through oxygen atom of carboxylic functional group; while in *Cys*, the sulphur atom from the thiol functional group also participated in the Cys-Fe complex formation along with the carboxylic group. These observations led to a prominent conclusion that the inhibition efficiency of both the compounds are high but molecules of *Cys* are more strongly attracted to the metal surface than *Ser* which led to the development of much adherent layer with high resistance against corrosion. A chelating ring is formed in the case of *Cys* as CoI (refer Figure 4.10b); while, for *Ser*, no chelate ring was formed. The reason is that the bond dissociation energy of –S-H is lower than -O-H due to the low electronegativity of sulphur atom than oxygen atom (due to larger size of S atom) *(Verma et al., 2021*) which makes *Cys* a more potent compound to form bonds with the metal surface by acting as a stronger ligand than *Ser*. Alongside, the in-silico studies performed on *Ser* and *Cys* for Fe in order to relate their electronic structure with inhibition efficiencies has also shown that the energy required for the removal of an electron from the last occupied orbital of *Cys* is less than *Ser,* providing higher inhibition efficiency to *Cys* (*Fu et al., 2010*). The study also mentioned that $\triangle E$ i.e., the difference between the E_{HOMO} and E_{LUMO} calculated for *Cys* was smaller than that for *Ser* which can be directly linked with the corrosion inhibition capacity of the molecules *(Xu et al., 2022*). Similar observations are made in the current experimental research program.

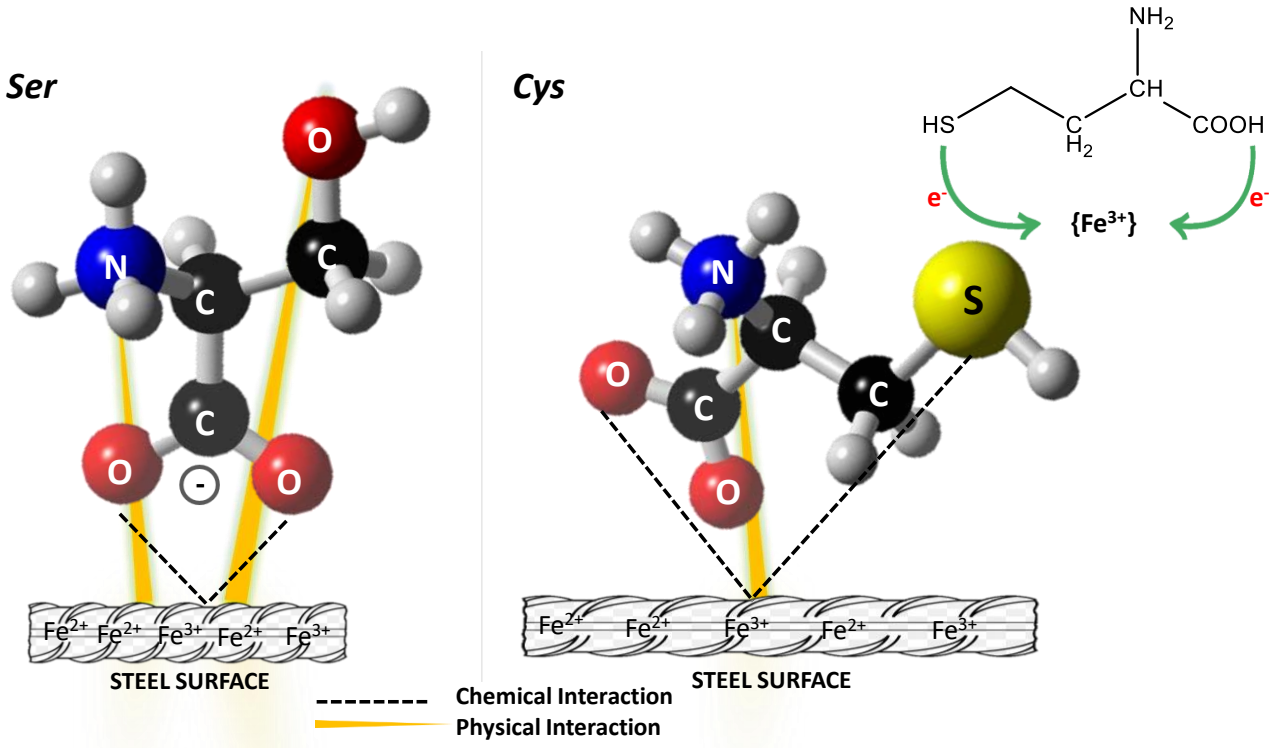

(a) (b)

Figure 4.10 Interaction between steel surface and Set 1 compounds

4.5.3 Analysis of test results obtained for Set 2 compounds: Phe and Trp

4.5.3.1 Analytical imaging test results for Set 2

Optical and SEM results: Figure 4.11a1 shows the optical micrograph of steel coupon immersed in C0+Phe0.05. The image is evident of the presence of a compact film on the coupon surface. SEM micrograph (Figure 4.11a2 and a3) of the same sample displays the formation of a film with some cracks. This indicates that *Phe* formed a film on the steel surface which protected it from corrosion (also indicated by low i_{corr} values during PDP scans). The similar kind of film was visible on *Trp* (shown in Figure 4.11b1) that had a morphology of interlaced fibrous structure as visible from SEM images (Figure 4.11and b3). The well-connected structure appears to have grown from some particular locations (marked with red). These locations are probably the anodic sites (as *Trp* inhibited the anodic reactions: revealed by PDP test), where the inhibitor molecules settled initially and with time, the surface coverage increased leading to the formation of the fibrous microstructure. The formation of Fe-*Trp* complex on the coupon submerged in C0+Trp0.05 has protected the surface from getting corroded.

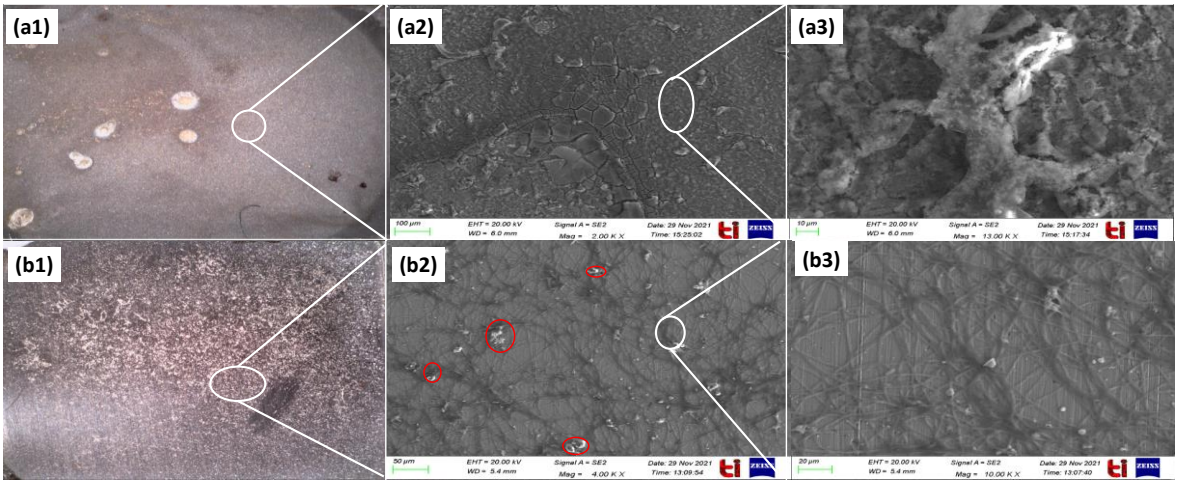

Figure 4.11 Optical images of steel immersed in (a1) B0+Phe0.05, (b1) B0+Trp0.05 and SEM morphology of steel immersed in (a2), (a3) B0+Phe0.05, (b2), (b3) B0+Trp0.05

4.5.3.2 Characterization test results for Set 2

FTIR test results: In the case of *Phe* and *Trp,* the infrared spectra IR spectra is shown in an overlapping form for better comparison purpose. The peaks obtained for both the compounds revealed some obvious similarities and some differences between reaction products formed (shown in Figure 4.12). Normally, the absorption band cantered at 3400 cm^{-1} corresponds to the stretching bands of O-H and N-H in amino acids. However, in the case of Phe and Trp, these peaks have shifted to 3281 cm^{-1} and 3155 cm^{-1}, respectively. This suggests a strong likelihood that one or both of these groups are engaged in a complexation reaction with ferrous ions. A prominent peak was also observed at 1564 cm^{-1} in *Phe* and 1565 cm^{-1} in *Trp*, that is assigned to $–COO^-$ (carbonyl) stretching (*Jayaprakash et al., 2015*) which might be due to the formation of –COO-Fe. Two peaks noticed at wavenumbers 1451.45 cm^{-1} and 1381 cm^{-1} in *Phe;* and 1453 and 1344 cm^{-1} in *Trp* of varying intensities are due to the C=C absorbance arising from benzene and indole rings. A low intensity peak spotted at 1143 cm^{-1} in the *Phe* spectrum is due to the swing absorption of $–NH_2$ (*Zheng et al., 2018*), while in *Trp* the peak at 1008 cm^{-1} arises due to the C-N stretching in aryl amines.

Thus, it is clear from the FTIR results that $–NH_2$ and –COOH functional groups of *Phe* and *Trp* are the main binding sites with ferrous ions in the carbonated concrete pore solution. N and O, comprise of unbonded electron pairs (lone pair) which have excellent ability to combine with iron to form co-ordinate bonds and in case of *Trp*, chelation, due to the presence of additional heteroatom in its cyclic structure. Due to this binding, the corrosion of rebar is hampered even

after 240 hrs of exposure in aggressive carbonated environment. Similar finding was reported by a researcher where it was stated that the binding mode of iron and amine-carboxylate containing compound was N and O in $FeCl_2.4H_2O$ solution *(Fan et al., 2023*).

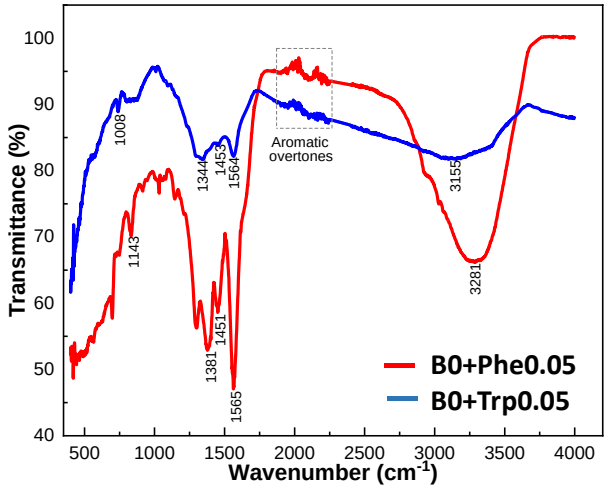

Figure 4.12 FTIR of steel sample after 240hr immersed in B0 with Phe and Trp

XPS test results: XPS analysis was accomplished to further confirm the chemical composition and oxidation states of the elements present in the adsorbed layer formed on steel coupons immersed in inhibitor-free and inhibitor-admixed concrete pore solution. The corrosion film developed on the specimen immersed in B0 primarily consists of three elements: carbon (C), iron (Fe), and oxygen (O) (shown in Figure 4.13). For samples immersed in B0+Phe0.05 and B0+Trp0.05, an additional peak for nitrogen (N) was attained which signifies that amino acids were involved in formation of an adsorbed layer over steel coupons. The intensified peak of C1s and O1s for *Phe* and *Trp* indicates high adsorption of organic substances on the surface of coupons.

Figure 4.14-Figure 4.17shows high resolution spectra of Fe2p, O1s, C1s and N1s, respectively for *Phe* and *Trp*. Through Figure 4.14a and b, it can be stated that the bonding between Phe-Fe and Trp-Fe varies as the wide spectra of Fe2p is different for both cases. Two characteristic peaks centered at 710.28 eV and 723.75 eV represent two different valence states of iron in Phe-Fe complex. The first peak is attributed to the Fe-O and the one at 723.75 eV is assigned to Fe_3O_4 formation. On the other hand, four peaks were obtained for *Trp* assigned to Fe metal and Fe-O functionality. In the high-resolution spectra of O1s (Figure 4.15), similar peaks are obtained for *Phe* and *Trp* designated to Fe-O and C=O bonds. This observation validates that ferrous ions strongly interact with O from amino acids making O as the adsorption center. The dominant peak

near 285 eV for *Phe* (285.16eV) and *Trp* (284.08eV) was attributed to C atoms bound to other C atoms and H atoms (Figure 4.16). Two other peaks near 288 eV and 293 eV were related to the carbon-oxygen bonds. An additional peak was obtained for *Trp* at 285.97 eV. In pure Trp, this peak appears at 286.2 eV (*Artemenko et al., 2021*) which is representative of =C-NH (from indole ring); as a shift of 0.23eV is noted, interaction between N and Fe ions is evident. In the N1s spectra (Figure 4.17), signal near 399 eV is related to C-N/C-H bonds for both *Phe* and *Trp.*

XPS analysis outcomes are in accordance with the infrared spectra results and validate the interaction of amino acids with Fe ions at the steel surface. The active adsorption center is oxygen from carboxylate groups for *Phe* and *Trp*. Alongside, nitrogen from indole ring of *Trp* is also involved in the chelation with ferrous ions (*Berdimurodov et al., 2022*).

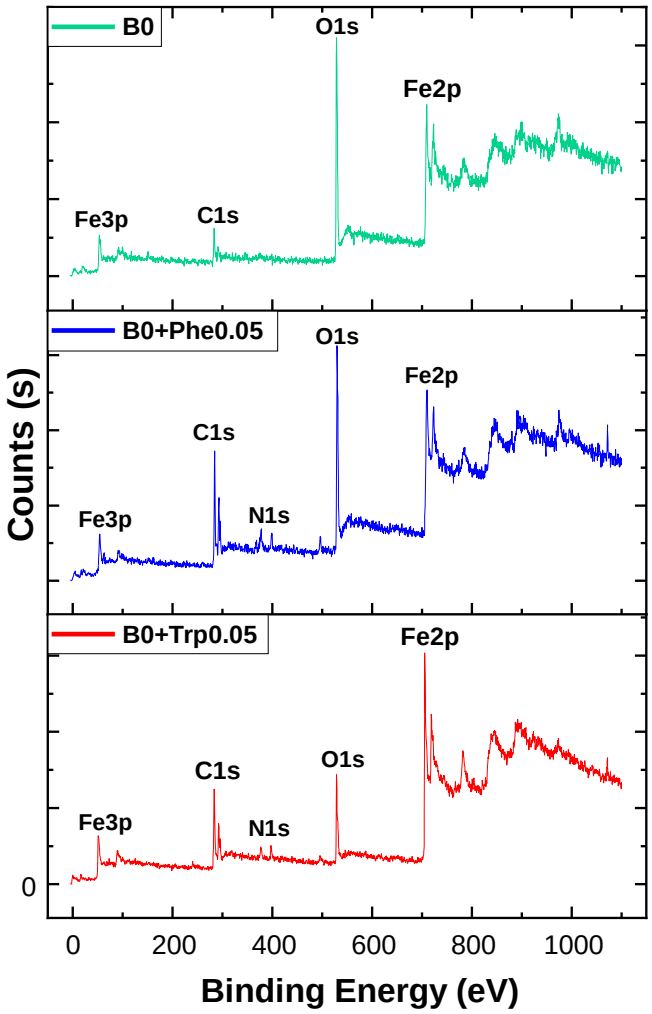

Figure 4.13 Survey spectra analysis for steel coupons immersed in (a) B0, (b) B0+Phe0.05 and (c) B0+Trp0.05

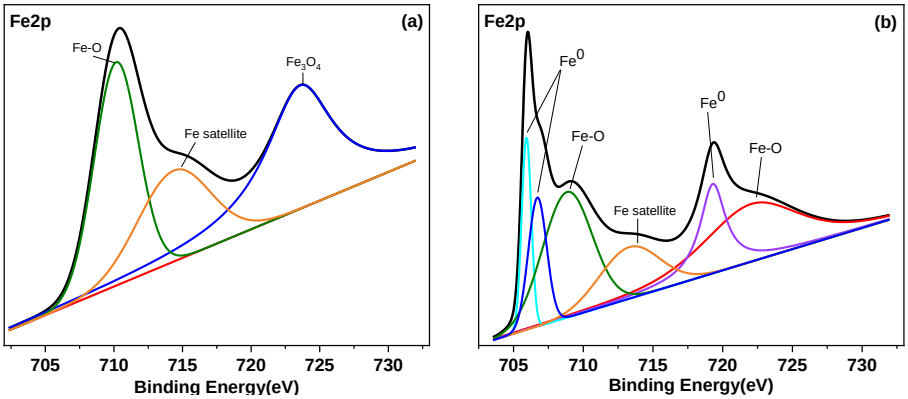

Figure 4.14 High resolution XPS spectra of Fe2p for steel coupons immersed in (a) Phe; (b) Trp

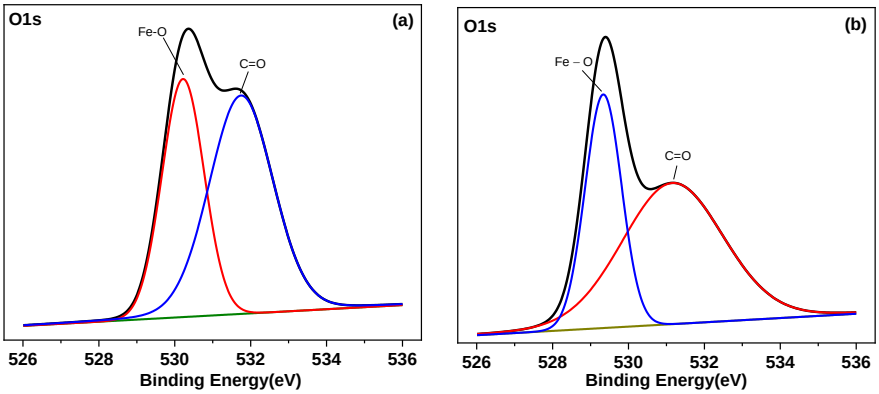

Figure 4.15 High resolution XPS spectra of O1s for steel coupons immersed in (a) Phe; (b) Trp

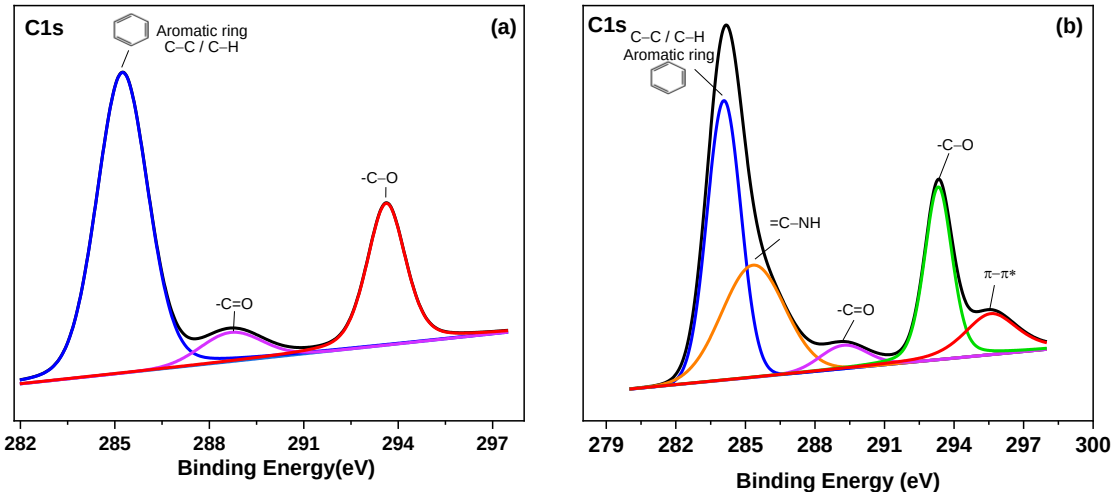

Figure 4.16 High resolution XPS spectra of C1s for steel coupons immersed in (a) Phe; (b) Trp

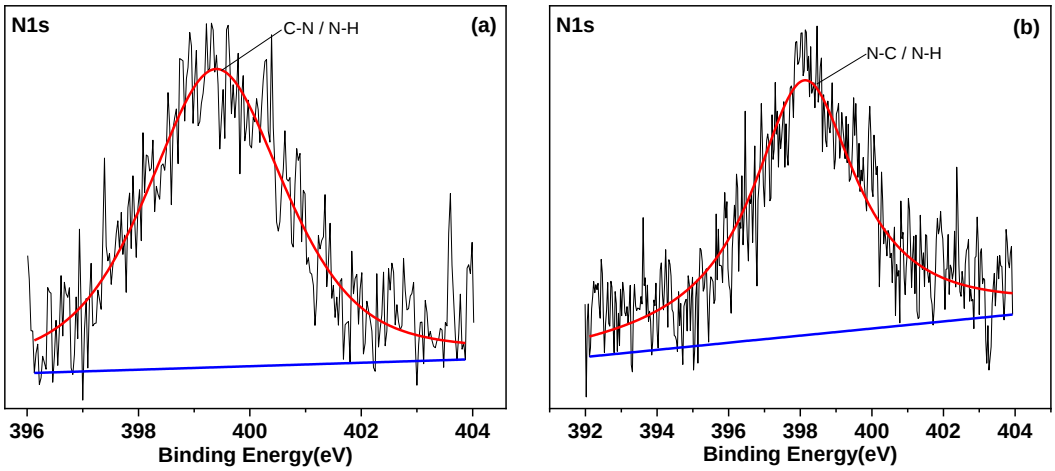

Figure 4.17 High resolution XPS spectra of N1s for steel coupons immersed in (a) Phe; (b) Trp

4.5.3.3 Inhibition mechanism of Set 2 compounds

Phe and *Trp* are efficient as corrosion inhibitors with >90% efficiency at 0.05M and 0.1M concentration in aggressive carbonated concrete environment (as presented in CHAPTER 2 set results). The optimum concentration of inhibition is 0.05M. The efficiency of *Phe* and *Trp* is attributed to the passive layer formation through physio-chemisorption process. Slight changes in the nature of the protective layer so formed are observed which are associated with the variation in their molecular structure, benzene ring in *Phe* and pyrrole heterocycle in *Trp*.

Figure 4.18a and b show the interaction of *Phe* and *Trp* ions with Fe, respectively. The figure also illustrates the reaction centers and the probable orientation of inhibitor molecules on the metal surface during adsorption. The electrons of the carboxylate functional groups in *Phe* and *Trp* donate themselves to the vacant d-orbitals of the ferrous ions and chemically interact with Fe ions. In addition, the hydrophobic part (benzyl ring) of *Phe* molecules is oriented away from the metal surface, creating a barrier shield for the corrosive media and excluding the water molecules to adsorb on steel surface, as shown in Figure 4.18a. On the other hand, in *Trp,* the indole ring also participates in the chemical interaction where lone pairs of N atom are transferred to the Fe ions giving rise to the formation of a 7-membered chelate ring (as shown in the Figure 4.18b). The presence of additional heterocycle facilitated the formation of chelate ring in *Trp* which resulted in more adherently formed protective layer over its surface. The delocalized π-electrons from the aromatic ring (in *Phe* and *Trp*) also have the tendency to donate themselves to the d-orbital of Fe. Additionally, some d-electrons are also re-shared by the ferrous with the benzoyl rings termed as

retro-donation. *Phe* and *Trp*, both form an inhibitive film over metal that forces it into passivating region.

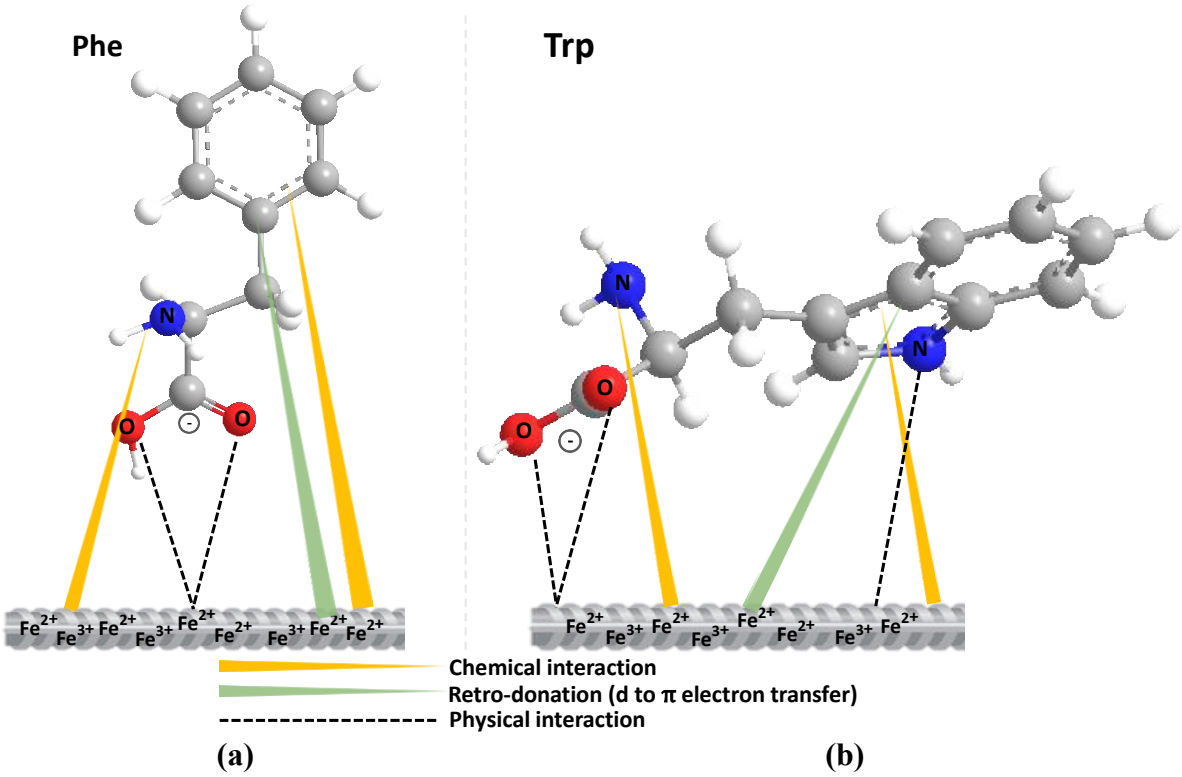

Figure 4.18 Interaction of set 2 compounds with steel surface in B0

4.5.4 Analysis of test results obtained for Set 4 compounds: Asn and Gln

4.5.4.1 Analytical imaging test results for Set 4

Optical and SEM results: The optical and SEM images of steel coupons after immersion in B0+Asn0.05 and B0+Gln0.05 are shown in Figure 4.19.

No signs of corrosion even after 240 hrs of immersion in carbonated corrosive solution were visible on the steel surfaces. This indicates that the addition of *Asn* and *Gln* in B0 retarded the dissolution process of Fe efficiently. Furthermore, there is a difference in the surfaces of *Asn* and *Gln* dipped coupons. *Asn* shows clear surface which is completely protected against corrosion. A thin layer that is white in colour is seen to be however, present which was further analyzed by FTIR and XPS techniques. On the other side, the coupon submerged in B0+Gln0.05 shows the formation of net-like layer over its surface. The development of physical layer and lowered current values indicate that it was due to this passive layer formation that shielded the metal against

corrosion. The amino-acids are considered to adsorb on the surface of metal they are interacting with; similar observation is made in the present research *(Chauhan et al., 2021; Hamadi et al., 2018*). The morphology of steel coupons in B0 with *Asn* and *Gln* is completely different from each other, which was analyzed through SEM images at two different magnifications. *Asn* appears to have formed a smooth finished layer with small crater-like formations distributed at some locations (refer Figure 4.19a3), while *Gln* appears to form a net-like structures with fibre-like formations that are connected to each other (refer Figure 4.19b3). Thus, both the inhibitors are present on the rebar surface and form a good protective film by adsorption process. This passive film formation curbed the dissolution of iron and resulted in high inhibition against corrosion.

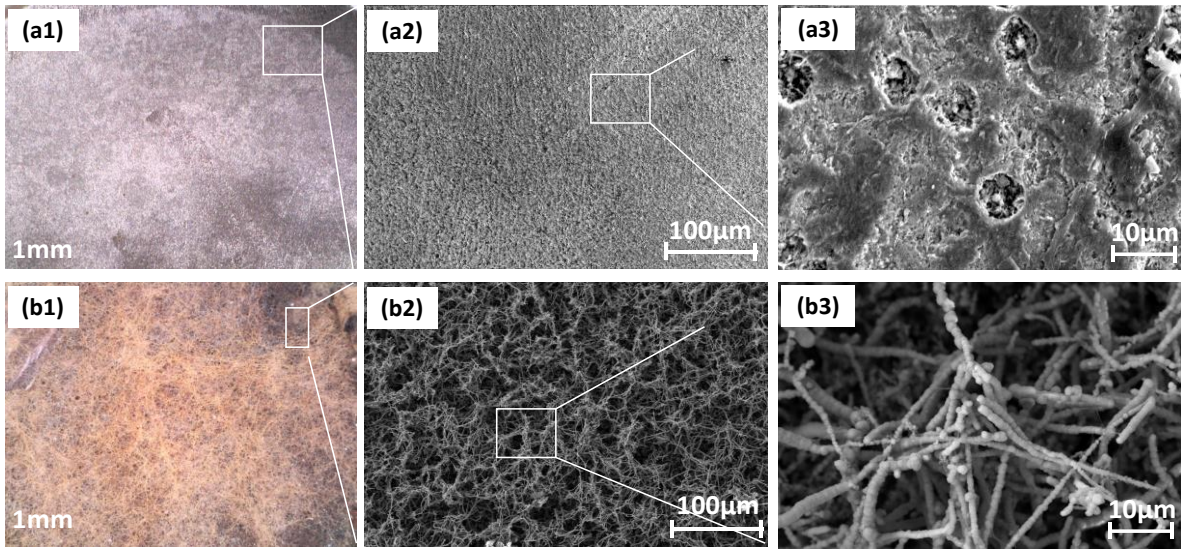

Figure 4.19 Optical images of steel immersed in (a1) B0+Asn0.05, (b1) B0+Asn0.05 and SEM morphology of steel immersed in (a2), (a3) B0+Gln0.05, (b2), (b3) B0+Gln0.05.

These observations developed two inferences, first, that the addition of *Asn* and *Gln* as CoI in B0 protected the steel specimens against corrosion efficiently even at a small concentration of 0.05M and second, that the difference in the chemical structure of a compound can change the nature of the layer formation over metal surface.

4.5.4.2 Characterization test results for Set 4

FTIR results: The overlapped FTIR spectra of steel coupons immersed in B0+Asn0.05 and B0+Gln0.05 are shown in Figure 4.20. It can be noticed from the spectra that the peaks for *Asn* and *Gln* are recorded at same wavenumbers but the intensity of the B0+Asn0.05 is lower than that for B0+Gln0.05. This can be related with the optical and SEM results where the surface of steel

coupon with *Asn* as CoI is seen to develop a thinner layer as compared to that for *Gln* as CoI. Both spectra presented bands at ~705 cm^{-1} that is due to the out of plane N-H bending. The peaks spotted near 860 cm^{-1} and 1017 cm^{-1} were allocated to C-H out of plane deformation and to C-N in -C-NH_2 (*T. Zhang et al., 2017*), respectively. The peak at 1239 cm^{-1} arise due to to the symmetric stretching of carbonyl group from $-COO^-$ (*Łojewski et al., 2010*). The strong band appearing at 1402 cm^{-1} for *Gln* and a suppressed band for *Asp* is corresponding to the stretching vibrations C-N in carboxamide in the structure of both the amino acids (*Ma et al., 2021*). The peak near 1671 cm^{-1} is also primarily governed the amide functional group indicating its parallel orientation in peptide bond (*X. Geng et al., 2019*) and the absorbance of C=O group can be seen near 1800 cm^{-1} (*M. Zhang et al., 2018*). The peaks located at 2321 cm^{-1} and 2916 cm^{-1} arise due to $-CH_2$ and $-NH_2$ stretching (*Naderi et al., 2022*). Further, a broad and intensive signal appearing at 3340 cm^{-1} (3290- 3370 cm^{-1}) suggest the presence of intermolecular hydrogen bonds (N-H-O-C) amongst *Asn-Asn* and *Gln-Gln* ions; such bonds are generally seen in amide containing groups *(Fazal et al., 2011*).

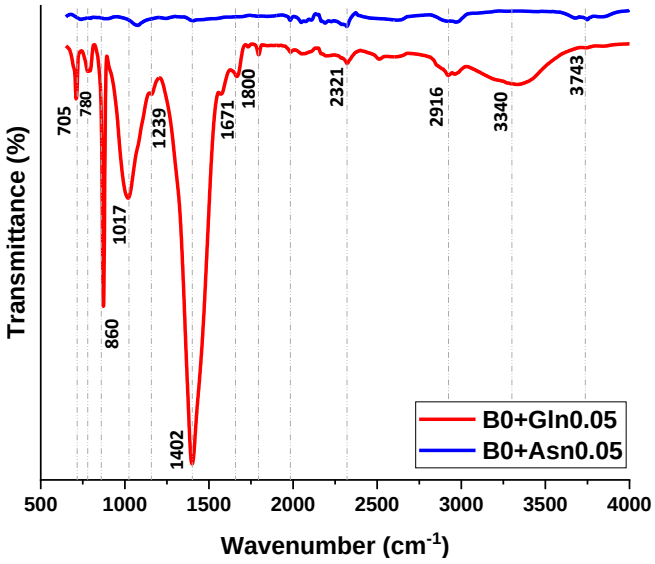

Figure 4.20 FTIR spectra of steel coupon immersed for 240 hrs in CPS with Asn and Gln at0.05M.

From these, it can be concluded that, the functional groups amide and carboxylate interacted with the surface of steel coupons via O atom. These functional groups are present in the chemical structure of *Asn* and *Gln*, confirming their adsorption. Metal-inhibitor complexes: *Asn*-$Fe_{complex}$ and *Gln*-$Fe_{complex}$ are conformingly formed on steel coupon surface, which in turn reduced steel dissolution and corrosive solution invasion (*Z. Zhang et al., 2022*). It has been reported previously

also that the electron rich moieties (here, amide and carboxylate) become adsorption centers and amino acids get easily adsorbed on the steel coupon leading to the development of a protective film inhibiting corrosion (*Raghavendra, 2018*).

XPS results: Figure 4.21 shows the survey spectra of layer formed on steel coupons when immersed in pore solution without inhibitor and with inhibitors i.e., B0, B0+Asn0.05 and B0+Gln0.05. The corroded film formed on specimen dipped in B0 is mainly composed of three elements, C (carbon), Fe (iron) and O (oxygen) as shown in Figure 4.21a. For samples in B0+Asn0.05 and B0+Gln0.05, similar major peaks were observed along with the peak for N (nitrogen) as shown in Figure 4.21b. The additional peaks of heteroatom, N, signifies that this element was involved in formation of an adsorbed layer over the steel specimen which is a constituent of the amino acids added as CoI. Fe and O elements in the corroded as well as passive films come from the steel matrix and hydroxides present in the carbonated pore solution, respectively.

Table 4.4 presents the atomic percentage of various atoms calculated from the XPS results. The reduced percentage of Fe on coupons immersed CoI-admixed concrete pore solution in comparison with inhibitor-free coupons (i.e., 10.12% and 13.21% in B0+Asn0.05 and B0+Gln0.05, respectively and 21.65% in B0) clearly indicates that the rate of metal dissolution was decreased in the presence of CoI and layer of CoI is formed over coupon surface. Furthermore, the increase in C percentage and an additional N percentage, 1.06% and 4.55% in B0+Asn0.05 and B0+Gln0.05, respectively, after the addition of CoI denotes the adsorption of CoI molecules as they constitute the amide and amine group (which comprise N atom) in their structure which interacts with Fe ions during the layer formation which in turn reduced the metal dissolution.

Figure 4.22 to Figure 4.25shows high resolution spectra of Fe2p, C1s, O1s and N1s, for *Asn* and *Gln*. From the Figs.16a_1 and a_2, it can be seen that the widespread spectra of Fe2p is similar for steel in B0+Asn0.05 and B0+Gln0.05; signifying the bonding between *Asn*-Fe and *Gln*-Fe was also similar. Majorly, three characteristic peaks were obtained at 707 eV, 710 eV and 723 eV corresponding to Fe(0) (*Li et al., 2021; Lin & Zuo, 2019*), Fe (III) and Fe (II) *(Monrrabal et al. 2019; Xiao et al., 2015*), respectively. This states that Fe was present in three different valence states in the adsorbed film over steel coupon. Fe (II) might be due to the presence

of Fe_3O_4 and Fe (III) due to ɤ-Fe_2O_3 (maghemite) as observed in the passive films formed in the presence of amino acids in pore solution (*Tran et al., 2023*)

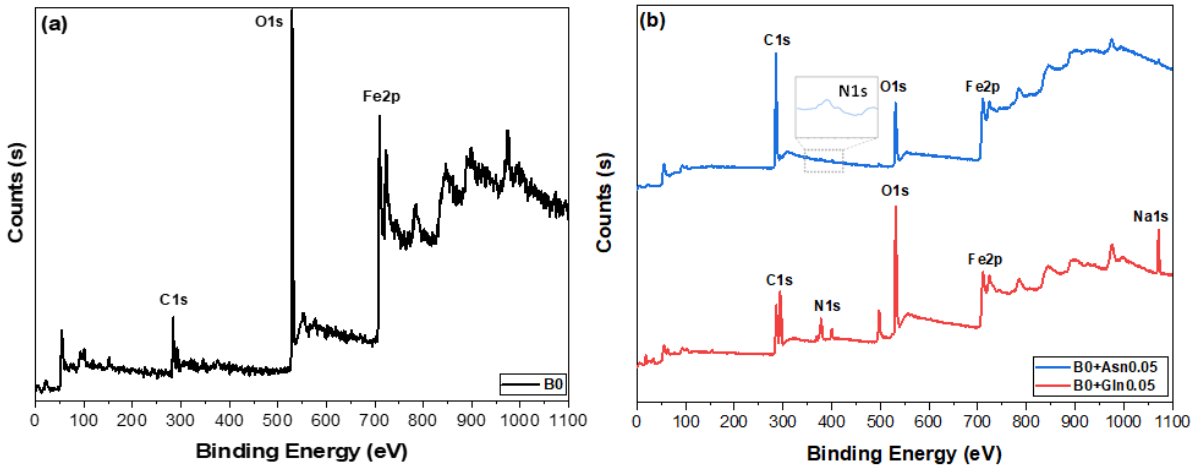

Figure 4.21 XPS surface survey scan of steel coupons immersed in (a) B0; (b) B0 admixed with Asn and Gln as CoI

Table 4.4 Atomic percentage of various elements obtained from XPS analysis.

Solutions	Fe (at.%)	C (at.%)	N (at.%)	O (at.%)
B0	21.65	21.34	-	57
B0+Asn0.05	10.12	70.51	1.06	18.30
B0+Gln0.05	13.21	41.16	4.55	41.09

.

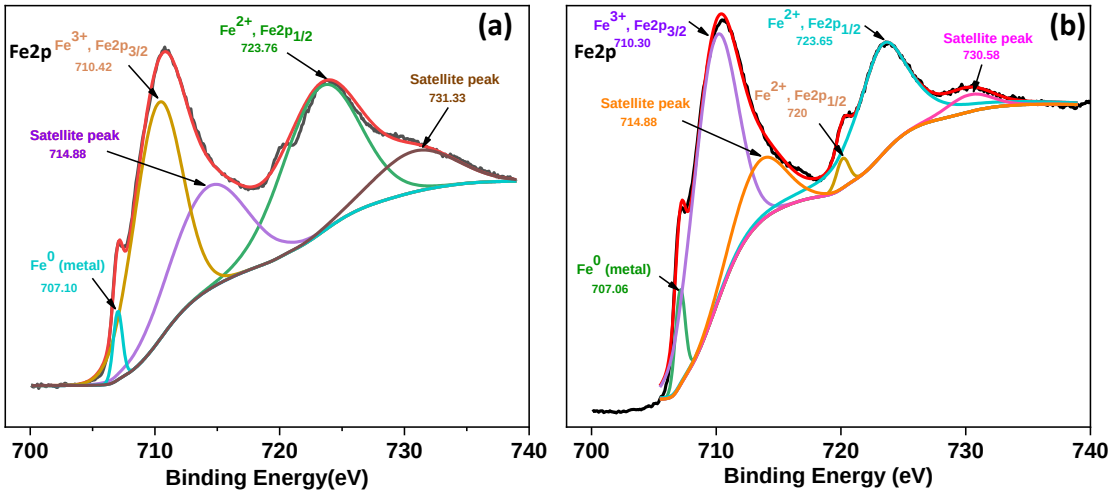

Figure 4.22 High resolution XPS spectra of Fe2p for steel coupons immersed in (a) Asn; (b) Gln

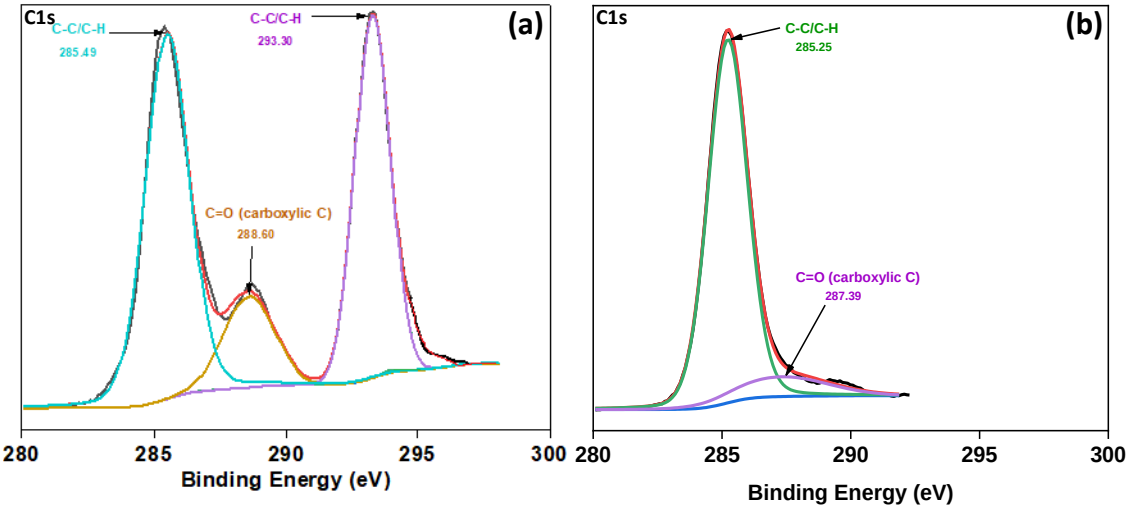

Figure 4.23 High resolution XPS spectra of C1s for steel coupons immersed in (a) Asn; (b) Gln

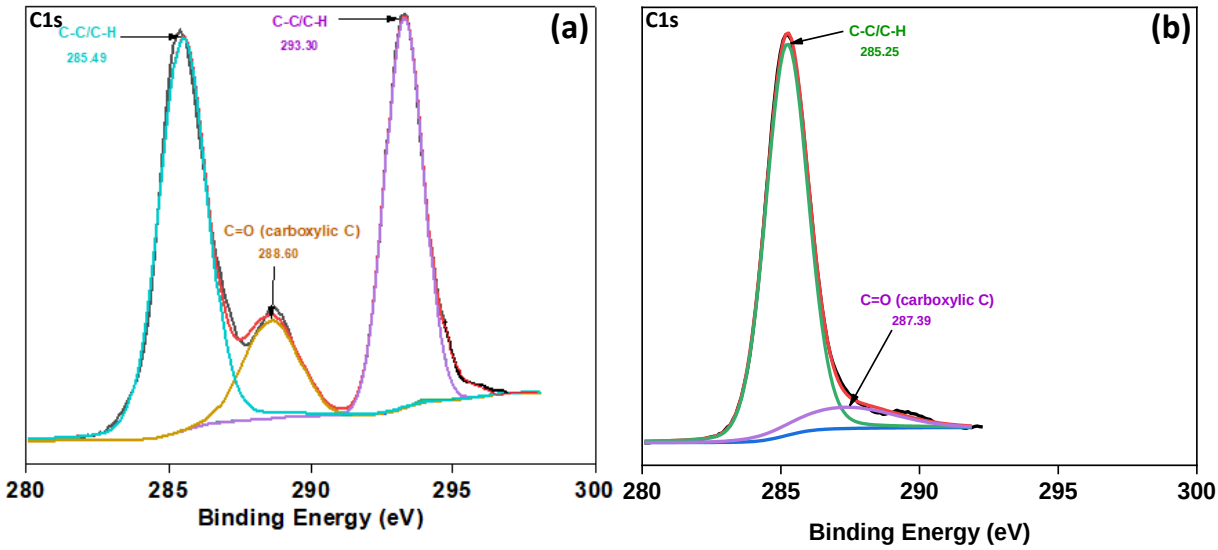

Figure 4.24 High resolution XPS spectra of O1s for steel coupons immersed in (a) Asn; (b) Gln

The C1s high resolution spectra was deconvoluted into two peaks for *Asn* and three peaks for *Gln* (Figure 4.23a and b). The first peak for both the compounds i.e., 285.49 eV in *Asn* and 285.25 eV in *Gln* was primarily due to C-C/C-H (carbon bound to other carbon and hydrogen atoms). These peaks have aroused either due to the adventitious carbon or due to the carbon atoms present in the amino acids that were admixed in CPS (*Naderi et al., 2022*). The second peak at 287.39 eV for *Asn* and 288.60 eV for *Gln* was assigned to carbon- oxygen bonds (C=O) *(Kasperek et al., 1998*). The additional peak of *Gln* at nearly 299 eV was also due to the C-C/C-H bonds.

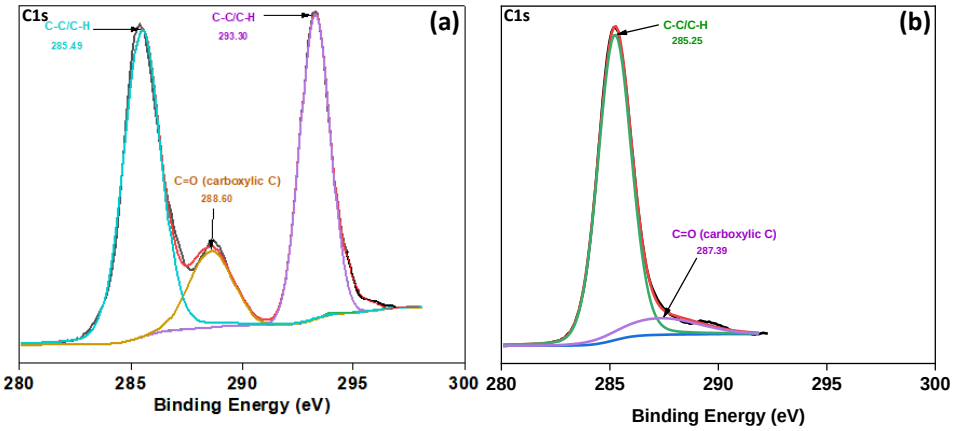

Figure 4.25 High resolution XPS spectra of N1s for steel coupons immersed in (a) Asn; (b) Gln

The XPS spectra of O1s is shown in (Figure 4.23a and b) for *Asn* and *Gln*, respectively. The dominant peaks at nearly 531 eV and 532 eV are associated with amine (-NH_2) and amide (NH_2-C=O-) functional groups arising from the adsorbed amino acids on Fe surface. Another peak at 532 eV, observed only for *Asn*, was due to the signals from C-O or C=O; due to the carboxylic functional group present in *Asn* and involved in adsorption over steel coupons. High resolution spectra of N1s for *Asn* and *Gln* (shown in Figure 4.25a and b) reveal only one peak cantered at ~399 eV which is due to the carbon-nitrogen bonds (*Saraswat et al., 2022*).

XPS characterization outcomes are in accordance with the infrared spectra results and validate the interaction of amino acids with Fe ions at the steel surface. *Asn*-$Fe_{complex}$ and *Gln*-$Fe_{complex}$ is formed on steel coupon surface. The active adsorption centre is O atom from carboxylate and amide functional groups present in *Asn* and *Gln*.

4.5.4.3 Inhibition mechanism of Set 4 compounds

Asn and *Gln* are efficient as corrosion inhibitors with >90% efficiency at 0.05M and 0.1M concentration in aggressive carbonated concrete environment (as presented in CHAPTER 3 set 4 results). The optimum concentration of inhibition is 0.05M for Asn and 0.1 M for Gln; but as the efficiency of Gln was >95% at 0.05 M also and also for the sake of comparing the nature of layer developed by both the compounds, a concentration of 0.05 M was fixed for mechanism study for both the compounds. The efficiency of *Asn* and *Gln* is attributed to the passive layer formation through physio-chemisorption process. The interactions of the Set 4 compounds with Fe ions on the steel coupon surface are further illustrated through Figure 4.26. Slight changes in the nature of

the protective layer so formed are observed which are associated with the variation in their molecular structure; four carbon atom straight chain in *Asn* and five carbon atom straight chain in *Gln*.

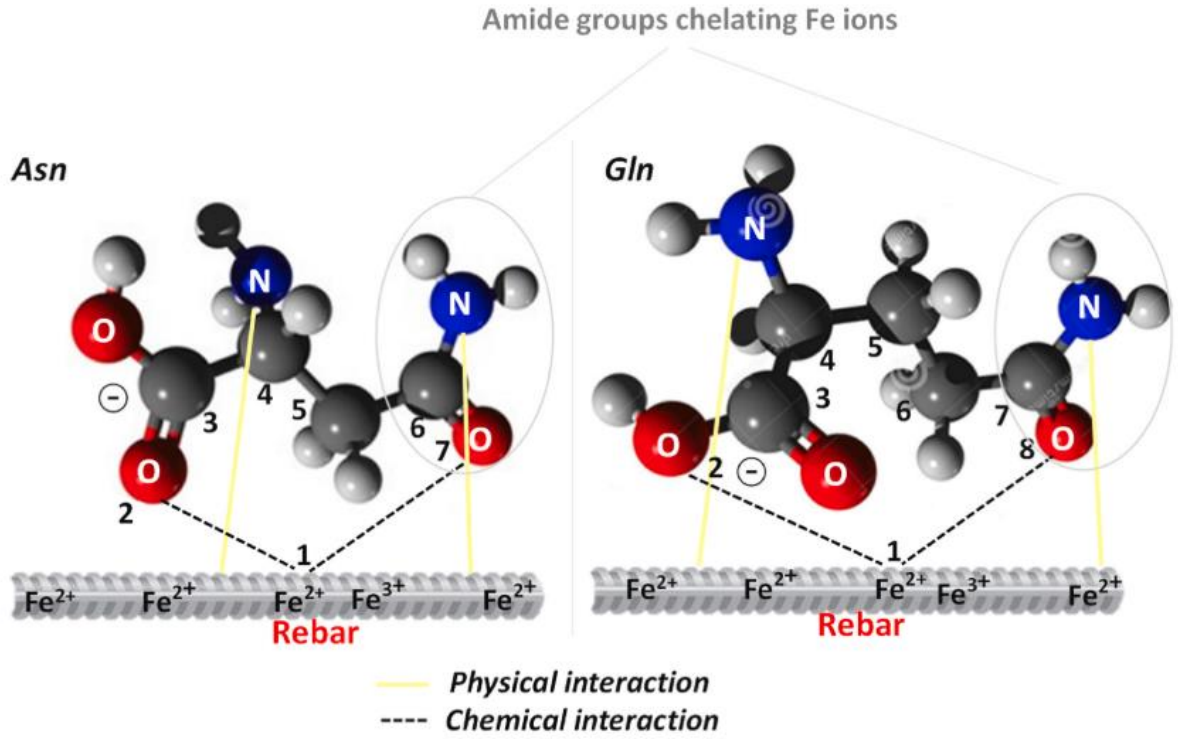

Figure 4.26 Interaction of Set 4 compounds with steel coupon surface

The presence of N and O in the molecular structure of the selected amino acids were the susceptible positions for physical and chemical bond formation with Fe at steel surface. Such conditions favored the adsorption of *Asn* and *Gln* over steel specimens which in turn lead to the development of inhibitive layer (as seen from the passive region in PDP curves for steel immersed in CoI admixed B0 in CHAPTER 3, Section 3.5.4.2). Typically, the carboxylate group and the amide group were involved in the interaction with Fe ions through O atom as indicated by FTIR and XPS results. Additionally, intermolecular hydrogen bonding between inhibitor ions containing amide groups is also a probable reason for high inhibition. A dense, tightly compact layer is developed over rebar due to (i) metal-inhibitor interactions and (ii) intermolecular hydrogen bonding between inhibitor ions. This layer insulated the steel specimens from corrosive media, hindering the corrosion process and protecting the metal from corrosion. The inhibition efficiency was in the order: *Gln* > *Asn.* This is owed to the longer chain length of *Gln* in comparison with *Asn*. The reaction centres of bonding with Fe and mechanism of chelate development are same in

both the compounds, however, due to shorter chain length of *Asn*, smaller chelate ring is formed resulting in higher steric hinderance. 7-membered chelate ring is formed with *Asn* while 8-membered chelate ring is formed with *Gln* as shown in the Fig. 18a. A denser and compacter film developed over steel specimens in the case of *Gln* as CoI as compared to *Asn* as CoI (as seen from the k_{ads} and C_{dl} values). The developed adsorption models of *Asn* and *Gln* over steel surface is illustrated through Figure 4.26.

4.6 GENERALIZED INHIBITION MECHANISM OF AMINO ACIDS IN B0

In the carbonated system, breakdown of the initially formed protective oxide film occurs due to the lowering of pH in the vicinity of rebar. This led the metal surface to have positive charge accumulation (Fe^{+}) as Fe loses electrons to form ferrous/ferric oxides (Fe_2O_3) that are corrosive in nature (the detailed corrosion mechanism is explained in the current Chapter in Section 4.5.1). As represented by inhibition mechanisms of various amino acids, layer formation by the amino acids protects the steel surface against corrosion. The reaction mechanisms followed during such a process is explained here.

When amino acids (its molecules abbreviated as Inh) are added to B0, they get converted to their anionic form as Inh^{-} (equation 4.5), respectively. Thereafter, Inh^{-} are adsorbed onto the metal surface by opposite charge attraction termed as physisorption (equation 4.6). In addition to this, some inhibitor ions are also involved in chemical reactions with the ferrous ions to form Inh-Fe adsorbed complexes on the metal surface (equation 4.7). This type of adsorption is termed chemisorption. The typical process is summarized as follows:

$$Inh(aq.) \rightarrow Inh^{-}(aq.) + H^{+} \quad \ldots(4.5)$$

$$Inh^{-}(aq.) \leftrightarrow Inh^{-}(ads.) \quad \ldots(4.6)$$

$$Inh^{-}(aq.) + Fe^{2+}(aq.) \rightarrow Inh - Fe_{complex}(ads.) \quad \ldots(4.7)$$

4.7 CLOSING REMARKS

The study of corrosion mechanism in inhibitor-free synthetic pore solution simulating carbonated concrete (B0) and inhibition mechanism of amino acids as Green CoIs in B0 after 240 hours was carried out via analytical imaging techniques (optical and SEM) and characterization techniques (FTIR and XPS).

The test results indicate that slight change in the chemical structure of a compound changes the nature of the protective layer formed on the steel coupon surface. Thicker and more adherent inhibitive layers are formed in the case of compounds with more electronegative hetero atom. Most importantly, in a generalized manner, a similar kind of inhibition mechanism is followed by all the amino acids in B0 i.e., physio-chemisorption process. Thus, it can be said that amino acids can be used as efficient ‘Green CoIs’ in carbonated concrete environment.

CHAPTER 5 : APPLICATION OF AMINO ACIDS ON CONCRETE

5.1 GENERAL

Rebar in concrete can be safeguard from corrosion by using various corrosion mitigation techniques. Amongst the available methods, application of corrosion inhibitors (CoI) is the most economical, effective and widely adopted technique *(Xu et al., 2023; Zomorodian, 2023)*. There are two processes by which corrosion inhibitors (CoI) can be introduced in reinforced concrete (RC) structures i.e., admixed and surface applied. The former can be considered as preventive measure, in which CoI are directly added into a freshly mixed concrete; while, the latter is applied onto the surface of hardened concrete. Studies reveal that the CoIs, when used in admixed form, affects the concrete properties by interacting with hydrated and un-hydrated phases of cement *(Ann et al., 2006; Dharmaraj & Malathy, 2015; Saraswathy & Song, 2007; Shi et al., 2022)***.** The negative effect of the CoIs on the properties of concrete can be avoided by applying inhibitors on the surface of the concrete and are referred as surface applied corrosion inhibitors (SACoI). When evaluating Self-Adhesive Carbon-Based Coatings (SACoIs), it's crucial to focus on two key factors. Firstly, there are concerns about their ability to move through the concrete cover *(Ngala et al., 2003; Tritthart, 2003).* Secondly, their interaction with the components of concrete is of utmost importance. To effectively function as a SACoI, a compound should possess substantial percolation capabilities while minimizing or completely avoiding interactions with the concrete's constituents. This ensures that a maximum concentration of the compound can reach the reinforcing steel (rebar), resulting in a high inhibition efficiency. Moreover, SACoIs can serve as a physical obstacle, impeding the percolation of corrosive ions into the concrete by obstructing the pores within the concrete's surface and matrix *(Söylev et al., 2007)*.

Further, the application of SACoI can be utilized in two formats: preventive and reparative. The application is classified as ‘preventive’ when the SACoI is applied while the rebar in concrete is in passive state (devoid of corrosion); whereas, in ‘reparative’ strategy, the inhibitor is applied on the concrete surface after the rebar has reached the active state of corrosion. As the present research is dedicated on repairing RC exposed to carbonated environment, the test program deals with the application of SACoIs as a repair measure.

The current chapter is focussed on the application of amino acids as SACoIs on RC concrete as reparative strategy. Initially, an evaluation of the percolation ability of the amino acids which demonstrated effective performance in the pore solution testing (elaborated in Chapters 3 and 4) was conducted within the matrix of PPC concrete. Also, an investigation into the impact of SACoI on concrete surface/pore blocking was also conducted. Taken together, these investigations are denoted as migration studies. Subsequently, the compounds that exhibited effective percolation through the concrete were applied as SACoI on RC specimens with rebar in active stage of corrosion. Therefore, this chapter incorporates the examinations pertaining to Level 2 (migration study) and Level 3 (corrosion inhibition efficiency in RC). The test regime for these investigations is illustrated in Figure 5.1.

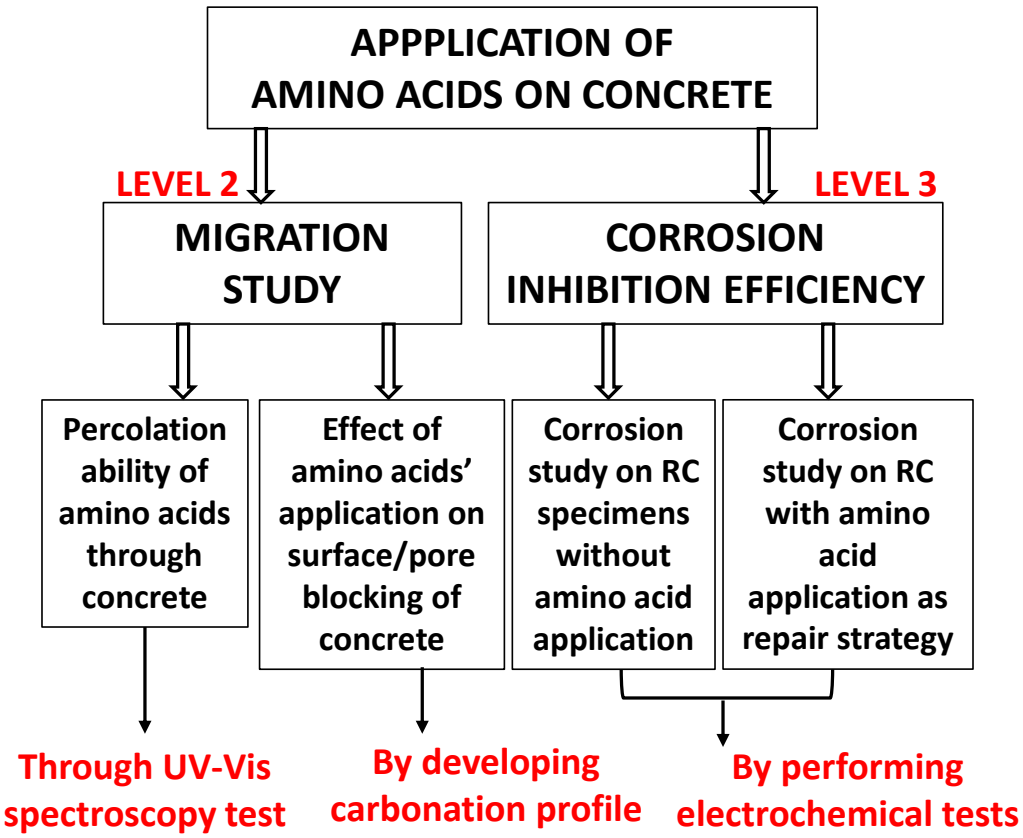

Figure 5.1 Schematic illustration of Level 2 and Level 3 of testing

5.2 MATERIAL SYSTEM

The major materials used for the experimental program includes cement, aggregates, water, generic compounds, and TMT steel bars. Along with this, chemicals required for testing the carbonation depth and solvent for CoI solution, were also used. The details are presented in the section below.

5.2.1 Cement

Portland pozzolana cement i.e., a fly-ash blended cement (PPC) conforming to IS 1489 (BIS:1489 (Part 1), 1991) was utilized and Table 5.1 presents its chemical composition and physical properties. Fly-ash is the mostly commonly used pozzolan. Also, PPC concrete has shown 2-4 times higher corrosion rates in carbonation corrosive environment than ordinary portland cement (OPC) (*Justnes et al., 2020; Karthick et al., 2016; Królikowski & Kuziak, 2011; Lye et al., 2015; Priya & Rao, 2017*). Furthermore, many studies have reported that fly-ash blended concretes show highest corrosion rate in comparison with other pozzolans; such as, ground granulated blast furnace slag and silica fume (*Alonso & Andrade, 1988; Lye et al., 2015; Medagoda Arachchige, 2008; Stefanoni et al., 2018)*. Hence, PPC was chosen as the cement of choice for investigating the carbonation and inhibition mechanisms, due to its wide acceptance and vulnerability in extreme carbonation conditions.

Table 5.1 Chemical composition and physical properties of cement

Properties			**PPC**
Chemical compounds (%)	SiO_2		26.84
	Al_2O_3		9.10
	Fe_2O_3		4.86
	CaO		49.75
	MgO		0.95
	SO_3		2.34
	Na_2O		0.18
	K_2O		1.24
	LOI		1.72
Physical properties	Fineness (m^2/kg)		340
	Specific gravity		3.04
	Setting Time (minutes)	Initial	190
		Final	210

5.2.2 Aggregates

Two types of aggregates i.e., coarse and fine aggregate were used in the present study. The basic properties of both the aggregates are presented in the following sections.

a) Coarse aggregates: Crushed gravel of size 20mm and 10mm was used in the ratio of 1:1. The specific gravity and water absorption of 20 mm aggregates were 2.82 and 0.53%; while the corresponding properties for 10 mm aggregates were 2.84 and 0.65% respectively. The

sieve analysis for 20 mm and 10 mm aggregates are presented in Table 5.2 and Table 5.3, respectively.

b) Fine aggregates: The fine aggregates used in the present study confirmed to Zone-II as per IS: 383-2016 (*IS:383, 1970*). The values of specific gravity, water absorption and fineness modulus were 2.64, 3.02% and 0.87, respectively. The test results of sieve analysis are presented in Table 5.3. From sieve analysis result (shown in Table 5.4) it can be seen that the percentage finer for all sieve sizes lies within the range of values recommended for Zone II sand.

Table 5.2 Sieve analysis for coarse aggregate (20 mm).

S.No.	IS Sieve size (mm)	% weight retained	Cum. % wt retained	% passing
1	40	0.00	0.00	100
2	20	0.40	0.40	99.6
3	10	97.2	97.6	2.4
4	4.75	2.1	99.7	0.3
5	Pan	0.3	100	0

Table 5.3 Sieve analysis for coarse aggregate (10 mm).

S.No.	IS Sieve size (mm)	% weight retained	Cum. % wt retained	% passing
1	20	0.00	0.00	100
2	12.5	8.1	8.1	91.9
3	10	38.2	46.3	53.7
4	4.75	52.6	98.9	1.1
5	Pan	1.1	100	0

Table 5.4 Sieve analysis for fine aggregates

S.No.	IS Sieve size (mm)	% weight retained	Cum. % wt retained	% passing	IS Limit for Zone II
1	10	0.00	0.00	100	100
2	4.75	2.5	2.5	97.5	90-100
3	2.36	8.1	10.6	89.4	75-100
4	1.18	25.3	35.9	64.1	55-90
5	0.6	17.6	53.5	46.5	35-59
6	0.3	29.4	82.9	17.1	8-30
7	0.15	14.4	97.3	2.7	0-10
8	Pan	2.7	100	0	0

5.2.3 Steel Bars

Thermo Mechanically Treated (TMT) bars of 12 mm diameter conforming to BIS: 1786-2008 (*IS:1786-2008, 2008*) were used in the preparation of RC prismatic specimens. The chemical composition of rebar obtained from the manufacture has already been present in Chapter 3 under section 3.2. The bars were cut in the length of 360 mm and a threaded hole was made at one end of the bar in order to assure electrical connectivity. Before embedding the bars in concrete, they were prepared according to ASTM guidelines (*G-109, 2011*). The preparation started with rubbing the surface with a wire brush to remove any rust. They were then degreased by soaking in analytical grade reagent, hexane and allowing to air dry for some time. Out of 360 mm length, central 200 mm was exposed to corrosion. The remaining 80 mm length on each side was insulated by applying epoxy and insulating tape on this portion, followed by mounting a 3 mm thick neoprene rubber tube over the insulating tape. The line diagram and actual prepared steel specimens are shown in Figure 5.20.

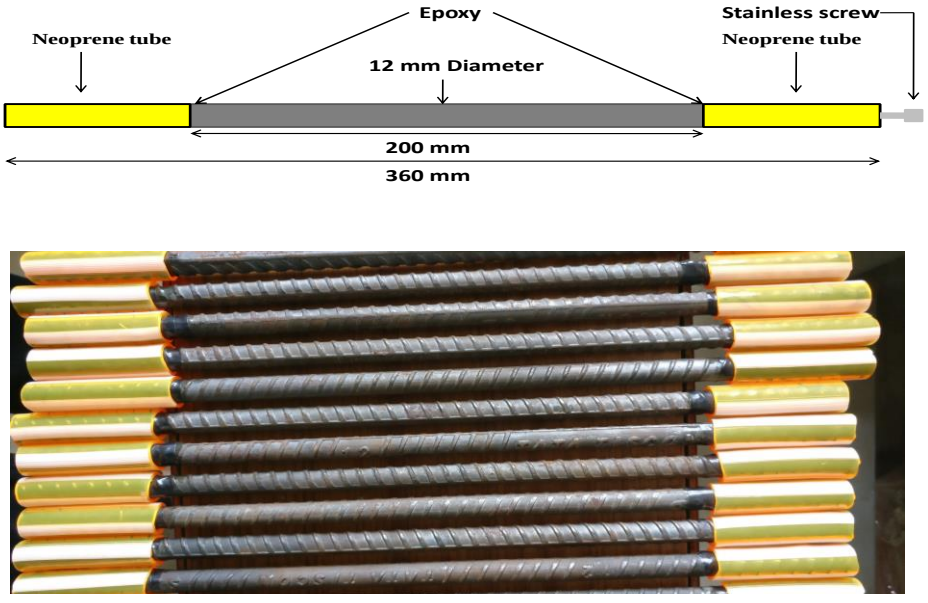

Figure 5.2 Line diagram and actual prepared TMT steel bars

5.2.4 Corrosion Inhibitors

Amino acids are green organic compounds that were used as corrosion inhibitor (CoIs) in the current study. These compounds necessarily constitute of amine (-NH_2) and carboxylic functional group (-COOH); along with additional functional groups. Among various amino acids, eight were picked due to their solubility, the arrangement of functional groups, and their chain lengths. These

selected amino acids were then grouped into four sets, each containing two amino acids. The compounds within each set had a slight variation in their structure so as to understand the variation in the inhibition mechanism. In level 1 of testing (testing in pore solution), out of eight, six were observed to efficiently inhibit the corrosion due to carbonation. Hence, six amino acids that were finalized to be applied on concrete are: *Ser* & *Cys* (Set 1), *Phe* & *Trp* (Set 2) and *Asn* & *Gln* (Set 4). The description of the compounds chosen for concrete application study is presented in Table 4.3 given in Chapter 3 under section 4.2.2.

5.2.5 Phenolphthalein Indicator

Phenolphthalein is a chemical compound used primarily as an indicator for acid-base titration. When phenolphthalein comes in contact with concrete having high pH interstitial pore solution (pH>10), the solution shows bright pink colour; whereas, in low pH (<10), concrete surface shows no colour change after its application on concrete. Since the carbonated concrete has pH < 10, the bright pink colour after phenolphthalein spray on freshly exposed concrete surface indicates un-carbonated concrete; while zone with no colour change indicates carbonated concrete. Phenolphthalein solution can be prepared by mixing ethanol solution (1%) with phenolphthalein powder (1g) and 90 ml ethanol (95 v/v%) diluted in water to 100 ml. In the present study, phenolphthalein indicator was procured from local market as it is easily available in the solution form.

5.2.6 Water

In the present study, tap water was used during casting and curing purpose. The utilized water was free from organic material, turbidity, other impurities, and negligible amount of chloride.

5.2.7 Other Chemicals

Besides the CoIs and phenolphthalein indicator, some other chemicals were also used during the studied conducted on concrete. Reagent grade calcium hydroxide ($Ca(OH)_2$), potassium hydroxide (KOH), and sodium hydroxide (NaOH) were used to a concrete pore solution simulating sound concrete. This served as a solvent for CoI solution preparation during its application as SACoI on concrete. Along with this, analytical reagent grade hexane and methanol was used for cleaning of steel specimens and laboratory glassware. To ensure that the corrosion is imitated over a specific

area, only a small portion of the bare steel specimen was exposed to corrosion process and the remaining area was sealed with epoxy; details of which are given in Chapter 3 under Section 3.2.3.

5.3 CONCRETE MIX PROPORTIONING

A concrete mix was designed as per IS: 10262-2019 (BIS, 2019). The water cement ratio was 0.43 and the mix design ratio adopted was 1:1.33:2.92 (cement: fine aggregates: coarse aggregates). Concrete constituents for 1m^3 of mix are presented in Table 5.5.

Table 5.5 Mix proportions of concrete specimens.

w/c ratio	Cement (kg/m^3)	Water (kg/m^3)	Fine Aggregate (kg/m^3)	Coarse Aggregate (kg/m^3)	
				20 mm	10 mm
0.43	410	184.5	572.4	598	598

5.4 CASTING OF SPECIMENS

Two types of concrete specimens were cast for each level of the study, as shown in Figure 5.1. For level 2, un-reinforced cubes of 100 mm dimension were cast while, for level 3, reinforced prisms 300 × 300 × 42 mm were cast. The prism specimens were prepared with one rebar embedded at a clear cover of 15 mm. The line diagram and actually prepared prism specimens are shown in Figure 5.3. Special type of molds was procured for casting of the prism specimens. To maintain rebar cover depth, holes with appropriate diameter were drilled at the exact location in the steel mold. Since 20 mm size aggregate was used in the concrete mix, care was taken that aggregate did not come in the cover zone during casting.

For the preparation of both types of specimens, firstly, the constituents of concrete were dry mixed and water was then added subsequently to ensure a consistent mix. After casting, all the samples were demolded after 24 hours of setting. The reinforced specimens were water cured using jute bags; while the un-reinforced specimens were completely submerged in a water tank for 7 days. The water used for curing was regular tap water and the curing conditions were ensured as 100 % RH at 25 ± 2° C temperature. The specimens were then kept in laboratory environment at a RH of 60 %. Thereafter, all the specimens' surfaces except one, were coated with epoxy to ingress of CO_2 and CoI from one side only. Preconditioning of the specimens was done at 30 ± 2° C temperature and RH 60-70 % in a climate chamber to ensure uniform moisture/humidity

distribution inside concrete matrix (*Cui et al., 2018*). All the testing was carried out in triplicate to generate a reliable data set. In total 297 cubes and 15 RC prisms were cast.

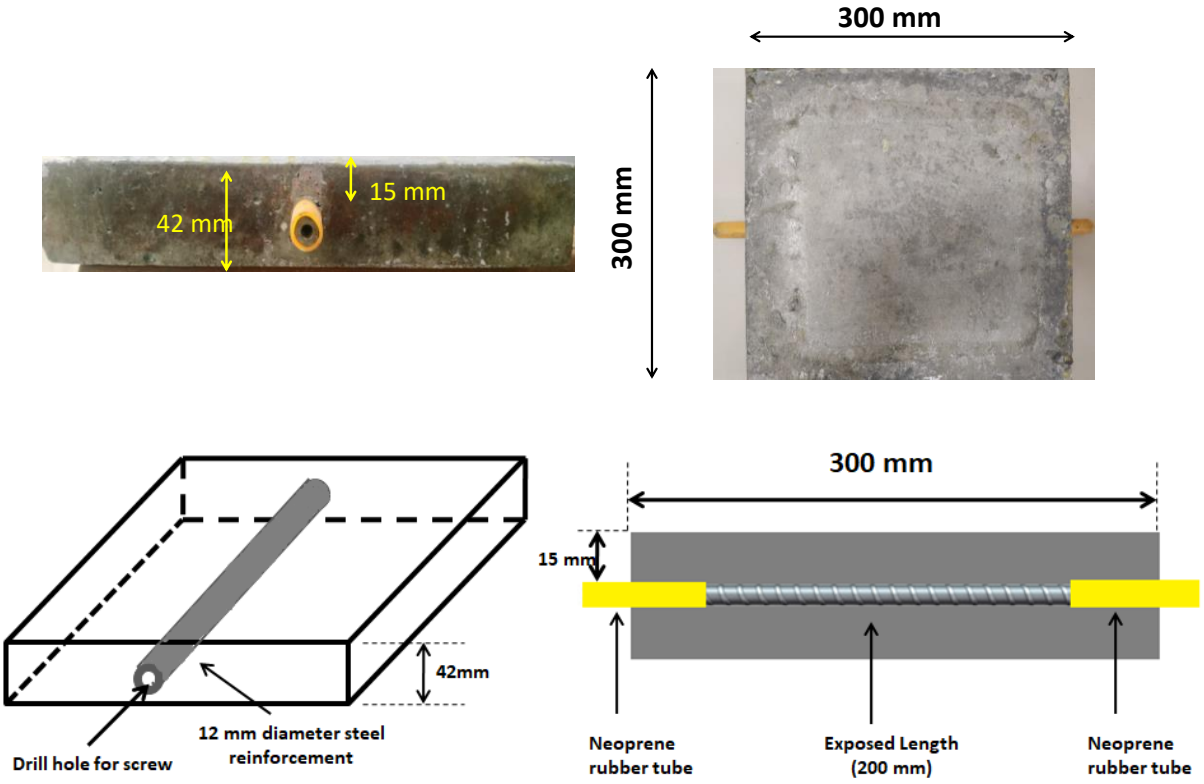

Figure 5.3 Line diagram and actually cast RC prism specimens

5.5 CARBONATION EXPOSURE CONDITIONS

To study the carbonation depth progression through un-reinforced concrete and to study the rebar condition in RC prisms when exposed to long-term accelerated carbonation exposure, the concrete samples were exposed to a carbonation chamber. The chamber had controlled CO_2 concentration of 3 %, RH as 60-70 % and temperature of 30 ± 2° C. In the current study, 15 days of carbonation exposure constituted of one exposure cycle.

5.6 SPECIMEN TESTING: METHODS AND TECHNIQUES

Three different tests were performed on the concrete specimens: development of CoI profile, development of carbonation profile (in the presence and absence of CoI) and rebar condition assessment (in the presence and absence of CoI) through electrochemical tests. The distribution of the concrete specimens for each test in given in Figure 5.4.

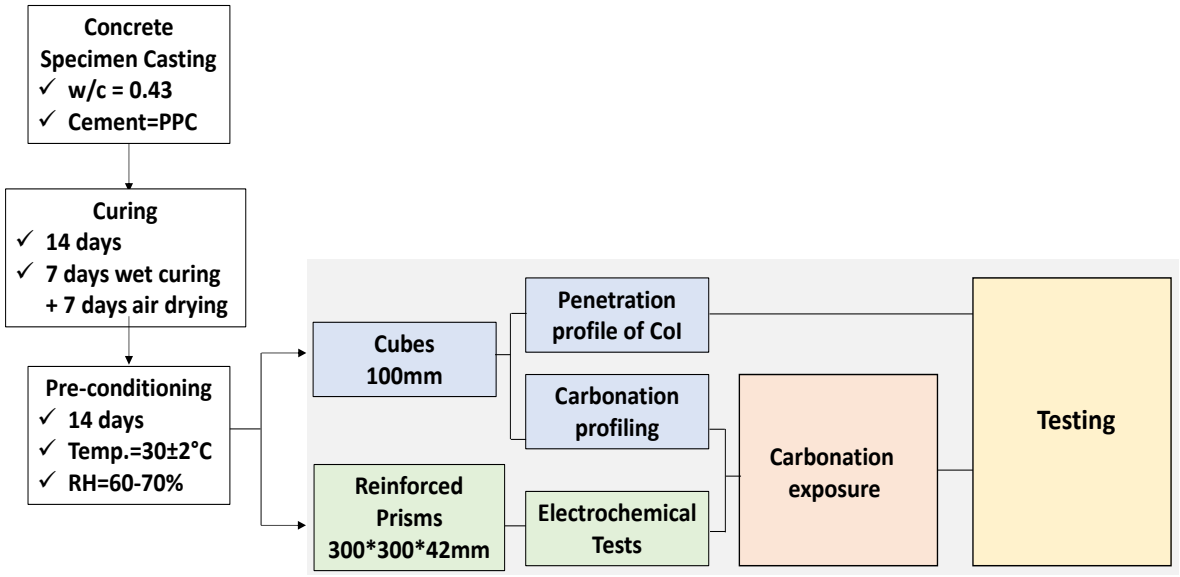

Figure 5.4 Distribution of specimens for each test.

5.6.1 Ultraviolet Visible (Vis) Spectroscopy

For an inhibitor to be employed as a SACoI, the compound shall necessarily possess the property of percolation through concrete. Thus, the percolation profile of the six CoIs was obtained by drilling the un-reinforced concrete cubes from four different depths i.e., 5-10 mm, 10-15 mm, 15-20 mm, 20-25 mm and nine different locations (shown in Figure 5.5) after 15, 30, 45 and 60 days of CoI application. The powdered drilled from surface (initial 5 mm) was discarded to eliminate the anomaly in the results due to surface accumulation of the inhibitor. In total 72 cubes were cast for the application of six amino acids and its subsequent testing after percolation.

For the application of amino acids, 1M solution was prepared with amino acids as solutes (individually) and simulated concrete pore solution (synthetic concrete pores solution simulating sound concrete conditions) as solvent. The application concentration was chosen on the basis of previous study done by our group, where it was established that 1M of inhibitor application on hardened concrete surface was sufficient for percolation *(Tiwari et al., 2023)*. The solution so prepared was applied on concrete in three consecutive layers at a rate of 500ml/m^2 with the aid of a brush. There was a duration of 2-3 hours between each layering, allowing the previous applied inhibitor layer to percolate. Powdered samples were drilled and tested for traces of inhibitor by using UV-vis spectroscopy technique which is a quantitative technique that performs on the principle of light absorbance. It is a molecular spectroscopy technique which involves the study of interaction of UV-vis radiation with molecules.

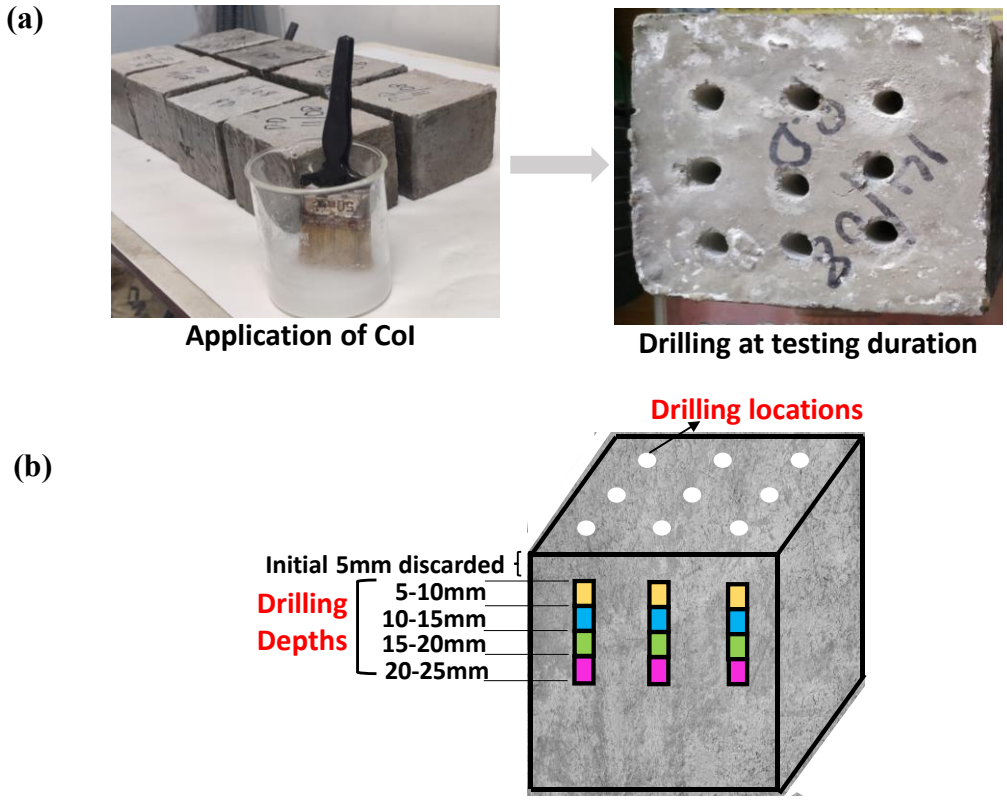

Figure 5.5(a) Application of CoI and drilling locations on concrete cube; (b) Schematic of drilling depths for CoI percolation profiling

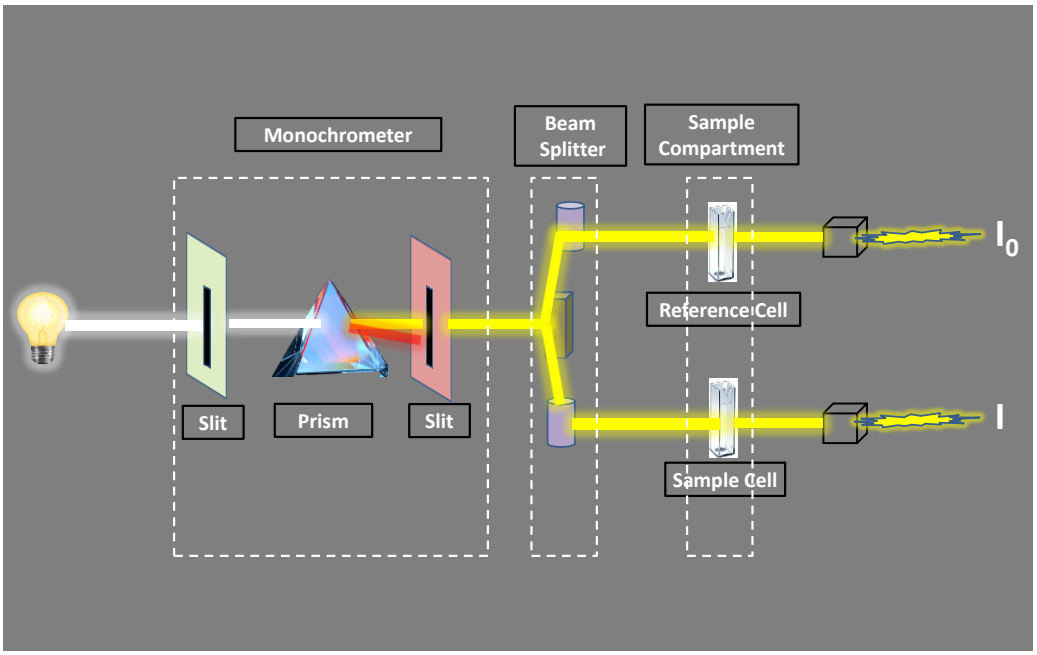

Figure 5.6 Mechanism of UV-vis spectroscopy

For solution preparation, 4 gm of drilled concrete powder was added to 20 ml of distilled water, followed by heating the solution till boiling. As a result, bound inhibitor molecules are transformed into a free-form state and subsequently mixed with distilled water. After cooling at room temperature, the solution was filtered through filter paper (Whatman No 1). The filtrate is then tested on UV machine (Schimadzu UV Machine).

The spectra were measured in 185 nm to 300 nm range so that their absorbance peak could be easily detected. Similar range of wavelength and test method was set for recording the UV spectra of pure amino acids *(Pang et al., 2010).* The absorbance peaks of pure compounds for reference and concrete samples were recorded carefully. If both the peaks occurred at the same wavelength, confirmation of the CoI presence could be ensured. Any shift in the peak could be associated with the interaction of CoI molecules and the cement hydration products. After recording the absorbance value from different samples, concentration of compound was found by using Beer-lamberts relationship. According to this, absorption is proportional to the concentration of absorbing molecules and the path length of the light through the sample (at a given wavelength).

$$A = \log (I_o/I) = \varepsilon.b.C \qquad \ldots 5.1$$

Where, I_o and I are the intensity of incident and transmitted radiation respectively, ε is known as the molar absorptivity, b is the path length and C is the concentration expressed as moles/lit.

5.6.2 Carbonation depth profiling

The carbonation depth profiling was done in order to get insights about, (i) the time in which CO_2 will reach the rebar level and cause depassivation and (ii) concrete pore/surface blocking effect of the SACoIs. Carbonation depth was measured after 15 days of exposure till an exposure duration of 225 days (15 cycles). At the testing age, triplicate cube specimens were split into two halves under universal testing machine (UTM). Phenolphthalein solution were sprayed on the specimens immediately after splitting the cubes. The depth of uncoloured region vertically from the exposed surface was measured using vernier calliper at 5 different points along the edge of broken surface (shown in Figure 5.7) and the average value was taken as the carbonation depth for each sample. Markedly, the measurement locations were chosen to eliminate the impermeability effect of coarse aggregate in carbonation depth of concrete (*Huang et al., 2012*). In total 225 cubes were cast and tested for carbonation depth analysis.

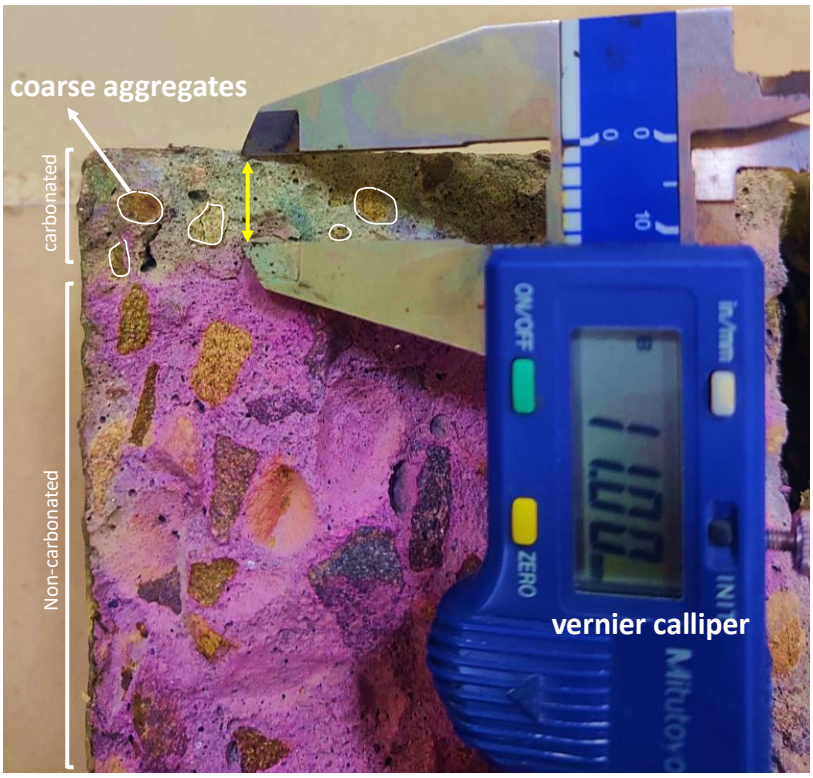

Figure 5.7 Carbonation depth measurement on concrete cube

5.6.3 Corrosion Monitoring by Electrochemical Techniques

In order to study the long-term effect of carbonation and inhibition effect of amino acids as SACoI, the test program was continued up to 35 exposure cycles (525 days ~ 1.5 years). Corrosion behaviour of embedded rebar in concrete exposed to carbonation environment was monitored by various electrochemical techniques. Corrosion rate was determined by performing Tafel extrapolation (LPR) measurements and to get the insight details of concrete microstructure and steel-concrete interface, electrochemical impedance spectroscopy (EIS) technique was used effectively. The detailed procedure for each of the technique is described in the succeeding sections.

5.6.3.1 Linear Polarization Resistance (LPR)

LPR method was employed on the prism specimens with the help of guard ring arrangement provided along with Gill AC corrosion analyzer. Polarization tests were by polarizing the working electrode (steel rebar) to ±25 mV at a sweep rate of 10 mV/min. Before commencement of test, specimens were saturated to obtain a uniform moisture content on the cover concrete. This was done by placing a wetted sponge on the top of the prism specimen for two hours. After achieving

a desired saturation, guard ring was placed along with wet sponge on the top of the prism. The wet sponge provides the proper ionic conductivity during the test. The working electrode and guard ring were connected to the corrosion analyzer with the help of connection wires. The arrangement for performing LPR test by using guard ring method is shown in Figure 5.8.

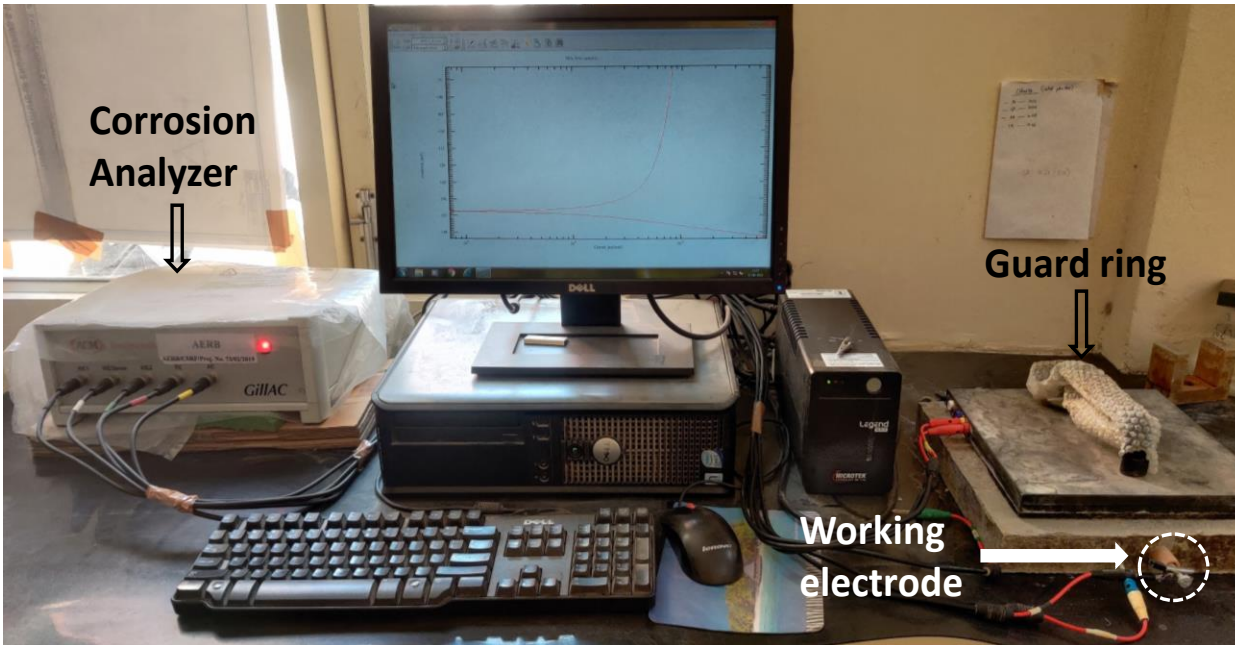

Figure 5.8 Experimental arrangement of electrochemical measurements LPR and EIS

Typical polarization curve obtained by using LPR technique is shown in Figure 5.9. The curve consists of two branches i.e., anodic branch representing anodic dissolution reaction and cathodic branch representing cathodic reaction on steel surface. The slope of the two branches represented in figure as anodic Tafel slope and cathodic Tafel slope are obtained by extrapolating linearly and the point of intersection of these two slopes at x-axis gives the corrosion current density (i_{corr}) while the potential (at y-axis) at which it lies gives the potential of rebar called as corrosion potential (E_{corr}). Based on the obtained Tafel plots and Tafel extrapolation technique, corrosion current density (i_{corr}) was obtained for all the specimens.

The corrosion inhibition efficiency of the SACoI was calculated using equation 5.2.

$$\eta_{LPR}, \% = \frac{i_{0,LPR} - i_{1,LPR}}{i_{0,LPR}} \times 100 \qquad \ldots(5.2)$$

where, $i_{0,LPR}$ and $i_{1,LPR}$ are the i_{corr} values recorded by Tafel extrapolation of LPR curves for un-treated and treated RC specimens, respectively.

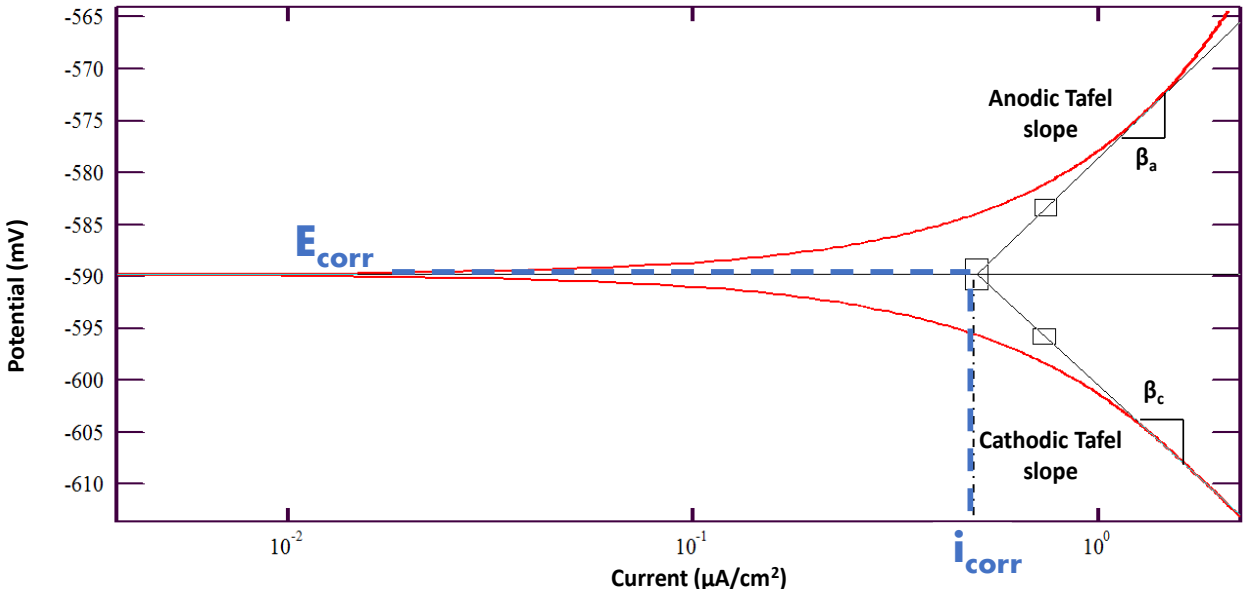

Figure 5.9 Typical polarization curve for RC specimen

5.6.3.2 Electrochemical Impedance Spectroscopy (EIS)

The principle of the EIS technique is to apply AC signal amplitude to the working electrode (rebar) embedded in an electrolyte (concrete). It provides abundant information about concrete pore structure and corrosion mechanism i.e. electrical resistivity, dielectric properties of concrete, rate of corrosion, steel/concrete interface properties and the kinetic information *(Montemor et al., 2003; Rodrigues et al., 2021; Song & Saraswathy, 2007)*. EIS test was performed on the prism specimens after 5 exposure cycles (i.e., 75 days) till the end of testing age i.e., until 35 exposure cycles. The measurement was carried out with the help of guard ring arrangement provided with ACM Gill AC corrosion analyser. The test setup used for EIS measurement was similar to that used in LPR measurement and represented in Figure 5.8. The test was performed at a sinusoidal voltage of 10 mV, applied in the frequency range of 100 KHz to 1 mHz. According to ASTM G3 *(ASTM, 2004)* EIS data can be represented in two formats, Nyquist and Bode plot. Nyquist plot corresponds to graph of $Z = Z' + jZ''$ (where Z' is the real part and Z'' is the imaginary part) plotted at different frequencies. Bode plot format further has two representations (i) Bode magnitude plot (ii) Bode phase angle plot. In the current study, EIS results (at 0, 5, 10, 15, 20, 25, 30 and 35 cycles) are represented in the form of Nyquist and Bode magnitude plots. Furthermore, the utilization of ZMAN software was incorporated to analyze the EIS data of the carbonated system. This choice

stemmed from the software's capacity to straight-forward and adaptable fitting of an equivalent circuit model (ECM), offering a comprehensive analytical approach.

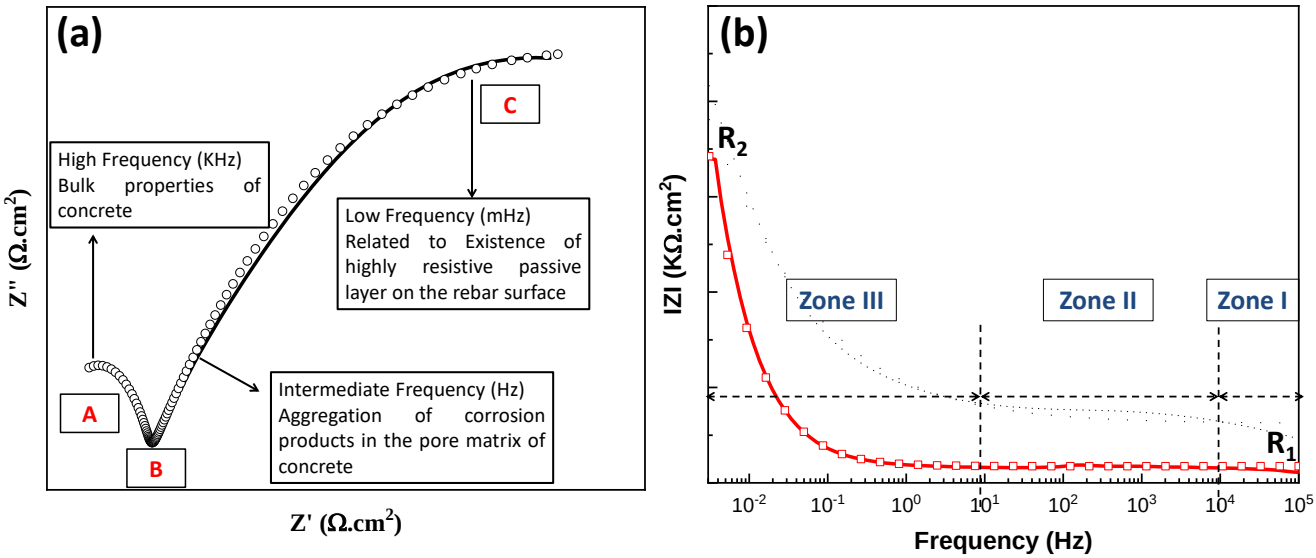

Figure 5.10 Distinguish features of (a) Nyquist plot (b) Bode plot

Figure 5.10a shows a typical Nyquist plot with three distinct traits (A, B, C). These traits are frequently seen in impedance spectra *(Ford et al., 1998)* and each trait defines the distinct feature of Nyquist plot. Most often, trait B is not distinctively visible as it gets veiled by C. The changes in the capacitive arc of Nyquist and impedance in Bode plot display the ongoing process in concrete matrix as well as on steel surface. In Nyquist plot, the increase and decrease in radii of HF arc displays the changes occurring in concrete matrix while changes in LF arc describes the condition of embedded rebar surface *(B. Q. Dong et al., 2014; Ford et al., 1998; Kaur et al., 2017a)*. Also, shift in spectra wrt the x-axis shows the dominant process of either chloride or carbonation. Similarly in Bode magnitude plots (shown in Figure 5.10b) the distinguished region can be divided in three zones i.e. Zone I corresponds to High frequency (HF) region (100 KHz-10 KHz) and changes in impedance in this region correlates to the change in concrete matrix, Zone II corresponds to Mid frequency region (10 KHz-10 Hz) and change in this region is attributed to change in concrete microstructure and its composition at steel/concrete interface, Zone III corresponds to Low frequency (LF) region (10 Hz-1 mH) in which impedance change is associated with the changes in passivity of steel. In studies related to application of migratory inhibitors, mid frequency range which is attributed to the steel/concrete interface properties is important as the inhibitor is expected to reach the rebar and form a protective layer that affects steel-concrete interface. From an electrochemical perspective, a typical electrochemical system

consists of electrodes and an electrolyte, typically in a solution form. This entire electrochemical system can be simplified into an equivalent circuit, referred to as the Randles circuit model, shown in Figure 5.11 (proposed by John Edward Brough Randel). The circuit is composed of electrolyte resistance: R_s (known as pore solution resistance) in series with parallel combination of charge transfer resistance between electrodes and electrolyte: $R_{ct,1}$ and double layer capacitance: $C_{dl,1}$ *(Ribeiro & Abrantes, 2016).*

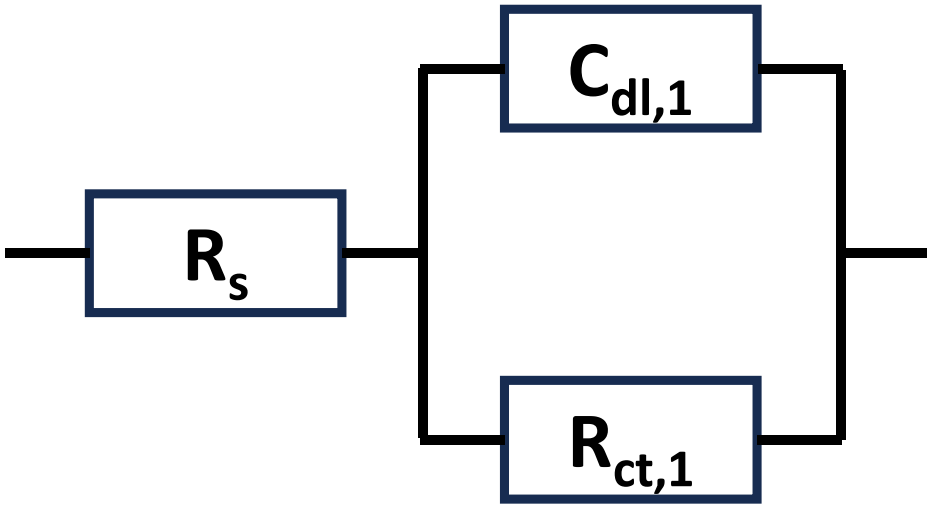

Figure 5.11 Typical Nyquist plot and its equivalent circuit

While employing the Randles circuit to fit an impedance spectrum offers a practical means to extract quantitative electrochemical data from the circuit components, it simplifies the electrolyte in this electrochemical system as a singular entity and presumes that electrochemical reactions exclusively transpire at the electrode surfaces. Nevertheless, when dealing with fly ash blended cement materials, the electrochemical system becomes notably more complex. Since the corrosion process in aggressive environment and inhibition process by corrosion inhibitor involves various physical processes, therefore, simple Rendell circuit cannot be used to interpret the EIS data of reinforced concrete. Hence, other equivalent circuit models shall be introduced.

In the present work, several models were tried in order to obtain the best fit electrochemical equivalent circuit (EEC) and the circuit that best fitted is shown in Figure 5.12. Therefore, in the current study, we apply this model to explore the carbonation behaviour of blended cements containing fly ash. This equivalent circuit model has proven effective in tracking carbonation in OPC and OPC mortar *(B. Dong et al., 2016).*

In the equivalent circuit, R_s represents the electrolytic pore solution resistance in concrete followed by series of Impedances (Z). EEC consist of two impedances, Z_c and Z_{rf}. Impedance Z_c corresponds to Faradaic procedure inside the concrete matrices, whereas impedance Z_{rf} corresponds to Faradaic procedure between the interfacial film and rebar. Impedance Z_c consist of resistance (R_c) and constant phase element ($C_{dl,1}$) between solid/liquid phase in the concrete bulk. Similarly, Z_{rf} consist of resistance (R_{ct}); also known as charge transfer resistance and constant phase element ($C_{dl,2}$) between the interfacial film and steel. In the present circuit, constant phase element is used instead of pure capacitor for fitting a depressed semi-circle. The depression in semi-circle is due to surface reactivity, in-homogeneity, porosity of concrete, roughness and irregularities on rebar surface. The impedance of CPE depends upon the angular frequency and determined by the equation 5.3.

$$Z = 1/Q(j\omega)^{\alpha} \qquad \ldots(5.3)$$

where Q is the admittance, ω is the angular frequency and α is the exponent for constant phase element due to depressed semicircle. When α equals 1, CPE behaves as pure capacitor and α equals 0, CPE behaves as pure resistor.

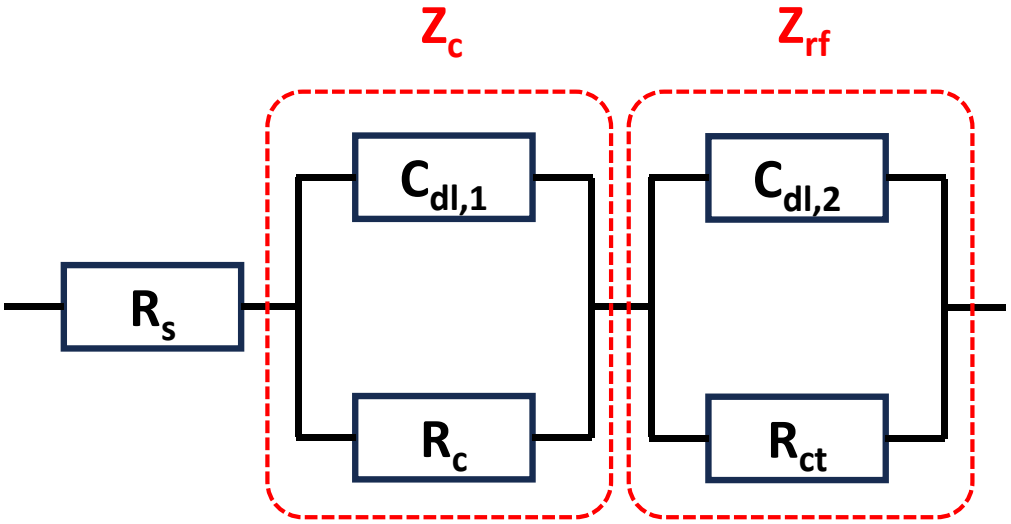

Figure 5.12 Electrochemical equivalent circuit

Further, a schematic representation that describes the typical steel-concrete interface is shown in Figure 5.13 and it consists of various interface layers such as compact iron-oxide layer and interfacial film layer adjoining the concrete matrix. The interfacial layer consists of calcium

hydroxides, calcium carbonate and other cement hydration products on the steel surface *(Kaur et al., 2017b).*

Figure 5.13 Schematic representation of steel-concrete interfaces

5.6.4 Visual inspection of extracted rebars

At the end of the testing duration, the RC specimens were broken and the rebars were extracted in order to assess their physical conditions. The testing was conducted till 35 carbonation exposure cycles as the SACoI-applied specimens started to show active signs of corrosion. Hence, the treated as well as un-treated specimens were monitored till 35 exposure cycles and then broke opened for visual analysis.

5.7 RESULTS AND DISCUSSIONS

5.7.1 Percolation ability of amino acids

In order to apply amino acids as SACoI, it is vital for them to percolate and reach the rebar level at a considerable concentration. Hence, six amino acids, namely, *Ser* & *Cys* (Set 1), *Phe* & *Trp* (Set 2) and *Asn* & *Gln* (Set 4) were applied on the 100 mm cubes in aqueous form and their percolation profiles were obtained wrt to depth and duration. The peaks of pure compounds and that of concrete powder drilled from SACoI-applied specimens were seen to coincide exactly on each other for four of the compounds and the peaks are shown in *Annexure A* (Figure A8 to A11); while, no peaks were obtained for *Cys* and *Trp* concrete powders. Thus, the presence of *Ser, Phe, Asn* and *Gln* was confirmed inside the concrete cubes upto ~25 mm. Hence, percolation profile of *Ser, Phe, Asn* and *Gln* was developed with the exact concentration values reaching at various depths (calculated by the Beer's law using equation 5.1) and is presented in Figure 5.14.

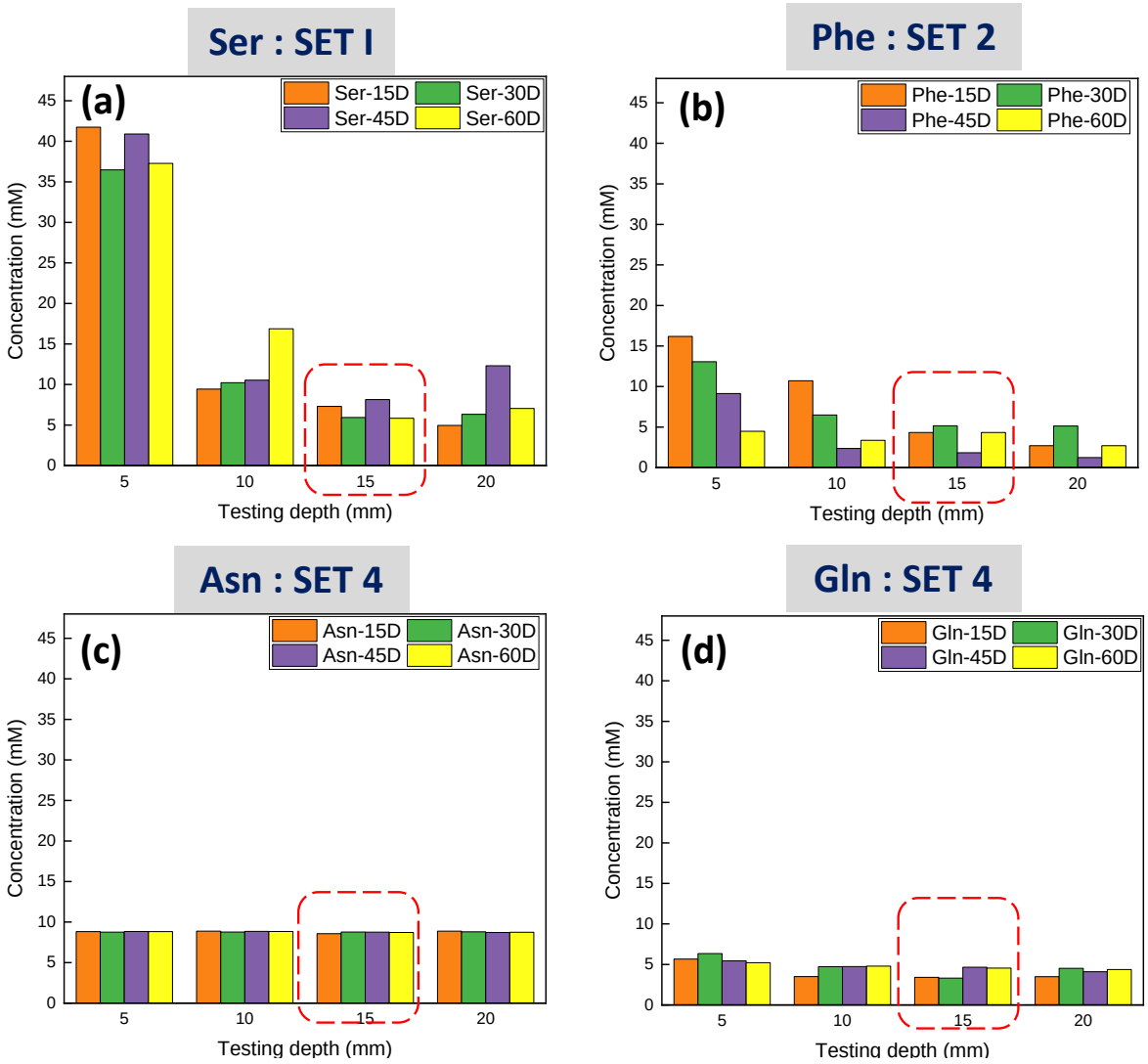

Figure 5.14 Concentration of amino acids at various depths and durations

Generally, SACoIs are known to percolate through concrete pores by process of capillary sorption (Bolzoni, et al., 2014), therefore, requiring a few days to reach the rebar level. Considering this, the first powder sample was drilled after a period of 15 days after application. Furthermore, concentration profile of Ser displays slight variation with the increase in the testing duration; implying that, for Ser to percolate, a period of 15 days was enough. When observing the variation with depth, it was noted that the percolated amount reduced with increasing depth. This can be owed to the dense microstructure of fly-ash blended concretes which resulted in retainment of Ser molecules at lower depth of 5-10 mm. An important point worth mentioning is that even after retention, a maximum concentration of 8.5 mM reached at the cover depth of 15 mm considered in the current study. In the obtained profile of Phe, it could be seen that the concentration of the

compound, at a particular depth reduced with increasing duration. This suggests that the compound showed continuous dispersion till 60 days. The maximum concentration reached at 15 mm was 5 mM.

From the figure, it can be seen that *Asn* and *Gln* showed a more uniform profile as compared to that obtained for *Ser* and *Phe,* which remained uniform throughout the testing duration as well as tested depths. This suggests that amide-based organic compounds (as compared to other functional-groups) can percolate through PPC based concrete matrix with minimum resistance from the microstructure. A maximum concentration of 8 mM for *Asn* and 5 mM for *Gln* was obtained at 15 mm depth.

Hence, it can be stated that *Ser, Phe, Asn* and *Gln* have the capability to percolate through PPC concrete and reach the rebars with a significant concentration. Hence, these four amino acids were finalized to be applied as SACoIs. The order of concentration was *Ser>Asn>Gln>Phe.*

5.7.2 Carbonation depth profile

The carbonation profile of concrete specimens with and without the applications of SACoIs was obtained for 15 exposure cycles and the results are presented in Figure 5.15.

In general, the carbonation depth increases with exposure duration. For PC (without SACoI), the results indicate that nearly 83.46 % of the area is carbonated within 60 days. Further, after 75 days of exposure, the concrete got carbonated till a depth of 16.24 mm i.e., more than the cover depth for RC specimens in the current study. This indicates that CO_2 will reach the steel-concrete interface after 75 days in reinforced specimens which will reduce the pH in its vicinity and can cause depassivation of the embedded bars with further exposure (i.e., >75 days). Another observation that was noticed is that, initially the increase was high but after a period of 11 exposure cycles, the values became almost stagnant. This has seen by a few other researchers when observing the carbonation profile of concrete *(Kaur et al., 2016)*.

Further, for SACoI-applied specimens, a significant reduction in carbonation depth of concrete was observed after *Phe*, *Asn* and *Gln* application, while no such variation was observed after *Ser* application. From the obtained concentration profile and carbonation depth results, it can be said that *Ser* does not have any significant surface accumulation effect and percolates easily

without any pore blocking effect; whereas the other compounds have some surface accumulation that reduces the ingress of CO_2 from outside. Among the three, *Phe* reduces the carbonation depth by 46% followed by *Gln* (23%) and *Asn* (20%).

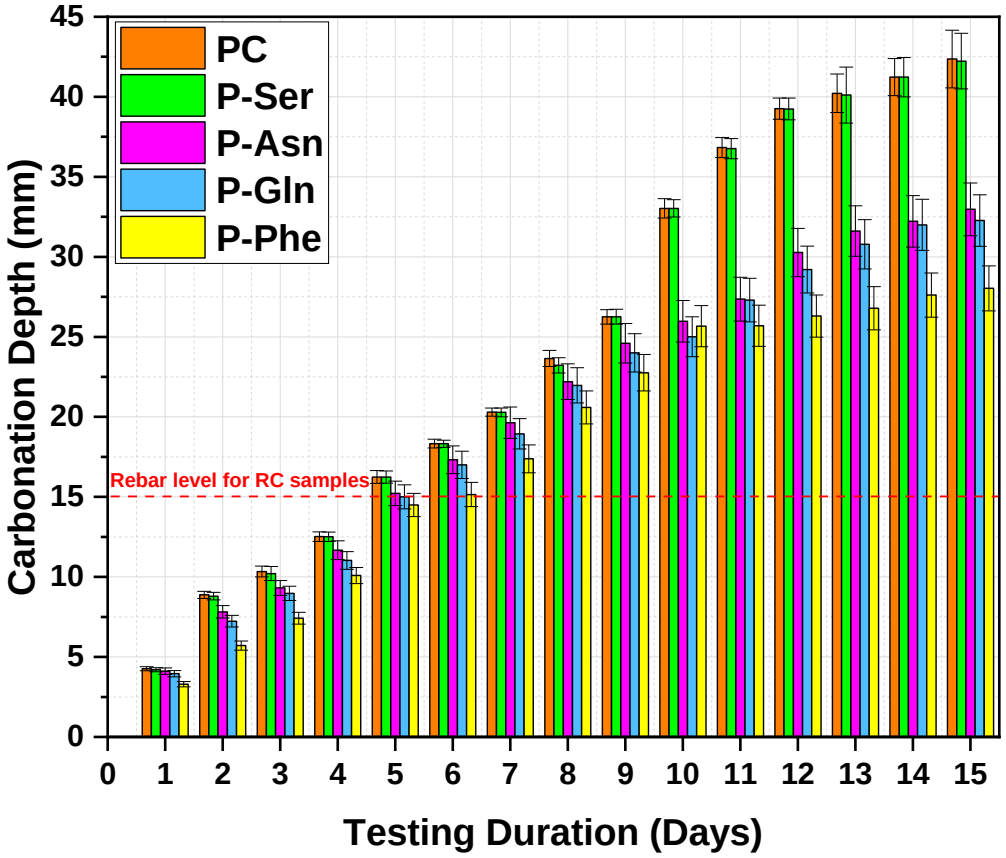

Figure 5.15 Carbonation depth profile of concrete cubes

5.7.3 Corrosion Monitoring by Electrochemical Techniques

In the present study, corrosion monitoring of RC prism specimens was done by using various electrochemical techniques namely, LPR and EIS method. Initially, all the RC prisms were exposed to carbonated corrosive environment; LPR reading were taken after every exposure cycle (i.e., 15 days) and EIS readings were taken after every five cycles (i.e., 125 days). The results were analyzed and once, the active corrosion condition of rebars was confirmed, the RC specimens were divided into two sets: treated RC prisms and un-treated RC prisms. The un-treated RC prisms (#3 in number) were not applied with any SACoI and the treated RC prisms (#12 in number) were applied with four SACoIs (*Ser*, *Phe*, *Asn* and *Gln*) each in order to study the amino acids' re-passivation capacity. Figure 5.16 shows the test regime and nomenclature for the RC prisms. Along

with this, surface condition of rebar was assessed by optical images at the end of testing age. The following section presents the LPR ad EIS results for untreated and treated RC prisms.

5.7.3.1 LPR results

The current section presents the results obtained from LPR test after each exposure cycle. The confirmation of the active stage of corrosion of rebars was done by analyzing the LPR test results. Figure 5.17 shows the test readings for un-treated and treated RC prisms; i_{corr} values are plotted as a function of carbonation exposure cycle.

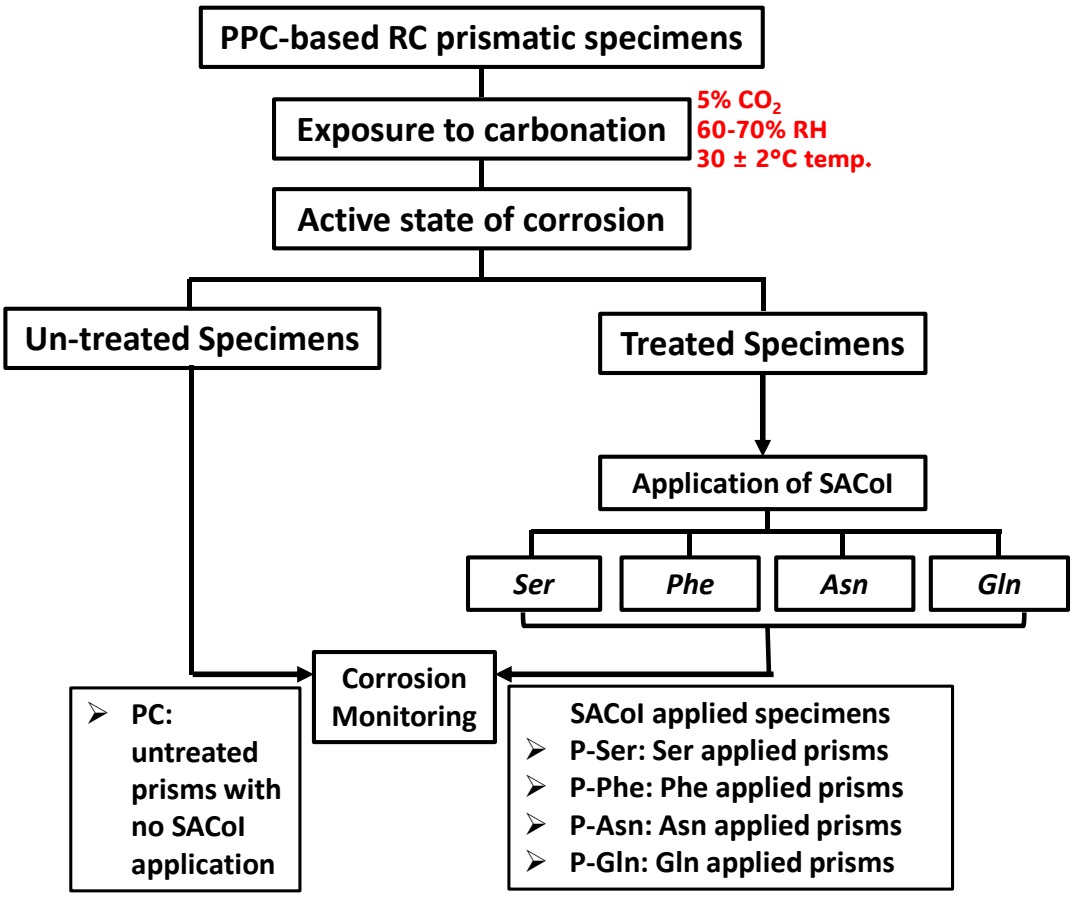

Figure 5.16 Flowchart showing the test regime of RC prisms and their nomenclature used in the study

Depending upon the i_{corr} values, rebar corrosion condition is divided into 4 categories: the rebar is said to be in 'passive' condition if the $i_{corr} < 0.1 \mu A/cm^2$, 'low to moderate' corrosion rate zone for i_{corr} between 0.1 and 0.5 $\mu A/cm^2$, 'moderate to high' corrosion rate zone for between 0.5 and 1 $\mu A/cm^2$ and 'high' corrosion rate zone if the value of icorr > 1 $\mu A/cm^2$; corrosion rate zones are assigned in Figure 5.17*(François, 2021)*.

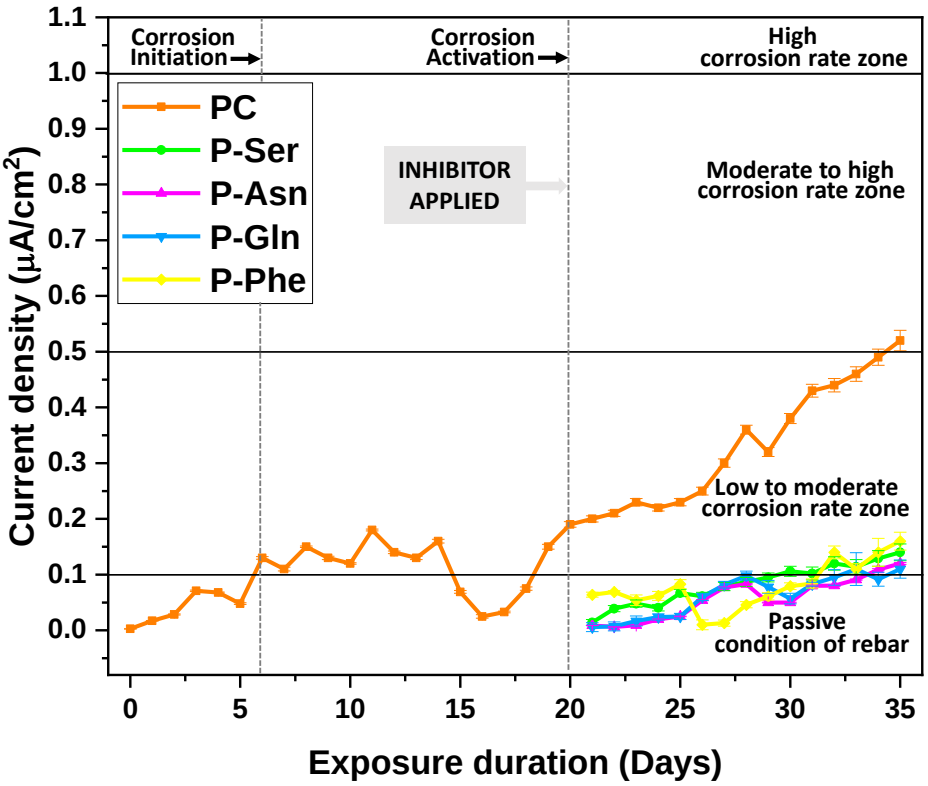

Figure 5.17 LPR graph for un-treated and SACoI treated RC prisms

It can be seen that initially, before the prisms were exposed to carbonation, the rebars displayed very low i_{corr} value of 0.0027 μA/cm^2 . This clearly demonstrates that a passive layer was present over the steel surface owed to the alkaline concrete environment of sound concrete. After the exposure to carbonation, the 'passive' condition of rebar was seen to pertain till 5 exposure cycles after which the rebars entered the zone of 'low to moderate' corrosion rate. This indicates that it took 5 exposure cycles (i.e., 90 days) for the CO_2 to de-passivate the embedded rebars. The results are in line with the carbonation depth results where it was observed that >75 days of exposure will lead to de-passivation of rebars. The phase is referred as the 'corrosion initiation phase' and the time duration of 5 cycles is referred as the 'time to corrosion initiation'. The i_{corr} values were seen to show instability and were seen to re-enter the zone of 'passive' rebar condition after 15 exposure cycles (i.e., 225 days). The reason for this behaviour is the deprivation of oxygen and moisture at the steel-concrete interface due to accumulation of initially formed corrosion products' layer over the rebar. Alongside this, the decrease in permeability of the concrete due to $CaCO_3$ precipitation (insoluble product formed by the reaction between $Ca(OH)_2$ and CO_2) in the concrete pore lining also limits the oxygen availability at stee-concrete interface

(a necessary condition for corrosion); suggesting that the cover concrete also provided some kind of protection against corrosion. It was only after 20 exposure cycles that the rebars displayed >0.1 $\mu A/cm^2$ of i_{corr} values. The values were seen to rise towards higher values after 20 exposure cycles. This phase (after 20 exposure cycles) is referred to as the propagation phase where the corrosion current values keep on rising. An important point worth mentioning is that the phase between 'initiation' and 'propagation' is referred to as the 'activation phase'; in the current study this phase was seen to occur between 5^{th} and 20^{th} exposure cycles. Melchers 2020 has also stated that after the initiation of corrosion of rebars, there exists a time period in which, due to unavailability of moisture and oxygen, the corrosion rates again fell. It is after this period that the corrosion rate again rises and the rebars are then said to be under the state of 'active corrosion'(*Melchers, 2020)*. The same has also been explained in Chapter 2, Section 2.3. Hence, RC specimens were divided into sets after 20 exposure cycles; Set 1: un-treated specimens that were considered as reference samples and Set 2: treated specimens that were applied with SACoIs.

Amino acids were applied on set 2 specimens (treated RC prisms) and were left un-disturbed in laboratory environment for 15 days (time required for the percolation of amino acids and reach the rebar level). The application procedure was same as that adopted during the percolation ability test (explained in Section 5.6.1 in the current chapter). After 15 days SACoI application, the i_{corr} values recorded for P-Ser, P-Asn, P-Gln and P-Phe were 14.28, 22.72, 35.08 and 3.12 times lower than the un-treated samples, respectively. These observations clearly evinced that the amino acids, upon reaching the rebar level, reduced the corrosion kinetics and provided a protection against corrosion. It has been stated that in PPC carbonated concrete, the pore structure gets coarser with progressive carbonation, thus, allowing un-hindered percolation to the inhibitor solution *(Tiwari et al., 2023; Wu & Ye, 2017)* (even more than that recorded during the percolation ability test of amino acids). Generally, it is seen that organic corrosion inhibitors with hetero-atoms such as N, O, P and/or S protect the rebar surface by adsorbing on its surface via the hetero-atoms and de-localized π electrons from their aryl constituent. Also, the reported mechanism of inhibition by *Ser, Asn, Gln and Phe* is the physiochemisorption of negatively charged inhibitor ions (Ser^-, Asn^-, Gln^- *and* Phe^-) on the positively charged rebar surface (Fe^{2+or3+}) as mentioned in Chapter 4 and reported in *Purnima et al. 2023 (Purnima, Goyal, et al., 2023; Purnima, Shweta, et al., 2023; Purnima, Tiwari, et al., 2023)*. The heteroatoms in the molecular structures of amino acids become the reaction centres and form chemical as well as physical bonds with the available

sites on rebar surface as well as with the accumulated corrosion products. Although, the i_{corr} data was to seen rise with carbonation exposure but the slope of SACoI treated specimens was much smaller than that obtained for PC; indicating the suppressed corrosion rate of SACoI treated samples. There was a competition between the passivation and the de-passivation reactions, which was being dominated by amino acids' molecules. Further, even after the harsh carbonation exposure of 210 days after inhibitor application, the i_{corr} values recorded for P-Ser, P-Asn, P-Gln and P-Phe were 3.7, 4.3, 4.7 and 3.25 times lower than PC, respectively. Also, it is worth mentioning that the values for treated specimens remained in the zone of 'low to moderate' corrosion rate zone; while, that for PC entered the 'moderate to high' corrosion rate zone. This indicates sustainment of some passivity over the rebar surface even after prolonged carbonation. An inhibition efficiency of 73.07%, 69.23% 76.92% and 78.84% was recorded for *Ser, Phe, Asn* and *Gln*, respectively, at the end of the test programme, as per equation 5.2; order of efficiency being: *Gln>Asn>Ser>Phe*.

The order of efficiency can be explained on the basis of the percolation capacity of the amino acids as well as on the presence of functional groups. The order of percolation was *Ser>Asn>Gln=Phe*. Although *Gln* and *Asn* has lower percolation capacity than *Ser*, even than they both displayed higher efficiency than *Ser*. This was due to the presence of amide functional group in their molecular structure which is considered to be one of the most effective in chelating Fe ions during the inhibition process. The amide functional group is more electronegative than alcohol functional group in *Ser* and hence, the exhibition of higher inhibition efficiency by *Asn* and *Gln* than *Ser.* Out of *Asn* and *Gln*, *Gln* showcased higher inhibition efficiency (slightly higher) than *Asn*, which is attributed to longer carbon chain length of *Gln* leading to the formation of stabler chelate ring. Similar observation was also recorded in Level 1: Pore solution testing where *Gln* developed a more thermodynamically stable protective layer on rebar surface than *Asn* (explained in detail in Chapter 4). Furthermore, *Phe* which displayed the lowest percolation capacity displayed the lowest inhibition capacity during LPR test.

In conclusion, it can be said that all the amino acids that showed the ability to percolate through the concrete cover were able to display a minimum of 70% inhibition efficiency in controlling the rate of on-going carbonation-induced corrosion. Out of all, amide based amino acids are seen to perform with the highest inhibition capacity.

5.7.3.2 EIS results

The current section presents the results obtained from EIS test conducted on RC specimens after every 5 exposure cycles. The test results helped to study the processes occurring in the bulk concrete, at the steel-concrete interface and at the rebar surface. The data is presented in the form of Nyquist and Bode plots for SACoI treated as well as for the un-treated RC specimens.

EIS test results for un-treated RC prisms

Figure 5.18a shows the Nyquist plots for un-treated specimen recorded from 0 to 35 exposure cycles (i.e., from before exposing to carbonated environment till 525 days of continuous exposure) and the corresponding curves are denoted as PC-0 to PC-35. Here, PC specifies that the specimen was un-treated, and the numeric value specifies the exposure cycle at which the Nyquist plot was attained. Figure 5.18a' shows the magnified (clearer) view of the HF arcs of PC-0 to PC-35. Figure 5.18b shows the corresponding Bode plots for un-treated specimen recorded from 0 to 35 exposure cycles.

From the Nyquist plot (Figure 5.18a), it can be noticed that the LF arc obtained before exposing the prisms to carbonation exposure had a very large diameter (largest in comparison with all the LF arcs); indicating the existence of a passive film on the surface of rebar, which originated from the alkaline conditions within sound concrete. This observation is in line with the low i_{corr} value obtained during the LPR test for PC before exposure. After 5 cycles of exposure, diameter of the LF arc was seen to reduce which could be due to the exposure to corrosive environment. This arc was seen to further fall and get diminished by the end of the testing duration (after 35th exposure cycle), suggesting the complete de-passivation of the initially formed passive film on rebar surface. This observation was associated with signs of active corrosion of the rebar with the continuous carbonation exposure. An important observation that can be made from the magnified HF arcs (Figure 5.18a') is that the diameter of the arcs was seen to rise from 0 to 15 exposure cycles. This is due to the densification of the concrete matrix and reduction in conductivity of the concrete's interstitial liquid (*B. Dong et al., 2014; B. Q. Dong et al., 2014)*. $CaCO_3$ is formed (as a product of a chemical reaction between $Ca(OH)_2$ and CO_2) and gets deposited onto the pore lining of concrete leading to a decrease in the concrete's pore size, which in turn causes an increase in its overall density. Furthermore, the interstitial liquid present within the pores of concrete typically contains a high concentration of charged particles (OH^-, Ca^{2+}, Na^+, K^+) making it

conductive. However, when the process of carbonation takes place, carbonate ions present in the electrolyte solution interact with calcium ions (Ca^{2+}). This interaction results in a reduction of hydroxyl ion (OH^-) concentration within the concrete. Notably, *Snyder et al. (2003)* reported that the OH^- ions have the most significant impact on the electrical conductivity (*Snyder et al., 2003*). Hence, carbonation significantly contributed to the decrease in OH^- ion concentration, subsequently leading to a reduction in the electrical conductivity of the interstitial liquid present in concrete.

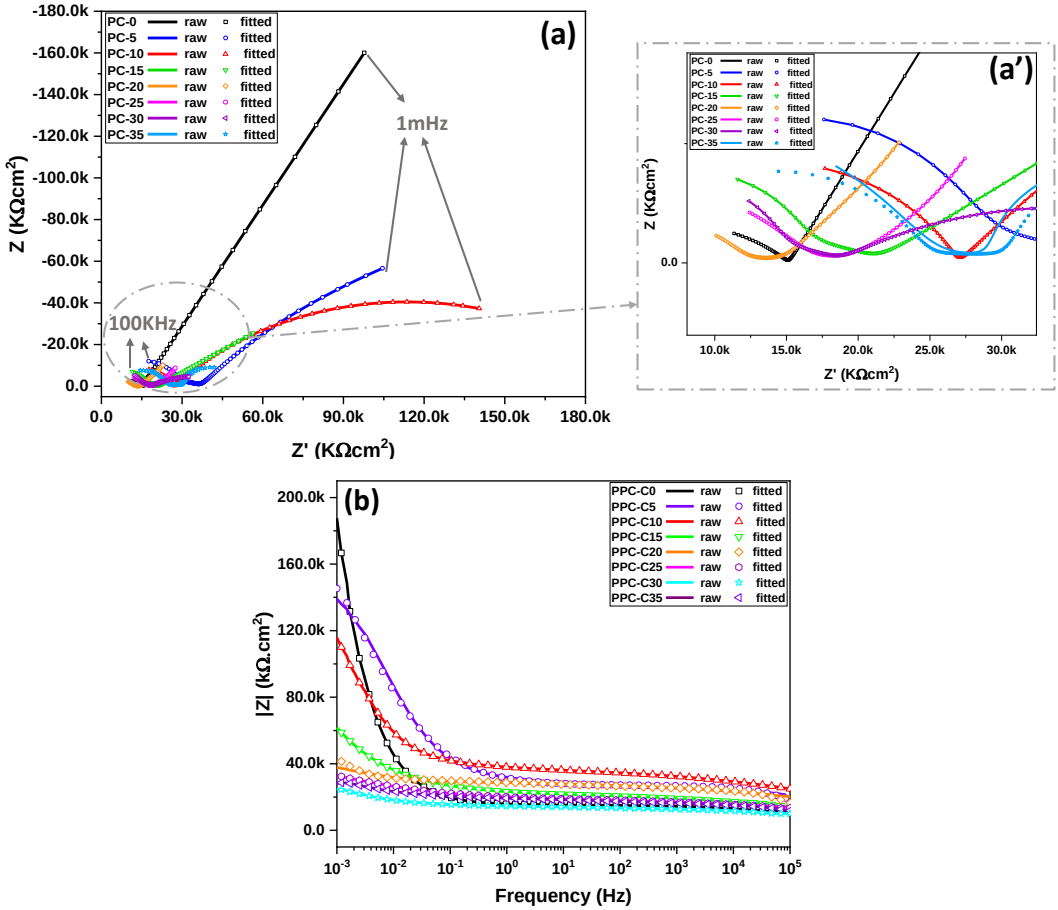

Figure 5.18(a) and (a') Nyquist plot; (b) Bode plot for un-treated RC specimen

This phenomenon continued till 15 exposure cycles (i.e., 225 days), however, after further exposure, the diameter of the HF arc was seen to decline. It could be correlated with the observation that prolonged exposure of $CaCO_3$ to carbonation causes its transformation from a soluble form to an insoluble bicarbonate form i.e., from $CaCO_3$ to $Ca(HCO3)_2$ (*Bjørge et al., 2019; Zhang et al., 2018)*. Simultaneously, the absence of unreacted calcium hydroxide within the concrete matrix makes the calcium silicate hydrate (CSH) gel susceptible to carbon dioxide (CO_2)

attack and coarsening of the SCM-based concrete microstructure (*Kumar Tiwari et al., 2023; Morandeau et al., 2014; Tiwari et al., 2023)*. These concurrent chemical reactions result in increased porosity and enhanced pore interconnectivity within the concrete matrix. Hence, the observed reduction in high-frequency electrical response beyond the 225-day mark.

From the Figure 5.18b (Bode plots of PC), it is evident that the low-frequency (LF) impedance of PC exhibits an initial high value of 180 $k\Omega.cm^2$. This signifies a substantial resistance to charge transfer at the steel surface, attributed to the presence of a passive layer formed on the rebar surface due to the elevated alkalinity of the concrete before exposure to a corrosive environment. As the exposure cycles increase, this impedance gradually decreases, indicative of active corrosion. This decline corresponds to the progressive depletion of the passive layer due to continuous carbonation exposure. Notably, after the 35^{th} exposure cycle, the LF impedance drops to 23 $k\Omega.cm^2$, representing an 87% reduction from the initial value. This dramatic decrease indicates the complete erosion of the passive layer due to the deteriorative effects of carbonation. When comparing the HF impedance value, initially increasing trend was witnessed upto 15 exposure cycle that might be due to modification in pore matrix. As explained by the Nyquist plot, CO_2 leads to the formation of $CaCO_3$ precipitates that can enhance the pore structure's density and elevate resistance against ionic movement. However, as continuous carbonation progresses, the previously insoluble precipitate undergoes a conversion into a soluble carbonate. This conversion triggers a reconfiguration of the pore structure, subsequently diminishing resistance to ionic movement. This transformation becomes evident in the HF impedance, which gradually began to decrease after the 20^{th} exposure cycle and continued to decrease till the end of the testing period.

Further, the EIS data was fitted into an electrical circuit as displayed in Figure 5.12. R_s signifies the resistance of the pore solution that is present in the interstitial space of the concrete pore matrix; R_c is the resistance of the bulk concrete which varies with the changes in the physical changes in the pore matrix; R_{ct} is the resistance against the charge transfer which is due to the combined resistance of the interfacial film (reaction products) and the resistance of the steel itself against any transfer of charge through itself. The trend of each parameter for PC specimens was studied and the results were analysed to develop an understanding about the corrosion kinetics occurring in the un-treated RC specimens. Figure 5.19a to c show the trend in R_s, R_c and R_{ct}, respectively.

The pore solution resistance (R_s) of the PC exhibited a slight decline from the 5th to the 10th exposure cycle, followed by an increase from the 10th to the 15th cycle (refer to Figure 5.19a). The initial decrease in R_s is attributed to $CaCO_3$ precipitation, which reduces ion conductance. Subsequently, the rise in R_s after the 15th cycle is due to increased ion conductance resulting from two factors: (i) coarsening of pore matrix (*Kumar Tiwari et al., 2023; Morandeau et al., 2014; Tiwari et al., 2023)* and (ii) conversion of insoluble $CaCO_3$ to soluble $Ca(HCO_3)_2$ (*Bjørge et al., 2019; Zhang et al., 2018*). This phenomenon enhances ion transfer near the steel-concrete interface, subsequently impacting corrosion reactions as evident in increased icorr values from LPR tests.

Additionally, the charge transfer resistance (R_c) initially increased from 0 to the 15th exposure cycle, with slight variations (see Figure 5.19b). During carbonation of the PPC matrix, initial pore matrix densification occurred due to calcite precipitation, resulting in pore blockage and increased concrete resistivity. R_c values surged from 85 kΩ·cm² to as high as 1568 kΩ·cm². However, continuous exposure led to increased pore volume and diameter. At the 20th exposure cycle, a drop in R_c occurred, primarily due to changes in the pore structure. The ongoing conversion of insoluble $CaCO_3$ to water-soluble $Ca(HCO_3)_2$ from continuous carbonation also contributed to reduced Rc values, a trend supported by R_s values. Possible factors include the decomposition of CSH gel due to CO_2. Subsequently, from the 20th to the 35th exposure cycle, minimal changes occurred in the concrete matrix, consistent with static R_c values. Also, the changes in the R_c values indicated from the EIS result analysis are in line with Hernandez at al. 2019 where the carbonation process was studied in detail through resistivity and EIS tests (*Herrera Hernández et al., 2019*).

The trends in the charge transfer resistance (R_{ct}) offer insights into rebar condition. Initially, R_{ct} values were high (215 kΩ·cm²) due to a robust, adherent passive film around the rebars (refer to Figure 5.19c). The first significant drop in R_{ct} occurred after 5 cycles, indicating de-passivation and corrosion initiation. A second drop was observed after 20 exposure cycles, signifying corrosion activation. These results align with i_{corr} values obtained from LPR tests, suggesting active corrosion of the corroded rebars. Similar observations were noted in the Nyquist plots.

The EIS parameters in PC reveal microstructural changes during carbonation exposure, schematically shown through Figure 5.20. The process can be divided into two phases: Phase I (up

to 15 cycles) and Phase II (15 to 20 cycles), shown in Figure 5.20a and b, respectively. Densification occurs in Phase I, while Phase II sees increased porosity and interconnectivity. Ultimately, PPC concrete's microstructure exhibits increased pore diameter and volume with prolonged carbonation exposure (beyond 525 days, or 35 cycles), shown in Figure 5.20c.

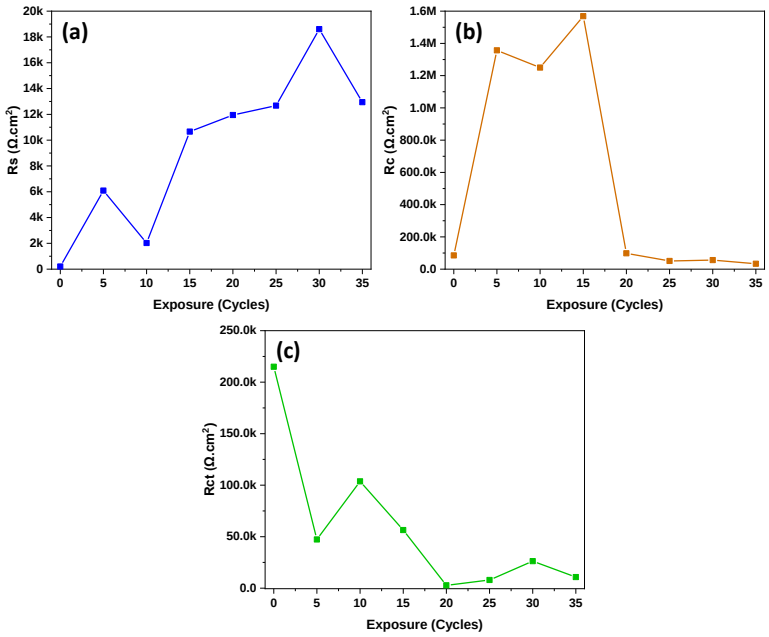

Figure 5.19 Trend of the resistive parameters for un-treated RC prisms

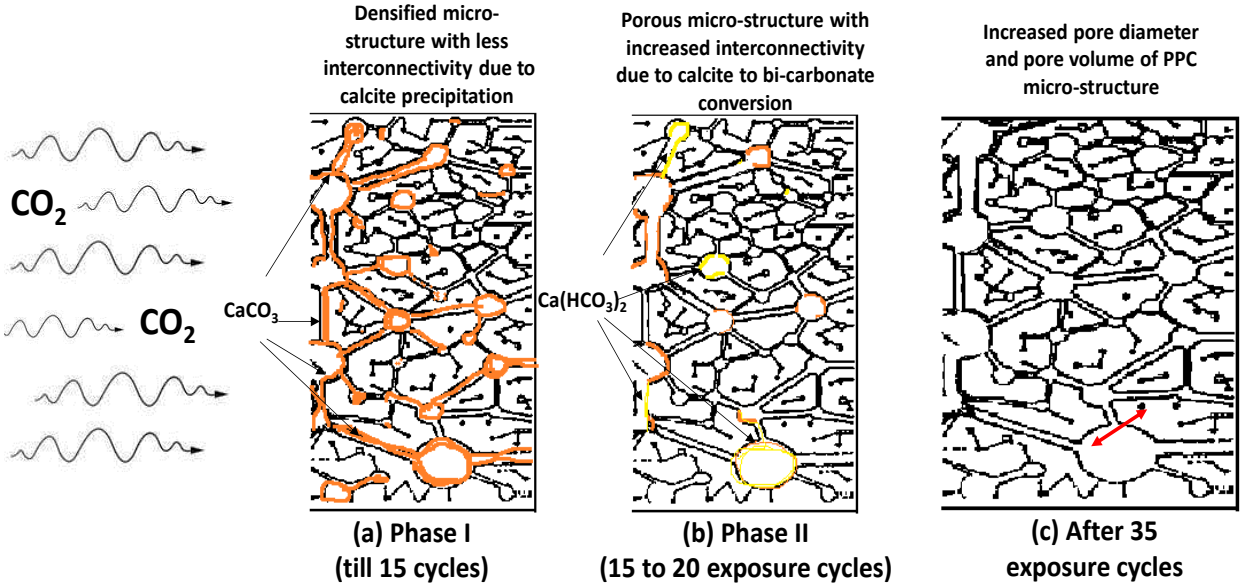

Figure 5.20 Microstructural changes occurring in PPC un-treated concrete with continuous carbonation exposure

EIS test results for treated RC prisms (SACoI-applied)

After 20 exposure cycles, as corrosion of the rebars became active, SACoIs (*Ser, Phe, Asn,* and *Gln*) were applied onto the RC specimens following the procedure in section 5.6.1. EIS plots (Nyquist and Bode) for these SACoI-treated RC specimens are shown in Figure 5.21to Figure 5.24.

After application, the specimens were kept in the lab for percolation, and EIS plots were taken at 5, 10, and 15 days post-application. Subsequently, the specimens were reintroduced to carbonation, and plots were recorded from the 25th to the 35th exposure cycles (i.e., one cycle after SACoI application until the end of the 35 exposure cycles).

EIS results of Ser applied specimens: Figure 5.21a and b display Nyquist and Bode plots for Ser-applied RC prisms, labelled as PSer-25, PSer-30, and PSer-35, compared to PC-20. Here, PSer specifies that the specimen was treated with *Ser* as SACoI and the numeric value specifies the exposure cycle at which the plot was attained. Similar abbreviations were used for other amino acids as well. Further, Figure 5.21a' and b' shows the Nyquist and Bode plots for Ser-applied RC prisms, respectively, after 5, 10 and 15 days of *Ser* application.

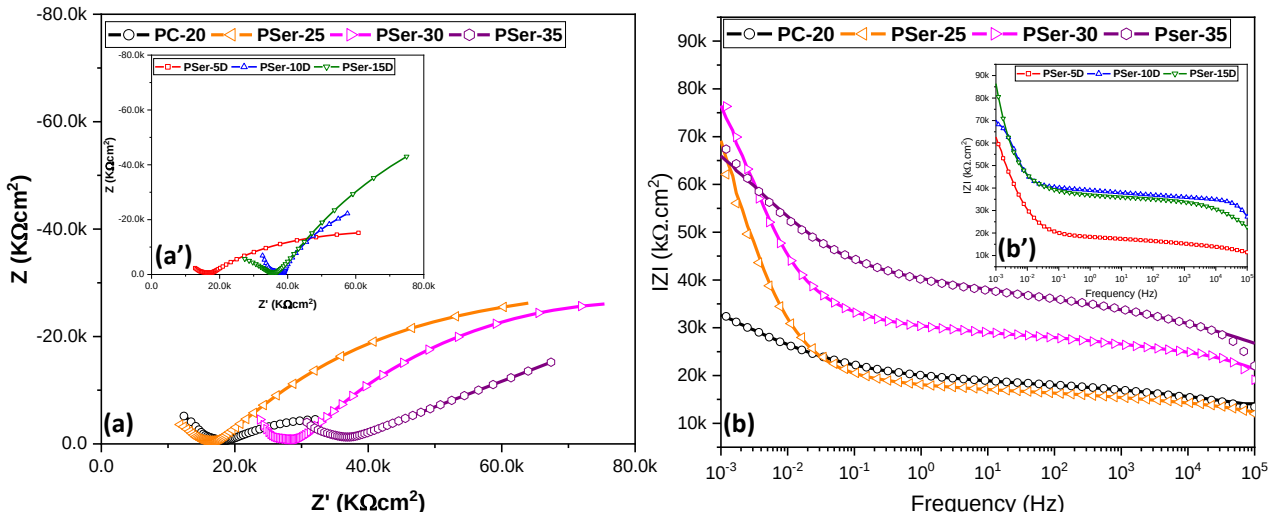

Figure 5.21(a) Nyquist; (b) Bode plots for *Ser* applied RC prisms

From Figure 5.21a', it can be seen that the diameter of LF arc increases from 5 to 15 days after *Ser* application: signifying gradual percolation and subsequent layer development at steel-concrete interface. In contrast, there is no discernible alteration in the diameter of the HF arc, implying that there are no significant changes occurring in the bulk concrete after *Ser* application.

On observing the Nyquist plots (shown in Figure 5.21a), it can be noticed that LF arc of PSer-25 (i.e., 5 cycles after *Ser* application) was higher in diameter in comparison to PC-20 i.e., un-treated RC specimen. Also, no change in the HF arc dimeter was seen. This can be due to the sustainment of passive film over rebar surface that was formed by the *Ser* molecules after 15 days of application. With further exposure (i.e., PSer-30), the diameters of the LF as well HF arc did not reflect any significant changes, indicating the maintenance of the passive film over rebar surface even after 10 exposure cycles after SACoI application. At the end of the testing duration, the diameter of LF arc decreased, with no change in HF arc. The decrease in the LF arc diameter signifies the commencement of the de-passivation process of the protective film formed by the *Ser* molecules on rebar surface. This process is instigated by the ongoing carbonation attack. Another prominent observation is the shift of Nyquist spectra towards higher impedance values (towards right) after 30 exposure cycles, reflecting increased concrete resistivity due to the protective film at the steel-concrete interface.

From the corresponding Bode plots, it has been observed PC-25 showed a 2.65-fold increase in impedance compared to PC-20, signifying enhanced rebar resistance against carbonation attack post-*Ser* application. Notably, PSer-25 exhibited increased |Z| values in the mid-frequency and high-frequency regions, validating that a layer has developed at the steel-concrete interface which led to the rise in rebar's resistance against corrosion. With further increase in exposure cycles, the trend in the |Z| value was same as that of the LF arc in the corresponding Nyquist plots.

EIS results of Phe applied specimens: Figure 5.22a and b shows the Nyquist and Bode plots for *Phe* applied RC prisms, respectively, in comparison with PC-20 and the corresponding curves are denoted as PPhe-25, PPhe-30 and PPhe-35. Figure 5.22a' and b' shows the Nyquist and Bode plots for *Phe* applied RC prisms, respectively, after 5, 10 and 15 days of *Phe* application.

In Figure 5.22a', the LF arc diameter gradually increases from 5 to 15 days post-Phe application, indicating percolation and layer development at the steel-concrete interface. Minor fluctuations in the HF arc diameter suggest minimal alterations in the bulk concrete after 5 days of Phe application.

In Figure 5.22a, LF arc diameter for PPhe-25 significantly surpassed PC-20, indicating the development of a protective film on the rebar surface after Phe application. However, as carbonation exposure increased, the LF arc gradually reduced, indicating carbonation's adverse impact on the protective film formed by Phe molecules. HF arc diameter showed no significant changes post-Phe application, but a shift towards higher |Z| values occurred after the 30th exposure cycle, possibly due to the slow dispersion of Phe molecules within the concrete matrix over time.

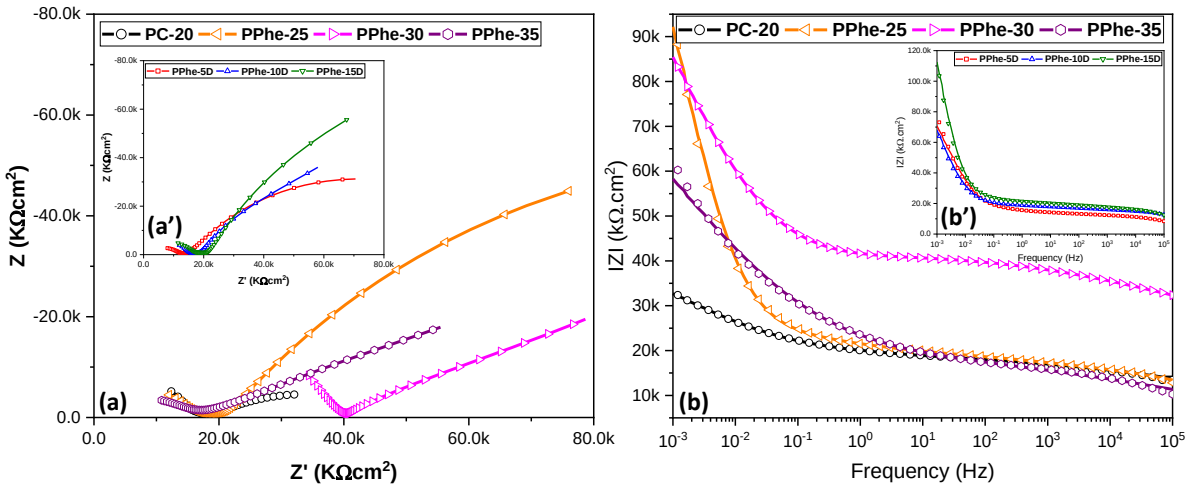

Figure 5.22(a) Nyquist; (b) Bode plots for *Phe* applied RC prisms

The corresponding Bode plot (Figure 5.22b) signifies the similar behaviour that has been observed in the Nyquist plots. The increase in LF impedance post-SACoI application indicates re-passivation of the rebar surface, with no shift observed in HF impedance, suggesting no interaction with concrete hydration products. However, after the 30th exposure cycle, an increase in intermediate and HF impedance is attributed to the uniform distribution of surface-accumulated *Phe* molecules within the concrete microstructure. After extended exposure, impedance values decreased across all frequencies after the 35th exposure cycle. When comparing impedance between PPhe-35 and PC-35, PPhe-35 showed three times higher impedance, suggesting that even after prolonged carbonation, *Phe*-applied specimens retained some corrosion resistance.

EIS results of Asn and Gln applied specimens: Figure 5.23a and b shows the Nyquist and Bode plots for Asn-applied RC prisms, respectively, in comparison with PC-20 and the corresponding curves are denoted as PAsn-25 to PAsn-35. Alongside, Figure 5.24a and b shows the Nyquist and Bode plots for Gln-applied RC prisms, respectively, in comparison with PC-20 and the corresponding curves are denoted as PGln-25 to PGln-35. Figure 5.23a' and b' shows the Nyquist and Bode plots for Asn-applied RC prisms, respectively, after 5, 10 and 15 days of *Asn* application;

while Figure 5.24a' and b' shows the Nyquist and Bode plots for Gln-applied RC prisms, respectively, after 5, 10 and 15 days of *Gln* application.

The plots of Asn and Gln-applied RC specimens are discussed together as they are both amide-based compounds with similar nature with regard to the percolation. From Figure 5.23a' and Figure 5.24a', it can be seen that the diameter of LF arc increases from 5 to 15 days after *Asn* and *Gln* application; signifying gradual percolation and subsequent layer development at steel-concrete interface. No significant changes occurred in the HF arc diameter, suggesting negligible alterations in the bulk concrete.

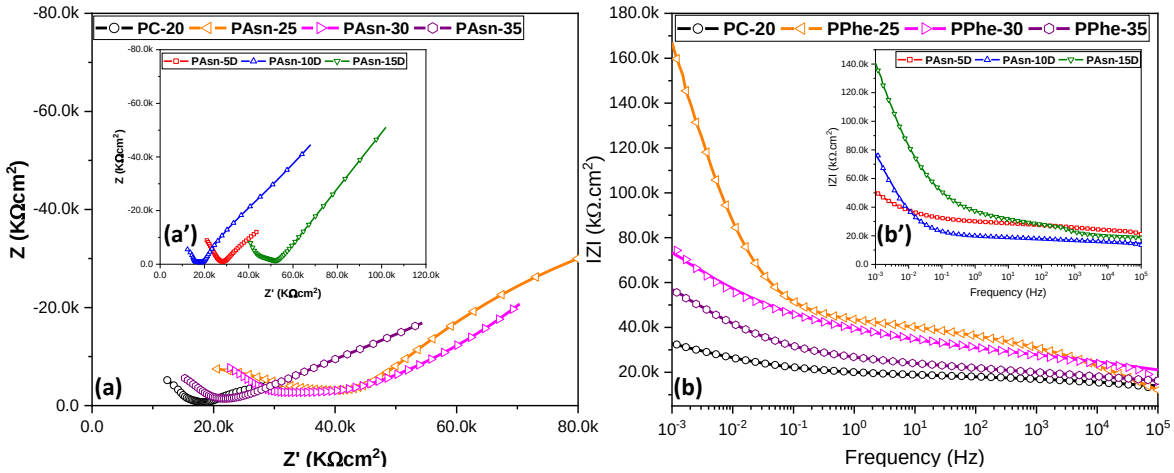

Figure 5.23(a) Nyquist; (b) Bode plots for *Asn* applied RC prisms

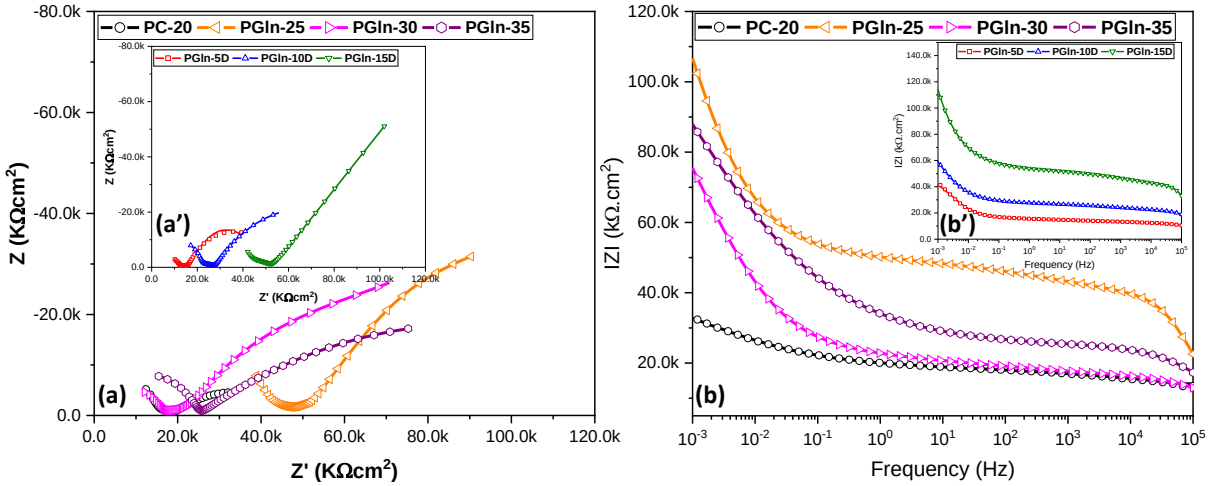

Figure 5.24(a) Nyquist; (b) Bode plots for *Gln* applied RC prisms

Both PAsn-25 and PGln-25 showed enlarged LF arc diameters compared to PC-20, attributed to passive layer development by *Asn* and *Gln* molecules on the rebar surface, enhancing

corrosion resistance through interaction with Asn-Fe and Gln-Fe. Subsequently, both PAsn-30 and PGln-30 demonstrated decreasing LF arc diameters, signifying gradual passive film depletion on the rebar surface. HF arc diameters remained unaltered, indicating no interaction with hydration products or changes in the concrete microstructure. A shift toward higher |Z| values was observed after the 25th exposure cycle, indicating increased concrete resistivity following SACoI application. Slight differences in *Asn* and *Gln*-applied RC specimens' behaviour may be due to variations in their percolation, as noted in migration studies.

The corresponding Bode plots validate the Nyquist observations. LF impedance increased from 35 kΩ·cm² to higher values (165 kΩ·cm² for *Asn* and 115 kΩ·cm² for *Gln*), indicating efficient re-passivation by both inhibitors. With extended exposure, LF impedance decreased, indicating gradual layer depletion. Even at the test's conclusion, *Asn* and *Gln*-applied specimens exhibited impedance values nearly 1.35 times higher than the control specimen, suggesting that the condition of *Asn* and *Gln*-applied RC specimens was better than control specimen.

The HF impedance values in Bode showed no significant changes, indicating that the presence of these molecules did not alter the concrete microstructure, which aligns with the percolation data. Notably, the Bode plot revealed a noteworthy increase in impedance values in the intermediate frequency region for the amide-based inhibitors. These changes in this region reflect variations at the steel-concrete interface, possibly signifying interaction between the inhibitor and Fe ions or complex formation due to their interaction. However, with extended exposure, these values decreased, indicating corrosion reactivation and increased ionic movement with a reduced decline.

EIS plots for treated and un-treated prisms at the at of the testing

Figure 5.25a and b shows the Nyquist and Bode plots for un-treated and SACoI-treated RC specimens, respectively, at the end of the testing age (after 35 exposure cycles). The graphs clearly show that while the LF arc of un-treated specimen exhibited a reduced diameter, the SACoI-treated specimens managed to maintain it. This signifies that all the SACoIs were efficient in maintaining their protective character even after prolonged carbonation exposure. Comparatively, all inhibitors displayed similar performance.

5.7.3.3 Corrosion and inhibition mechanism

To understand the corrosion inhibition mechanism, it is important to understand the corrosion rate controlling factors of steel in carbonated concrete (corrosion mechanism of steel in carbonated concrete). According to the corrosion rate analysis in the current study and a model proposed by *Glass et al. 1991*, the corrosion process of steel in carbonated concrete is controlled by the anodic dissolution of iron ions and their diffusion after this oxidation reaction *(Stefanoni et al., 2018)*. In the absence of inhibitor ions (i.e., in PC), the dissolution and subsequent diffusion of Fe ions could take place un-interruptedly, therefore, higher i_{corr} values and higher rate of increase in i_{corr} was recorded.

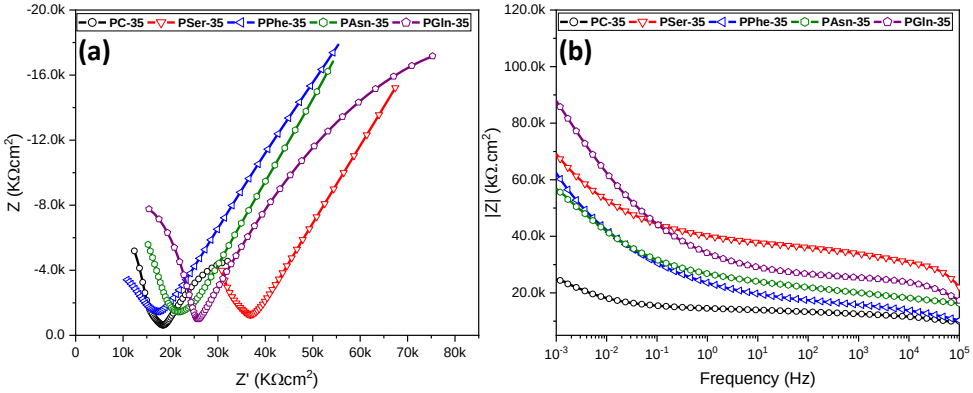

Figure 5.25 (a) Nyquist; (b) Bode plots after 35 exposure cycle

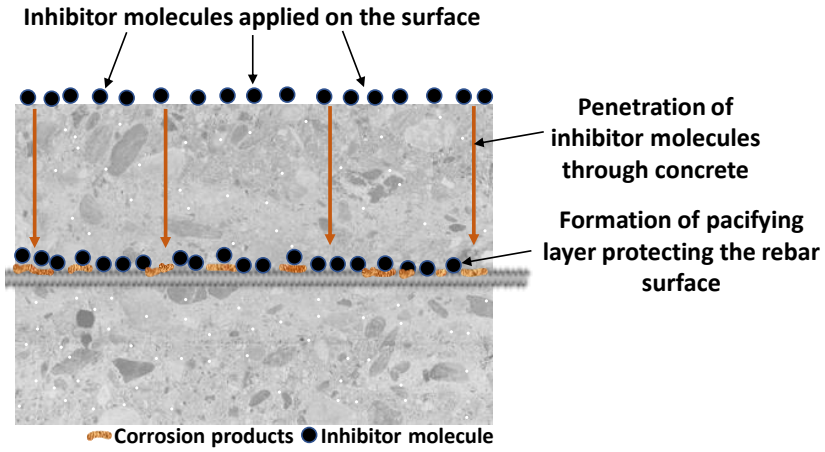

Figure 5.26 Mechanism of pacifying layer formation on rebar by the penetrated inhibitor molecules

When inhibitor ions were applied on the concrete surface, their molecules penetrated through the cover concrete and reached the rebar level. After reaching, the molecules interacted

with the accumulated corrosion products and also with the available free sites on the rebar surface. This led to the development of an interfacial film over the previously formed corrosion film, which can be termed as a "pacifying layer". This process has been schematically illustrated in Figure 5.26. The binding of ferrous ions by N and O hetero-atoms of *Ser* inhibitor molecules interrupted the diffusion process and hence, the i_{corr} values in treated RC specimens (PPC-Ser) was seen to reduce (as confirmed by the LPR results during laboratory investigations).

5.7.4 Results of visual inspection of extracted bars

The testing program was ended after 35 exposure cycles. The RC specimens were broke opened and rebars were extracted. Figure 5.27 shows the visual view of the rebars from PC-35, PSer-35, PPhe-35, Pasn-35 and PGln-35 specimens. The rebar extracted from PC-35 (un-treated specimen) showed severe corrosion throughout the surface area of steel (uniform corrosion). The bar was seriously damaged due to continuous carbonation and lowering of concrete pH; leading to de-passivation and subsequent accumulation of corrosion products.

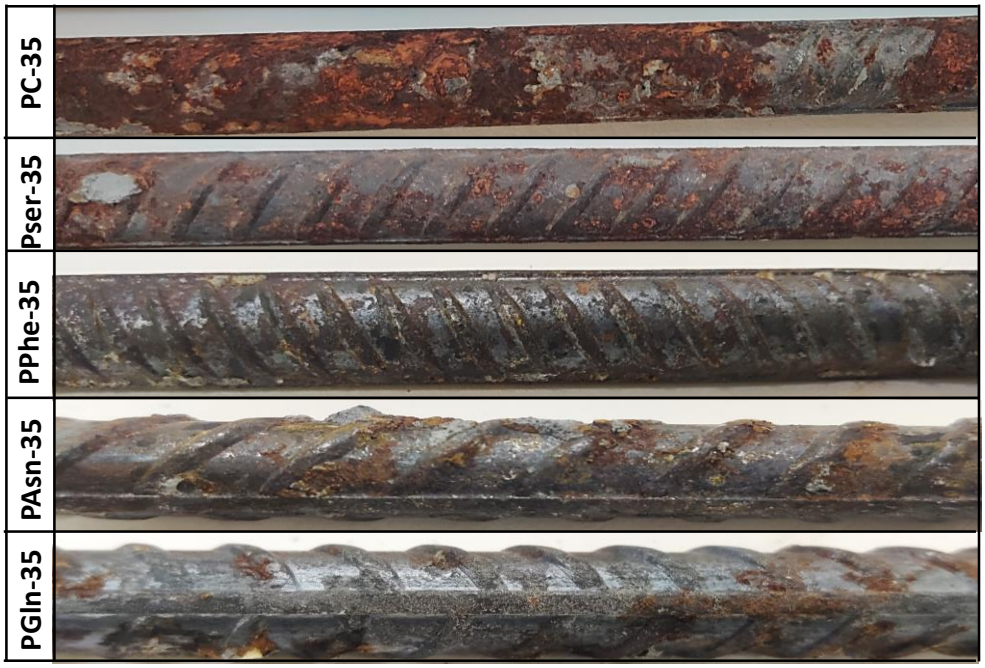

Figure 5.27 Visual images of extracted rebars from un-treated and treated RC specimens at the end of the testing program (35 exposure cycles)

On the other hand, rebar specimens extracted from RC prismatic samples treated with SACoIs exhibited moderate corrosion, which was distributed over smaller areas in comparison to the un-treated specimens. Upon closer examination, similar corrosion patterns were noted for

specimens treated with *Ser*, *Phe*, and *Asn*, while the *Gln* treated specimen displayed relatively less extensive corrosion. This observation aligns with the highest inhibition efficiency (78.84%) demonstrated by the RC specimens treated with *Gln* during Linear Polarization Resistance (LPR) testing, surpassing the performance of other amino acids.

In conclusion, it is noteworthy to mention that despite the presence of corrosion in the treated specimens after 35 exposure cycles, the extent of corrosion remained notably lower than that observed in the un-treated specimens. This highlights the potential utility of SACoIs in enhancing the longevity of RC structures susceptible to carbonation-induced corrosion.

5.8 CLOSING REMARKS

In the present chapter, the amino acids that successfully reduced the rates of carbonation-induced corrosion during Level 1 of testing were applied on concrete. Their capacity to percolate through concrete and their effect on the carbonation progression was assessed initially. The compounds that percolated through the concrete cover were then applied RC prisms to assess their inhibition capacity in controlling the rate of on-going corrosion (as repair strategy). LPR and EIS test were conducted periodically on the RC prisms for assessing the rebar condition during the testing period.

Reinforced PPC concrete showed active signs of corrosion after 20 exposure cycles and hence, the amino acids, Serine (*Ser*), Phenylalanine (*Phe*), Asparagine (*Asn*) and Glutamine (*Gln*) were applied after the 20 cycles. The compounds reached the rebar surface and developed a pacifying layer at the steel-concrete interface, as a result of interaction between the Fe ions and/or accumulated corrosion products with the negatively charged amino acids' ions. This pacifying layer reduced the Fe dissolution process and hence, resulted in reduced corrosion rates and increased resistance against ion transfer post the SACoI application. Comparatively, all the amino acids efficiently reduced the rate of carbonation-induced corrosion. An inhibition efficiency of 73.07%, 69.23% 76.92% and 78.84% was recorded for *Ser, Phe, Asn* and *Gln*, respectively. Amide-based amino acids have the highest inhibition capacity in reducing the rate of on-going carbonation-induced corrosion in fly-ash blended RC.

CHAPTER 6 : SITE APPLICATION OF THE PROPOSED SYSTEM

6.1 GENERAL

The major aim of the present work was to assess the corrosion inhibition efficiency of amino acids as surface applied corrosion inhibitors (SACoI) for the protection of rebar embedded in portland pozzolana cement (PPC) concrete. In the previous chapters, this was achieved by conducting systematic laboratory investigations. A three-level testing program involving pore solution study, migration study and corrosion monitoring of reinforced concrete (RC) specimen with eight amino acids as SACoI was executed. The test results revealed that Serine (*Ser*), Phenylalanine (*Phe*), Asparagine (A*sn*) and Glutamine (*Gln*) successfully reduced the rate of on-going corrosion of rebar embedded in PPC concrete subjected to carbonation-induced corrosion. The compounds showed >70% corrosion inhibition efficiency. Hence, it can be said that *Ser, Phe, Asn* and *Gln* can be used as SACoI for the repair of RC elements undergoing carbonation-induced corrosion.

To corroborate the findings of this research, a practical test was undertaken on-site, involving the application of amino acids to repair a corroding reinforced concrete (RC) slab on a small scale. Hence, the current chapter is focussed on presenting the tests performed and the results obtained when amino acid was used for the repair of RC slab.

6.2 BRIEF DESCRIPTION OF THE CASE STUDY: Structure, Methodology and Material System

To test the corrosion inhibition efficiency of amino acids in real-time conditions, a deteriorating RC slab was identified at the Thapar Institute of Engineering and Technology, Patiala, Punjab, India. It was an un-sheltered cantilever slab with longitudinal and lateral reinforcement bars of 12mm diameter (12mm-ϕ). The actual picture of the deteriorated slab is shown in Fig. 6.1a, while, the schematic side-view and top-view of the slab is shown in Fig. 6.1b and c, respectively.

To repair, restore or rehabilitate a corroding RC structure/element, it is important that the true causes of deterioration are identified. To design an effective repair strategy and identify the underlying cause of deterioration, the current condition of the damaged slab was monitored through visual examination, followed by partially destructive and destructive testing. After analysing the test results obtained, a repair strategy was designed and implemented. Fig. 6.2 briefly

describes the step-wise methodology adopted for on-site repair and evaluation of RC slab. The following section discusses the methodology adopted and the material system used for on-site investigation in detail.

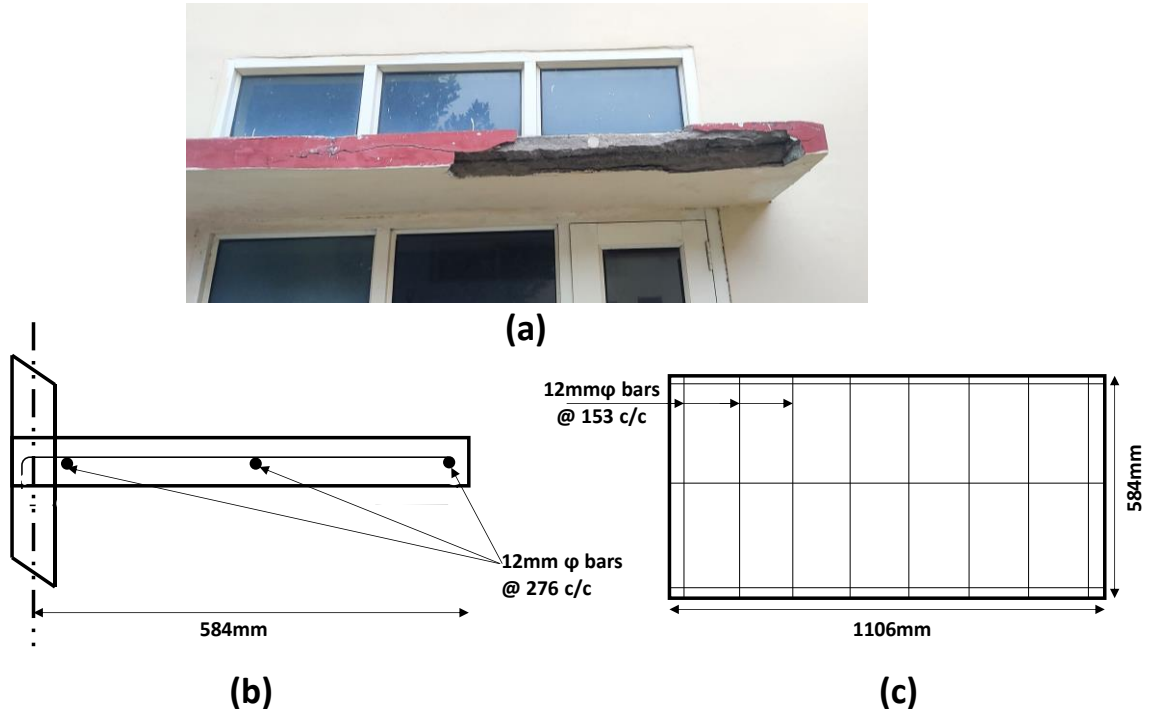

Figure 6.1(a) Actual image; (b) Side view; (c) Top-view of the RC slab to be repaired

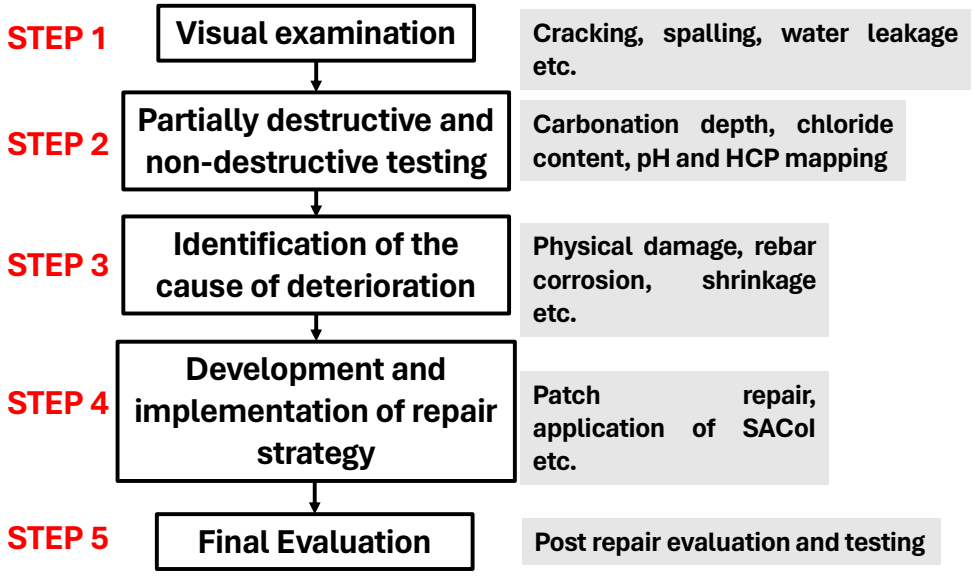

Figure 6.2 Methodology adopted for on-site repair of RC slab

6.2.1 STEP 1: 'Visual Examination'

Visual inspection offers valuable insights into the structure's integrity. These observations can pertain to craftsmanship, structural functionality, and material degradation. It's imperative for engineers to distinguish between various types of cracks that may manifest. Surface cracks and concrete spalling often signify material deterioration, and analysing the crack patterns can provide information about the underlying causes. However, confirming the root cause typically requires both on-site and laboratory testing. The most common cause behind structural damage includes rebar corrosion, primarily due to insufficient concrete cover, high chloride levels or prolonged exposure to carbonation. Rebar corrosion is typically evident through cracks running along the bars, possibly accompanied by rust stains. Sulfate attack may produce an irregular crack pattern and leave a white residue on the surface; while, alkali–aggregate reactions (while not always) can lead to a star-shaped crack pattern *(Bungey, J.H.; Millard, S.G.; Grantham, 2006).*

Therefore, in the current study, careful visual examination was carried out and the observations were noted. No material system was required for Step 1 of investigation.

6.2.2 STEP 2: 'Non-Destructive and Partially Destructive Testing'

A non-destructive test and various partially destructive tests were carried out in order to confirm the root cause of corrosion. Detailed information about the tests conducted and the material system required are explained below.

6.2.2.1 Non-Destructive Test

Non-destructive test (NDT) was conducted to assess condition of the rebar embedded in concrete. The details of the test and standards followed for result interpretation are mentioned below.

Half-cell potential (HCP) mapping: HCP mapping is a method that is widely adopted for on-site investigations where rebar corrosion is susceptible. The technique involves the measurement of potential of embedded rebar relative to a reference half-cell placed on the concrete surface. Generally, it is essential to break away the concrete cover and create an electrical connection with the underlying rebars; but in the current study, the rebar was exposed and hence, connection was made by welding a self-tapping screw. Prior to this connection, electrical connectivity between the rebar mesh was ensured. The schematic and real-time picture of the conductance of HCP survey is

shown in Figure 6.3a and b, respectively. The readings were taken with the help of a high impedance multimeter at the intersection of the rebars as per the reinforcement detailing.

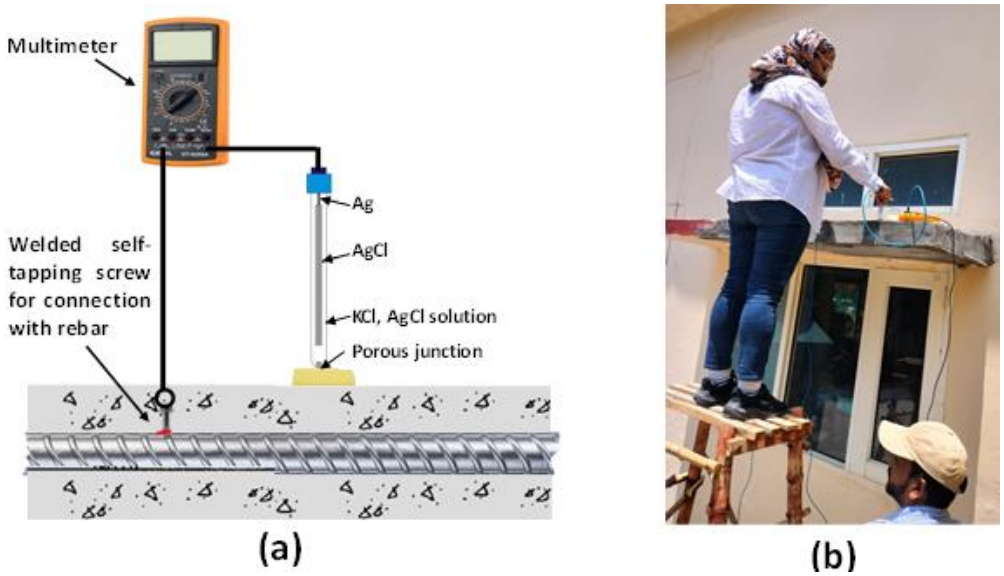

Figure 6.3(a) Schematic; (b) Real time picture of rebar potential measurement

For conducting the HCP survey, initial grid was marked on the top surface of the slab and is shown in Figure 6.4. Before initiating the test, pre-wetting of the testing surface was done by using methods explained in ASTM C876 *(ASTM International, 2015)*. For HCP, conducting sponge wetted with soap solution was placed on the surface of the RC slab to ensure proper electrical contact of embedded rebar with reference electrode. The measurements were made by placing the reference electrode at the intersection of the grids. Silver/silver chloride (Ag/AgCl/0.5M KCl) reference electrode was used in the present study. The readings so obtained were converted to saturated calomel electrode equivalent *(ASTM G3-14, 2012)*. Thereafter, iso-potential contour maps were prepared.

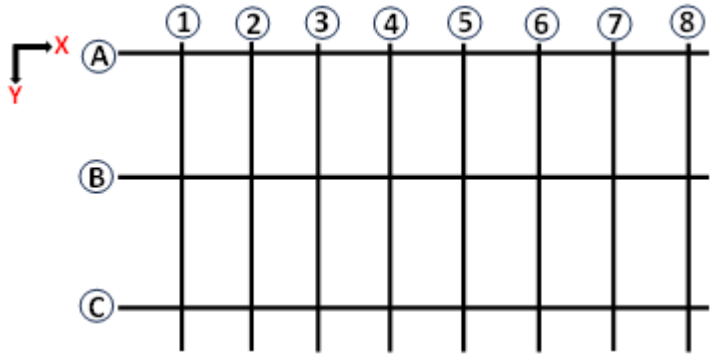

Figure 6.4 Grid marked on the top surface of the RC slab for HCP survey

6.2.2.2 Destructive Tests

Once the probability of corrosion was confirmed from the NDT tests, destructive tests were conducted in order to chemically analyze the hardened concrete and get information about the chloride content, carbonation depth and pH of the concrete. The tests were undertaken on concrete samples that were taken from three different locations of the slab in order to incorporate variability in concrete properties. The samples collected were in the form of single concrete pieces and free from rebar. Further, while sample collection, the first 2 mm of the drilled material was rejected as it is un-representative of bulk concrete (to avoid the effect of any coating or paint on concrete surface during chemical analysis). The concrete pieces were then converted into powder form and following tests were conducted.

Determination of chloride content: Volumetric titration was done to calculate chloride concentration as per IS code 3025 (Part 32) – 1988 *(IS: 3025 (Part 32), 2003)*. Approx. 2 grams of concrete sample was tested using titration and chloride content was determined. Three titration trials were done and the average is taken as chloride content.

The sample was mixed with 5ml of nitric acid in 15ml of distilled water and heated for 20 minutes. After cooling down, it was filtered using Whatman filter paper No. 1 and the filtrate was titrated using 0.04 M $AgNO_3$ (silver nitrate) as titrant and potassium chromate (yellow coloured) as the colour indicator. 3-4 drops of colour indicator were added to 10 ml of the filtrate and solution was titrated with the titrant until the yellow colour changes to reddish brown. Figure 6.5 shows the initial and final colour of the concrete sample during titration process, respectively. The determination of chloride content was done as per equation 6.1 given below.

$$Cl(\frac{mg}{L}) = \frac{0.04(V_2 - V_1)35450}{V_3} \quad \ldots(6.1)$$

where, 0.04 is the concentration of $AgNO_3$ (M), V_1 & V_2 are the initial and final volume of $AgNO_3$ (ml), V_3 is the volume of the concrete sample (ml) and 35450 is the molecular weight of chlorine (mg). The value of chloride content obtained from the above equation was then converted to percentage of chloride w.r.t. the cement content in concrete.

Carbonation depth measurement: Measuring carbonation depth in RC element during on-site investigations is essential for assessing structural integrity, corrosion risk, and maintenance

planning. Carbonation can weaken the concrete structure over time. It reduces the alkalinity of concrete, which is essential for the passivation of rebar. As carbonation progresses, the concrete becomes less effective at protecting the embedded steel from corrosion. In the present study, the carbonation depth was measured using phenolphthalein indicator test. The procedure of the test was the same as that followed during the laboratory investigations (given in Chapter 5 Section 5.6.2).

Determination of pH: Approx. 2 grams of concrete sample was taken and added to 15ml of distilled water. The solution was slowly heated for nearly 5 minutes. After cooling down, it was filtered using Whatman filter paper No. 1 and pH of the filtrate was then measured using a pH meter. This test acts as a validation for concrete carbonation as carbonated concrete demonstrates a pH<10 (non-carbonated concrete, pH = 12.5 to 13.5).

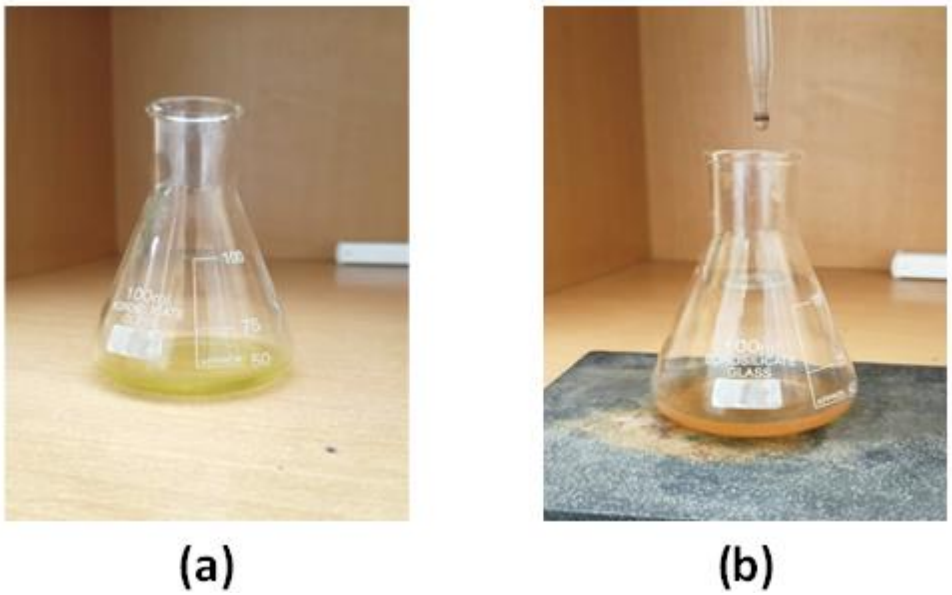

Figure 6.5 Colour of the concrete sample (a) just after adding potassium chromate; (b) at the end-point of titration

6.2.3 STEP 3, 4 and 5: 'Identification of the cause of corrosion', 'Design and implementation of the repair strategy' and 'Final evaluation'

The results obtained from Step 1 and 2 were analyzed and the cause of corrosion was identified. Thereafter, a repair strategy was designed and implemented. For final evaluation of the RC slab HCP mapping was done and iso-potential contour map was prepared. The contour map prepared in Step 2 and in Step 5 are then compared to assess the efficiency of the repair strategy with SACoI.

The result analysis of Step 1 and 2 and subsequent discussion of Step 3, 4 and 5 is done in the upcoming section.

6.3 OBSERVATIONS, RESULTS AND DISCUSSIONS

6.3.1 Observations from STEP 1: Visual examination

Figure 6.6 shows the picture of the RC slab with exposed longitudinal rebar along with spalled and delaminated concrete. The exposed rebar was severely corroded as seen by the accumulated corrosion products and reduced cross-section at few regions. Horizontal cracks were also seen at the edge of the slab. From the visual inspection, it can be stated that the possible cause of spalling, delamination and cracking in concrete is corrosion of the embedded bars. Accumulation of corrosion products on the rebars increased its volume and caused the generation of expansive stresses in concrete.

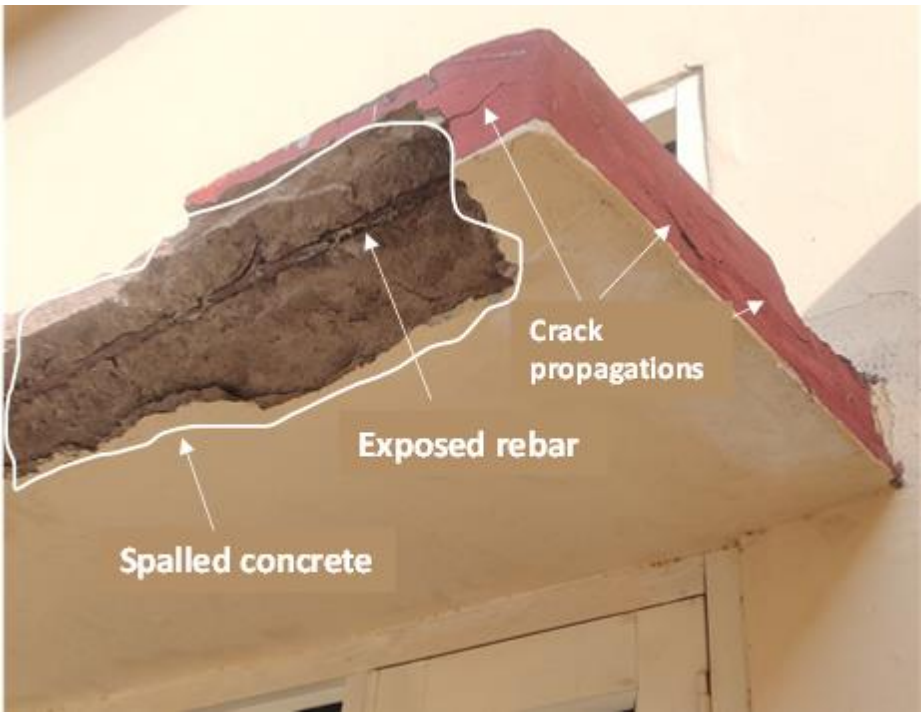

Figure 6.6 Observations from visual inspection of RC slab to be repaired

6.3.2 Results from STEP 2: 'Partially Destructive and Non-Destructive Testing'

In Step 2, HCP mapping of the rebar was done to monitor steel/concrete potentials; alongside chloride content determination, carbonation depth and pH measurement of concrete was also determined. The results of each test are discussed hereunder.

HCP contour mapping: Rebars were located, and grid was marked before conducting the HCP test (grid shown in Figure 6.4). The HCP values, before initiating any sort of treatment process is presented through a contour map, shown in Figure 6.7. The legend displays variation in the colour as per the increasing HCP values (light to dark: increasing severity of corrosion; black being most severe). The areas displaying most severe corrosion are the edges of the slab. This is due to the exposure of rebar in the x-direction which drastically increased its steel/concrete potential and also, due to spalling, delamination and cracking of concrete which permitted easy access to moisture ingress in both, x and y-directions. According to ASTM C 876-91 *(ASTM C876-22b, n.d.)* the corrosion probability is 'low' for HCP values > −125 mV_{SCE}; 'intermediate' for HCP values between −125 mV_{SCE} to −275 mV_{SCE}; and is 'high' for potential values < −276 mV_{SCE}. The HCP values in the current study lied in the range of -307 to -460 mV_{SCE}; clearly indicating 'high' risk of corrosion. The results imply that corrosion of the embedded bars was the major cause of deterioration of the RC slab.

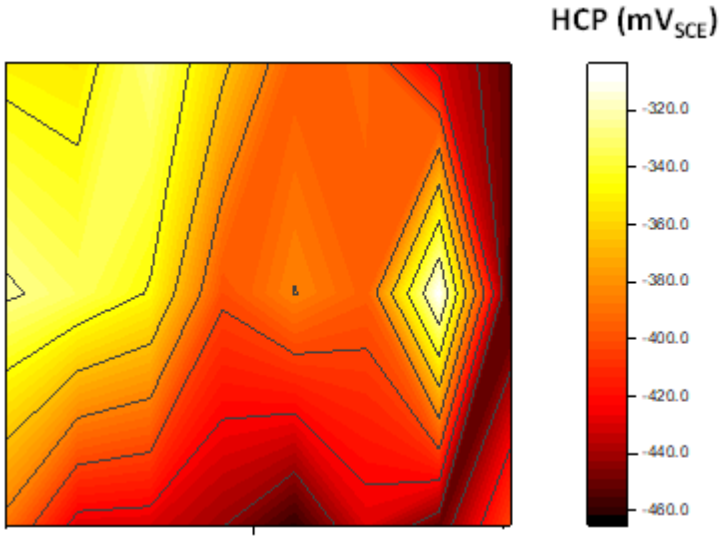

Figure 6.7 Iso-potential HCP contour map of RC slab before repair treatment

Chloride content, carbonation depth and pH: To identify the cause of corrosion, carbonation depth and chloride content were measured. For the measurement of carbonation depth, phenolphthalein solution was sprayed on the slab and it was observed that the concrete remained colourless; indicating complete carbonation of the concrete slab. The chloride content in concrete was measured as 0.12% by weight of cement which is below the threshold value (0.4%) of chloride required to cause chloride-induced corrosion in concrete *(Angst et al., 2009; Chalhoub et al., 2020)*; eradicating chloride as the possible cause of corrosion here. To further validate carbonation

of concrete, pH of the concrete was also measured as 8.72. The pH of sound concrete lies in the range of 12.5-13.5 due to its alkaline nature. Lowering of the pH from this value is a clear sign of carbonation of concrete. Thus, it can be stated that the rebars in RC slab were affected by carbonation-induced corrosion.

6.3.3 Result of STEP 3: 'Identification of the cause of deterioration'

As clearly observed during the observations of Step 1, the major reason for the deterioration of the RC slab was corrosion of embedded rebars. Alongside, the cause of corrosion, as identified from Step 2, was the exposure of slab to continuous carbonation.

6.3.4 Results of STEP 4: 'Design and implementation of repair strategy'

As the RC slab was affected by prolonged carbonation exposure and the rebars were corroded, the application of SACoI was adopted as a repair strategy. Out of the four amino acids that performed efficiently during the laboratory investigations, *Ser* was chosen to be applied as SACoI on the RC slab. The reason of choice (apart from the compound exhibiting 73% inhibition efficiency during LPR testing in laboratory) was that *Ser* does not have any surface accumulation effect on RC which allows easy percolation of SACoI. Also, the compound displayed highest percolation capacity as compared to the other tested compounds.

Before the application of SACoI, continuity of the rebars was checked by using the multimeter. Further, two self-tapping screws were welded at two different rebars for continuous monitoring of the repair system (two connections were made for safe side; monitoring was done from one only). The exposed area and that affected by cracking was then patch repaired with mortar (1:3 = cement: fine aggregate). The cement used was ordinary portland cement (OPC) complying to IS: 8112-1989 *(Bureau of Indian Standard(BIS), 2013)* and fine aggregates used were the same as used during laboratory investigations (detailed information given in Chapter 5, Section 5.2.2). The slab was cured using gunny bags (cured twice a day using potable tap water) for a period of one week. Thereafter, *Ser* was applied in 1M concentration adopting the methodology provided in Chapter 5, section. After the SACoI application, the RC slab was covered with an oil cloth (momjama) so as to avoid any evaporation losses of the SACoI. Figure 6.8 shows the sequence of repair strategy implemented.

HCP readings were again taken just before the SACoI application, and the HCP contour map is shown in Figure 6.9. From the figure, it can be seen that the HCP values shifted towards positive values which could be attributed to the development of passive film around the rebar as a result of contact with sound mortar.

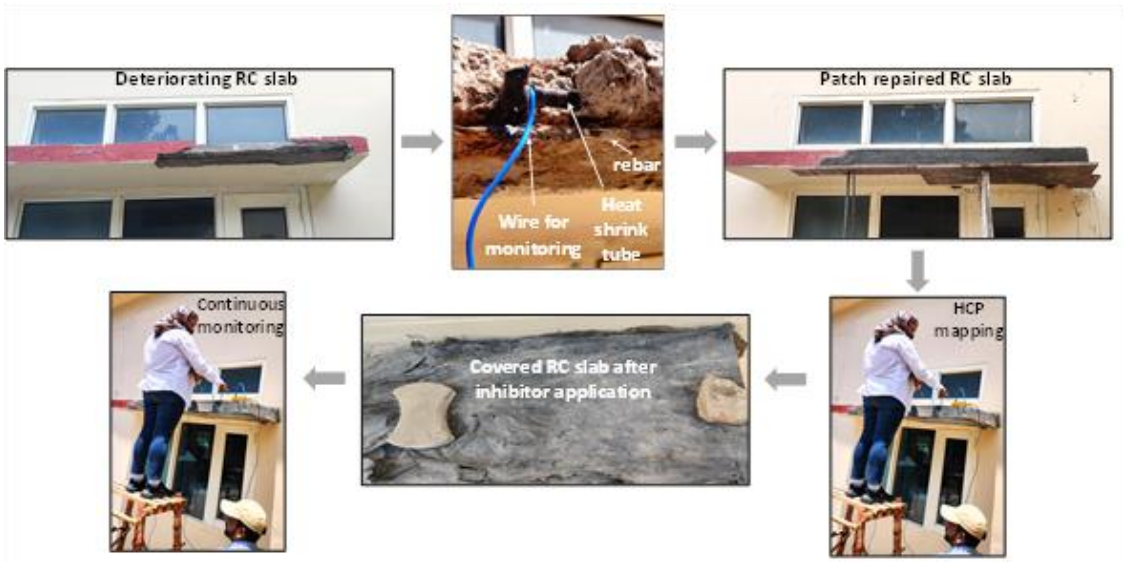

Figure 6.8 Image of the RC slab after patch repair

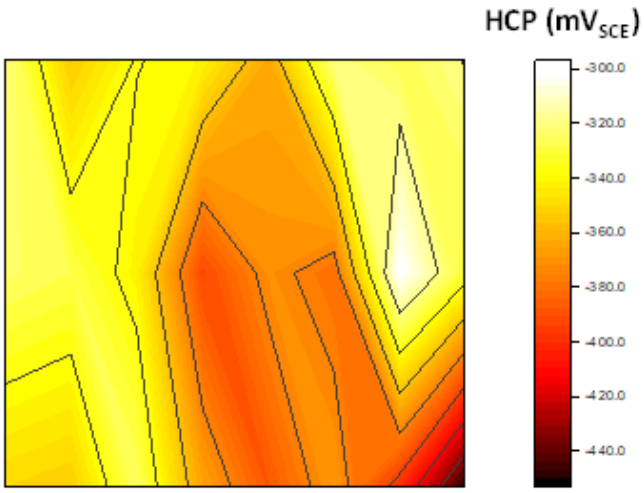

Figure 6.9 Iso-potential HCP contour map after patch repair of RC slab

6.3.5 Results of STEP 5: 'Final evaluation'

After treating the RC slab with SACoI, HCP readings were taken biweekly. The readings were recorded till a period of two months after treatment. Figure 6.10 shows the iso-potential HCP contour map of RC slab after two months of repair.

From the figure, it can be seen that the steel/concrete potentials dropped to nobler values (- 250 mV_{SCE} to -320 mV_{SCE}) after two months of application; indicating that inhibitor has provided some protection to the rebars against corrosion. *Ser* molecules must have reacted with the corrosion products and formed a protective interfacial layer on the rebar which curbed its further corrosion.

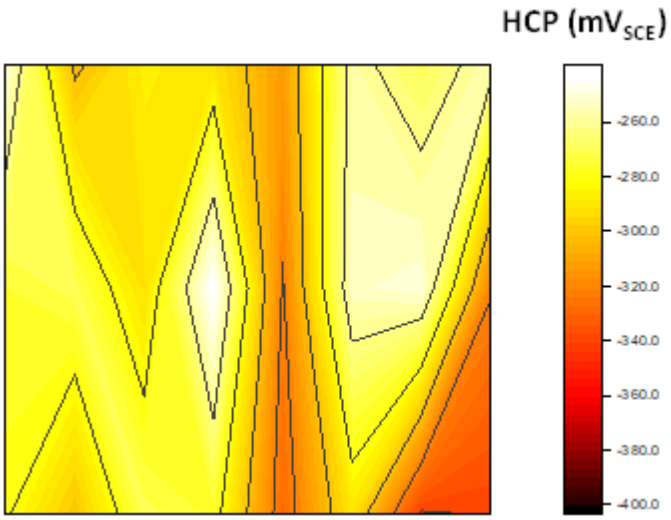

Figure 6.10 Iso-potential HCP contour map after two months of Ser application

6.4 CLOSING REMARKS

A deteriorating RC slab was identified at Thapar Institute of Engineering and Technology, Patiala and was decided to be repaired. Following a 5-step methodology, the cause of deterioration was identified, and a repair strategy was designed.

The cause of deterioration of RC slab was carbonation-induced corrosion and the repair strategy involved the application of *Ser* as SACoI. Prior to the treatment, patch repair of the deteriorated concrete was conducted. HCP contour mapping was done before and after the treatment of the slab.

The test results indicated that *Ser* effectively shifted steel/concrete potentials towards the noble side, maintaining themselves even two months after treatment. This confirms the successful restoration of passivation in the corroding on-site RC slab through SACoI application.

CHAPTER 7 : CONCLUSIONS AND FUTURE SCOPE

7.1 GENERAL

The aim of this thesis was to investigate the efficiency of amino acids (100 % ecologically safe organic compounds) as surface applied corrosion inhibitors (SACoI) in inhibiting the on-going carbonation-induced corrosion. The study was conducted on fly-ash blended cement (portland pozzolana cement: PPC) concrete; as it is widely used but has low resistance against carbonation-induced corrosion. For achieving the aim, the research was systematically divided into three levels of testing. Level 1 was the pore solution testing; out of twenty, eight amino acids were selected on the basis of their chemical nature (molecular structure, presence of functional groups and aromaticity) and their solubility in alkaline media. In this (i) efficient amino acids were identified that can inhibit the carbonation-induced corrosion and (ii) inhibition mechanism of amino acids was conjectured. Next, Level 2 was the migration studies conducted on concrete. In this, the percolation ability of efficient amino acids and their effect on carbonation progression was investigated through PPC-based concrete. In Level 3, the amino acids that were able to percolate through concrete were applied on corroding reinforced concrete (RC) prisms as SACoIs and the condition of rebar was assessed. This was the ultimate test of the study where the re-passivation capability of the amino acids was investigated. Thereafter, an on-site investigation of the proposed system was conducted on a corroding RC slab. Based on the test results at various levels of testing and the on-site investigation, following conclusions are drawn:

7.2 PERFOMANCE OF STEEL IN SIMULATED PORE SOLUTION

During the pore solution testing, the performance of eight amino acids was explored. The compounds were categorized as Set 1 (polar with no charge): Serine (*Ser*) & Cysteine (*Cys*), Set 2 (non-polar): Phenylalanine (*Phe*) & Tryptophan (*Trp*), Set 3 (polar with negative charge): Aspartic Acid (*Asp*) & Glutamic Acid (*Glu*) and Set 4 (polar with no charge): Asparagine (*Asn*) & Glutamine (*Gln*). The conclusions are:

1. The tests conducted showed that amino acids belonging to categories: “polar with no charge” and “non-polar” can be successfully used as eco-friendly corrosion inhibitors for carbonated concrete environment; while, amino acids that belong to the category of “polar with negative charge” are seen to be in-effective. Their addition to the carbonated concrete

media lowers the pH value of the solution creating corrosive conditions for the rebar. Therefore, six out of eight amino acids efficiently reduced the corrosion rate (*Ser, Cys, Phe, Trp, Asn* and *Gln*). All the six compounds act as anodic type inhibitors and are seen to exhibit >85% inhibition efficiency.

2. The inhibition by efficient amino acids is associated with their adsorption on rebar surface, following physical as well as chemical interactions. Amino acids attain negative charge when admixed in carbonated concrete media which get attracted towards the negatively charged metal surface ($Fe \rightarrow Fe^{2+}$ or Fe^{3+}). This leads to physical interaction between the amino acids and rebar surface. Furthermore, sharing of electrons also occurred between the amino acids and ferrous/ferric ions as amino acids possess lone pairs of electrons as well as negative charge which are shared with the empty d-orbital of Fe. This type of adsorption (physical + chemical) is referred and physiochemisorption.

3. Slight difference in the structure of a compound, even if belonging to the same category, can change the nature of the protective layer formed on the rebar surface. It can be stated that the compounds containing more electronegative atoms (in the carbon chain or heterocycle) lead to the development of thicker and more thermodynamically stable layer on rebar surface.

7.3 MIGRATION STUDIES ON AMINO ACIDS

1. Out of the six efficient amino acids, four were seen to percolate through the concrete within 15 days of application and reach till the depth of 20 mm. The compounds were, *Ser, Phe, Asn* and *Gln*. Furthermore, the percolated compounds did not interact with the constituents of concrete (bulk concrete) which was confirmed by no shift in peaks during the UV Vis spectroscopic results. No microstructure modification is caused by the application of amino acids on concrete. Therefore, it can be said that these compounds can be used as surface applied corrosion inhibitors (SACoI) on concrete. The order of percolation was: *Ser>Asn>Gln=Phe.*

2. From the carbonation analysis, it was concluded that PPC based concrete is highly susceptible to corrosion as the CO_2 front reaches the 15 mm cover in 70 days of carbonation exposure. Further, it was observed that *Ser* did not cause any surface accumulation affect

after it was applied on concrete (no reduction in CO_2 depth); while the rest of the three compounds did (reductions in CO_2 depth was noticed). *Asn* & *Gln* moderately accumulated on the surface and *Phe* accumulated highly.

7.4 RE-PASSIVATION CAPABILITY OF AMINO ACIDS

1. In carbonated concrete, the initiation of corrosion occurs in 225 days (15 exposure cycles), however, the activation took 300 days (20 exposure cycles). Therefore, it can be said that carbonation-induced corrosion in RC follows the 'Modified Tuuti Model' proposed by R.E. Melchers in which, an activation phase comes between the initiation and propagation phase of corrosion. During this activation phase, the rebar shows almost passive behaviour due to the oxygen and moisture deficiency at the steel-concrete interface. This deficiency is further attributed to the accumulation of $CaCO_3$ precipitates in the pore lining. Additionally, the uniformly developed corrosion products on the rebar surface also protects the underlying rebar surface from getting corroded during this phase. After 20 exposure cycles, the corrosion current density (i_{corr}) values shifted from passive to active state; rebars were then actively corroding.

2. The corrosion process of steel in carbonated concrete is controlled by the anodic dissolution of Fe ions and their diffusion after this oxidation reaction. The dissolution and subsequent diffusion of Fe ions took place un-interruptedly, therefore, high i_{corr} values and high rate of increase in i_{corr} was recorded.

3. The amino acids were therefore, applied onto the RC prisms after 20 exposure cycles. Application of amino acids as SACoI raise the resistance of rebar against charge transfer post-application. The compounds reach the rebar surface and develop a pacifying layer on it by interacting with the already present corrosion products and by chelating the Fe ions at the available sites (free from corrosion).

4. An inhibition efficiency of >70% was achieved with the application of amino acids as SACoI. Out of all. *Gln* and *Asn* showed the maximum efficiency of 78% which can be attributed to the presence of amide functional groups. While, *Ser* percolated in maximum concentration, the hydroxyl group has low affinity towards Fe as compared to amide functional group. *Phe* exhibited the 70% inhibition efficiency (lower than other three)

because it reached the rebar surface at least concentration. Order of efficiency being: *Gln>Asn>Ser>Phe.*

5. The rebars were seen to again start corroding after 35 exposure cycles and hence, the testing was ceased. The RC prisms were broke-opened. Despite the presence of corrosion in the treated specimens after 35 exposure cycles, the extent of corrosion remained notably lower than that observed in the un-treated specimens. This highlights the potential utility of SACoIs in enhancing the longevity of RC structures susceptible to carbonation-induced corrosion.

6. Pore solution testing and migratory test results can be employed in conjunction for the selection of organic compounds as SACoI to control corrosion induced by carbonation. The compounds that will be efficient in both, pore solution testing and migration ability tests will efficiently reduce the corrosion in RC specimens as well. The strategy is illustrated in the figure below.

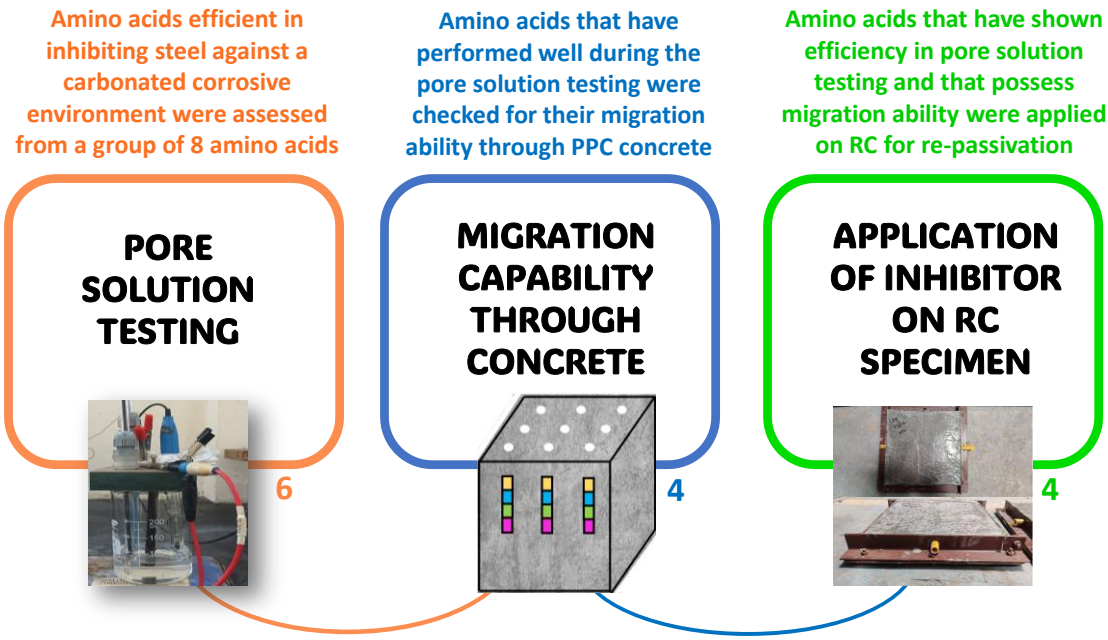

7.5 RESULTS FROM SITE APPLICATION OF THE PROPOSED SYSTEM

1. A deteriorating RC slab was identified at Thapar Institute of Engineering and Technology, Patiala and was decided to be repaired. Following a 5-step methodology, the cause of deterioration was identified and a repair strategy was designed.

2. The cause of deterioration of RC slab was carbonation-induced corrosion and the repair strategy involved the application of *Ser* as SACoI. This compound was chosen as it had no surface accumulation effect and showed 73% efficiency during laboratory investigations. Prior to the treatment, patch repair of the deteriorated concrete was conducted. Steel/concrete potential contour mapping was done before and after the treatment of the slab.

3. The test results indicated that *Ser* effectively shifted steel/concrete potentials towards the noble side, maintaining themselves even two months after treatment. This confirms the successful restoration of passivation in the corroding on-site RC slab through SACoI application.

7.6 SCOPE FOR FUTURE WORK

1. Attempts can be made to study the microstructural changes in concrete during different phases of corrosion.

2. A large-scale site-application of the amino acids as SACoI can be conducted to study their effectiveness at larger scale.

3. The effectiveness of amino acids can be studied in other concrete systems as well, such as in simultaneous presence of chlorides and carbon dioxide. In addition, their effectiveness can also be studied when admixed in concrete during casting.

REFERENCES

109, G. (2011). Standard Test Method for Determining Effects of Chemical Admixtures on Corrosion of Embedded Steel Reinforcement in Concrete Exposed to. 07(Reapproved 2013), 3–8. https://doi.org/10.1520/G0109-07R13.2

8044-2020, I. (2020). Corrosion of metals and alloys-Vocabulary Corrosion, ISO 8044:2020. International Organization for Standardization, 2020, 12. https://standards.iteh.ai/catalog/standards/sist/df5c915c-e6ff-4cfc-b323-

Aguiar, J. B., & Júnior, C. (2013). Carbonation of surface protected concrete. Construction and Building Materials, 49, 478–483. https://doi.org/10.1016/j.conbuildmat.2013.08.058

Ahmad, S. (2003). Reinforcement corrosion in concrete structures, its monitoring and service life prediction - A review. Cement and Concrete Composites, 25(4-5 SPEC), 459–471. https://doi.org/10.1016/S0958-9465(02)00086-0

Alonso, C., & Andrade, C. (1988). Corrosion of steel reinforcement in carbonated mortar containing chlorides. Advances in Cement Research, 1(3), 155–163. https://doi.org/10.1680/1988.1.3.155

Alonso, C., Andrade, C., Argiz, C., & Malric, B. (1996). Na2PO3F as inhibitor of corroding reinforcement in carbonated concrete. Cement and Concrete Research, 26(3), 405–415. https://doi.org/10.1016/S0008-8846(96)85028-9

Angst, U., Elsener, B., Larsen, C. K., & Vennesland, Ø. (2009). Critical chloride content in reinforced concrete - A review. Cement and Concrete Research, 39(12), 1122–1138. https://doi.org/10.1016/j.cemconres.2009.08.006

Angulo Ramirez, D. E., Meira, G. R., Quattrone, M., & John, V. M. (2023). A review on reinforcement corrosion propagation in carbonated concrete – Influence of material and environmental characteristics. Cement and Concrete Composites, 140(April), 105085. https://doi.org/10.1016/j.cemconcomp.2023.105085

Ann, K. Y., Jung, H. S., Kim, H. S., Kim, S. S., & Moon, H. Y. (2006). Effect of calcium nitrite-based corrosion inhibitor in preventing corrosion of embedded steel in concrete. Cement and Concrete Research, 36(3), 530–535. https://doi.org/10.1016/j.cemconres.2005.09.003

Aperador, W., Vera, R., & Carvajal, A. M. (2012). Industrial byproduct- based concrete subjected to carbonation. Electrochemical behavior of steel reinforcement. International Journal of Electrochemical Science, 7(12), 12870–12882.

Arias, J. M., Tuttolomondo, M. E., Díaz, S. B., & Altabef, A. Ben. (2015). FTIR and Raman analysis of l -cysteine ethyl ester HCl interaction with dipalmitoylphosphatidylcholine in anhydrous and hydrated states. Journal of Raman Spectroscopy, 46(4), 369–376. https://doi.org/10.1002/jrs.4659

Artemenko, A., Shchukarev, A., Štenclová, P., Wagberg, T., Segervald, J., Jia, X., & Kromka, A. (2021). Reference XPS spectra of amino acids. IOP Conference Series: Materials Science and Engineering, 1050(1). https://doi.org/10.1088/1757-899X/1050/1/012001

Ashassi-Sorkhabi, H., Majidi, M. R., & Seyyedi, K. (2004). Investigation of inhibition effect of some amino acids against steel corrosion in HCl solution. Applied Surface Science, 225(1–4), 176–185. https://doi.org/10.1016/j.apsusc.2003.10.007

ASTM C876-22b. (n.d.). Standard Test Method for Corrosion Potentials of Uncoated Reinforcing Steel in Concrete. https://doi.org/10.1520/C0876-22B.2

ASTM G3-14. (2012). Standard Practice for Conventions Applicable to Electrochemical Measurements. ASTM Standards, i(Reapproved 2010), 1–9. https://doi.org/10.1520/G0003-14R19.2

ASTM International. (2015). Standard test method for corrosion potentials of uncoated reinforcing steel in concrete. ASTM C876 - 15. G01.14,. ASTM International, 1–8. https://doi.org/10.1520/C0876-15.2

Bai, L., Feng, L. J., Wang, H. Y., Lu, Y. Bin, Lei, X. W., & Bai, F. L. (2015). Comparison of the synergistic effect of counterions on the inhibition of mild steel corrosion in acid solution:

Electrochemical, gravimetric and thermodynamic studies. RSC Advances, 5(6), 4716–4726. https://doi.org/10.1039/c4ra12286k

Berdimurodov, E., Kholikov, A., Akbarov, K., Guo, L., Kaya, S., Katin, K. P., Verma, D. K., Rbaa, M., Dagdag, O., & Haldhar, R. (2022). Novel gossypol–indole modification as a green corrosion inhibitor for low–carbon steel in aggressive alkaline–saline solution. Colloids and Surfaces A: Physicochemical and Engineering Aspects, 637(December 2021). https://doi.org/10.1016/j.colsurfa.2021.128207

Berke, N. S., & Hicks, M. C. (2004). Predicting long-term durability of steel reinforced concrete with calcium nitrite corrosion inhibitor. Cement and Concrete Composites, 26(3), 191–198. https://doi.org/10.1016/S0958-9465(03)00038-6

Bertolini, L., Elsener, B., Pedeferri, M., & Polder, R. (2004). Corrosion of Steel in Concrete: Prevention, Diagnosis, Repair. Wiley-VCH.

BIS:1489 (Part 1). (1991). Portland-pozzolana cement-specification. Bureau of Indian Standard (BIS), New Delhi,India.

BIS. (2019). IS 10262:2019, Indian standard, Concrete mix Proportioning – Guidelines (Second Revision). -. Bis, January. https://www.google.com/search?q=IS+10262%3A2019%2C+Indian+standard%2C+Concrete+mix+Proportioning+–+Guidelines+(Second+Revision).&rlz=1C1CHBF_enIN984IN984&oq=IS+10262%3A2019%2C+Indian+standard%2C+Concrete+mix+Proportioning+–+Guidelines+(Second+Revision).&a

Bisschop, J. (2016). Forschungsbericht Modelling the corrosion. February.

Bjørge, R., Gawel, K., Chavez Panduro, E. A., & Torsæter, M. (2019). Carbonation of silica cement at high-temperature well conditions. International Journal of Greenhouse Gas Control, 82(January), 261–268. https://doi.org/10.1016/j.ijggc.2019.01.011

Blajiev, O., & Hubin, A. (2004). Inhibition of copper corrosion in chloride solutions by amino-mercapto-thiadiazol and methyl-mercapto-thiadiazol: An impedance spectroscopy and a

quantum-chemical investigation. Electrochimica Acta, 49(17–18), 2761–2770. https://doi.org/10.1016/j.electacta.2004.01.037

Bogas, J. A., Real, S., & Ferrer, B. (2016). Biphasic carbonation behaviour of structural lightweight aggregate concrete produced with different types of binder. Cement and Concrete Composites, 71, 110–121. https://doi.org/10.1016/j.cemconcomp.2016.05.006

Bolzoni, F., Brenna, A., Fumagalli, G., Goidanich, S., Lazzari, L., Ormellese, M., & Pedeferri, M. (2014). Experiences on corrosion inhibitors for reinforced concrete. International Journal of Corrosion and Scale Inhibition, 3(4), 254–278. https://doi.org/10.17675/2305-6894-2014-3-4-254-278

Bolzoni, F., Goidanich, S., Lazzari, L., & Ormellese, M. (2006). Corrosion inhibitors in reinforced concrete structures Part 2 - Repair system. Corrosion Engineering Science and Technology, 41(3), 212–220. https://doi.org/10.1179/174327806X111234

Broomfield, J. P. (2006). Corrosion of Steel in Concrete: Understanding, Investigation and Repair, Second Edition (2nd ed.). CRC Press. https://doi.org/https://doi.org/10.1201/9781482265491

Bungey, J.H.; Millard, S.G.; Grantham, M. G. (2006). Testing of Concrete in Structures (4th editio). Taylor & Francis.

Bureau of Indian Standard(BIS). (2013). IS: 8112 – 1989, Specification for 43 grade Ordinary Portland Cement. Bureau of Indian Standards,New Delhi, 17.

Cabrini, M., Fontana, F., Lorenzi, S., Pastore, T., & Pellegrini, S. (2015). Effect of Organic Inhibitors on Chloride Corrosion of Steel Rebars in Alkaline Pore Solution. Journal of Chemistry, 2015. https://doi.org/10.1155/2015/521507

Cañón, J., & Teplyakov, A. V. (2021). XPS characterization of cobalt impregnated SiO2 and γ-Al2O3. Surface and Interface Analysis, 53(5), 475–481. https://doi.org/10.1002/sia.6935

Cao, Y., Gehlen, C., Angst, U., Wang, L., Wang, Z., & Yao, Y. (2019). Critical chloride content in reinforced concrete — An updated review considering Chinese experience. Cement

and Concrete Research, 117(December 2018), 58–68. https://doi.org/10.1016/j.cemconres.2018.11.020

Chalhoub, C., François, R., & Carcasses, M. (2020). Critical chloride threshold values as a function of cement type and steel surface condition. Cement and Concrete Research, 134(April), 106086. https://doi.org/10.1016/j.cemconres.2020.106086

Chauhan, D. S., Quraishi, M. A., Srivastava, V., Haque, J., & ibrahimi, B. El. (2021). Virgin and chemically functionalized amino acids as green corrosion inhibitors: Influence of molecular structure through experimental and in silico studies. Journal of Molecular Structure, 1226, 129259. https://doi.org/10.1016/j.molstruc.2020.129259

Chaussadent, T., Nobel-Pujol, V., Farcas, F., Mabille, I., & Fiaud, C. (2006). Effectiveness conditions of sodium monofluorophosphate as a corrosion inhibitor for concrete reinforcements. Cement and Concrete Research, 36(3), 556–561. https://doi.org/10.1016/j.cemconres.2005.09.006

Chigondo, M., & Chigondo, F. (2016). Recent Natural Corrosion Inhibitors for Mild Steel: An Overview. Journal of Chemistry, 2016. https://doi.org/10.1155/2016/6208937

Corrêa, S., Lacerda, L. C. T., Pires, M. D. S., Rocha, M. V. J., Nogueira, F. G. E., Da Silva, A. C., Pereira, M. C., De Brito, A. D. B., Da Cunha, E. F. F., & Ramalho, T. C. (2016). Synthesis, Structural Characterization, and Thermal Properties of the Poly(methylmethacrylate)/δ-FeOOH Hybrid Material: An Experimental and Theoretical Study. Journal of Nanomaterials, 2016. https://doi.org/10.1155/2016/2462135

Cui, D., Sun, W., & Banthia, N. (2018). Use of tomography to understand the influence of preconditioning on carbonation tests in cement-based materials. Cement and Concrete Composites, 88, 52–63. https://doi.org/10.1016/j.cemconcomp.2018.01.011

Dariva, C. G., & Galio, A. F. (2014). Corrosion Inhibitors - Principles Mechanisms and Applications. Developments in Corrosion Protection, 365–379. https://doi.org/10.5772/57255

De Schutter, G., & Luo, L. (2004). Effect of corrosion inhibiting admixtures on concrete properties. Construction and Building Materials, 18(7), 483–489. https://doi.org/10.1016/j.conbuildmat.2004.04.001

Dhanya, B. S., Rathnarajan, S., Santhanam, M., Pillai, R. G., & Gettu, R. (2019). Carbonation and its effect on microstructure of concrete with fly ASH and ground granulated blast furnace slag. Indian Concrete Journal, 93(4), 10–21.

Dharmaraj, R., & Malathy, R. (2015). Performance evaluation of sodium nitrite corrosion inhibitor in self compacting concrete. Indian Journal of Science and Technology, 8(36). https://doi.org/10.17485/ijst/2015/v8i36/87647

Dhouibi, L., Triki, E., Salta, M., Rodrigues, P., & Raharinaivo, A. (2003). Studies on corrosion inhibition of steel reinforcement by phosphate and nitrite. Materials and Structures/Materiaux et Constructions, 36(262), 530–540. https://doi.org/10.1617/13893

Dong, B. Q., Qiu, Q. W., Xiang, J. Q., Huang, C. J., Xing, F., Han, N. X., & Lu, Y. Y. (2014). Electrochemical impedance measurement and modeling analysis of the carbonation behavior for cementititous materials. Construction and Building Materials, 54, 558–565. https://doi.org/10.1016/j.conbuildmat.2013.12.100

Dong, B., Qiu, Q., Gu, Z., Xiang, J., Huang, C., Fang, Y., Xing, F., & Liu, W. (2016). Characterization of carbonation behavior of fly ash blended cement materials by the electrochemical impedance spectroscopy method. Cement and Concrete Composites, 65, 118–127. https://doi.org/10.1016/j.cemconcomp.2015.10.006

Dong, B., Qiu, Q., Xiang, J., Huang, C., Xing, F., & Han, N. (2014). Study on the carbonation behavior of cement mortar by electrochemical impedance spectroscopy. Materials, 7(1), 218–231. https://doi.org/10.3390/ma7010218

Dong, Z. H., Shi, W., Zhang, G. A., & Guo, X. P. (2011). The role of inhibitors on the repassivation of pitting corrosion of carbon steel in synthetic carbonated concrete pore solution. Electrochimica Acta, 56(17), 5890–5897. https://doi.org/10.1016/j.electacta.2011.04.120

Eddy, N. O. (2010). Adsorption and inhibitive properties of ethanol extract of Garcinia kola and Cola nitida for the corrosion of mild steel in H2SO4. Pigment and Resin Technology, 39(6), 348–354. https://doi.org/10.1108/03699421011085849

Eddy, N. O. (2011). Experimental and theoretical studies on some amino acids and their potential activity as inhibitors for the corrosion of mild steel, part 2. Journal of Advanced Research, 2(1), 35–47. https://doi.org/10.1016/j.jare.2010.08.005

El-Deab, M. S. (2011). Interaction of cysteine and copper ions on the surface of iron: EIS, polarization and XPS study. Materials Chemistry and Physics, 129(1–2), 223–227. https://doi.org/10.1016/j.matchemphys.2011.03.083

Elsener, B. (2000). Migrating corrosion inhibitor blend for reinforced concrete: Part 2 - Inhibitor as repair strategy. Corrosion, 56(7), 727–732. https://doi.org/10.5006/1.3280576

Fan, C., Ge, X., Hao, J., Wu, T., Liu, R., Sui, W., Geng, J., & Zhang, M. (2023). Identification of high iron – chelating peptides with unusual antioxidant effect from sea cucumbers and the possible binding mode. Food Chemistry, 399(August 2022), 133912. https://doi.org/10.1016/j.foodchem.2022.133912

Fawzy, A., Abdallah, M., Zaafarany, I. A., Ahmed, S. A., & Althagafi, I. I. (2018). Thermodynamic, kinetic and mechanistic approach to the corrosion inhibition of carbon steel by new synthesized amino acids-based surfactants as green inhibitors in neutral and alkaline aqueous media. Journal of Molecular Liquids, 265, 276–291. https://doi.org/10.1016/j.molliq.2018.05.140

Fazal, M. A., Haseeb, A. S. M. A., & Masjuki, H. H. (2011). Effect of different corrosion inhibitors on the corrosion of cast iron in palm biodiesel. Fuel Processing Technology, 92(11), 2154–2159. https://doi.org/10.1016/j.fuproc.2011.06.012

Finšgar, M. (2013). 2-Mercaptobenzimidazole as a copper corrosion inhibitor: Part I. Long-term immersion, 3D-profilometry, and electrochemistry. Corrosion Science, 72, 82–89. https://doi.org/10.1016/j.corsci.2013.03.011

Ford, S. J., Shane, J. D., & Mason, T. O. (1998). Assignment of features in impedance spectra of the cement-paste/steel system. Cement and Concrete Research, 28(12), 1737–1751. https://doi.org/10.1016/S0008-8846(98)00156-2

Fouda, a. S., Nazeer, A. A., & Ashour, E. a. (2011). Amino acids as environmentally-friendly corrosion inhibitors for Cu10Ni alloy in sulfide-polluted salt water: Experimental and theoretical study. Udc, 52, 34.

François, R. (2021). A discussion on the order of magnitude of corrosion current density in reinforcements of concrete structures and its link with cross-section loss of reinforcement. RILEM Technical Letters, 6(2021), 158–168. https://doi.org/10.21809/rilemtechlett.2021.116

Fu, J. J., Li, S. N., Cao, L. H., Wang, Y., Yan, L. H., & Lu, L. De. (2010). L-Tryptophan as green corrosion inhibitor for low carbon steel in hydrochloric acid solution. Journal of Materials Science, 45(4), 979–986. https://doi.org/10.1007/s10853-009-4028-0

Fu, J. J., Li, S. N., Wang, Y., Cao, L. H., & Lu, L. De. (2010). Computational and electrochemical studies of some amino acid compounds as corrosion inhibitors for mild steel in hydrochloric acid solution. Journal of Materials Science, 45(22), 6255–6265. https://doi.org/10.1007/s10853-010-4720-0

Fu, J. J., Li, S. N., Wang, Y., Liu, X. D., & Lu, L. De. (2011). Computational and electrochemical studies on the inhibition of corrosion of mild steel by l-Cysteine and its derivatives. Journal of Materials Science, 46(10), 3550–3559. https://doi.org/10.1007/s10853-011-5267-4

G1-03, A. (1999). Standard Practice for Preparing, Cleaning, and Evaluating Corrosion Test Specimens. ASTM Codes and Standards.

Gaidis, J. M. (2004). Chemistry of corrosion inhibitors. Cement and Concrete Composites, 26(3), 181–189. https://doi.org/10.1016/S0958-9465(03)00037-4

Gao, D., Tai, Y., Yang, L., Zhang, Z., Liu, G., & You, P. (2023). Corrosion of Steel Fibers in Chloride-Contaminated Simulated Concrete Pore Solutions. Journal of Materials in Civil Engineering, 35(2), 1–11. https://doi.org/10.1061/(asce)mt.1943-5533.0004591

Geng, J., Liu, J., Yan, J., Ba, M., He, Z., & Li, Y. (2018). Chemical Composition of Corrosion Products of Rebar Caused by Carbonation and Chloride. International Journal of Corrosion, 2018. https://doi.org/10.1155/2018/7479383

Geng, X., Sun, Y., Li, Z., Yang, R., Zhao, Y., Guo, Y., Xu, J., Li, F., Wang, Y., Lu, S., & Qu, L. (2019). Retrosynthesis of Tunable Fluorescent Carbon Dots for Precise Long-Term Mitochondrial Tracking. Small, 15(48), 1–8. https://doi.org/10.1002/smll.201901517

Ghelichkhah, Z., Sharifi-Asl, S., Farhadi, K., Banisaied, S., Ahmadi, S., & Macdonald, D. D. (2015). L-cysteine/polydopamine nanoparticle-coatings for copper corrosion protection. Corrosion Science, 91(November), 129–139. https://doi.org/10.1016/j.corsci.2014.11.011

Gilbert, R. I. (2011). The serviceability limit states in reinforced concrete design. Procedia Engineering, 14, 385–395. https://doi.org/10.1016/j.proeng.2011.07.048

Goyal, A., Ganjian, E., Pouya, H. S., & Tyrer, M. (2021). Inhibitor efficiency of migratory corrosion inhibitors to reduce corrosion in reinforced concrete exposed to high chloride environment. Construction and Building Materials, 303(August), 124461. https://doi.org/10.1016/j.conbuildmat.2021.124461

Hamadi, L., Mansouri, S., Oulmi, K., & Kareche, A. (2018). The use of amino acids as corrosion inhibitors for metals: A review. Egyptian Journal of Petroleum, 27(4), 1157–1165. https://doi.org/10.1016/j.ejpe.2018.04.004

Heiyantuduwa, R., Alexander, M. G., & Mackechnie, J. R. (2006). Performance of a Penetrating Corrosion Inhibitor in Concrete Affected by Carbonation-Induced Corrosion. Journal of Materials in Civil Engineering, 18(6), 842–850. https://doi.org/10.1061/(asce)0899-1561(2006)18:6(842)

Herrera Hernández, H., González Díaz, F., Fajardo San Miguel, G. D. J., Velázquez Altamirano, J. C., González Morán, C. O., & Morales Hernández, J. (2019). Electrochemical Impedance Spectroscopy as a Practical Tool for Monitoring the Carbonation Process on Reinforced Concrete Structures. Arabian Journal for Science and Engineering, 44(12), 10087–10103. https://doi.org/10.1007/s13369-019-04041-z

Huang, Q., Jiang, Z., Zhang, W., Gu, X., & Dou, X. (2012). Numerical analysis of the effect of coarse aggregate distribution on concrete carbonation. Construction and Building Materials, 37, 27–35. https://doi.org/10.1016/j.conbuildmat.2012.06.074

Idczak, K., Idczak, R., & Konieczny, R. (2016). An investigation of the corrosion of polycrystalline iron by XPS, TMS and CEMS. Physica B: Condensed Matter, 491, 37–45. https://doi.org/10.1016/j.physb.2016.03.018

Inam, M. A., Khan, R., Park, D. R., Lee, Y. W., & Yeom, I. T. (2018). Removal of Sb(III) and Sb(V) by ferric chloride coagulation: Implications of Fe solubility. Water (Switzerland), 10(4), 1–13. https://doi.org/10.3390/w10040418

IS: 3025 (Part 32). (2003). IS 3025 (Part 24): Method of Sampling and Test (Physical and Chemical) for Water and Wastewater, Part 24: Sulphates (First Revision). http://www.iitk.ac.in/ce/test/IS-codes/is.3025.53.2003.pdf

IS:1786-2008. (2008). High Strength Deformed Steel Bars and Wires for Concretereinforcement— Specification. Bureau of Indian Standards, New Delhi, 1–12.

IS:383. (1970). Specification for Coarse and Fine Aggregates From Natural Sources for Concrete. Indian Standards, 1–24.

Ismail, K. M. (2007). Evaluation of cysteine as environmentally friendly corrosion inhibitor for copper in neutral and acidic chloride solutions. Electrochimica Acta, 52(28), 7811–7819. https://doi.org/10.1016/j.electacta.2007.02.053

Jamil, H. E., Shriri, A., Boulif, R., Bastos, C., Montemor, M. F., & Ferreira, M. G. S. (2004). Electrochemical behaviour of amino alcohol-based inhibitors used to control corrosion of reinforcing steel. Electrochimica Acta, 49(17–18), 2753–2760. https://doi.org/10.1016/j.electacta.2004.01.041

Jayaprakash, N., Judith Vijaya, J., John Kennedy, L., Priadharsini, K., & Palani, P. (2015). Antibacterial activity of silver nanoparticles synthesized from serine. Materials Science and Engineering C, 49(April), 316–322. https://doi.org/10.1016/j.msec.2015.01.012

Jiang, S. B., Jiang, L. H., Wang, Z. Y., Jin, M., Bai, S., Song, S., & Yan, X. (2017). Deoxyribonucleic acid as an inhibitor for chloride-induced corrosion of reinforcing steel in simulated concrete pore solutions. Construction and Building Materials, 150, 238–247. https://doi.org/10.1016/j.conbuildmat.2017.05.157

Jin, Z., Xiong, C., Zhao, T., Du, Y., Zhang, X., Li, N., Yu, Y., & Wang, P. (2022). Passivation and depassivation properties of Cr–Mo alloyed corrosion-resistant steel in simulated concrete pore solution. Cement and Concrete Composites, 126(July 2021), 104375. https://doi.org/10.1016/j.cemconcomp.2021.104375

Joseline, D., & Pillai, R. G. (2020). Enhancing service life of prestressed concrete structures by using fly ash and corrosion inhibitors. Indian Concrete Journal, 94(11), 54–67.

Justnes, H., Skocek, J., Østnor, T. A., Engelsen, C. J., & Skjølsvold, O. (2020). Microstructural changes of hydrated cement blended with fly ash upon carbonation. Cement and Concrete Research, 137(August), 106192. https://doi.org/10.1016/j.cemconres.2020.106192

Kania, H. (2023). Corrosion and Anticorrosion of Alloys/Metals: The Important Global Issue. Coatings,MDPI.

Karthick, S. P., Madhavamayandi, A., Muralidharan, S., & Saraswathy, V. (2016). Electrochemical process to improve the durability of concrete structures. Journal of Building Engineering, 7, 273–280. https://doi.org/10.1016/j.jobe.2016.07.005

Kasperek, J., Verchere, D., Jacquet, D., & Phillips, N. (1998). Analysis of the corrosion products on galvanized steels by FTIR spectroscopy. Materials Chemistry and Physics, 56(3), 205–213. https://doi.org/10.1016/S0254-0584(98)00167-9

Kaur, K., Goyal, S., Bhattacharje, B., Oh, T., Kim, J., Lee, C., & Park, S. (2017a). Electrochemical Impedance Spectroscopy to study the carbonation behavior of concrete treated with corrosion inhibitors. 14, 172–182. https://doi.org/10.3151/jact.15.738

Kaur, K., Goyal, S., Bhattacharje, B., Oh, T., Kim, J., Lee, C., & Park, S. (2017b). Electrochemical Impedance Spectroscopy to study the carbonation behavior of concrete treated

with corrosion inhibitors. Journal of Advanced Concrete Technology, 15(12), 738–748. https://doi.org/10.3151/jact.15.738

Kaur, K., Goyal, S., Bhattacharjee, B., & Kumar, M. (2016). Efficiency of migratory-Type organic corrosion inhibitors in carbonated environment. Journal of Advanced Concrete Technology, 14(9), 548–558. https://doi.org/10.3151/jact.14.548

Kaur, K., Goyal, S., Bhattacharjee, B., & Kumar, M. (2017). Electrochemical Impedance Spectroscopy to Study the Carbonation Behavior of Concrete Treated with Corrosion Inhibitors. Journal of Advanced Concrete Technology, 15(12), 738–748. https://doi.org/10.3151/jact.15.738

Khan, M. Z. H., Aziz, M. A., Hasan, M. R., & Al-Mamun, M. R. (2016). The role of drug as corrosion inhibitor for mild steel surface characterization by SEM, AFM, and FTIR. Anti-Corrosion Methods and Materials, 63(4), 308–315. https://doi.org/10.1108/ACMM-11-2015-1597

Kim, J., Park, K. T., & Kwon, T. H. (2022). Influencing Factors of Steel States in Concrete Based on Electrochemical Impedance Spectroscopic Measurements. Applied Sciences (Switzerland), 12(24). https://doi.org/10.3390/app122412611

Koch, G., Varney, J., Thompson, N., Moghissi, O., Gould, M., & Payer, J. (2016). International Measures of Prevention, Application, and Economics of Corrosion Technologies Study. February, 3.

Kogelheide, F., Kartaschew, K., Strack, M., Baldus, S., Metzler-Nolte, N., Havenith, M., Awakowicz, P., Stapelmann, K., & Lackmann, J. W. (2016). FTIR spectroscopy of cysteine as a ready-to-use method for the investigation of plasma-induced chemical modifications of macromolecules. Journal of Physics D: Applied Physics, 49(8). https://doi.org/10.1088/0022-3727/49/8/084004

Kondratova, I. L., Montes, P., & Bremner, T. W. (2003). Natural marine exposure results for reinforced concrete slabs with corrosion inhibitors. Cement and Concrete Composites, 25(4-5 SPEC), 483–490. https://doi.org/10.1016/S0958-9465(02)00088-4

Kozlica, D. K., Kokalj, A., & Milošev, I. (2021). Synergistic effect of 2-mercaptobenzimidazole and octylphosphonic acid as corrosion inhibitors for copper and aluminium – An electrochemical, XPS, FTIR and DFT study. Corrosion Science, 182. https://doi.org/10.1016/j.corsci.2020.109082

Królikowski, A., & Kuziak, J. (2011). Impedance study on calcium nitrite as a penetrating corrosion inhibitor for steel in concrete. Electrochimica Acta, 56(23), 7845–7853. https://doi.org/10.1016/j.electacta.2011.01.069

Kulakowski, M. P., Pereira, F. M., & Molin, D. C. C. D. (2009). Carbonation-induced reinforcement corrosion in silica fume concrete. Construction and Building Materials, 23(3), 1189–1195. https://doi.org/10.1016/j.conbuildmat.2008.08.005

Kumar Tiwari, A., Purnima, Goyal, S., & Luxami, V. (2023). Surface application of multifunctional compound to prevent and control combined chloride and carbonation corrosion in concrete. European Journal of Environmental and Civil Engineering, 0(0), 1–27. https://doi.org/10.1080/19648189.2023.2197484

Lagrenée, M., Mernari, B., Bouanis, M., Traisnel, M., & Bentiss, F. (2002). Study of the mechanism and inhibiting efficiency of 3,5-bis(4-methylthiophenyl)-4H-1,2,4-triazole on mild steel corrosion in acidic media. Corrosion Science, 44(3), 573–588. https://doi.org/10.1016/S0010-938X(01)00075-0

Lalitha, A., Ramesh, S., & Rajeswari, S. (2005). Surface protection of copper in acid medium by azoles and surfactants. Electrochimica Acta, 51(1), 47–55. https://doi.org/10.1016/j.electacta.2005.04.003

Lee, H. S., Saraswathy, V., Kwon, S. J., & Karthick, S. (2018). Corrosion Inhibitors for Reinforced Concrete: A Review. IntechOpen, 11, 13. https://www.intechopen.com/books/advanced-biometric-technologies/liveness-detection-in-biometrics

Leemann, A., Nygaard, P., Kaufmann, J., & Loser, R. (2015). Relation between carbonation resistance, mix design and exposure of mortar and concrete. Cement and Concrete Composites, 62, 33–43. https://doi.org/10.1016/j.cemconcomp.2015.04.020

Lengyel, J., Ončák, M., Herburger, A., Van Der Linde, C., & Beyer, M. K. (2017). Infrared spectroscopy of O- and OH- in water clusters: Evidence for fast interconversion between O- and OHOH-. Physical Chemistry Chemical Physics, 19(37), 25346–25351. https://doi.org/10.1039/c7cp04577h

Li, Q., Wang, H., Chen, Z., He, X., Liu, Y., Qiu, M., & Wang, X. (2021). Adsorption-reduction strategy of U(VI) on NZVI-supported zeolite composites via batch, visual and XPS techniques. Journal of Molecular Liquids, 339. https://doi.org/10.1016/j.molliq.2021.116719

Lin, B., & Zuo, Y. (2019). Inhibition of Q235 carbon steel by calcium lignosulfonate and sodium molybdate in carbonated concrete pore solution. Molecules, 24(3). https://doi.org/10.3390/molecules24030518

Liu, G., Zhang, Y., Ni, Z., & Huang, R. (2016). Corrosion behavior of steel submitted to chloride and sulphate ions in simulated concrete pore solution. Construction and Building Materials, 115, 1–5. https://doi.org/10.1016/j.conbuildmat.2016.03.213

Liu, Q., Liu, J., Wang, J., & Chong, Y. (2023). Corrosion inhibition effect of betaine type quaternary ammonium salt on AA2024-T3 in 0.01 mol·L−1 NaOH: Experimental and theoretical research. Journal of Molecular Structure, 1274, 134395. https://doi.org/10.1016/j.molstruc.2022.134395

Liu, R., Jiang, L., Xu, J., Xiong, C., & Song, Z. (2014). Influence of carbonation on chloride-induced reinforcement corrosion in simulated concrete pore solutions. Construction and Building Materials, 56, 16–20. https://doi.org/10.1016/j.conbuildmat.2014.01.030

Łojewski, T., Miśkowiec, P., Missori, M., Lubańska, A., Proniewicz, L. M., & Łojewska, J. (2010). FTIR and UV/vis as methods for evaluation of oxidative degradation of model paper: DFT approach for carbonyl vibrations. Carbohydrate Polymers, 82(2), 370–375. https://doi.org/10.1016/j.carbpol.2010.04.087

Lye, C. Q., Dhir, R. K., & Ghataora, G. S. (2015). Carbonation resistance of fly ash concrete. Magazine of Concrete Research, 67(21), 1150–1178. https://doi.org/10.1680/macr.15.00204

Ma, W., Wang, B., Yang, Y., & Li, J. (2021). Photoluminescent chiral carbon dots derived from glutamine. Chinese Chemical Letters, 32(12), 3916–3920. https://doi.org/10.1016/j.cclet.2021.05.021

Magdalena Osial, D. W. (2016). Organic substances as corrosion inhibitors for steel in concrete – an overview. September 2021. https://doi.org/10.17461/j.buildchem.2016.107

Maréchal, Y., & Chanzy, H. (2000). The hydrogen bond network in I(β) cellulose as observed by infrared spectrometry. Journal of Molecular Structure, 523(1–3), 183–196. https://doi.org/10.1016/S0022-2860(99)00389-0

Medagoda Arachchige, A. D. (2008). Influence of cement content on corrosion resistance. Proceedings of Institution of Civil Engineers: Construction Materials, 161(1), 31–39. https://doi.org/10.1680/coma.2008.161.1.31

Melchers, R. E. (2020). Long-term durability of marine reinforced concrete structures. Journal of Marine Science and Engineering, 8(4). https://doi.org/10.3390/JMSE8040290

Melchers, R. E., & Jeffrey, R. (2007). CORROSION SCI E NC E S E C T ION M odeling of L ong- T erm Corrosion L oss and Pitting for Chromium- B earing and Stainless Steels in Sea w ater. 2.

Mohammad Mobin, IrfanAhmad, Megha Basik, Manilal Murmu, P. B. (2020). Experimental and theoretical assessment of almond gum as an economically and environmentally viable corrosion inhibitor for mild steel in 1 M HCl. Sustainable Chemistry and Pharmacy, 18(100337). https://www.sciencedirect.com/science/article/abs/pii/S2352554120305763

Mokubung, K. E., Moloto, M. J., & Moloto, N. (2018). Low temperature synthesis of L-cysteine capped Cu2Se quantum dots. Chalcogenide Letters, 15(11), 529–533.

Monrrabal, G., Bautista, A., & Velasco, F. (2019). Use of innovative gel electrolytes for electrochemical corrosion measurements on carbon and galvanized steel surfaces. Corrosion, 75(12), 1502–1512. https://doi.org/10.5006/3309

Montemor, M. F., Cunha, M. P., Ferreira, M. G., & Simões, A. M. (2002). Corrosion behaviour of rebars in fly ash mortar exposed to carbon dioxide and chlorides. Cement and Concrete Composites, 24(1), 45–53. https://doi.org/10.1016/S0958-9465(01)00025-7

Montemor, M. F., Simões, A. M. P., & Ferreira, M. G. S. (2003). Chloride-induced corrosion on reinforcing steel: From the fundamentals to the monitoring techniques. Cement and Concrete Composites, 25(4-5 SPEC), 491–502. https://doi.org/10.1016/S0958-9465(02)00089-6

Montes, P., Bremner, T. W., & Lister, D. H. (2004). Influence of calcium nitrite inhibitor and crack width on corrosion of steel in high performance concrete subjected to a simulated marine environment. Cement and Concrete Composites, 26(3), 243–253. https://doi.org/10.1016/S0958-9465(03)00043-X

Monticelli, C., Frignani, A., Balbo, A., & Zucchi, F. (2011). Influence of two specific inhibitors on steel corrosion in a synthetic solution simulating a carbonated concrete with chlorides. Materials and Corrosion, 62(2), 178–186. https://doi.org/10.1002/maco.201005764

Morad, M. S. (2008). Corrosion inhibition of mild steel in sulfamic acid solution by S-containing amino acids. Journal of Applied Electrochemistry, 38(11), 1509–1518. https://doi.org/10.1007/s10800-008-9595-2

Morandeau, A., Thiéry, M., & Dangla, P. (2014). Investigation of the carbonation mechanism of CH and C-S-H in terms of kinetics, microstructure changes and moisture properties. Cement and Concrete Research, 56, 153–170. https://doi.org/10.1016/j.cemconres.2013.11.015

Moreno, M., Morris, W., Alvarez, M. G., & Duffó, G. S. (2004). Corrosion of reinforcing steel in simulated concrete pore solutions effect of carbonation and chloride content. Corrosion Science, 46(11), 2681–2699. https://doi.org/10.1016/j.corsci.2004.03.013

Naderi, R., Bautista, A., Velasco, F., Soleimani, M., & Pourfath, M. (2022). Green corrosion inhibition for carbon steel reinforcement in chloride-polluted simulated concrete pore solution using Urtica Dioica extract. Journal of Building Engineering, 58(May), 105055. https://doi.org/10.1016/j.jobe.2022.105055

Nahali, H., Dhouibi, L., & Idrissi, H. (2014). Effect of phosphate based inhibitor on the threshold chloride to initiate steel corrosion in saturated hydroxide solution. Construction and Building Materials, 50, 87–94. https://doi.org/10.1016/j.conbuildmat.2013.08.054

Neville, A. (1995). Chloride attack of reinforced concrete: an overview. Materials and Structures, 28(2), 63–70. https://doi.org/10.1007/BF02473172

Ngala, V. T., Page, C. L., & Page, M. M. (2003). Corrosion inhibitor systems for remedial treatment of reinforced concrete. Part 2: Sodium monofluorophosphate. Corrosion Science, 45(7), 1523–1537. https://doi.org/10.1016/S0010-938X(02)00248-2

Nie, S., Zhou, Z., Yang, F., Lan, M., Li, J., Zhang, Z., & Chen, Z. (2022). Analysis of theoretical carbon dioxide emissions from cement production: Methodology and application. Journal of Cleaner Production, 334(130270). https://www.sciencedirect.com/science/article/abs/pii/S0959652621044358

Nikolic, G., Zlatkovic, S., Cakic, M., Cakic, S., Lacnjevac, C., & Rajic, Z. (2010). Fast fourier transform IR characterization of epoxy GY systems crosslinked with aliphatic and cycloaliphatic EH polyamine adducts. Sensors, 10(1), 684–696. https://doi.org/10.3390/s100100684

Nmai, C. K. (2004). Multi-functional organic corrosion inhibitor. Cement and Concrete Composites, 26(3), 199–207. https://doi.org/10.1016/S0958-9465(03)00039-8

Noor, E. A. (2007). Temperature effects on the corrosion inhibition of mild steel in acidic solutions by aqueous extract of fenugreek leaves. International Journal of Electrochemical Science, 2(12), 996–1017.

Olivares-Xometl, O., Likhanova, N. V., Domínguez-Aguilar, M. A., Hallen, J. M., Zamudio, L. S., & Arce, E. (2006). Surface analysis of inhibitor films formed by imidazolines and amides on mild steel in an acidic environment. Applied Surface Science, 252(6), 2139–2152. https://doi.org/10.1016/j.apsusc.2005.03.178

Omoare, A., Arum, C., & Olanitori, L. M. (2022). Models for the Prediction of Service Life of Buildings – A Review. LAUTECH Journal of Civil and Environmental Studies, 9(1), 48–68. https://doi.org/10.36108/laujoces/2202.90.0160

Ormellese, M., Bolzoni, F., Lazzari, L., Brenna, A., & Pedeferri, M. (2011). Organic substances as inhibitors for chloride-induced corrosion in reinforced concrete. Materials and Corrosion, 62(2), 170–177. https://doi.org/10.1002/maco.201005763

Ormellese, M., Lazzari, L., Goidanich, S., Fumagalli, G., & Brenna, A. (2009). A study of organic substances as inhibitors for chloride-induced corrosion in concrete. Corrosion Science, 51(12), 2959–2968. https://doi.org/10.1016/j.corsci.2009.08.018

Pang, X., Zeng, H., Liu, J., Wei, S., & Zheng, Y. (2010). The Properties of Nanohydroxyapatite Materials and its Biological Effects. Materials Sciences and Applications, 01(02), 81–90. https://doi.org/10.4236/msa.2010.12015

Poursaee, A., & Hansson, C. M. (2007). Reinforcing steel passivation in mortar and pore solution. Cement and Concrete Research, 37(7), 1127–1133. https://doi.org/10.1016/j.cemconres.2007.04.005

Priya, P. V., & Rao, N. S. P. (2017). Comparative study on various methods used for corrosion protection of rebar in concrete. International Journal of Applied Research, 3(1), 426–431.

Purnima, Goyal, S., & Luxami, V. (2023). Corrosion inhibition mechanism of aromatic amino acids for steel in alkaline pore solution simulating carbonated concrete environment. Materials and Corrosion, 2023(July), 1–22. https://doi.org/10.1002/maco.202313949

Purnima, Shweta, G., & Vijay, L. (2023). Exploring the corrosion inhibition mechanism of Serine (Ser) and Cysteine (Cys) in alkaline concrete pore solution simulating carbonated environment. Construction and Building Materials, 384(April), 131433. https://doi.org/10.1016/j.conbuildmat.2023.131433

Purnima, Tiwari, A. K., Goyal, S., & Luxami, V. (2023). Developing the inhibition mechanism for amide-based amino acids in carbonated concrete environment and assessing the migration

ability in concrete. Journal of Building Engineering, 76(May), 107048. https://doi.org/10.1016/j.jobe.2023.107048

Rabehi, M., Mezghiche, B., & Guettala, S. (2013). Correlation between initial absorption of the cover concrete, the compressive strength and carbonation depth. Construction and Building Materials, 45, 123–129. https://doi.org/10.1016/j.conbuildmat.2013.03.074

Raghavendra, N. (2018). Areca Plant Extracts as a Green Corrosion Inhibitor of Carbon Steel Metal in 3 M Hydrochloric Acid: Gasometric, Colorimetry and Atomic Absorption Spectroscopy Views. Journal of Molecular and Engineering Materials, 06(01n02), 1850004. https://doi.org/10.1142/s2251237318500041

Rakanta, E., Zafeiropoulou, T., & Batis, G. (2013). Corrosion protection of steel with DMEA-based organic inhibitor. Construction and Building Materials, 44, 507–513. https://doi.org/10.1016/j.conbuildmat.2013.03.030

Ribeiro, D. V., & Abrantes, J. C. C. (2016). Application of electrochemical impedance spectroscopy (EIS) to monitor the corrosion of reinforced concrete: A new approach. Construction and Building Materials, 111, 98–104. https://doi.org/10.1016/j.conbuildmat.2016.02.047

Rodrigues, R., Gaboreau, S., Gance, J., Ignatiadis, I., & Betelu, S. (2021). Reinforced concrete structures: A review of corrosion mechanisms and advances in electrical methods for corrosion monitoring. Construction and Building Materials, 269, 121240. https://doi.org/10.1016/j.conbuildmat.2020.121240

Rosenberg, A. M., & Gaidis, J. M. (1979). MECHANISM OF NITRITE INHIBITION OF CHLORIDE ATTACK ON REINFORCING STEEL IN ALKALINE AQUEOUS ENVIRONMENTS. Materials Performance, 18(11). https://doi.org/http://worldcat.org/issn/00941492

Ryu, H. S., Singh, J. K., Yang, H. M., Lee, H. S., & Ismail, M. A. (2016). Evaluation of corrosion resistance properties of N, N′-Dimethyl ethanolamine corrosion inhibitor in saturated Ca(OH)2 solution with different concentrations of chloride ions by electrochemical

experiments. Construction and Building Materials, 114, 223–231. https://doi.org/10.1016/j.conbuildmat.2016.03.174

Sanjuán, M. A., Andrade, C., & Cheyrezy, M. (2003). Concrete carbonation tests in natural and accelerated conditions. Advances in Cement Research, 15(4), 171–180. https://doi.org/10.1680/adcr.2003.15.4.171

Saraswat, V., Kumari, R., & Yadav, M. (2022). Novel carbon dots as efficient green corrosion inhibitor for mild steel in HCl solution: Electrochemical, gravimetric and XPS studies. Journal of Physics and Chemistry of Solids, 160(August 2021). https://doi.org/10.1016/j.jpcs.2021.110341

Saraswathy, V., & Song, H. W. (2007). Improving the durability of concrete by using inhibitors. Building and Environment, 42(1), 464–472. https://doi.org/10.1016/j.buildenv.2005.08.003

Shi, J., Guan, X., Ming, J., & Zhou, X. (2022). Improved corrosion resistance of reinforcing steel in mortars containing red mud after long-term exposure to aggressive environments. Cement and Concrete Composites, 130(December 2021), 104522. https://doi.org/10.1016/j.cemconcomp.2022.104522

Shi, J., Wu, M., & Ming, J. (2020). Degradation effect of carbonation on electrochemical behavior of 2304 duplex stainless steel in simulated concrete pore solutions. Corrosion Science, 177(May), 109006. https://doi.org/10.1016/j.corsci.2020.109006

Shi, J., Wu, M., & Ming, J. (2022). In-depth insight into the role of molybdate in corrosion resistance of reinforcing steel in chloride-contaminated mortars. Cement and Concrete Composites, 132(June), 104628. https://doi.org/10.1016/j.cemconcomp.2022.104628

Singh, P., Brar, S. K., Bajaj, M., Narang, N., Mithu, V. S., Katare, O. P., Wangoo, N., & Sharma, R. K. (2017). Self-assembly of aromatic α-amino acids into amyloid inspired nano/micro scaled architects. Materials Science and Engineering C, 72, 590–600. https://doi.org/10.1016/j.msec.2016.11.117

Sirojiddin, Z. S. (2023). Protecting Metals from Corrosion : Preserving Durability and Longevity. 01(05), 11–13.

Snyder, K. A., Feng, X., Keen, B. D., & Mason, T. O. (2003). Estimating the electrical conductivity of cement paste pore solutions from OH À , K + and Na + concentrations. 33, 793–798. https://doi.org/10.1016/S0008-8846(02)01068-2

Song, H. W., & Saraswathy, V. (2007). Corrosion monitoring of reinforced concrete structures - A review. International Journal of Electrochemical Science, 2(1), 1–28.

Söylev, T. A., McNally, C., & Richardson, M. G. (2007). The effect of a new generation surface-applied organic inhibitor on concrete properties. Cement and Concrete Composites, 29(5), 357–364. https://doi.org/10.1016/j.cemconcomp.2006.12.013

Stefanoni, M., Angst, U., & Elsener, B. (2018). Corrosion rate of carbon steel in carbonated concrete – A critical review. Cement and Concrete Research, 103(June 2017), 35–48. https://doi.org/10.1016/j.cemconres.2017.10.007

Stewart, M. G., & Rosowsky, D. V. (1998). Structural Safety and Serviceability of Concrete Bridges Subject to Corrosion. Journal of Infrastructure Systems, 4(4), 146–155. https://doi.org/10.1061/(asce)1076-0342(1998)4:4(146)

Susanti, E., Wulandari, P., & Herman. (2018). Effect of localized surface plasmon resonance from incorporated gold nanoparticles in PEDOT:PSS hole transport layer for hybrid solar cell applications. Journal of Physics: Conference Series, 1080(1). https://doi.org/10.1088/1742-6596/1080/1/012010

Teymouri, F., Allahkaram, S. R., Shekarchi, M., Azamian, I., & Johari, M. (2021). A comprehensive study on the inhibition behaviour of four carboxylate-based corrosion inhibitors focusing on efficiency drop after the optimum concentration for carbon steel in the simulated concrete pore solution. Construction and Building Materials, 296, 123702. https://doi.org/10.1016/j.conbuildmat.2021.123702

Tharial Xavier, G., Thirumalairaj, B., & Jaganathan, M. (2015). Effect of Piperidin-4-ones on the Corrosion Inhibition of Mild Steel in 1 N H 2 SO 4. International Journal of Corrosion, 2015(1), 1–15. https://doi.org/10.1155/2015/410120

Tiwari, A., Goyal, S., Luxami, V., Chakraborty, M. K., & Gundlapalli, P. (2021). Evaluation of inhibition efficiency of generic compounds with additional heteroatom in simulated concrete pore solution and migration potential in concrete. Journal of Building Engineering, 43. https://doi.org/10.1016/j.jobe.2021.102490

Tiwari, A., Goyal, S., Luxami, V., Chakraborty, M. K., & Prabhakar, G. (2021). Assessment of corrosion inhibition efficiency of generic compounds having different functional groups in carbonated pore solution with chlorides and migration ability in concrete. Construction and Building Materials, 290, 123275. https://doi.org/10.1016/j.conbuildmat.2021.123275

Tiwari, A. K., Purnima, Goyal, S., & Luxami, V. (2023). Influence of corrosion inhibitors on two different concrete systems under combined chloride and carbonated environment. Structures, 48(August 2022), 717–735. https://doi.org/10.1016/j.istruc.2022.12.093

Tran, D. T., Lee, H. S., & Singh, J. K. (2023). Influence of phosphate ions on passive film formation in amino acid-containing concrete pore solutions with chloride ions. Journal of Building Engineering, 66(August 2022), 105834. https://doi.org/10.1016/j.jobe.2023.105834

Tritthart, J. (2003). Transport of a surface-applied corrosion inhibitor in cement paste and concrete. Cement and Concrete Research, 33(6), 829–834. https://doi.org/10.1016/S0008-8846(02)01067-0

Uddin, M. T., Islam, N., Sutradhar, S. K., Chowdhury, M. H. R., Hasnat, A., & Khatib, J. M. (2013). Carbonation coefficient of concrete in Dhaka City. Sustainable Construction Materials and Technologies, 2013-Augus(August).

Varvara, S., Berghian-grosan, C., Bostan, R., Lucacel, R., Salarvand, Z., Talebian, M., Raeissi, K., Izquierdo, J., & Souto, R. M. (2021). Electrochimica Acta Experimental characterization , machine learning analysis and computational modelling of the high effective inhibition of copper environment. Electrochimica Acta, 398, 139282. https://doi.org/10.1016/j.electacta.2021.139282

Vergnat, V., Heinrich, B., Rawiso, M., Muller, R., & Masson, P. (2021). Iron Oxide / Polymer Core – Shell Nanomaterials with Star-like Behavior. 1–19.

Verma, C., Alrefaee, S. H., Rhee, K. Y., Quraishi, M. A., & Ebenso, E. E. (2021). Thiol (-SH) substituent as functional motif for effective corrosion protection: A review on current advancements and future directions. Journal of Molecular Liquids, 324, 115111. https://doi.org/10.1016/j.molliq.2020.115111

Verma, C., Quraishi, M. A., & Rhee, K. Y. (2022). Hydrophilicity and hydrophobicity consideration of organic surfactant compounds: Effect of alkyl chain length on corrosion protection. Advances in Colloid and Interface Science, 306(June), 102723. https://doi.org/10.1016/j.cis.2022.102723

Verma, C., Singh, P., & Quraishi, M. A. (2016). A thermodynamical, electrochemical and surface investigation of Bis (indolyl) methanes as Green corrosion inhibitors for mild steel in 1 M hydrochloric acid solution. Journal of the Association of Arab Universities for Basic and Applied Sciences, 21, 24–30. https://doi.org/10.1016/j.jaubas.2015.04.003

Vernekar, D., & Jagadeesan, D. (2015). Tunable acid-base bifunctional catalytic activity of FeOOH in an orthogonal tandem reaction. Catalysis Science and Technology, 5(8), 4029–4038. https://doi.org/10.1039/c5cy00361j

Vijayaraghavan, K., Padmesh, T. V. N., Palanivelu, K., & Velan, M. (2006). Biosorption of nickel(II) ions onto Sargassum wightii: Application of two-parameter and three-parameter isotherm models. Journal of Hazardous Materials, 133(1–3), 304–308. https://doi.org/10.1016/j.jhazmat.2005.10.016

Viramontes-Gamboa, G., Rivera-Vasquez, B. F., & Dixon, D. G. (2007). The Active-Passive Behavior of Chalcopyrite. Journal of The Electrochemical Society, 154(6), C299. https://doi.org/10.1149/1.2721782

Wang, J. C., Ren, J., Yao, H. C., Zhang, L., Wang, J. S., Zang, S. Q., Han, L. F., & Li, Z. J. (2016). Synergistic photocatalysis of Cr(VI) reduction and 4-Chlorophenol degradation over hydroxylated α-Fe2O3 under visible light irradiation. Journal of Hazardous Materials, 311(July 2016), 11–19. https://doi.org/10.1016/j.jhazmat.2016.02.055

Wong, H. S., Zhao, Y. X., Karimi, A. R., Buenfeld, N. R., & Jin, W. L. (2010). On the penetration of corrosion products from reinforcing steel into concrete due to chloride-induced corrosion. Corrosion Science, 52(7), 2469–2480. https://doi.org/10.1016/j.corsci.2010.03.025

Wu, B., & Ye, G. (2017). Development of porosity of cement paste blended with supplementary cementitious materials after carbonation. Construction and Building Materials, 145, 52–61. https://doi.org/10.1016/j.conbuildmat.2017.03.176

Xiao, D., Dai, K., Qu, Y., Yin, Y., & Chen, H. (2015). Hydrothermal synthesis of α-Fe 2 O 3 /g-C 3 N 4 composite and its efficient photocatalytic reduction of Cr(VI) under visible light. Applied Surface Science, 358(Vi), 181–187. https://doi.org/10.1016/j.apsusc.2015.09.042

Xu, X. T., Xu, H. W., Li, W., Wang, Y., & Zhang, X. Y. (2022). A combined quantum chemical, molcular dynamics and Monto Carlo study of three amino acids as corroison inhibitors for aluminum in NaCl solution. Journal of Molecular Liquids, 345. https://doi.org/10.1016/j.molliq.2021.117010

Xu, Z., Wu, Y., Zhang, Z., Wang, Y., & Hu, J. (2023). A review on the research progress of LDHs as corrosion inhibitors for reinforced concrete. Journal of Building Engineering, 70(January), 106303. https://doi.org/10.1016/j.jobe.2023.106303

Yadav, M., Kumar, S., Sinha, R. R., Bahadur, I., & Ebenso, E. E. (2015). New pyrimidine derivatives as ef fi cient organic inhibitors on mild steel corrosion in acidic medium : Electrochemical , SEM , EDX , AFM and DFT studies. Journal of Molecular Liquids, 211, 135–145. https://doi.org/10.1016/j.molliq.2015.06.063

Ye, H., Radlińska, A., & Neves, J. (2017). Drying and carbonation shrinkage of cement paste containing alkalis. Materials and Structures/Materiaux et Constructions, 50(2). https://doi.org/10.1617/s11527-017-1006-x

Yohai, L., Schreiner, W., Vázquez, M., & Valcarce, M. B. (2016). Phosphate ions as effective inhibitors for carbon steel in carbonated solutions contaminated with chloride ions. Electrochimica Acta, 202, 231–242. https://doi.org/10.1016/j.electacta.2015.10.167

Yohai, L., Vázquez, M., & Valcarce, M. B. (2013). Phosphate ions as corrosion inhibitors for reinforcement steel in chloride-rich environments. Electrochimica Acta, 102, 88–96. https://doi.org/10.1016/j.electacta.2013.03.180

Zavala Olivares, G., Hernández Gayosso, M. J., & Mora Mendoza, J. L. (2007). Corrosion inhibitors performance for mild steel in CO2 containing solutions. Materials and Corrosion, 58(6), 427–437. https://doi.org/10.1002/maco.200604023

Zerfaoui, M., Oudda, H., Hammouti, B., Kertit, S., & Benkaddour, M. (2004). Inhibition of corrosion of iron in citric acid media by aminoacids. Progress in Organic Coatings, 51(2), 134–138. https://doi.org/10.1016/j.porgcoat.2004.05.005

Zhang, D. Q., Cai, Q. R., Gao, L. X., & Lee, K. Y. (2008). Effect of serine, threonine and glutamic acid on the corrosion of copper in aerated hydrochloric acid solution. Corrosion Science, 50(12), 3615–3621. https://doi.org/10.1016/j.corsci.2008.09.007

Zhang, J., Peng, Z., Zou, C., & Chen, D. (2018). Improving the carbonation resistance of cement stone for oil wells by a polymer with acid response characteristic. Journal of Petroleum Science and Engineering, 164(July 2017), 382–389. https://doi.org/10.1016/j.petrol.2018.01.080

Zhang, M., Hu, L., Wang, H., Song, Y., Liu, Y., Li, H., Shao, M., Huang, H., & Kang, Z. (2018). One-step hydrothermal synthesis of chiral carbon dots and their effects on mung bean plant growth. Nanoscale, 10(26), 12734–12742. https://doi.org/10.1039/c8nr01644e

Zhang, Q. H., Li, Y. Y., Lei, Y., Wang, X., Liu, H. F., & Zhang, G. A. (2022). Comparison of the synergistic inhibition mechanism of two eco-friendly amino acids combined corrosion inhibitors for carbon steel pipelines in oil and gas production. Applied Surface Science, 583(January). https://doi.org/10.1016/j.apsusc.2022.152559

Zhang, T., Zhao, N., Li, J., Gong, H., An, T., Zhao, F., & Ma, H. (2017). Thermal behavior of nitrocellulose-based superthermites: Effects of nano-Fe2O3 with three morphologies. RSC Advances, 7(38), 23583–23590. https://doi.org/10.1039/c6ra28502c

Zhang, Y., Wu, Y., Li, N., Jiang, Y., Qian, Y., Wang, L., & Zhang, J. (2021). Synergistic inhibition effect of L-Phenylalanine and zinc salts on chloride-induced corrosion of magnesium alloy: Experimental and theoretical investigation. Journal of the Taiwan Institute of Chemical Engineers, 121(3), 48–60. https://doi.org/10.1016/j.jtice.2021.03.047

Zhang, Z., Yang, B., Tai, B., & Zhu, Y. (2022). Effect of maize gluten meal extract as natural corrosion inhibitor on steel in mortar corroded by chloride. Journal of Building Engineering, 62(July), 105394. https://doi.org/10.1016/j.jobe.2022.105394

Zhao, R., Yu, Q., & Niu, L. (2022). Corrosion inhibition of amino acids for 316L stainless steel and synergistic effect of I− ions: Experimental and theoretical studies. Materials and Corrosion, 73(1), 31–44. https://doi.org/10.1002/maco.202112511

Zhao, Y., Pan, T., Yu, X., & Chen, D. (2019). Corrosion inhibition efficiency of triethanolammonium dodecylbenzene sulfonate on Q235 carbon steel in simulated concrete pore solution. Corrosion Science, 158, 108097. https://doi.org/10.1016/j.corsci.2019.108097

Zheng, H., Li, W., Ma, F., & Kong, Q. (2012). The effect of a surface-applied corrosion inhibitor on the durability of concrete. Construction and Building Materials, 37, 36–40. https://doi.org/10.1016/j.conbuildmat.2012.07.007

Zheng, X., Xu, K., Wang, Y., Shen, R., & Wang, Q. (2018). Study of hydrogen explosion control measures by using l-phenylalanine for aluminum wet dust removal systems. RSC Advances, 8(72), 41308–41316. https://doi.org/10.1039/c8ra08587k

Zhou, Y., & Zuo, Y. (2015). The inhibitive mechanisms of nitrite and molybdate anions on initiation and propagation of pitting corrosion for mild steel in chloride solution. Applied Surface Science, 353(2), 924–932. https://doi.org/10.1016/j.apsusc.2015.07.037

Zhu, W., François, R., Fang, Q., & Zhang, D. (2016). Influence of long-term chloride diffusion in concrete and the resulting corrosion of reinforcement on the serviceability of RC beams. Cement and Concrete Composites, 71, 144–152. https://doi.org/10.1016/j.cemconcomp.2016.05.003

Zhuang, J., Li, M., Pu, Y., Ragauskas, A. J., & Yoo, C. G. (2020). Observation of potential contaminants in processed biomass using fourier transform infrared spectroscopy. Applied Sciences (Switzerland), 10(12), 1–13. https://doi.org/10.3390/app10124345

Zomorodian, A. (2023). Review of Corrosion Inhibitors in Reinforced Concrete : Conventional and Green Materials.

Zomorodian, A., Bagonyi, R., & Al-Tabbaa, A. (2021). The efficiency of eco-friendly corrosion inhibitors in protecting steel reinforcement. Journal of Building Engineering, 38(December 2020), 102171. https://doi.org/10.1016/j.jobe.2021.102171

ANNEXURE A

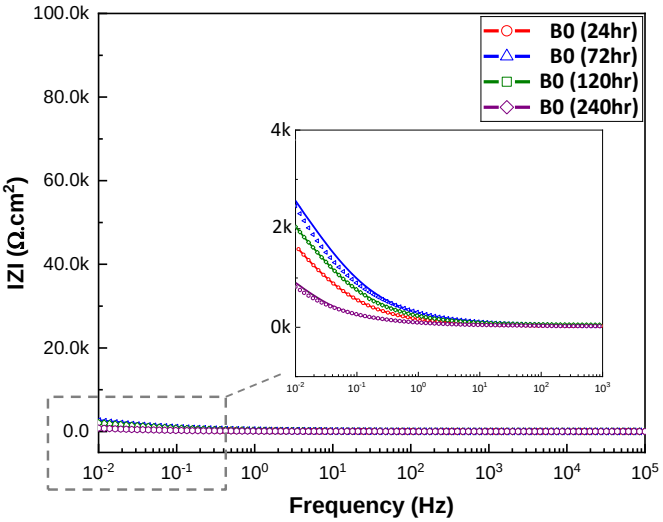

Figure A1 Bode plot of steel samples immersed in inhibitor-free pore solution (B0)

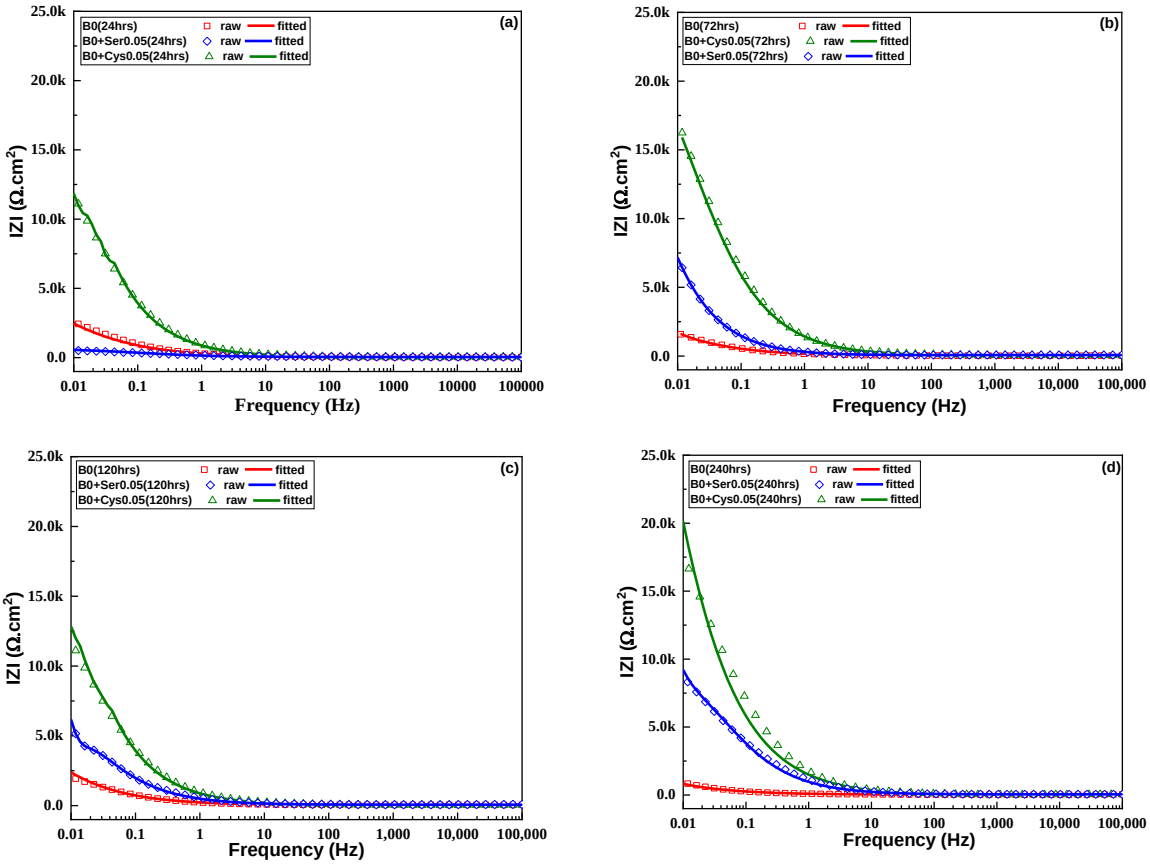

Figure A2 Bode plot of base solution and *Ser/Cys* added solutions for <u>0.05M</u> at (a)24 hrs; (b)72 hrs; (c)120 hrs; (d)240 hrs

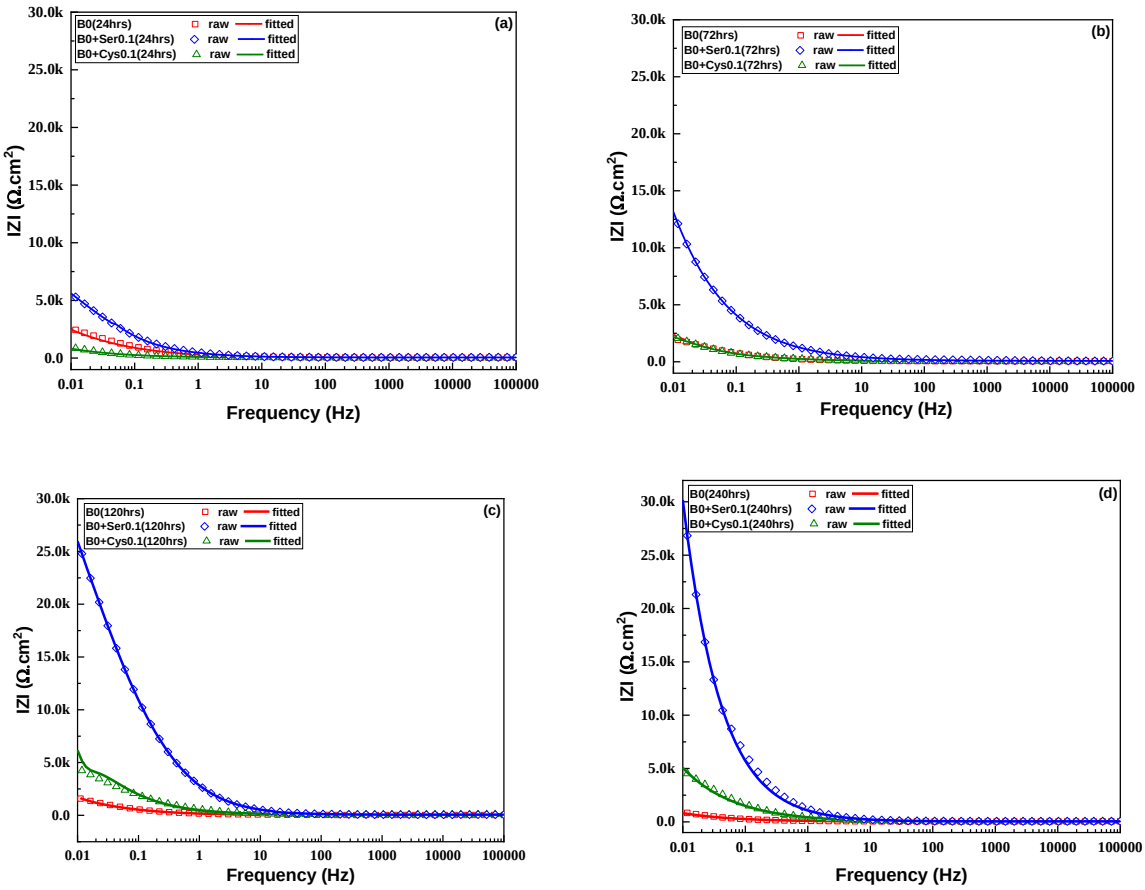

Figure A3 Bode plot of base solution and *Ser/Cys* added solutions for <u>0.1M</u> at (a)24 hrs; (b)72 hrs; (c)120 hrs; (d)240 hrs

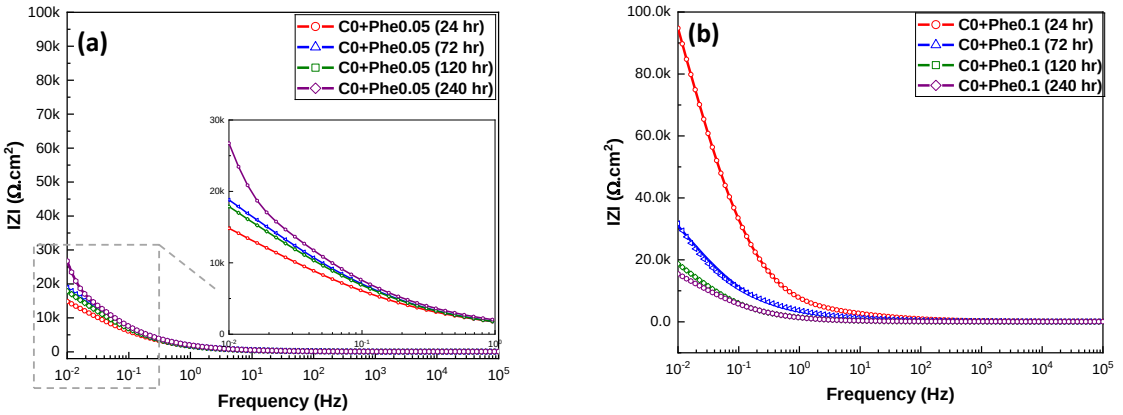

Figure A4 Bode plots of steel samples immersed in (a)B0+Phe0.05; (b)B0+Phe0.1

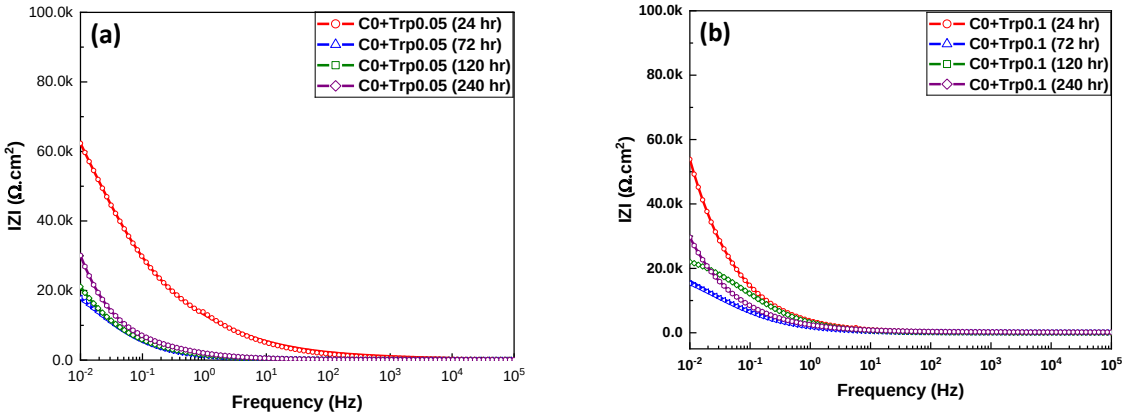

Figure A5 Bode plots of steel samples immersed in (a)B0+Trp0.05; (b)B0+Trp0.1

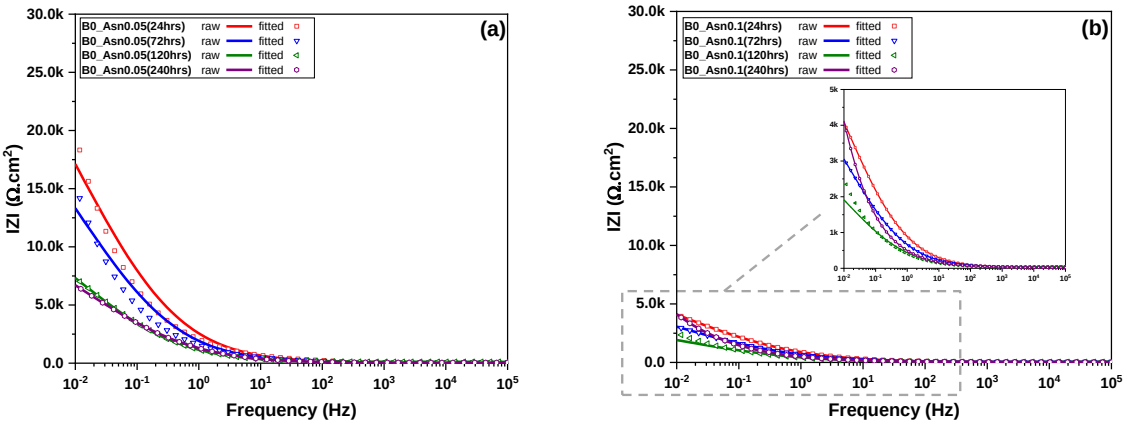

Figure A6 Bode plots of steel samples immersed in (a)B0+Asn0.05; (b)B0+Asn0.1

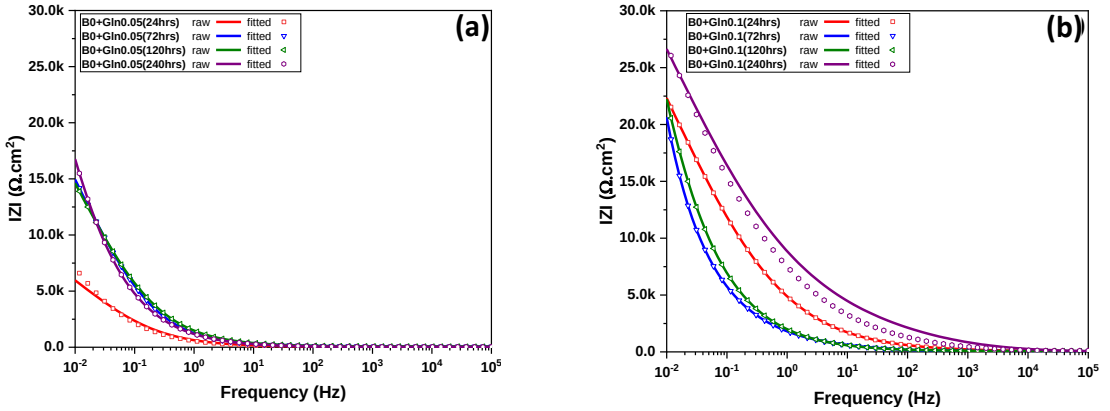

Figure A7 Bode plots of steel samples immersed in (a) B0+Gln0.05; (b) B0+Gln0.1

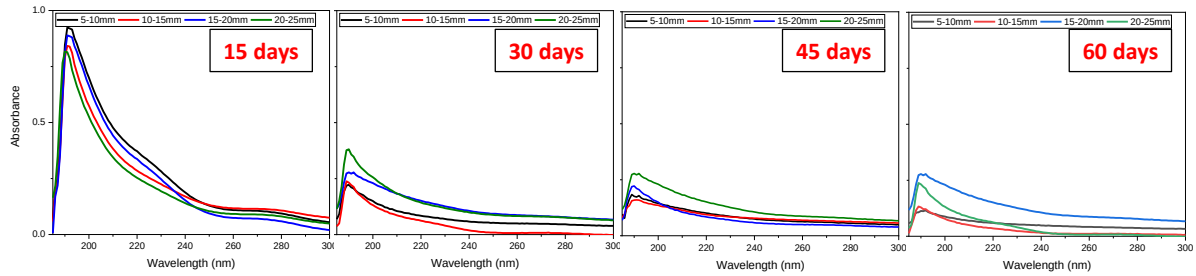

Figure A8 Absorbance peak of *Ser* after 1M application at different durations

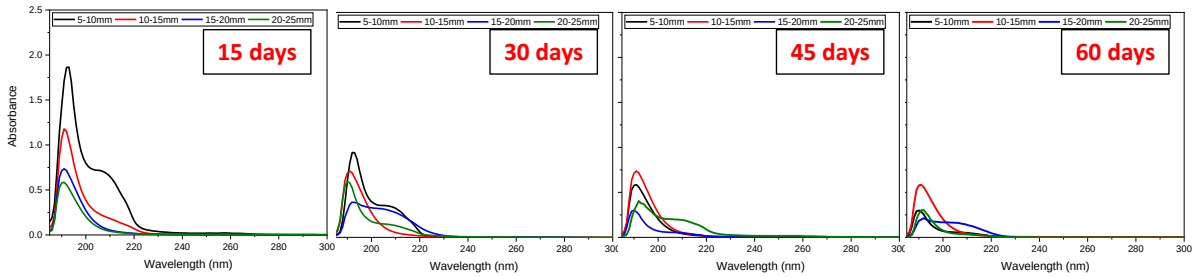

Figure A9 Absorbance peak of *Phe* after 1M application at different durations

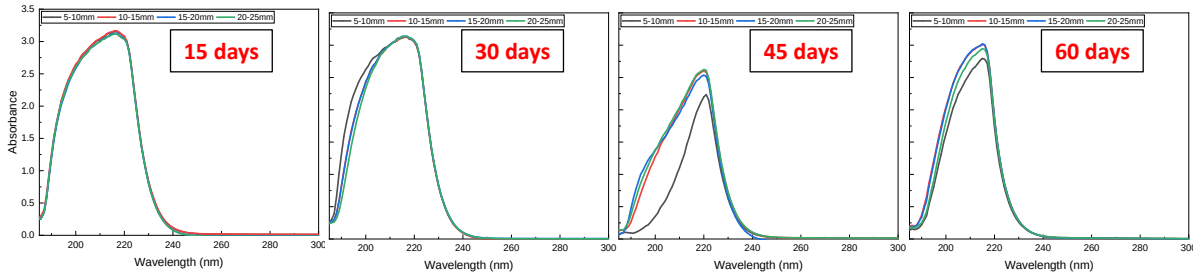

Figure A10 Absorbance peak of *Asn* after 1M application at different durations

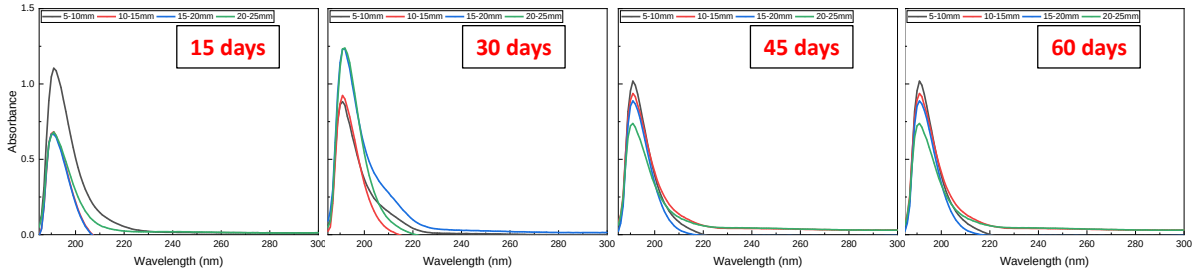

Figure A11 Absorbance peak of *Gln* after 1M application at different durations